Thermal Conduction in the Vortex State of Unconventional Superconductors

by

Etienne Boaknin

A thesis submitted in conformity with the requirements
for the degree of Doctor of Philosophy
Graduate Department of Physics and Astronomy
University of Toronto

Your file Votre référence
ISBN: 0-612-84833-7
Our file Notre référence
ISBN: 0-612-84833-7

Abstract

Thermal Conduction in the Vortex State of Unconventional Superconductors

Etienne Boaknin
Doctor of Philosophy
Graduate Department of Physics and Astronomy
University of Toronto
2003

When a magnetic field is applied to a type II superconductor, the field penetrates in the form of vortices wherein the superconducting order parameter vanishes over a length scale of 100 Å or so. Each vortex supports localized electronic states. Above the upper critical field H_{c2}, the normal state is recovered and the electronic states are fully delocalized. A basic question is to ask how the electronic states evolve from being localized to delocalized as the intervortex distance is reduced (*i.e.* as the magnetic field is increased).

For that purpose, we have performed systematic studies of the electronic thermal conductivity κ_e/T through the vortex state at temperatures as low as 50 mK and fields as high as 13 Tesla. This was done in a variety of systems: V_3Si, $LuNi_2B_2C$, $NbSe_2$ and $Tl_2Ba_2CuO_{6+\delta}$.

The work performed on the phonon-mediated V_3Si, $LuNi_2B_2C$ and $NbSe_2$ led to many surprises. V_3Si is an archetypal type-II superconductor and displays the expected activated behavior. It provides a solid basis for comparison. However, we found that the borocarbide superconductor $LuNi_2B_2C$ has a highly anisotropic gap of unprecedented magnitude (a factor of 10), while the layered compound $NbSe_2$ is found to display multi-band superconductivity.

We also studied the overdoped cuprate superconductor $Tl_2Ba_2CuO_{6+\delta}$ where the upper critical field was low enough for us to reach the normal state. The Wiedemann-Franz law was tested and found to be satisfied with a 1% experimental accuracy. This rep-

resents the first unambiguous evidence that the overdoped side of the phase diagram is a Fermi liquid and displays no sign of spin-charge separation and thus provides a solid basis for a comprehensive theory of the phase diagram of cuprate superconductors. In the superconducting state, we find that $Tl_2Ba_2CuO_{6+\delta}$ is the textbook example of a d-wave superconductor as it shows quantitative agreement with theory.

In summary we obtained a range of behaviors in several different types of superconductors, from the test case of the conventional V_3Si to the highly unconventional cuprates and through highly anisotropic and multi-band superconductors.

Statement of Originality

It is important to recall the earthquake that was started in the field of strongly correlated electron systems by the discovery of high temperature superconductors. It represents still today one of the biggest challenge in condensed matter physics. As such, it has led to much research on high T_c cuprates themselves, but has also generated interest in many peripheral issues which are thought to be of prime importance to its understanding. Good examples of this include 1/ the ruthenates, first thought to be directly related to cuprates due to the similarity in their crystal structures, but which have been seen to display new phenomena such as spin-triplet superconductivity in Sr_2RuO_4; 2/ the physics of quantum criticality has also been strongly revived in part due to the belief that it may govern the phase diagram of cuprates; 3/ the interplay of superconductivity and magnetism which has been studied in such systems as organic conductors, heavy fermion systems and the borocarbides. These examples are a small subset of the phenomena pertaining to high T_c's which have been studied and for which a growing understanding exists. In this thesis, we are concerned with cuprates themselves but we have also turned our attention to other forms of superconductivity.

The first project pertains to the non-magnetic members of the borocarbide family, in particular, to $LuNi_2B_2C$. These materials were discovered in 1994 and were soon thought to be quite conventional phonon-mediated superconductors with an s-wave gap. It is only six or seven years later that we gave the first unambiguous proof that their gap was highly anisotropic (Etienne Boaknin, R.W. Hill, Cyril Proust, C. Lupien, Louis Taillefer, and P.C. Canfield, Phys. Rev. Lett. **87**, 237001 (2001)). This situation is very reminiscent of the early debates in high T_c cuprates where the gap was thought to have s-wave symmetry until 1993 (seven years after their discovery) when it was convincingly showed to have d-wave symmetry. Also, our results now stand as the first report of such a large anisotropy (factor 10) in the gap of a superconductor with no topological nodes. I expect this case of a highly anisotropic s-wave gap to serve as a reference point to differentiate gaps with nodes and those with accidental minima in novel materials. All experimental parts of this project were done by myself, with the help of Rob Hill, Cyril Proust and Christian Lupien. The crystals were grown by our collaborator Paul Canfield. The paper was written in most part by myself, Louis Taillefer, and Rob Hill, and with the participation of all co-authors.

The recent discovery of the 40-K superconductor MgB_2 has led to a renewed interest

in exploring multi-band superconductivity were gaps of significantly different magnitudes exist on different Fermi surfaces of a material. While much effort has been focused on MgB_2 itself, we reported some of the first evidence for multi-band superconductivity in a second compound, namely, $NbSe_2$ (Etienne Boaknin, M. A. Tanatar, Johnpierre Paglione, D. Hawthorn, F. Ronning, R. W. Hill, M. Sutherland, Louis Taillefer, Jeff Sonier, S. M. Hayden, and J. W. Brill, Phys. Rev. Lett. **90**, 117003 (2003)). This was yet another surprise as this material has been studied extensively since the early 60's and was thought to be a rather conventional superconductor. We also show that previous reports of anomalous properties could now be understood naturally with this new interpretation. All experimental parts of this project were done by myself with the help of Makariy Tanatar, Johnpierre Paglione and the support of other members of the group. The samples of $NbSe_2$ were grown by Joe Brill. Jeff Sonier kindly provided us with the same samples used in previous studies of both specific heat and muon spin resonance. Steve Hayden provided us with V_3Si samples which were also used previously for de Haas-van Alphen studies. The paper was written in most part by myself, Louis Taillefer, Makariy Tanatar, Johnpierre Paglione, and Filip Ronning, and with the participation of all co-authors.

The Wiedemann-Franz law was experimentally observed 150 years ago and is extremely robust with no reports of it being violated until very recently by our group. It relates, in a universal way, the electrical and thermal transport in a solid, and states simply that the carriers of charge and heat are one and the same. In the context of high temperature superconductivity, where the issue of spin-charge separation has been central since their discovery in 1986, testing this law is a simple and elegant way to verify or negate the existence of spin-charge separation. However, this law only applies in the normal state of superconductors such that one needs to apply a magnetic field large enough to suppress the superconductivity completely. This turns out to be a difficult task. After the observation of such a violation in the optimally doped superconductor PCCO by our group, we turned our attention to the overdoped side of the phase diagram, where the normal state is thought to be a conventional Fermi-Liquid. In highly overdoped $Tl_2Ba_2CuO_6$, we have found that the Wiedemann-Franz law is satisfied with an experimental accuracy of 1% (Cyril Proust, Etienne Boaknin, R. W. Hill, Louis Taillefer, and A. P. Mackenzie Phys. Rev. Lett. **89**, 147003 (2002)). These results provide a strong basis for a comprehensive theory of the phase diagram in cuprate superconductors by establishing that there is no spin-charge separation in the overdoped regime but rather

that these systems form a Fermi-Liquid. The experimental work was done in equal parts by myself and postdoctoral fellow Cyril Proust and with the support of other members of the group. The paper was written by myself, Cyril Proust, and Louis Taillefer, and with the participation of all co-authors. The crystals were grown by our collaborator Andrew Mackenzie.

In summary, this thesis presents studies of several forms of unconventional superconductivity. Many unexpected and novel results were obtained with the discovery of a highly anisotropic gap in the borocarbides (long thought to have an isotropic gap), the phenomenon of multi-band superconductivity in $NbSe_2$, a material studied for over 40 years, and a clear experimental proof that there is no spin-charge separation, in the overdoped regime of high T_c cuprates, contrary to some theoretical proposals.

The work presented in this thesis has appeared in the following publications:

- "Heat conduction in the borocarbide superconductor $LuNi_2B_2C$", Etienne Boaknin, R.W. Hill, Christian Lupien, Louis Taillefer and P.C. Canfield Physica C, **341-348**, 1845 (2000). (Invited Paper at the M2MS-HTSC-VI conference, Houston Texas)

- "Highly Anisotropic Gap Function in Borocarbide Superconductor $LuNi_2B_2C$", Etienne Boaknin, R.W. Hill, Cyril Proust, C. Lupien, Louis Taillefer, and P.C. Canfield, Phys. Rev. Lett. **87**, 237001 (2001).

- "Heat Transport in a Strongly Overdoped Cuprate: Fermi Liquid and a Pure *d*-Wave BCS Superconductor", Cyril Proust, Etienne Boaknin, R. W. Hill, Louis Taillefer, and A. P. Mackenzie, Phys. Rev. Lett. **89**, 147003 (2002).

- "Heat Conduction in the Vortex State of $NbSe_2$: Evidence for Multiband Superconductivity", Etienne Boaknin, M. A. Tanatar, Johnpierre Paglione, D. Hawthorn, F. Ronning, R. W. Hill, M. Sutherland, Louis Taillefer, Jeff Sonier, S. M. Hayden, and J. W. Brill, Phys. Rev. Lett. **90**, 117003 (2003).

Acknowledgements

It is with great pleasure that I write these lines which will hopefully express my tremendous gratitude to the people that I have walked with for the past few years.

I would first want to thank Louis Taillefer for more than I know I should thank him for. Not only did he open the door to the world of research, invited me in, but he gave me a tour of the place which showed me all its beauty and wonderful little corners. All this with an ingenious blend of freedom, guidance and toughness, adding a heavy pinch of enthusiasm and love, care, tenderness or whatever you want to name it. For all of this and for his friendship which is very dear to me, I am eternally grateful. Merci Louis!

It is also with many others that I have shared this experience, that I have made my first steps and my later ones in the world of research. Without them, the journey would have been impossible and quite boring. Many thanks to May, Christian (F), Rob, Cyril (F), Makariy, Johnpierre, Dave, Mike, Andrew, Harry, Chris and Robert (F) for the good times and the bad, for your friendships, for the laughs and for more to come (the "F" is for names that should be pronounced in french).

I have also had the chance to work with an uncountable number of scientists which have showed me the international and the dynamic nature of research. For this, I thank in particular close collaborators such as Smitha Vishveshwara, Courtney Lannert, Zlatko Tešanović, Paul Canfield, Andy Mackenzie, Jeff Sonier, Steve Hayden, Saša Dukan, Patrick Fournier, Cedomir Petrović, Adam Durst, all the members and students of the CIAR superconductivity program, the many friends met at conferences and summer school I attended (with special thanks to the organizers of the Boulder summer school on condensed matter physics).

One of the reasons I came to Toronto to do graduate work was the great research environment, and I was not disappointed. What a wonderful place to develop! The many different fields of research (both within and outside of physics), the dynamic between the experimental and theoretical groups, the fellow graduate students... I would like to thank in particular Mike Walker and John Wei for the many discussions (sometimes in the middle of the night), Hae-Young Kee, Yong Baek Kim, Bryan Statt and Robert Birgeneau. Also Marianne Khurana for all her help, support and motherly instincts, Judy Fotherby for making life so simple, Rob Henderson for quenching our neverending thirst for liquid helium and the rest of the staff which really made the environment very pleasant. Thanks also to Amanda Peet for her enthusiasm and her dedication to

pedagogy which I so gladly shared.

The writing of a thesis can often be a laborious task. I would like to thank Martin Grant and the staff at the Department of Physics at McGill University for their hospitality while this thesis was being written.

As most graduate students, I often had to explain to friends that I was getting paid to study. This concept was quite foreign to them and I must thank the National Sciences and Engineering Research Council of Canada (NSERC), the Sumner Foundation, the Ontario Graduate Scholarship Program, the University of Toronto and the Van Kranendonk teaching awards for making this concept a reality. They provided me with much needed funding for my graduate experience.

These four years in Toronto did include some hard work but also involved a lot of fun. I can't thank enough my many friends both in Toronto and in Montréal for the good times. Sidney, Sébastien (and the Poli Sci bunch), Andrew and Monia, Stev-o, Pet-o, Christian, Benoit, Tiago, the Judo group, and so many others. Rémi, Vadim, Marielle, Kiron, Nico, Dérev, Ed, Yusuke, Axel, les deux Sonia et tout les autres. Merci!

Finalement, j'aimerais remercier ma famille. M'man, grand papi, Nico, Leesa et les enfants, Hugo, Ben, mon père, Muriel, Emmanuelle et Vincent, Antoine, et tous les cousins-cousines, tantes-oncles... Ma source inépuisable d'amour.

A ma mère et à mon grand père.

Contents

List of Tables

List of Figures

Chapter 1

Superconductivity: an introduction

The phenomenon of superconductivity was discovered in 1911 by Kamerligh-Onnes in mercury. Its most prominent physical property is that a superconductor can carry charge perfectly well. In other words, its resistance is nil. It is not however until 1957 that a theoretical model was developed to understand this behavior: Bardeen, Cooper and Schriffer (BCS) [1, 2, 3] are responsible for this theoretical picture which is now seen as a milestone in the field of strongly correlated electron systems and in physics in general. It has made it possible to make superconductivity one of the best understood phenomenon in condensed matter physics, although perhaps too well. The field of research matured very rapidly, and soon, activity grew dim.

However, in the past 20 or 25 years, there has been a striking revival of interest. This is due to the discovery of new materials displaying superconductivity for which the BCS theory and its extensions are perhaps no longer entirely valid. New forms of superconductivity emerged and to this day a proper theoretical picture remains to be found.

The aim of this chapter is not to provide a complete or rigorous review of superconductivity. Instead, it will aim to first give an introduction of the main concepts that will be of prime importance within this thesis. Secondly, it will review the foundations of the original theory of superconductivity in order to show where it may fail in explaining new forms of superconductivity or, in other words, unconventional superconductivity. The chapter can altogether be skipped by a reader familiar with superconductivity.

1.1 BCS theory of superconductivity

The BCS theory of superconductivity was developed in 1957 [2, 3]. It is a masterpiece of theoretical work in the sense that it has provided a microscopic understanding of a macroscopic phenomenon where the interactions of an uncountable number of electrons is central. In addition to this, it is a theory with only one parameter: the critical transition temperature T_c.

In a superconductor, electrons form Cooper pairs (pairs of electrons). The mechanism that make these strongly repelling creatures pair is an attractive interaction which acts via the lattice of the crystal. The Cooper pairs then condense into a single state (the ground state of the system) which has a macroscopic coherence of both amplitude and phase. The central physical concept is the gap that forms in the energy spectrum. Let us follow the story of superconductivity through the eyes of BCS.

1.1.1 Cooper pairs

The first part in the development of the BCS theory was to show that the formation of electron pairs is possible if electrons are attracted to one another by some potential. This is called the Cooper problem [1]. He showed that this was indeed possible in a *Fermi-liquid* (FL) [4]. He asked whether it would be energetically more favorable to add a pair of bound electrons to a Fermi sea of electrons than to simply add two unbound electrons. And indeed it was (in the presence of an attractive potential). The Fermi sea is said to be unstable to Cooper pairs. The assumptions were the following:

- The ground state of the system is a Fermi-liquid
- Pairs have a total momentum equal to zero: one electron is in state **k** while the other is in state **-k**
- Pairs are spin singlets. Their spin component is $\frac{1}{\sqrt{2}}(|\uparrow\downarrow\rangle - |\downarrow\uparrow\rangle)$
- The attractive potential V_{kk} binding the two electrons is isotropic

The amazing result is that the pairing of electrons will occur independently of the strength of this attractive potential: it can be arbitrarily small. As a note, the size of these Cooper pairs is named the BCS coherence length and is given by $\xi_{BCS} = \xi_0 = a\frac{\hbar v_F}{k_B T_c}$ where $a = 0.15$, v_F is the Fermi velocity and T_c is the transition temperature. Typically,

this size is much larger than the average distance between two electrons in the material. The question remains: how can one obtain an attractive potential between two electrons?

1.1.2 Attractive interaction

To obtain a full microscopic picture, one needed to understand the mechanism behind the attractive interaction between electrons. Indeed, in a vacuum, electrons will always strongly repel one another due to the Coulomb force. In a material though, many other ingredients can add spice to the sauce and it was found that phonons were the culprits. That is, electrons can be attracted to one another via an interaction with a phonon. This can be most simply understood in the following way: 1/ a negatively charged electron creates a displacement of the positively charged lattice which is attracted to it, 2/ after the first electron has passed, the lattice has not yet had time to relax and creates a region of net positive charge with respect to the rest of the lattice, and 3/ a second electron is attracted by this region of positive charge. Effectively, the second electron is attracted to the second via a retarded interaction with the lattice. A rigorous treatment can be found for example in [5] .

1.1.3 Macroscopic wavefunction

Now that we know that we can obtain one pair of electrons, we must ask ourselves what happens to the entire system of electrons. It turns out that simply having all the electrons form Cooper pairs is not enough to achieve superconductivity. This is simply the beginning of the story.

The main achievement of the BCS theory was to find the *macroscopic wave function* Ψ_{BCS} of the system of electrons. But indeed, Cooper pairs rather than individual electrons are the starting components of the wavefunction. The latter is written in the following form within the framework of second quantization:

$$| \Psi_{BCS}\rangle = \prod_{\text{all k}} (u_k + v_k \, c^\dagger_{k\uparrow} \, c^\dagger_{-k\downarrow})|0\rangle \tag{1.1}$$

where u_k and v_k are the so-called coherence factors and are complex numbers , $c^\dagger_{k\uparrow}$ ($c^\dagger_{-k\downarrow}$) is the creation (destruction) operator for a state of momentum k ($-k$) and spin up (down). $|0\rangle$ is the vacuum state. The magnitudes of the coherence factors are related by $|u_k|^2+|v_k|^2 = 1$ and represent respectively the probability of finding the Cooper pair state

$(k\uparrow, -k\downarrow)$ empty ($|u_k|^2 = 1 - |v_k|^2$) or occupied ($|v_k|^2$). These parameters characterize the superconducting state.

Without venturing into the formalism, we note that the important result is that *all the Cooper pairs are condensed into a single state and are phase coherent.* This macroscopic coherence is in fact the main and only necessary requirement to obtain superconductivity.

1.1.4 The superconducting gap

One of the most characteristic features of a superconductor is a gap Δ in the electronic excitation spectrum which develops below T_c. It is given by the following relation:

$$\Delta_{kk'} = -\sum_k V_{kk'} u_{k'} v_{k'} \tag{1.2}$$

where $V_{kk'}$ is the attractive potential between two electrons. In its simplest form (the one used by BCS), it is given by:

$$V_{kk'} = \begin{cases} -V \text{ if } |\epsilon_k - \epsilon_F| \text{ and } |\epsilon_{-k} - \epsilon_F| < \hbar\omega_c \\ 0 \quad \text{otherwise} \end{cases} \tag{1.3}$$

where ϵ_k is the excitation energy (see below), ϵ_F is the Fermi energy and $\hbar\omega_c$ is some cutoff energy. Two main factors must be noticed about this relation: 1/ the potential is *isotropic* and 2/ it has no momentum dependence and has a sharp cutoff energy that is of the order of the Debye energy (the energy of the phonons responsible for the pairing). Following through, one obtains that the *superconducting gap is isotropic* and has a value at zero temperature of:

$$\Delta_{BCS}(T=0) = 1.76\ k_B T_c \tag{1.4}$$

Its temperature dependence is shown in Fig. 1.1a. It is zero above T_c and grows as $1.74(1 - T/T_c)^{1/2}$ near T_c to a constant value $\Delta_{BCS}(0)$ below about 0.4 T_c. In the weak coupling limit (when $N(\epsilon_F)V \ll 1$, where $N(\epsilon_F)$ is the density of states at the Fermi energy), it is also given by $\Delta_{BCS} \approx 2\hbar\omega_c e^{-1/N(\epsilon_F)V}$. To lighten the notation, we will refer to the BCS gap simply as Δ henceforth.

The superconducting gap plays a major role in the excitation spectrum which has the form:

$$E_k = \sqrt{(\epsilon_k - \epsilon_F)^2 + \Delta^2} \tag{1.5}$$

where ϵ_k refers to the excitation spectrum of the Fermi liquid and ϵ_F is the Fermi energy. It is displayed in Fig. 1.2a. Another way to present it is to look at the density of states

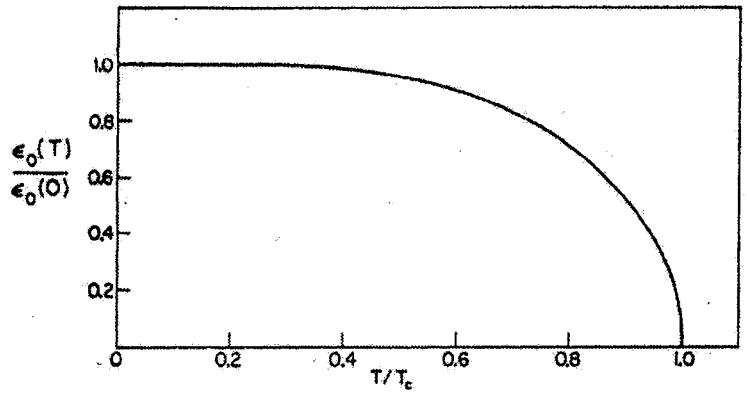

Figure 1.1: The temperature dependence of the superconducting gap (here labelled ϵ) [2]. At $T = 0$, the gap is predicted to be $\Delta(0) = 1.76\ k_B T_c$.

as a function of energy (see Fig. 1.2b) which is given by:

$$\frac{N_S(E)}{N_N(\epsilon_F)} = \begin{cases} \frac{E}{(E^2-\Delta^2)^{1/2}} & \text{if } E > \Delta \\ 0 \text{ if } E > \Delta \end{cases} \tag{1.6}$$

There are no states below Δ and a singularity at $E_k = \Delta$ where $E_k \equiv \epsilon_k - \epsilon_F$. The density of states then decreases to its normal state value $N_N(\epsilon_F)$.

The superconducting gap is central in explaining many of the physical properties of superconductors. But more importantly, it is also associated directly with the order parameter as will be discussed below [6].

1.1.5 Notable physical properties

The success of BCS theory was very quickly known as it predicted correctly all experimental observations. The most notable ones are presented here.

Thermodynamically, superconductivity appears through a second order phase transition. In this case, a discontinuity appears at T_c in the specific heat as seen in Fig. 1.3a. This discontinuity was correctly predicted to be $\frac{\Delta C}{C_N}|_{T_c} = \frac{C_s - C_N}{C_N}|_{T_c} = 1.43$ (for a table of values of this ratio in different materials, see for example [7]).

Also, many thermal or transport properties display an activated behavior below T_c. This is caused by the gap in the electronic excitation spectrum. For example, the heat capacity in the superconducting state normalized by its normal state value is seen to obey $\frac{C_s(T)}{C_N(T)} = e^{-\Delta/k_B T}$ [8] (although the BCS prediction is slightly different). The predicted thermal conductivity [9] is similar and was confirmed experimentally [10] (see Fig. 2.4).

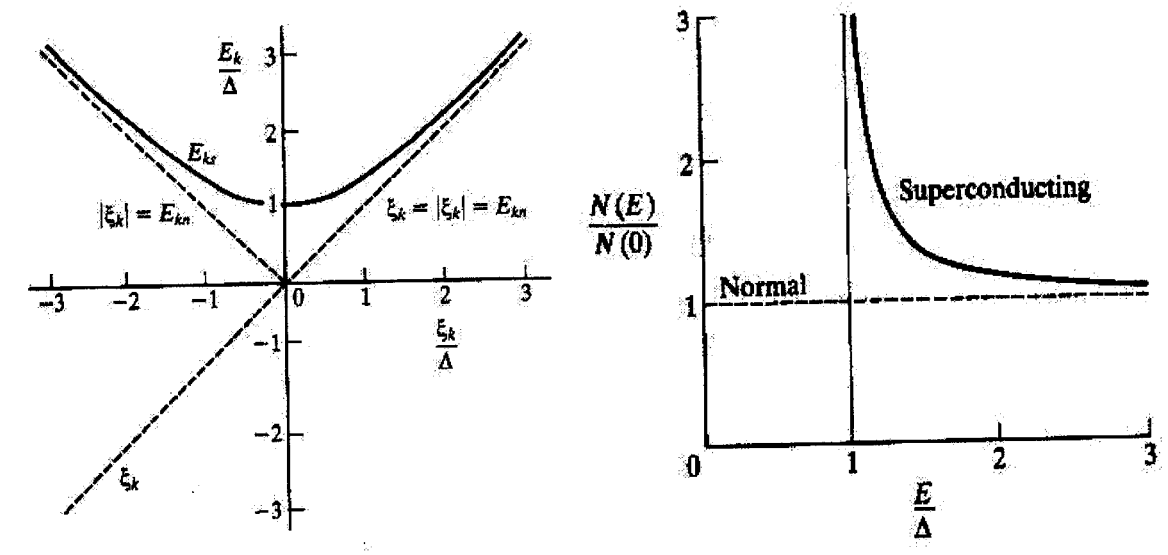

(a) (b)

Figure 1.2: (a) Normalized density of states as function of energy for an s-wave superconductor. It is nil below the superconducting gap. (b) The excitation spectrum for an s-wave superconductor near the Fermi surface. It is characterized by the superconducting energy gap.

Also, other effects were observed which were a directly related to the coherence factors from BCS theory. This was the case for ultrasound attenuation which shows a sharp drop at T_c and the nuclear relaxation rate $1/T_1$ which, instead, is predicted to rise below T_c (see Fig. 1.3b). This "peak" was first verified by Hebel and Slichter in 1957 [11].

1.2 Type II superconductivity

The most determining property of superconductors (after their nil resistivity) is the fact that they display perfect diamagnetism. Indeed the magnetic field inside a superconductor is always equal to zero. However, this is correct only for so-called Type I superconductors. Instead, for the second kind (Type II superconductors), the magnetic field can and does penetrate, but in a very particular way: in the form of vortices. This was first postulated theoretically by Abrikosov [12].

The generic phase diagram for type II superconductor is shown on Fig. 1.4a. One can see that, in addition to the Meissner state where one gets perfect diamagnetism (for $H < H_{c1}$), there exists another state where the magnetic field does penetrate in the form

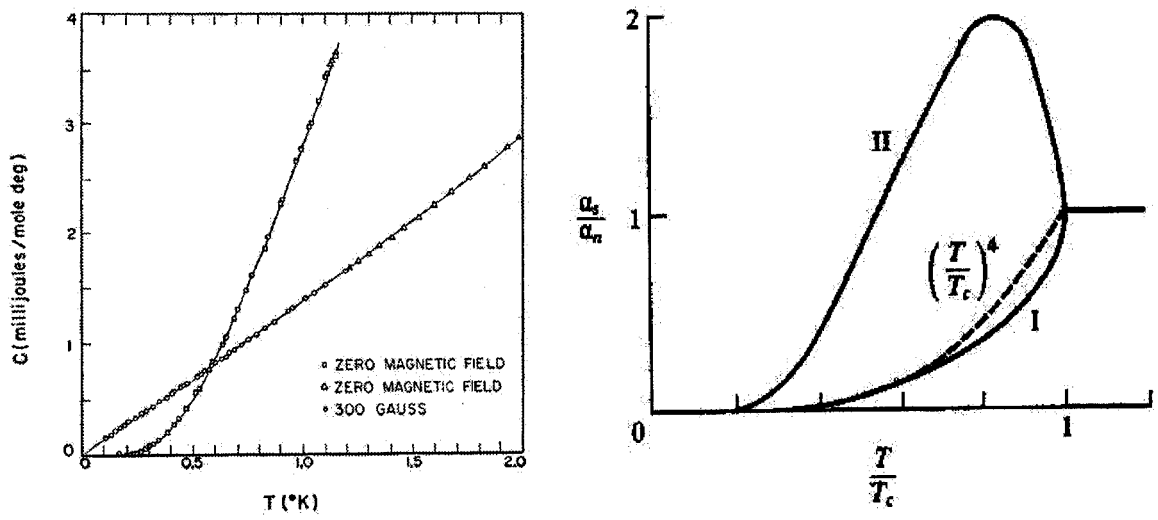

(a) (b)

Figure 1.3: (a) The heat capacity of Aluminium (T_c = 1.2 K) as a function of temperature in the superconducting state and in the normal state (for $H > H_c$) [8]. The jump at T_c is characteristic of a second order phase transition and its size is in agreement with BCS theory of superconductivity. Below T_c the behavior is activated and agrees with a superconducting gap of magnitude $\Delta(0) = 1.76\ T_c$. (b) The predicted behavior of the ultrasound attenuation α (labelled "I" here) and the nuclear relaxation rate (labelled "II"). The sharp drop in the former and the increase (or peak) in the latter are a product of the coherence factors from BCS theory.

of vortices. They form a vortex lattice that was rightfully predicted to be triangular [13]. Above the upper critical field H_{c2}, the normal state of the system is reached. Another way to express the magnetic diagram is seen in Fig. 1.4b. There, one sees that the internal magnetic field B is zero with respect to applied field H until $H = H_{c1}$. The magnetic field is then allowed to penetrate the sample but incompletely. Beyond H_{c2}, the superconductivity is destroyed and the normal state is recovered. Note that all superconductors of interest in the last two decades are of type II.

We will review the main characteristics of type II superconductors starting by introducing the two characteristic length scales (magnetic and electronic) to better review their main properties.

1.2.1 Length scales of superconductivity

A type II superconductor is defined as having $\kappa > \frac{1}{\sqrt{2}}$ where $\kappa = \frac{\lambda}{\xi}$. We will thus first discuss these two length scales associated with superconductivity: the coherence length

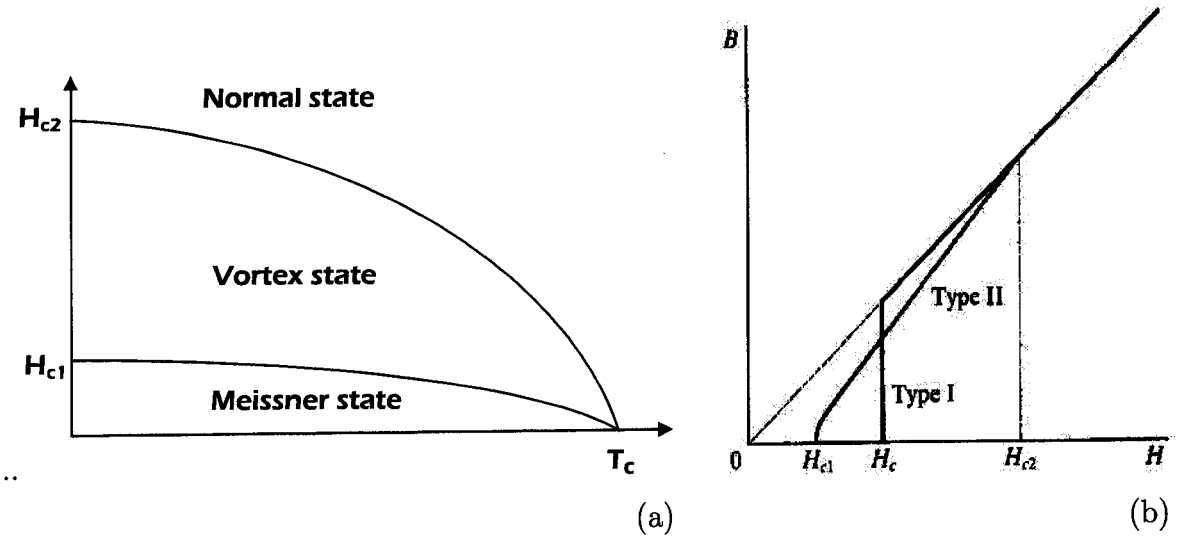

Figure 1.4: (a) The generic H-T phase diagram for a type II superconductor. Below H_{c1}, no field penetrates the superconductor: this is the Meissner state. Between H_{c1} and H_{c2} is the vortex state where the field penetrates in the form of vortices. Above H_{c2} the normal state is recovered. (b) Another way to see this is to look at the internal magnetic field B as a function of applied field H.

ξ and the magnetic penetration depth λ. They are both best understood in the context of the Ginzburg-Landau (GL) theory of second order phase transitions [14]. There, the order parameter of superconductivity is the macroscopic wave-function itself. It is nil above T_c and smoothly becomes non-zero below T_c. This is modelled simply by writing the free energy density as

$$f_s(0) = f_N(0) + \alpha|\Psi|^2 + \frac{\beta}{2}|\Psi|^4 + \frac{1}{2m^*}|(\frac{\hbar}{i}\nabla - \frac{e^*}{c}\mathbf{A})\Psi|^2 + \frac{h^2}{8\pi} \tag{1.7}$$

where the subscript refers to the superconducting or normal state and Ψ is the order parameter, in this case, the superconducting wave function. It was also identified by Gor'kov that the order parameter is the gap function such that $\Psi \propto \Delta$ [6]. The parameter α is negative below T_c and has a temperature dependence $|\alpha| \propto (T - T_c)$ whereas β is independent of temperature to first order. Minimizing the free energy one easily finds that $|\Psi|^2 = -\frac{\alpha}{\beta}$.

The London penetration depth λ_L

The magnetic field varies in a superconductor on the characteristic length scale called the London penetration depth λ_L. For example, in a magnetic field and at the interface

between a superconductor and vacuum, the magnetic field will go to zero inside the SC over this characteristic length scale. This result can be obtained by using the London approximation for the GL equations (assuming that the order parameter does not vary in space). This describes the spatial variation of the magnetic field in a superconductor and gives:

$$\lambda_L^2 = \frac{m^* c^2}{4\pi n_s e^{*2}} = \frac{mc^2}{4\pi n_s e^2} \tag{1.8}$$

where m^* and e^* are the masses and charge of the relevant particles: Cooper pairs and therefore $m^* = 2m$ and $e^* = 2e$. Also, $n_s = |\Psi|^2$ is defined to be the superfluid density and represents the density of Copper pairs. The temperature dependence is found to be: $\lambda(T) \simeq \frac{\lambda(0)}{[1-(T/T_c)^4]^{1/2}}$.

The penetration depth can be measured via several magnetic probes such as muon spin resonance (μSR), which measures the spatial variation of the magnetic field within the vortex lattice and infers an absolute value for λ_L. The temperature dependence $\lambda(T)$ can be measured more precisely in the Meissner state by following the effective volume which displays diamagnetism (for example, via magnetic induction or microwave cavity perturbation techniques). A rough estimate can also be obtained by the measured lower critical field H_{c1}. Indeed, they are related in the following way: $H_{c1} = \frac{\Phi_0}{4\pi\lambda_L^2}(ln(\kappa)+0.497)$ where Φ_0 is the flux quantum and $\kappa = \lambda/\xi$. And so, in many instances, $\lambda_L^2 \sim \frac{\Phi_0}{4\pi H_{c1}}$.

The Ginzburg-Landau coherence length ξ

The coherence length is the characteristic length scale over which the order parameter varies. For example, at the interface between a superconductor and a vacuum, $|\Psi|^2$ will go from zero outside to its full amplitude inside over this characteristic length scale. It is obtained via the GL equations which give:

$$\xi^2(T) = \frac{\hbar^2}{2m^*|\alpha(T)|} \tag{1.9}$$

Its temperature dependence is given by the coefficient $|\alpha(T)| \propto 1 - (T/T_c)$.

This quantity is very hard to measure directly. It is usually inferred by the upper critical field H_{c2}. They are related in the following way:

$$\xi^2(T) = \frac{\Phi_0}{2\pi H_{c2}(T)} \tag{1.10}$$

However, the radius of the vortex cores can be measured directly by Scanning Tunneling Microscopy (STM) or by μSR. The latter is a magnetic probe and may seem out

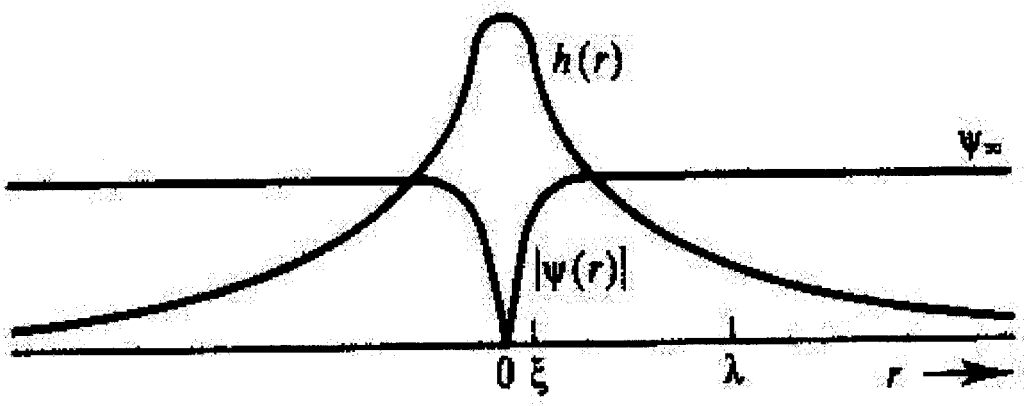

Figure 1.5: The spatial variation of the order parameter and the magnetization around a single vortex. The order parameter (*i.e.* the wave function or the gap) goes to zero at the center of the vortex whereas the internal field $h(r)$ is maximal there and zero outside of it.

of place, but there exists a magnetic signature of ξ in the spatial profile.

1.2.2 Vortex state

Vortices form because it is more energetically favorable to have domain walls between superconducting and normal metal in a type II superconductor. These walls are always found at the boundaries of a physical sample but vortices also constitute such walls.

Flux quantization

As explained above, the field penetrates the superconductor in the form of vortices. However, it turns out that the magnetic flux through each vortex has a fixed value: the flux quantum Φ_0. The physics that lies behind this is most easily understood by thinking of a superconducting ring. The macroscopic wave function must be single valued on that ring. For this reason, the flux going through this ring is quantized and has a value of:

$$\Phi = n\Phi_0 = n\frac{hc}{e^*} = n\frac{hc}{2e} = n\ 2.07 \times 10^{-12}\ \mathrm{T\ cm^2} \tag{1.11}$$

This result, first verified experimentally by Deaver and Fairbanks and by Doll and Näbauer [15, 16], comprises the fact that the "elementary" particles of the macroscopic wave function are Cooper pairs that have an effective charge $e^* = 2e$.

This result also implies that knowing the field B inside a superconductor, we can

estimate the density of vortices:

$$\frac{\text{Number of vortices}}{\text{unit area}} = \frac{B}{\Phi_0} \tag{1.12}$$

Or better yet, know the intervortex separation d as a function of field:

$$d \simeq \sqrt{\frac{\Phi_0}{B}} \tag{1.13}$$

This relation holds true for all type II superconductors. It also gives us a natural way to understand why the upper critical field is related to the coherence length by Eq. 1.10 (note that $B \simeq H$ near H_{c2}). The superconductor will reach the normal state when the intervortex distance is roughly equal to the diameter of a vortex core (*i.e.* $d \simeq 2\xi$).

Bound states in the vortex core

A vortex is, to first order, a core of normal metal surrounded by a superconductor. This arrangement can be seen as a potential well for the "normal electrons" that are in the vortex. As in any quantum mechanical potential well, discrete (quantized) energy levels are formed for states which have a wave function confined to the well. These so-called bound states were predicted by Caroli, de Gennes and Matricon in 1964 [17].

It has been very hard to detect the existence of these bound states. For one, an electronic probe is required and it must have a distinct signature of localization within the vortex state. Experimentally, the specific heat of a type II superconductor in the vortex state is rightfully predicted to be proportional to B, in other words, to the number of vortices. It then reaches its normal state value at H_{c2}. This is a volumic argument using the simple notion that the volume inside a vortex core is a normal metal. However, the verification of this property hardly gives information about the nature of the electronic excitations within the vortex cores, namely, whether they are localized or not. On the other hand, the thermal conductivity is a transport property and only delocalized quasiparticles can contribute to it. Its activated behavior with respect to a magnetic field (in Nb for example [20]) has perhaps been the first experimental verification of the existence of such localized states. More specifically, a growing heat capacity without the corresponding transport proves that the excitations are localized. This idea will be reviewed in more detail throughout this thesis as it is one of its central aspects (see Chapters 5 and 6).

Direct measurements of such states had to wait until 1989 when the vortex state of $NbSe_2$ was imaged directly via Scanning Tunneling Microscopy (STM) [18] and yielded

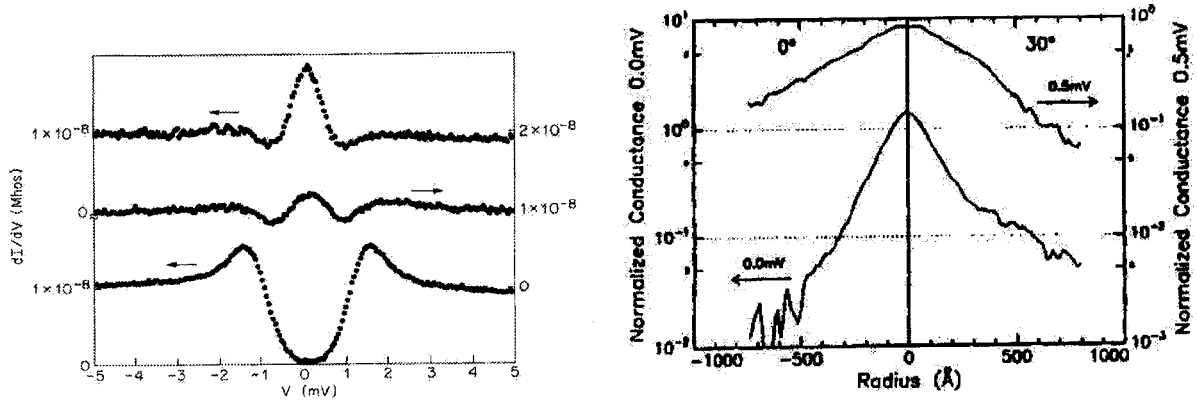

(a) (b)

Figure 1.6: Scanning tunneling spectroscopy in $NbSe_2$. (a) Local tunneling conductance at the center of the vortex core, near it and as far away from it (from [18]). One sees a peak in the conductance at the vortex center and the recovery of a superconducting gap away from the vortex core. (b) The conductance at both zero bias and at 0.5 mV as a function of distance away from the vortex core in two directions for $NbSe_2$ [19]. The decay is exponential and is taken to be the signature of bound states.

strong evidence for the existence of such states (see Fig. 1.6a). The signature for such bound states is a peak in the density of states (DOS) above the vortex core. This DOS is also found to drop exponentially away from the vortex core as expected (see Fig. 1.6b). One should note that additional theoretical treatment was necessary to correctly understand the experimental data [21]. It is also important to note that such bound states were not observed in other systems where STM studies have been possible [1]: YNi_2B_2C and MgB_2 [23, 24, 25]. The reason for this will be discussed and understood later in this thesis from results presented here.

1.3 Unconventional superconductivity

The revival of interest in superconductivity through the past 20 years has been fuelled mainly by the emergence of new forms of superconductivity found mainly in heavy fermion systems, high temperature cuprates and organic conductors. The term "unconventional superconductivity" is often used in this context. The definition of this term

[1] Bound states have been imaged however in the high temperature superconductor BSCCO [22]. These results are unexpected due to the *d*-wave nature of the superconducting gap.

is less clear and can differ significantly from one author to the next. This section will explain what is meant in this thesis by unconventional superconductivity. For this, it will review the basic assumptions of the traditional theories of superconductivity and see what extensions or modifications can occur.

1.3.1 Non *s*-wave superconducting gap

In the simplest theory, the attractive interaction between electrons is isotropic and therefore results in an isotropic *s*-wave superconducting gap. In fact, it has been rigourously shown that, in the case where the attractive interaction is mediated by an electron-phonon mechanism, the symmetry must be of this kind. Moreover, the superconducting gap represents the order parameter of the superconducting state and its symmetry is a defining factor of its nature. It is therefore important to have a good understanding of the gap of any superconductor.

Three types of "non *s*-wave" gaps will be discussed: gaps of lower symmetry, highly anisotropic gaps, and band-dependent gaps.

Gaps of lower symmetry

In the case of spin-singlet superconductivity, the symmetry of the gap function must be even in order not to violate Fermi-Dirac statistics. In general, in all superconductors, the gap is composed of all the symmetries that are permitted but with one channel being dominant (to various degrees). Of course, in conventional superconductors, the dominant channel is *s*-wave.

Remembering first-year orbital physics, the simplest even symmetry after *s* is *d*. It has been found very convincingly that the symmetry of the gap in high T_c superconductors (HTSC) is $d_{x^2-y^2}$ [26]. However, other symmetry groups have been proposed for other systems although the case is less clear than in HTSC. A good review of such symmetry groups can be found in [27].

The main characteristic of these symmetry groups are the topological nodes that are associated with them. In most cases, this implies that the gap function will be zero in some parts of the Fermi surface. There are two main types of nodes: line nodes (most common) and point nodes.

It has also been proposed that the gap function of HTSC may have an additional component to the $d_{x^2-y^2}$ one. A gap with a $d_{x^2-y^2} + ix$ symmetry where the imaginary

part x is either s or d_{xy} is being envisaged [28].

Highly anisotropic gap

Much debate is often raised when a superconductor is thought to have a gap with nodes (*i.e.* implying a symmetry other than s). Indeed, the gap may simply be highly anisotropic but without having topological nodes or zeros. The fact that a gap is highly anisotropic is still a strong deviation from the simplest theory and implies additional physics. As a note, the largest reported gap anisotropy in elemental superconductors is of a factor of 2 [29]. A highly anisotropic gap of s-wave symmetry has been proposed for borocarbide superconductors Re-Ni_2B_2C with Re = Lu, Y and will be the subject of Chapter 5.

Multi-band superconductivity

Multi-band superconductivity refers to the case where the superconducting gap has a significantly different value on different bands of the Fermi surface (see for example [30]). Usually, one uses the approximation that the system has effectively one band and one gap. There is a very good reason for this: bands are usually well coupled and can be treated in such a way. However, when there are two bands of distinct characters responsible for two sets of Fermi surfaces, it may be that these are strongly decoupled. It is then possible that superconductivity stems from one set of bands and is induced on the other via a proximity type of effect. On the other hand, the source of such poor coupling between bands is not well understood. This was first reported in 1980 in $SrTiO_3$ but is now being actively studied as it seems to be displayed in MgB_2 ($T_c = 40$ K) and in $NbSe_2$, a superconductor hitherto thought to be conventional. Chapter 6 will review the case of $NbSe_2$.

1.3.2 Non spin-singlet superconductivity

One of the first assumptions in the Cooper problem is that the pair is formed in a spin singlet state. This is naturally the lowest energy state since it has a total angular momentum of zero. However, it has been suggested that some superconductors display spin-triplet superconductivity. This has the effect of imposing that the symmetry of the superconducting gap be odd. The lowest such symmetry is p-wave, as has been proposed for Sr_2RuO_4 [31].

1.3.3 Non electron-phonon mechanism

Another source of unconventional superconductivity comes from a pairing mechanism not mediated by phonons. This is to say that it is mediated by a purely electronic mechanism of some form or other. It is a simple extension of BCS theory but with another *bosonic* excitation mediating the pairing. This is necessarily the case for superfluid ^{3}He [32] where spin fluctuations are thought to be the glue for Cooper pairs.

It is very difficult experimentally to verify such an assertion. However, if the gap function of a superconductor is found to have topological nodes, it is often inferred that the pairing is non-phononic. Another clear indication of unconventional pairing is the presence of several phases of superconductivity as seen, for example in UPt_3. There, two (or more) distinct superconducting order parameters are observed [33].

It is strongly thought to be the case for high T_c cuprates. A phononic interaction is not thought to be able to give such high transition temperatures. What's more, the order parameter is found to have d-wave symmetry. However, other proposals seek yet another answer: a form of superconductivity which does not even implicate Cooper pairing via a bosonic excitation.

1.3.4 Other proposals

With the emergence of new forms of superconductivity, many authors have argued that a complete change of paradigm was necessary to obtain a theoretical understanding. Many of them stem from the likelihood that the normal state of these materials may not be Fermi liquids. The most prominent examples of such new proposals are those involving spin-charge separation [34, 35, 36]. In one of these [36], the superconductivity would stem not from Cooper pairing but rather, from the condensation of novel excitations, namely, charge e bosons. These scenarios are extremely attractive but have yet to be verified experimentally.

1.3.5 Summary

In summary, many new materials display superconductivity which is not well described by the conventional BCS theory. Some of these forms of unconventional superconductivity are viewed as extensions of the BCS formalism (*e.g.* non-phonon pairing mechanism), whereas others propose a complete change of paradigm (*e.g.* no Cooper pairing).

1.4 Conclusion

We have reviewed some important concepts relevant to superconductivity which have been studied both theoretically and experimentally over the past century. In this thesis, we will be interested in three forms of unconventional superconductivity that have emerged only in the past 20 years or so. To this effect, we have defined what we mean by "unconventional superconductivity".

Chapter 2

Review of thermal conductivity

In this thesis, we present studies of several forms of superconductivity from the most conventional types to the elusive high T_c cuprates. Moreover, the superconducting state ($H = 0$), the vortex state ($H_{c1} < H < H_{c2}$), and the normal state ($H > H_{c2}$) are investigated successively by applying a magnetic field. To do so, we use thermal conductivity and resistivity measurements. This chapter will give a review of these transport properties, first in metals and insulators and then in superconductors. The reader will find an emphasis on the low temperature behavior which we are mostly interested in for two main reasons: an easy quantitative understanding of the measurements, and obtaining information about the ground state of the systems ($T \rightarrow 0$).

2.1 Transport properties: definition

The two main longitudinal transport properties of a solid are the electrical and thermal conductivity, σ_{xx} and κ_{xx}. These are defined to be the coefficient of proportionality between the current density of charge J_x^e (or heat J_x^q) applied along the x direction and the gradient of voltage $\nabla_x V$ (or temperature $\nabla_x T$) which develops along that same direction (see equations 2.1 and 2.2).

$$J_x^e = -\sigma_{xx} \times \nabla_x V \tag{2.1}$$

$$J_x^q = -\kappa_{xx} \times \nabla_x T \tag{2.2}$$

The negative sign indicates that the charge (or heat) flows from the high to the low voltage region (hotter to the colder region). We can write these expressions in a more

practical way and drop the subscripts for simplicity

$$\sigma = \frac{I/\text{cross} - \text{section}}{\Delta V/\text{length}} = \alpha \times I/\Delta V \tag{2.3}$$

$$\kappa = \frac{\dot{Q}/\text{cross} - \text{section}}{\Delta T/\text{length}} = \alpha \times \dot{Q}/\Delta T \tag{2.4}$$

where I and $\dot{Q}$ are the applied currents and the geometric factor α is the length divided by the cross section.

2.1.1 Carriers

The transport of charge in a solid is done solely by electrons. However, several carriers can contribute to the thermal conductivity. The two main carriers are electrons and phonons, but spin excitations can also contribute [37, 38, 39]. The only requirements are that the excitations be *extended* and that they *carry entropy.* The total thermal conductivity is the sum of all the contributions:

$$\kappa_{tot} = \kappa_e + \kappa_{ph} + ... \tag{2.5}$$

2.1.2 Scattering mechanism

In a simple picture, materials have a finite conductivity because the current of carriers can be degraded by various processes. These are usually described by a scattering rate τ^{-1} (where τ is usually referred to as the lifetime) which comes out from the relaxation time approximation [7]. However, several mechanisms can degrade a current of electrons or phonons. In other words, there exists several scattering rates τ_i^{-1} (where i refers to the mechanism; *e.g.* electron-phonon scattering) leading to an effective scattering rate τ_{eff}^{-1} given by Matthiessen's rule:

$$\tau_{\text{eff}}^{-1} = \tau_i^{-1} + \tau_j^{-1} + \tau_k^{-1} + ... \tag{2.6}$$

As a result, the electrical and thermal resistances ($\rho = \sigma^{-1}$ and κ^{-1}) of each scattering process are additive.

$$\rho = \rho_i + \rho_j + \rho_k + ... \tag{2.7}$$

$$\kappa_c^{-1} = \kappa_{ci}^{-1} + \kappa_{cy}^{-1} + \kappa_{cz}^{-1} + ... \tag{2.8}$$

where i, j and k refer to the type of scattering mechanism. For the thermal conductivity, c refers to the type of carrier (see equation 2.5).

2.2 Transport of electrons

The purpose of this section is to give a review of main concepts and assumptions related to electronic transport. It will also give the central usable relations but will not go in depth into rigorous theoretical treatments although the proper references are included.

2.2.1 Electrical conductivity

The conductivity (or resistivity $\rho = \sigma^{-1}$) of materials can yield very useful information such as the purity of a sample, the presence of strong electron-electron interactions, the onset of some type of ordering or even various phase transitions (most notably, a superconducting transition), map the Fermi surface via quantum oscillations (Shubnikov-de Haas effect), or reveal the presence of localization. What's more, it is very easy to measure in a wide range of environments such as very low temperatures, high pressure and high magnetic fields, and this, with a rare level of precision.

In its simplest form, the electrical conductivity is well described by the Drude theory of metals which gives [7]:

$$\sigma = ne^2\tau/m^* \tag{2.9}$$

where n is the electronic density [1], e is the charge of the electron and m^* is the effective mass of the electron [2]. Much information may be retrieved from the resistivity with a good understanding of the scattering mechanisms which may be at play, as discussed below. Countless other effects can also lead to precious information but will not be covered here.

2.2.2 Thermal conductivity

The thermal conductivity can also uncover useful information, in particular within the superconducting state. Indeed, the electrical conductivity is then "shorted out" and the only transport probe available is κ. However, let us first understand the behavior of κ in a metal.

There, it is dominated by electronic transport. In the semi-classical approach and

[1] Note that $N(E_F) = \frac{3n}{2E_F} = \frac{3n}{m^* v_F^2}$ with $N(E_F)$ being the density of states at the Fermi surface and E_F and v_F are respectively the Fermi energy and velocity.

[2] This is a consequence of Fermi-liquid theory [4] whereas a system of interacting electrons can be described in the same way as a system of non-interacting electrons which have a renormalized mass m^*.

using the relaxation time approximation, one arrives at the relation

$$\kappa_e = \frac{1}{3} C v_F^2 \tau = \frac{1}{3} C v_F l \tag{2.10}$$

where C is the heat capacity, v_F is the Fermi velocity, and l is the mean free path (defined as $l = v_F \tau$). The heat capacity is given by the well-known relation:

$$C = \frac{\pi^2}{3} N(E_F) {k_B}^2 T = \pi^2 k_B^2 \frac{n}{m^* v_F^2} T \tag{2.11}$$

The linear temperature dependence of C is a direct consequence of the fermionic nature of electrons. In the same stride, a linear thermal conductivity at $T \to 0$ (denoted $\kappa_{00}/T = \kappa/T|_{T \to 0}$) is fundamentally an indication of delocalized fermionic excitations in a system. At higher temperature, one also needs a good understanding of the possible scattering mechanism to obtain information from κ.

2.2.3 Scattering rates

Understanding the scattering rates through, for example, their magnitude and temperature dependence, will lead to a proper analysis of the transport properties in a material. Let us review the most common ones, namely, impurities, phonons and electrons although it must be reminded that this list is less than extensive. For these, the temperature dependence of the scattering rates, the resistivity, the heat capacity and the thermal conductivity are compiled in table 2.1 and are discussed briefly below. A good review of these mechanisms in alkali metals can be found in [40]. As a note, the Fermi velocity of the electrons is always assumed to be independent of temperature.

Impurities and crystal defects

The scattering of electrons by impurities is an elastic process in that the energy of the electron is conserved. It is easy to understand that this mechanism will be independent of temperature and lead to $\tau^{-1} \propto T^0$. It is dominant at low temperatures as shown in Fig. 2.1 and gives rise to what is referred to as the residual resistivity ρ_0. This value is a measure of the purity of the sample, *i.e.* of the density of impurities.

It is interesting to note that the Wiedemann-Franz law (described in detail below) which relates the electrical and thermal conductivity is satisfied if this scattering mechanism is dominant. Indeed, a condition for the applicability of the WF law is elastic scattering.

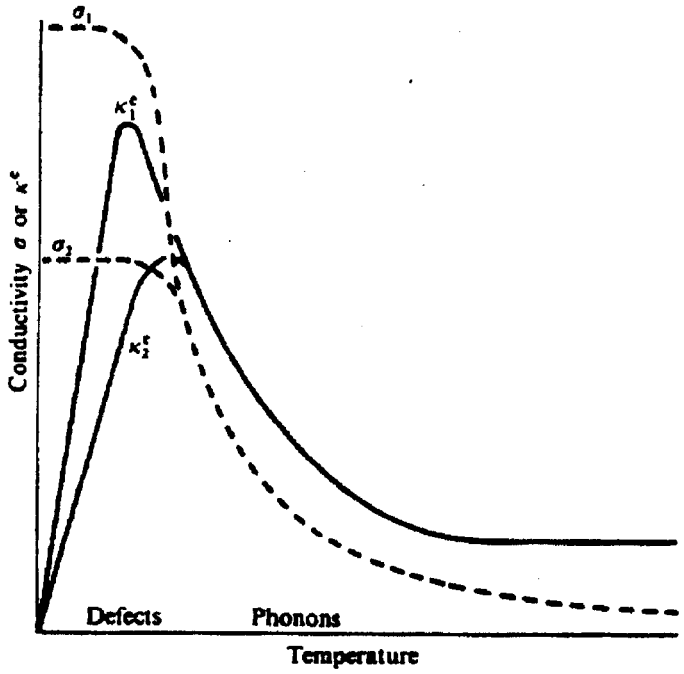

Figure 2.1: This figure shows the thermal and electrical conductivities in a conventional metal (after [41]). The dominant scatterers are impurities at low temperatures and phonons at higher temperatures. The higher curves are for purer samples.

Phonons

In a normal metal, phonons play a major role in the scattering of electrons. However, it leads to different temperature dependences for temperature of $T > 0.7\ \Theta_D$ and $T \ll \Theta_D$. For high temperatures, the scattering rate is found to be linear in temperature $\tau^{-1} \propto T$ and leads to a linear resistivity and a constant thermal conductivity (see Fig. 2.1). It is useful to note that the magnitude of this term is well understood within the Bloch-Grüneisen formalism and can lead to a measure of the electron-phonon coupling constant [42].

For $T < 0.1\ \Theta_D$, the scattering rate is proportional to T^3. It is however found theoretically that the resistivity will have a T^5 temperature dependence under certain conditions (for example, an isotropic Fermi surface). Indeed, at $T \ll \Theta_D$, only phonons with a small wavevector can contribute to a scattering event. As a result, the degradation of the electrical current will favorably be done via forward scattering [7, 40] and lead to this additional temperature dependence. In practice, the scattering mechanism is assigned to phonons for a resistivity $\rho \propto T^\alpha$ with $3 < \alpha < 5$ at low temperatures.

Electron scatterers	τ^{-1}	ρ	C	κ
Impurities	T^0	T^0	T	T
Phonons ($T < 0.1\Theta_D$)	T^3	T^α, $3 < \alpha < 5$	T	T^{-2}
Phonons ($T > 0.7\Theta_D$)	T	T	T	T^0
Electrons	T^2	T^2	T	T^{-1}

Table 2.1: Electrons are scattered via various mechanisms. This table shows the temperature dependence of the scattering rate τ^{-1}, the resistivity ρ, the heat capacity C and the thermal conductivity κ associated with several of these. Θ_D is the Debye temperature of the metal.

Note that a transition from a T^3 to a T^2 behavior of the resistivity is seen in superconductors with high electron-phonon coupling and high disorder [43].

Electrons

Electron-electron scattering is usually weak in metals. It becomes dominant in strongly correlated electron systems such as heavy Fermions. It results in $\tau^{-1} \propto T^2$ which leads to the celebrated T^2 resistivity seen as an indication of a Fermi-liquid ground state. What's more, the magnitude of the T^2 term of the resistivity is empirically observed to obey the Kadowaki-Woods ratio [44]. The latter shows the universal relation $A/\gamma^2 = 1 \times 10^{-5} \mu\Omega\text{cm (mole K mJ}^{-1})^2$ where $\rho = \rho_0 + AT^2$. It is also seen that $A/\gamma^2 \simeq 0.4 \times 10^{-6} \mu\Omega\text{cm (mole K mJ}^{-1})^2$ for transition metals such as Pd, Pt and Ni [45]. These relations may help determine if a T^2 resistivity is indeed due to electron-electron scattering and if a system shows strong correlations or not.

Summary

In summary, many scattering mechanism may lead to different power laws of the electric transport properties. The most common ones have been discussed. Some of them have been studied in detail and are understood quantitatively. It is also clear that different scattering mechanisms will dominate at different temperatures as is shown in Fig. 2.1 where the electrical and thermal conductivity of a metal is shown as a function of temperature for different purities.

2.2.4 Wiedemann-Franz law

Very often, the thermal conductivity does not yield much additional information from that obtained via resistivity. This is due to the fact that they are related directly by the Wiedemann-Franz law. This universal relation may be obtained by combining equations 2.9, 2.10 and 2.11, to get:

$$\frac{\kappa}{\sigma T} = \frac{\pi^2 k_B^2}{3e^2} \equiv L_0 = 2.45 \times 10^{-8} \text{W } \Omega \text{ K}^{-2} \tag{2.12}$$

where L_0 is the Sommerfeld value of the Lorenz number. It simply states that the carriers of charge and heat (or entropy) are one and the same. However, our interest stems in its possible violation in the normal state of cuprate superconductors as claimed by Hill *et al.* [46]. Let us review the universal nature of this law to better understand the profound implications of its violation.

Historically, it was first reported experimentally by Wiedemann and Franz in 1852 [47]. They found that the Lorenz number ($\frac{\kappa}{\sigma T}$) was the same for many metals at room temperature (for a table of values, see [7]). As it turns out, this law is extremely robust as has been demonstrated both experimentally and theoretically since this time.

The robustness of the WF law

The derivation of the WF law presented above is one of the simplest ways to achieve the result. However, we have used a number of assumptions to obtain it. Some of these are necessary and hold the essence of the WF law but others do not and can be generalized. For example, we have used simple results from the band theory of electrons with an isotropic Fermi surface, results from kinetic theory (equation 2.10), the relaxation time approximation, etc. The most general derivation of the WF law was made by Chester and Tellung [48] in 1961. They only assumed non-interacting electrons, an elastic scattering mechanism and an isotropic system [1]. They also showed that the WF law was valid for any strength of scattering [48]. The derivation was then further generalized to anisotropic systems [49], any level of disorder (weak or strong localization regimes) [50], any strength of a magnetic field [49] and in both 2 and 3 dimensions but not strictly in 1 dimension. This leads to the assumptions that are at the heart of the WF law:

1. Same carriers of heat and charge

[1] Note also that the "zeroth" assumption was that they were dealing with electrons, *i.e.* particles that obey Fermi-Dirac statistics and that carry a charge e

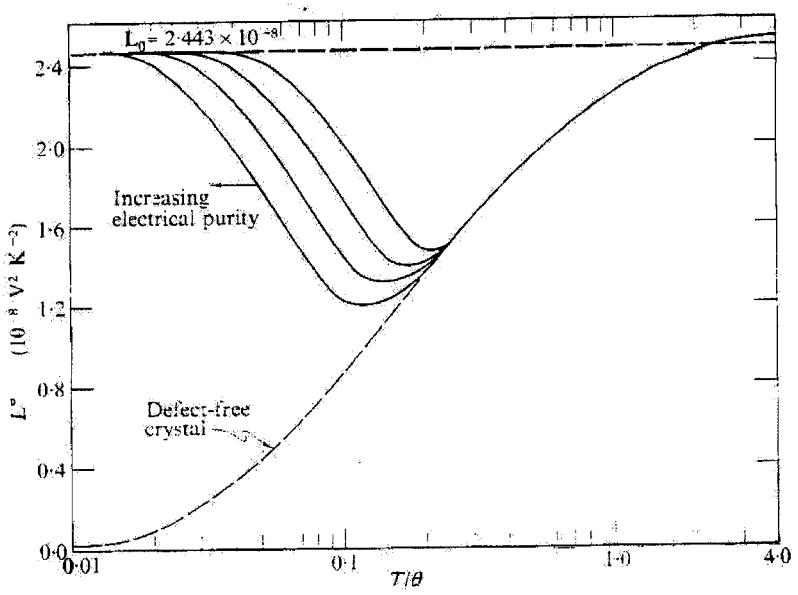

Figure 2.2: The normalized Lorenz ratio L/L_0 where $L = \frac{\kappa\rho}{T}$ as a function of temperature (T/Θ_D with Θ_D is the Debye temperature) for several purity regimes (after [41]). The Wiedemann-Franz law is satisfied in all cases at low temperatures. However, at higher temperatures, L/L_0 becomes smaller than 1 as the heat current is degraded more easily than the charge current.

2. Carriers have charge e [1]

3. Carriers obey Fermi-Dirac statistics

4. The scattering is elastic (no energy is transferred during a scattering event) [2]

Experimentally, the WF law has been verified at $T \to 0$ in all systems investigated to date. It is verified in simple metals of course, but also in systems with strong electronic correlations such as heavy Fermion systems (UPt_3 [51], $CeAl_3$ [52] and $CeCu_6$ [53] for example), quasi two dimensional systems such as Sr_2RuO_4 [54] and $NbSe_2$ [55] or even quasi one dimensional organic conductor $(TMTSF)_2ClO_4$ [56], systems in the proximity of a quantum critical point ($CeNi_2Ge_2$ [57], $Sr_3Ru_2O_7$ [58], $CeCoIn_5$ [59]), and in a quasi-two-dimensional system displaying weak-localization (pregraphitic carbon) [60].

[1] Note that if the carriers had a charge of say $a \times e$ where a is a real number, then the WF law would become $\frac{\kappa}{\sigma T} = \frac{\pi^2 k_B^2}{3(ae)^2} = L_0/a^2$.

[2] This is always true at $T = 0$ such that the WF law should always hold at $T = 0$.

The violation of the WF law

It is also well known that the WF law is violated in a number of instances. At finite temperatures, the scattering becomes inelastic and the conditions of applicability of the WF law are no longer satisfied (condition 4). The normalized Lorenz number L/L_0 becomes less than one as is shown in Fig. 2.2 for several levels of disorder for a simple metal [41]. It is well understood with the fact that a heat current can be degraded more easily than an electrical current when the scattering events involve, for example, small wavelength phonons (see [41] for a good discussion). The electrical current is degraded preferentially by forward scattering events while the thermal current has no such limitations. This also explains why the WF law is recovered at temperatures near Θ_D in metals: phonons with any wavelength can degrade the electrical current and the scattering rate is the same for σ and κ.

In fact, the deviation of the Lorenz number from L_0 at finite temperature may yield information about the scattering mechanism at play. This was studied in $CeNi_2Ge_2$ [57] in the context of spin-fluctuation scattering. Current work is interested in these deviations near a quantum critical point to better understand the role of scattering due to quantum fluctuations [58, 59].

The WF law is also seen to be violated when the thermal conductivity has contributions from other carriers than electrons. This is the case, for example, in dirty metals where the phononic contribution may be large. It has also been reported recently in systems where spin excitations contribute to the thermal conductivity [37, 38, 39]. This violates condition 1 for the validity of the WF law.

A superconductor is the most extreme violator of the WF law. There, the electrical thermal conductivity is zero while the conductivity is infinite. Condition 1 is again responsible as the carriers of charge are Cooper pairs while the carriers of heat are thermally excited quasiparticles.

These violations are well known and well understood in terms of the conditions of applicability of the WF law. However, a new and unexpected violation of the WF law in the normal state of a cuprate superconductor at $T \to 0$ was reported [46]. Since it is for $T \to 0$, it does not stem from an inelastic scattering mechanism. Moreover, the phononic contribution was successfully subtracted and no magnetic carriers are expected to participate in the conduction of heat as there is no magnetic ordering in this material. This lead the authors to turn to conditions 1, 2 and 3 in a novel way: the carriers

are known to be electronic in nature but are they indeed *fermions which carry charge e*? Instead, this result has been seen as a possible indication of spin-charge separation where the electrons may be splitting into a neutral spin carrying excitation and a charged boson with spin zero. This result along with other reports in cuprate superconductors will be the central theme of Chapter 7. The attempts at understanding this behavior theoretically will be reviewed there.

2.3 Phonon thermal conductivity

Phonons dominate the thermal conductivity of electrical insulators but may be important in dirty metals or in superconductors. In the same way as done for electrons, one can use the relaxation-time approximation and obtain:

$$\kappa_{ph} = \frac{1}{3} C {v_{ph}}^2 \tau = \frac{1}{3} C v_{ph} l \tag{2.13}$$

Where C is the heat capacity, v_{ph} is the phonon velocity, τ is the scattering lifetime and l is the mean free path. The temperature dependence of κ_{ph} is shown in Table 2.2.

2.3.1 Theoretical treatment

Let us start by deriving the heat capacity of phonons in the Debye theory. That is, we will consider only the acoustic branches which are the low energy ones. They are also the ones which will carry heat. Assuming a harmonic potential between the ions of a crystal, we obtain a linear dispersion relation:

$$E = \hbar\omega = \hbar c_s |\mathbf{k}| \tag{2.14}$$

where ω is the frequency, c_s is the velocity of branch "s" and $|\mathbf{k}|$ is the momentum wavevector. The heat capacity is given by:

$$C = \frac{dU}{dT} = \frac{d}{dT} \sum_{s,\mathbf{k}} E f(E) \tag{2.15}$$

where U is the internal energy, $f(E)$ is the distribution function and the sum is taken over the three phonon modes or branches (two are transverse and one is longitudinal). Since phonons obey Bose statistics, their distribution function is $f(E) = \frac{1}{exp(E/k_B T)-1}$.

Taking the integral over momentum space (assuming that it is continuous rather that discrete), and using equation 2.14, we obtain:

$$C = \frac{d}{dT}\sum_s \int \frac{d\mathbf{k}}{(2\pi)^3}\frac{\hbar\omega_s(\mathbf{k})}{e^{\hbar\omega_s(\mathbf{k})/k_BT}-1} = \frac{d}{dT}\sum_s \int_{\text{all space}} \frac{d\mathbf{k}}{(2\pi)^3}\frac{\hbar c_s(\mathbf{k})\mathbf{k}}{e^{\hbar c_s(\mathbf{k})\mathbf{k}/k_BT}-1} \tag{2.16}$$

We now define the Debye wave-vector k_D. The integral will be done over a sphere of radius k_D instead of over the first Brillouin zone. This sphere is made to contain as many wavectors as there are ions in the crystal such that $n = k_D^3/6\pi^2$ [7]. Also, an associated Debye temperature and Debye frequency are defined as

$$k_B\Theta_D = \hbar\omega_D = \hbar c_s|\mathbf{k_D}| \tag{2.17}$$

We also assume that the three phonon branches and participate equally and that the spectrum is isotropic to have equation 2.16 become:

$$C = \frac{3(\hbar v_{ph})^2}{2\pi^2 k_B T^2}\int_0^{k_D} \frac{dk\ k^4 e^{\hbar v_{ph}k/k_bT}}{(e^{\hbar v_{ph}k/k_BT}-1)^2} \tag{2.18}$$

where v_{ph} replaces c_s and is the phonon velocity. Using the substitution $x = \hbar c_s k/k_BT$, we obtain:

$$C = \frac{3k_B}{2\pi^2}(\frac{k_BT}{\hbar v_{ph}})^3\int_0^{\Theta_D/T}\frac{dx\ x^4e^x}{(e^x-1)^2} \tag{2.19}$$

Using the fact that the integral can be done up to infinity rather than simply up to Θ_D/T (as long as $T < \Theta_D$ in which case the error is exponentially small), we find that the heat capacity can be written in either of the following ways:

$$C = \frac{12\pi^4}{5}k_Bn(\frac{T}{\Theta_D})^3 = \frac{2\pi^2}{5}k_B(\frac{k_BT}{\hbar v_{ph}})^3 \tag{2.20}$$

Let us now turn to the thermal conductivity of phonons at low temperatures. The treatment is similar and one arrives, following Thatcher and Callaway [61, 62] to the relation:

$$\kappa = \frac{k_B}{2\pi^2}(\frac{k_BT}{\hbar})^3 v_{ph}\int_0^{\Theta_D/T} dx\ \tau(\omega,T)\frac{x^4e^x}{(e^x-1)^2} \tag{2.21}$$

which is very reminiscent of equation 2.19 keeping in mind the simple kinetic theory result $\kappa = \frac{1}{3}Cv^2\tau$. Here, $\tau(\omega,T)$ is the frequency (or momentum) and temperature dependent scattering rate. Eq. 2.21 is shown to remind the reader that the frequency dependence of the scattering rate will have an effect on the thermal conductivity: changing variables from $\tau(\omega,T)$ to $\tau(x,T)$ will lead to an additional temperature dependence. It is however usually sufficient to treat the lattice thermal conductivity with the simple kinetic theory used in equation 2.13.

Phonon scatterers	τ^{-1}	C	κ
Boundaries	T^0	T^3	T^3
Electrons	$\sim \omega$	T^3	T^2
	$\Rightarrow T$		
Phonons ($T \ll \Theta_D$)		T^3	$T^3 exp(\Theta_D/bT)$
Phonons ($T \gg \Theta_D$)	T	T^0	T^{-1} or T^{-x}

Table 2.2: Phonons are scattered via various mechanisms. This table shows the temperature dependence of the scattering rate τ^{-1}, the heat capacity C and the thermal conductivity κ associated with several of these mechanisms. Θ_D is the Debye temperature of the insulator. x is between 1 and 2.

2.3.2 Scattering mechanisms

The main sources of scattering of phonons are the boundaries at low temperature, the electrons (except in an insulator), other phonons and various types of defects. We will review the temperature dependence that they imply (see Table 2.2). The velocity of the phonons is assumed to be temperature independent. Note that the frequency dependence of the scattering rate τ^{-1} and the resulting "additional" temperature dependence is shown. This is a direct result of equation 2.21 and the necessary change of variable.

Boundaries If there are no electrons to scatter the phonons at low temperatures, their mean free path becomes very long and the only form of scattering becomes the crystal boundaries. For a single crystal, the mean free path becomes roughly the mean dimension of the cross-section. For example, it is given by the diameter for a sample with a circular cross-section or, for a rectangular cross-section, $d = 2\sqrt{\frac{w \times t}{\pi}}$ where w is the width and t is the thickness. In this case, the mean free path and therefore also the lifetime is constant as a function of temperature. Assuming that the scattering of the phonons from the crystal boundaries is diffuse (*i.e.* that it is frequency independent), the temperature dependence of κ comes solely from that of the heat capacity: $C \sim T^3$ so $\kappa_{ph-b} \sim T^3$. More quantitatively, we obtain

$$\kappa/T^3 = \frac{2\pi^2}{15}\frac{k_B^4}{\hbar^3}\frac{d}{< v_{ph} >^2} = 4.06 \times 10^{13}\frac{d\ [\text{cm}]}{< v_{ph} >^2\ [\text{cm/s}]^2}[\text{mW K}^{-4}\ \text{cm}^{-1}] \qquad (2.22)$$

directly from equations 2.13 and 2.20. Here, d is the mean free path (or the sample dimension) and $< v_{ph} >$ is the average phonon velocity.

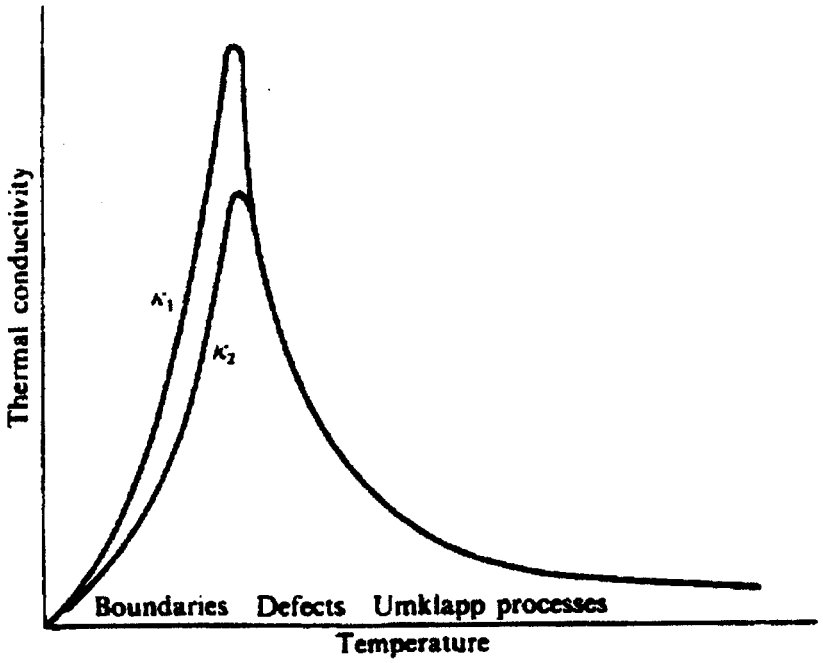

Figure 2.3: This figure shows the thermal conductivity of an electrical insulator (after [41]). The transport is only phononic and the dominant scattering mechanisms are boundaries at low T, defects at intermediate T and phonons at high T. A cleaner or larger sample will lead to a larger phonon peak as shown by the upper curve.

This relation has been experimentally verified in insulators up to temperatures of the order of 5-10 K (see, for example [61]). Note that the samples studied by Thatcher had their surfaces sandblasted to ensure that the scattering of the phonons was diffuse. If this is not the case and the scattering is specular (frequency dependent), the thermal conductivity acquires a modified temperature dependence which is reported to vary between $\kappa \propto T^{\alpha}$ with $2.1 < \alpha < 3$ [61, 63].

In our samples, the surfaces are usually polished or are naturally smooth. This gives rise to such an altered temperature dependence. However, assuming the T^3 dependence is usually a good approximation. Also, typical values for our crystals yield $< v_{ph} >= 5 \times 10^5$ cm/s and $d \simeq 0.05$ cm to give $\kappa_{ph-b}/T^3 \simeq 8$ mW K^{-4} cm^{-1}.

Electrons When the phonons are limited by electrons, the scattering rate is proportional to the frequency of the phonons. The scattering rate then brings an extra linear temperature dependence. Again, the heat capacity is cubic in T. This means that the thermal conductivity goes as $\kappa_{ph-e} \sim T^2$. Its magnitude was found to depend on the

residual resistivity ρ_0 in alloys [64].

This type of scattering can be very important in the vortex state of a superconductor. Indeed, vortices are electronic in nature and will scatter phonons strongly upon entering a sample (*i.e.* above H_{c1}).

Phonons Phonon-phonon scattering that leads to thermal resistance will do so through Umklapp processes. At low temperatures very few phonons have sufficiently large energies to take part in Umklapp processes. One gets $\kappa \sim T^3 e^{(\Theta_D/bT)}$ with $b \sim 1$. However, at temperatures above the Debye temperature, one obtains $\kappa \sim T^{-1}$. A more precise treatment leads to $\kappa \sim T^{-x}$ where x is between 1 and 2.

Defects Different types of defects will lead to different behavior of the associated scattering rate. For example, point defects (those which extend over a distance much smaller than the phonon wavelength) will lead to $\kappa \propto T^{-1}$ while dislocations will contribute a "core" term ($\kappa \propto T^0$) and a "strain field" term ($\kappa \propto T^2$). For a complete discussion, see [41].

The thermal conductivity of an insulator is presented in Fig. 2.3. The dominant scattering process for each temperature range is mentioned. Note that in a metal, electrons strongly suppress the phononic conductivity.

It is useful to point out here that we are actually not interested in the physics of phonons but rather that of electrons. Phonons only act to block our view of electrons and we need to understand them in order to extract the electronic thermal conductivity. Our approach for this is to do our measurements at the very lowest temperatures for two main reasons: 1/ The magnitude of κ_{ph} decreases faster ($\sim T^3$) than that of electrons ($\sim T$), and 2/ κ_{ph} is dominated by boundary scattering and is easily understood quantitatively, an additional test of our analysis.

2.4 Thermal conductivity in superconductors

2.4.1 Thermal conductivity of an *s*-wave superconductor

Upon cooling below the transition temperature of a superconductor, the electronic spectrum becomes gapped in the way described in Chapter 1. Many properties of an *s*-wave

superconductor are dictated by this superconducting gap. More precisely, it is the coherence factors which determine these properties.

It is insightful to view these properties in terms of the two fluid picture. The superconducting fluid is formed by the Cooper pairs. It carries charge perfectly but cannot carry entropy. As such, it does not contribute to the thermal conductivity. The normal fluid is formed by the excitations above the superconducting gap, *i.e.* the broken Cooper pairs. These are the excitations which will contribute to the thermal conductivity. Below T_c, the density of the normal fluid will decrease and will be exponentially suppressed for temperatures much lower than T_c and the electronic thermal conductivity will be nil.

Bardeen, Rickaysen and Tewordt (BRT) [9] calculated the thermal conductivity expected for an *s*-wave superconductor (see Fig. 2.4). They find that the ratio of the thermal conductivity in the superconducting and normal states (κ_s/κ_N) should be a universal function of T/T_c if the only scattering mechanism is elastic. Their results fit very well in the case of Aluminium as can be seen in Fig. 2.4b. There, one sees that for values of the residual resistivity (*i.e* the normal state thermal conductivity - *cf* WF law) differing by a factor of over 100 has no effect on κ_s/κ_N. The main features characteristic of this theory are the following: 1/ the thermal conductivity does not change slope at T_c and 2/ κ_e/κ_N falls below the 1% value around $T_c/5$ (see Fig. 2.4a).

In general though, the thermal conductivity is not as simple to understand. In addition to the BRT result, several other factors must be kept in mind: 1/ the contribution from phononic thermal conductivity, 2/ the different scattering mechanisms for both electronic and phononic contributions can be diverse, 3/ the scattering mechanisms can be modified very strongly by the effect of superconductivity. Cooper pairs can indeed not participate in any scattering event (this is the cause of the nil resistivity). Their increasing density at the expense of quasiparticles decreases the scattering of both the remaining normal fluid electrons and phonons. The first two statements are not proper to superconductors but apply to any material as was amply described in the previous sections. However, the third one is.

Concretely, the usual features that are observed in an *s*-wave superconductor can be seen in Fig. 2.5. These are explained in order of decreasing temperature starting at T_c:

- A change of slope at T_c (not seen clearly in Fig. 2.5). This may be due to several processes.
- The BRT decrease of the electronic thermal conductivity.

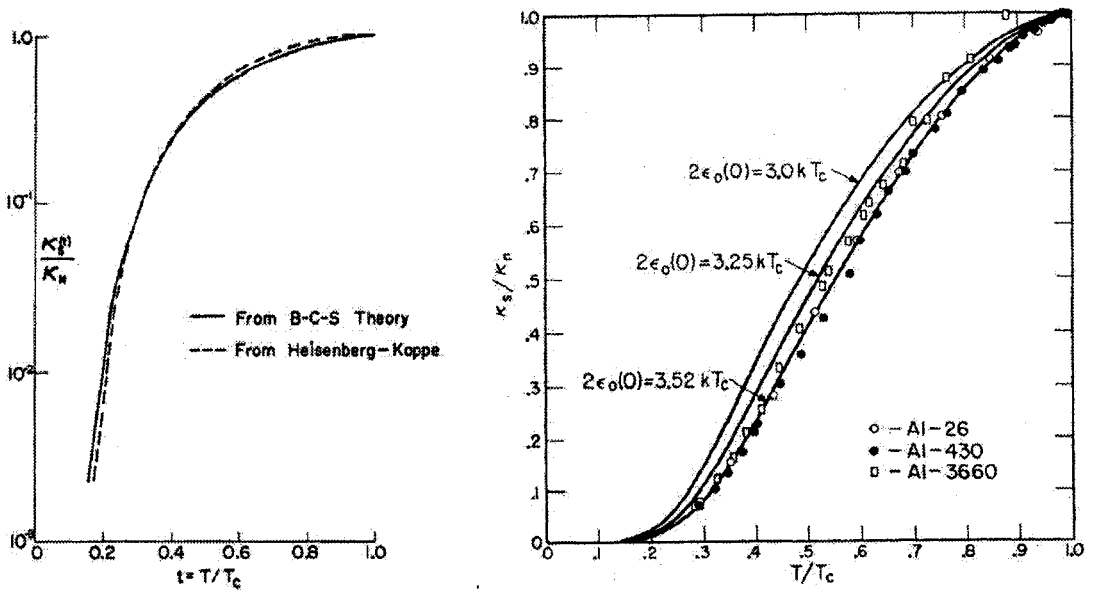

(a) (b)

Figure 2.4: (a) The electrical thermal conductivity for an s-wave superconductor as calculated by BRT [9]. Note that κ_s/κ_N reaches the 1% level at $T_c/5$. (b) The thermal conductivity of aluminium (Al) of different purities [10]. κ_s/κ_N is independent of purity and the BRT prediction fits the data very well.

- A phononic peak around $T_c/5$: the phononic thermal conductivity increases due to the decrease of electronic scattering.
- A decrease of the phononic thermal conductivity as the phonons start being scattered by the crystal boundaries.
- A purely cubic temperature dependence showing that the phonons are in the limit where the only scattering mechanism is via the boundaries of the crystal.

In summary, the superconducting gap of an s-wave superconductor will lead to a nil electronic thermal conductivity for $T \ll T_c$. Another way to say this is that the observation of a $\kappa/T = 0$ at $T \to 0$ is a good indication of a fully gapped Fermi surface.

2.4.2 Thermal conductivity in the vortex state of an s-wave superconductor

A key feature which defines thermal conductivity as an experimental probe is that it is only sensitive to extended or delocalized carriers. This is in contrast to heat capacity

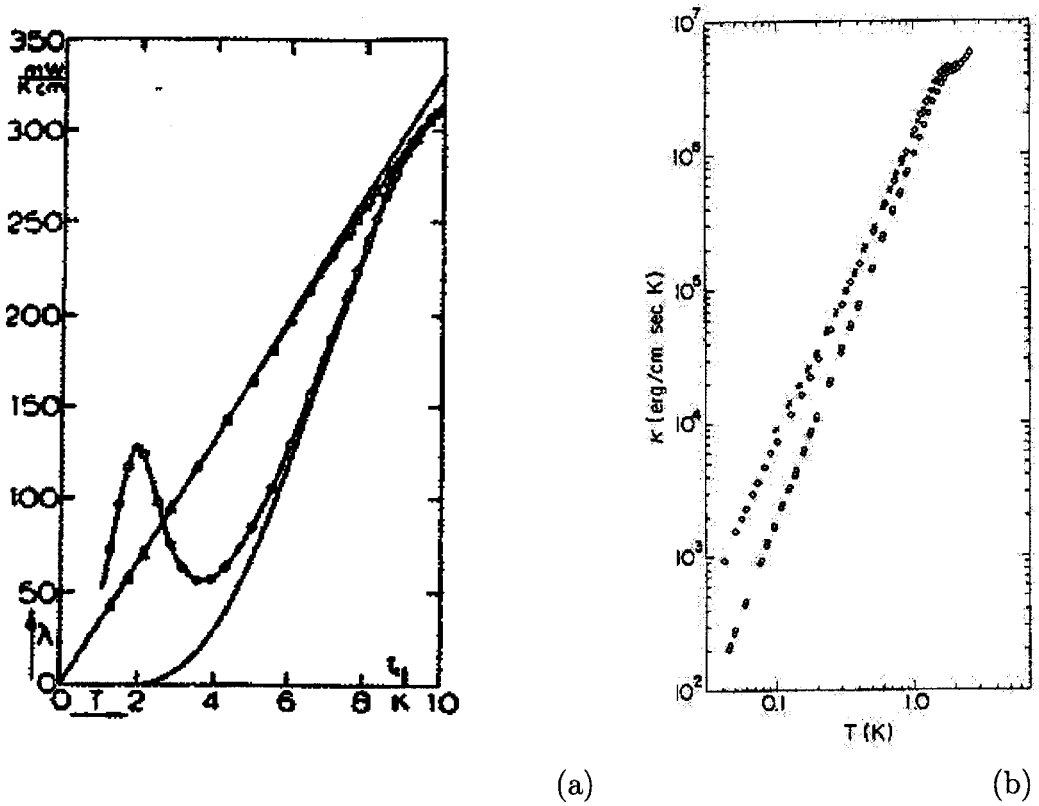

Figure 2.5: (a) The Thermal conductivity of Nb in the normal (triangles) and superconducting (circles) state [65]. The solid lines through the experimental data are guides to the eye. The lowest curve gives the result expected from the BRT theory. At $T_c/5$, a phonon peak develops. (b) The thermal conductivity at very low temperatures of Nb. κ_s is fully phononic and reaches the asymptotic regime of $\kappa \propto T^3$ when the sample is sandblasted (circles) [66]. When the same sample is polished (diamonds and crosses), κ shows a power law behavior higher lower than T^3, probably due to specular scattering on the crystal boundaries.

measurements which probes all excitations, be they extended or localized. It therefore offers a unique tool to probe the vortex state of superconductors. Indeed, in the mixed state of a superconductor, the electronic excitations are thought to be localized within the vortex cores [17] as described in Chapter 1.

Typical thermal conductivity in H

Typical thermal conductivity data as a function of field for a clean sample (*i.e.* for $\xi_0/l < 1$) is shown in Fig. 2.6. The characteristic features are seen for the data at $T = 5.5$ K. They are 1/ a sharp decrease at H_{c1}, 2/ a very rapid increase near H_{c2}

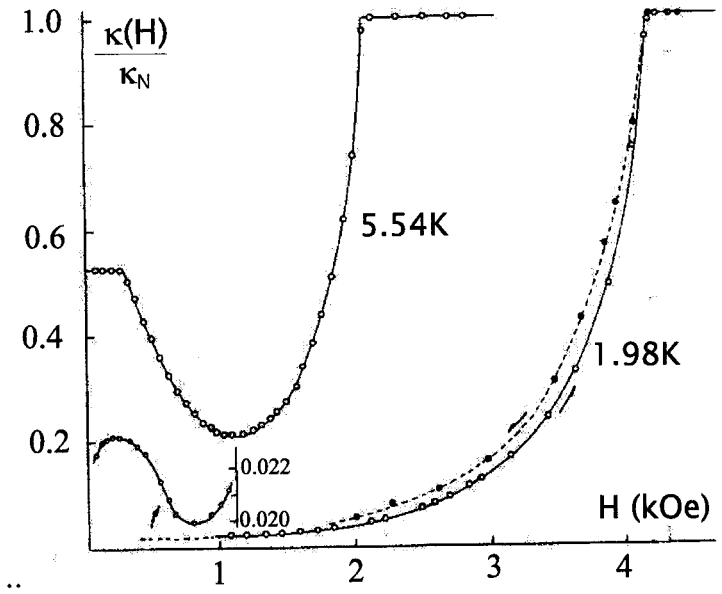

Figure 2.6: The thermal conductivity as a function of magnetic field for Nb at $T = 1.98$ K ($\simeq T_c/5$) and $T = 5.5$ K [20]. For the lowest temperature, one sees that the phononic contribution is far smaller than the electronic one. We can thus assume that the change in κ is entirely electronic. The slope at H_{c2} is nearly infinite.

with almost infinite slope until the normal state is reached. The first is due to a large increase in the scattering of phonons by the vortex cores. The phononic contribution thus decreases very quickly as vortices penetrate the sample. It is worth remembering that this scattering is electronic in nature. As for the second, the electronic contribution which is nil below $T_c/5$ in $H = 0$ (see Fig. 2.4 [9]) must rise to its normal state value which is given by the Wiedemann-Franz law. The electronic behavior is discussed below.

It must be stressed that the value of κ in $H = 0$ is mostly (if not completely) phononic whereas the value in the normal state is purely electronic (for good metals) and given by the Wiedemann-Franz law. Thus comparing the relative size of the two has no physical meaning. It also reminds us that the task of looking for the low field behavior of the electronic thermal conductivity is a difficult one as phonons effectively hide the view. To do so, one can try to minimize the phononic contribution (with a sample with a short mean cross-section (see eq. 2.22) and go to low temperatures since $\kappa_{ph} \propto T^3$ and $\kappa_e \propto T$. This is one of the tasks that we have done with the work comprised in this thesis.

κ_{ph} in the vortex state

At low temperature, when the so-called ballistic regime is reached, the phononic thermal conductivity has a cubic temperature dependence and its mean free path is limited by the boundaries of the sample. However, when vortices enter the sample, they may constitute an additional source of scattering. In this case, one would expect the temperature dependence of the phononic thermal conductivity to have the following temperature dependence:

$$1/\kappa_{ph} = 1/\kappa_{\text{boundary}} + 1/\kappa_{\text{vortices}} = 1/aT^3 + 1/bT^2 \tag{2.23}$$

where the aT^3 term refers to the boundary scattering and bT^2 refers to the scattering by vortices (it has a T^2 dependence since it is an electronic scattering mechanism [1]). Furthermore, one may expect the prefactor b to vary inversely as the density of vortices, namely, as $1/H$. Indeed, increasing the scattering will reduce the thermal conductivity. This has been seen for the first time in V_3Si and is shown in Fig. 4.9.

What's more, as is seen in Fig. 2.6, κ_{ph} decreases sharply as soon as vortices enter the sample. This turns out to be a useful way to indirectly measure the lower critical field H_{c1} (see Chapter 4).

Having described the phononic thermal conductivity in the vortex state, let us now turn to our main interest, namely, the electronic thermal conductivity.

κ_e in the vortex state

The best known property of electronic states excited by introducing vortices in a superconductor is that they are bound to these vortex cores. It would then seem that there would be no electronic contribution to the thermal conductivity since it is only sensitive to delocalized states. This would not be entirely correct. One needs to remember that the wave function of the bound states extend outside the vortex cores in an exponential way $e^{-d/2\xi}$ where ξ is the coherence length (and 2ξ is the diameter of the vortex core) and $d = \sqrt{\frac{\Phi_0}{H}}$ is the intervortex spacing. Thus, as soon as there is more than one vortex in a sample, these wave functions will overlap and lead to a finite thermal conductivity which will scale with $e^{-d/2\xi} = e^{-\alpha\sqrt{H_{c2}/H}}$ where α is a constant of order 1 [2]. This is

[1] Note that we are not aware of any formal theoretical formulation of the scattering of phonons by superconducting vortices. For this, although the temperature dependence will indeed be that of phonons scattered by electrons ($\sim T^2$), little a-priori information can be known about the prefactor b.

[2] Note that $d/2\xi = \frac{1}{2}\sqrt{\frac{2\pi\ H_{c2}}{H}} \simeq 1.25\ \frac{H_{c2}}{H}$ using Eq. 1.10 and 1.13.

indeed observed in Nb [20] and in V_3Si (see Chapter 4) at low fields.

However, to better understand the physical mechanism at play, it is useful to think of the thermal conductivity in the semi-classical way where $\kappa = \frac{1}{3}Cvl = \frac{1}{3}Cv^2\tau$ where C is the specific heat, v is the velocity of the carriers, l is the mean free path and τ is the scattering lifetime. Within this line of thought, one should realize that, strictly speaking, the bound states are always extended as long as there is more than one vortex in the sample. The overlap of their wave function creates a band structure which will change as a function of the intervortex spacing (*i.e.* of magnetic field) as has been calculated in [67, 68]. When vortices are far apart, the bands are extremely flat and give rise to extremely heavy excitations. In other words, their group velocity is very small. It will then increase as the magnetic field is increased itself. At the same time, the density of state (and C) will increase. We can further assume that the mean free path is independent of field. This should be a good approximation at low temperature when l is limited by impurity scattering. In this case, we would use the first relation $\kappa = \frac{1}{3}Cvl$. On the other hand, it is more conventional to think of the change of a transport property in terms of a changing scattering rate rather than a changing group velocity. We can then choose to fix the velocity as v_F, the usual velocity for electronic excitation, and talk about a field dependent scattering rate τ^{-1}. Then we can use the more common relation $\kappa = \frac{1}{3}Cv^2\tau$.

Unfortunately, these arguments are not rigorous. In fact, it is very difficult to treat this problem theoretically for low magnetic field value (or small vortex density). Up to recently, theoretical work describing the thermal conductivity in the vortex state was restricted to fields very near H_{c2} for clean superconductors [69, 70]. In this case, κ_s/κ_N was predicted to have a nearly infinite slope at H_{c2} and vary as $\kappa_s/\kappa_N - 1 \propto (1-(H/H_{c2}))^{\frac{1}{2}}$. This is indeed what is observed experimentally [20]. Recently, efforts were made using a quasi-classical formalism to extend the range of validity of the theory for thermal conductivity in the vortex state [71]. They find that the effective scattering rate is largely dependent on the purity level of the sample ξ_0/l. Dukan and Tešanović [72] have also done some analytical work and numerical calculations of the vortex state thermal conductivity which will be discussed in relation to our data on V_3Si (see Chapter 4).

In the dirty limit however ($\xi_0/l > 1$), the thermal conductivity is predicted to vary linearly with field near H_{c2} [73] as has been verified experimentally [20]. In light of these extremely different behaviors, it is crucial to know the in which regime (clean or dirty) a sample is when analyzing its thermal conductivity data in through the vortex state.

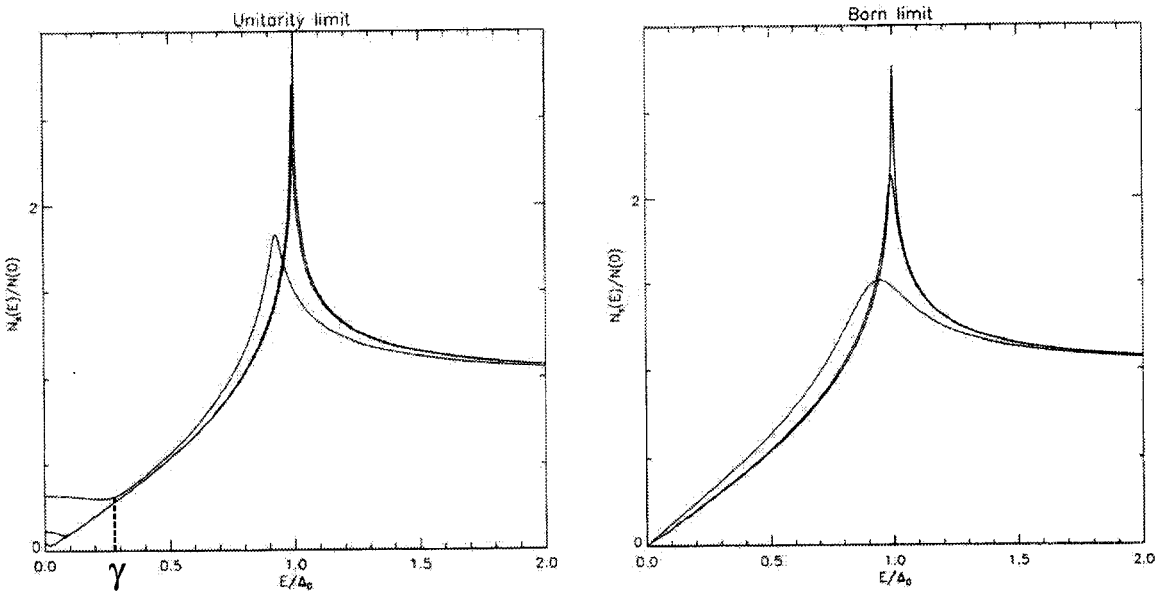

Figure 2.7: The effect of impurities on the density of states of a d-wave superconductor with unitary (a) and Born (b) scattering (after [75]). For unitary scattering, the DOS at zero energy increases as impurities are added. For Born scattering, the linear DOS slightly changes slope.

2.4.3 Thermal conductivity in unconventional superconductors

Thermal conductivity has been a terribly useful probe of unconventional superconductivity throughout the years. Much experimental and theoretical work has been done on the subject (see a review by Hussey [74] and references therein). In light of this, this section will not aim at giving a thorough review but rather, go over the main results. In addition, it will only focus on $T = 0$ results which will be important for this thesis.

As we want to understand the behavior of the thermal conductivity in a superconductor with a gap other than s-wave, we must realize that specific details will depend on the type of gap (for example, a gap with line or point nodes, a highly anisotropic gap, etc.). We will discuss here the case of a d-wave gap in a 2D system which is appropriate to describe high temperature superconductors. This will both give a good understanding of the generic features associated with a gap with line nodes and show that, in this case at least, a *quantitatively* correct picture emerges. The reader is directed to a recent review of the topic by N. Hussey [74] for a more complete treatment both on the theoretical and experimental fronts.

Density of states

Let us first discuss the density of states (DOS) for a superconductor with a d-wave gap. This will lead us naturally to the physical properties that are of interest to us. In contrast to the DOS of an s-wave superconductor where $N_s(E) = 0$ for energies below the gap maximum Δ_0 (see Fig. 1.2b and Eq. 1.6), the DOS $N_s(E)$ for a clean d-wave superconductor is *linear* with respect to energy at low energy, diverges at the superconducting gap (the SC coherence peak) and recovers the normal state value at high energy as seen in Fig. 2.7. However, the addition of non-magnetic impurities has a pair-breaking effect and creates a finite density of state at zero energy as also seen in Fig. 2.7a [75]. This is only true for unitary scattering ("scattering" here refers to the pair breaking mechanism). Unitary scattering is the extreme case of maximal scattering (*i.e.* introduces a $\pi/2$ phase shift). In the opposite limit of weak scattering, the Born limit, the DOS is not changed significantly: its slope with respect to energy is changed slightly and the DOS stays nil at zero energy (see Fig. 2.7b) [75].

There is good reason to believe that the scattering is unitary for high T_c cuprates although the possibility of a weaker scattering (one which is between the unitary and Born limits) is still being entertained. It should be reminded that adding non-magnetic impurities in an s-wave superconductor has no effect on the DOS but that adding magnetic impurities can create a finite DOS at zero energy [76]. This behavior was referred to as gapless superconductivity.

Let us now understand this effect more quantitatively. The density of states of a d-wave superconductor will depend on the density of impurities it contains. For this, we will use the normal state scattering rate $\Gamma = 1/2\tau_N$ as the parameter which will define the DOS. Fig. 2.7 shows $N_s(E)/N_N(0)$ for different values of $\hbar\Gamma/k_BT_c$ where $\Delta_0 = 2.14\ k_BT_c$, the weak-coupling value for the gap maximum for a d-wave gap. As the density of impurities increases, two things happen: 1/ the DOS is finite and constant up to higher energies and 2/ the DOS at zero energy $N_s(0)/N_N(0)$ increases.

We then distinguish a new energy scale separating the two behaviors: $N_s(E)/N_N(0) =$ constant and $N_s(E)/N_N(0) \propto E$. We introduce the parameter γ as the energy at which this occurs. This parameter is used to define two ranges of temperature relevant in experimental situations: the dirty limit for $T < \gamma$ and the clean limit for $\gamma < T \ll \Delta_0$. Note that $\gamma \simeq 0.61\sqrt{\Delta_0\Gamma}$ [77].

As for the density of state at low energy, it reaches a value of $N_s(0)/N_N(0) =$

$\frac{2\gamma}{\pi\Delta_0} ln(\Delta_0/\gamma) \simeq \frac{2\gamma}{\pi\Delta_0}$ and depends on the level of disorder [1]. A natural question arises: can one obtain a DOS in the superconducting state which surpasses the normal state DOS simply by adding a large quantity of impurities? Naturally, the answer is no: adding impurities also has the effect of destroying superconductivity in an unconventional superconductor by first reducing T_c as Γ is increased and by totally destroying the superconductivity for $\hbar\Gamma_{crit} = 0.88\ k_B T_c$ [78].

Although the specific formulation will vary depending on the gap topology, these results hold for any gap with lines of nodes. This is in stark contrast with an anisotropic gap where the nodes are accidental and not topological. Indeed, in this case, adding non-magnetic impurities will have the effect of making the gap more isotropic [79]. In other words, instead of increasing the DOS at low energies, it will decrease it.

Physical properties and κ

Before moving on to calculating physical properties, let us formulate the problem with the useful terminology introduced by Lee [80]. The latter parameterizes the excitation spectrum of the low energy quasiparticles. In momentum space, these will only be important at the gap nodes where the density of states is finite. This also allows to linearize the gap spectrum around the node. There, the Fermi velocity is defined in the usual way and a second velocity emerges as given by the slope of the gap at the node:

$$v_F = \frac{\partial \xi_k}{\partial \mathbf{k}} = v_F \widehat{\mathbf{k}}_\mathbf{1} \tag{2.24}$$

$$v_2 = \frac{\partial \Delta_k}{\partial \mathbf{k}} = v_2 \widehat{\mathbf{k}}_\mathbf{2} \tag{2.25}$$

where $\widehat{\mathbf{k}}_\mathbf{1}$ is perpendicular to the Fermi surface and $\widehat{\mathbf{k}}_\mathbf{2}$ is tangential to it. This forms a so-called Dirac cone which has an energy dispersion relation of the form:

$$E_k = \sqrt{\xi_k^2 + \Delta_k^2} = \hbar\sqrt{v_F^2 k_1^2 + v_2^2 k_1^2} \tag{2.26}$$

What's more, v_2 can be simply related to the slope of the gap at the node by $S = d\Delta/dk = \hbar k_F v_2$. For a true d-wave gap, this slope is given by $S = \Delta_0/2$. This allows us to reformulate the DOS of states in the dirty limit (for $E < \gamma$) the following way:

$$N_s(E) = \frac{2N_N(0)\gamma}{\pi\Delta_0} = \frac{4}{\pi^2\hbar^2}\frac{\gamma}{v_F v_2} \tag{2.27}$$

[1] The logarithm of Δ_0/γ is left out as it is a small correction.

using the fact that $N_N(0) = \frac{m}{\pi\hbar}$, $\hbar k_F = v_F/m$ and $\Delta_0 = \hbar k_F v_2/2$. From this, we can sketch a derivation of the heat capacity and the thermal conductivity which will capture the essential consequences of having a gap with line nodes. It also shows a natural way to obtain power law dependences for many physical properties (a distinctive signature of an unconventional gap) instead of activated behavior for s-wave superconductors. Let us first derive the energy of the ground state for such a density of states:

$$\begin{aligned} E &= E_0 + \int_0^\infty dE \text{ (DOS) (Distribution function) (Energy)} \\ &= E_0 + \int_0^\infty dE\ N_s(E)\ f(E)\ E \\ &= E_0 + \int_0^{k_B T} dE \frac{4}{\pi^2\hbar^2}\frac{\gamma}{v_F v_2} E \\ &= E_0 + \frac{2}{\pi^2\hbar^2}\frac{\gamma}{v_F v_2}(k_B T)^2 \end{aligned} \tag{2.28}$$

as long as $T < \gamma$ and with $f(E)$ being the Fermi distribution function (approximated to be a step function). The heat capacity is easily calculated to be:

$$C = \frac{dE}{dT} = \frac{4k_B^2}{\pi^2\hbar^2}\frac{\gamma}{v_F v_2} T \tag{2.29}$$

which depends on the level of purity γ. This result is natural since the DOS increases with the level of impurities. The thermal conductivity is obtained as $\kappa_0 = \frac{1}{2} C v_F^2 \tau$ where the factor of 1/2 is due to the 2D nature of the transport and the lifetime is given by $\tau = \hbar/\gamma$. This leads to

$$\frac{\kappa_0}{T} = \frac{2}{\pi^2}\frac{k_B^2}{\hbar}\frac{v_F}{v_2} \tag{2.30}$$

which has the property of being independent of the level of purity. This is of course counter-intuitive but is understood naturally: *the effect of the increasing DOS and the decreasing scattering lifetime with the increasing density of impurity exactly cancel one another.* For this, it is said that the thermal conductivity is *universal* with respect to impurity concentration [80, 81]. This was verified experimentally in both YBCO and BSCCO at optimal doping [82, 83, 84] (see Fig. 2.8a). What's more, it is only dependent on the ratio v_F/v_2. This derivation is simplistic and does not get the correct prefactors (it misses them by $\pi^2/6$). The proper calculation gives

$$\frac{\kappa_0}{T} = \frac{k_B^2}{3\hbar}\frac{n}{d}\left(\frac{v_F}{v_2} + \frac{v_2}{v_F}\right) \tag{2.31}$$

where $\frac{n}{d}$ is the average spacing between CuO_2 planes (n is the number of planes per unit cell and d is the c axis lattice constant) [81, 85]. This result was also shown to

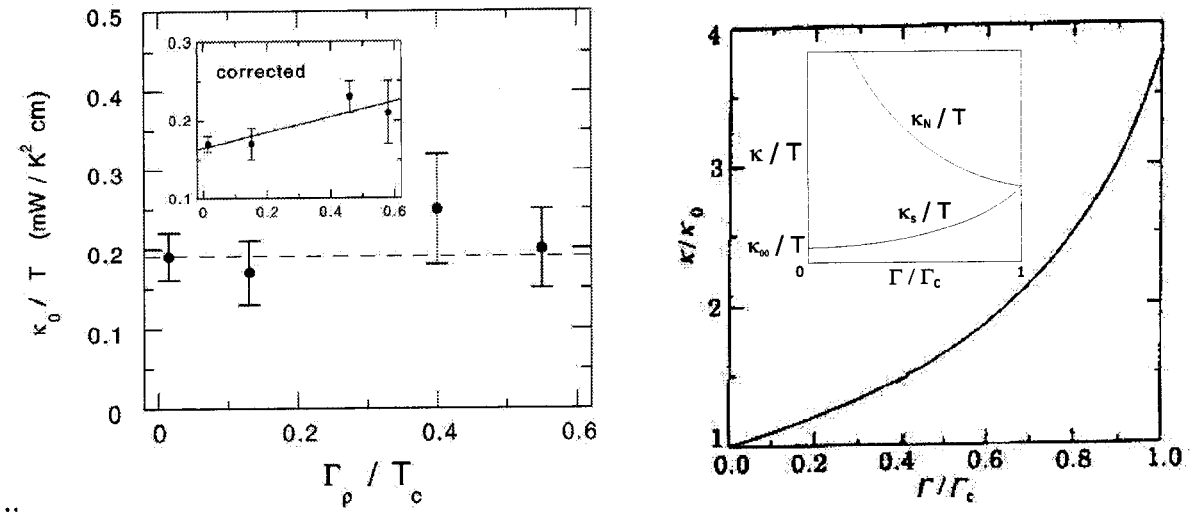

Figure 2.8: (a) The residual linear term κ_{00}/T as a function of disorder (Γ) for YBCO showing universal conductivity in a d-wave superconductor [82]. The inset shows the values of κ_{00}/T corrected for the finite values of Γ as shown in (b). (b) The correction to the universal conductivity with disorder where $\hbar\Gamma_c = 0.88\ k_B T_c$ (after [86]). The inset shows a schematic of the same graph with the normal state thermal conductivity.

be insensitive to vertex and Fermi-liquid corrections [85] which makes it a unique probe of the quasiparticle parameter v_F/v_2. But remembering that adding a large amount of impurities will actually destroy the superconductivity, we assume that the thermal conductivity will also deviate from this universal constant at large values of Γ. This is indeed the case as has been calculated by Maki [86] as shown in Fig. 2.8b.

Many other properties such as the charge conductivity $\sigma(T)$, the penetration depth $\lambda^2(0)/\lambda^2(T)$ and the heat capacity can be calculated in this way and are also dependent of the parameters v_F and v_2. In fact, these parameters can be measured directly by angle resolved photoemission spectroscopy [87]. A coherent quantitative picture has emerged in the high T_c cuprates [88, 89] giving credit to this formalism.

Summary

Let us now review what we have learned about the thermal conductivity of a superconductor with lines of nodes:

- The DOS is zero at $E = 0$ but has a power law behavior (linear for a d-wave gap)

below the gap.

- At low energies, the density of states will become finite as non-magnetic impurities are introduced (in the Unitary scattering limit) and will scale with the amount of impurities Γ.
- The density of states will then be constant up to an energy γ.
- This is in stark contrast to an anisotropic s-wave gap. There, adding non-magnetic impurities will make the gap more isotropic and effectively reduce the density of low energy quasiparticle states.
- The thermal conductivity is universal due to the cancellation of the increasing DOS and the decreasing scattering lifetime as one increases the level of disorder.
- In high T_c cuprates, a qualitatively and quantitatively correct picture has emerged. However, the quantitative formulation will be different depending on the gap topology (d-wave or other) and the dimensionality of the system (2D or 3D).

In summary, a residual linear thermal conductivity will be observed for an unconventional superconductor with lines of nodes in the gap. κ_{00}/T is also universal with respect to the level of disorder. This is in stark contrast with an s-wave superconductor where $\kappa_{00}/T = 0$ and with a superconductor with accidental nodes. There, impurities will make the gap more isotropic and yield no universal thermal conductivity.

2.4.4 Thermal conductivity in the vortex state of unconventional superconductors

It is a central theme of this thesis to explore the vortex state of several types of unconventional superconductors. This section can therefore not serve as a review of the findings that will be discussed in the following chapters. Instead, we will introduce the main concepts that will be useful in our interpretation of new behavior. It is most instructive to see which energy scales may be important in the mixed state of superconductors. The most common one is the so-called Doppler shift energy introduced by Volovik in 1993 [90] but we will also look at the Zeeman energy which has not been considered very often in recent theoretical treatments.

Before moving to our program, it is worth noting that unlike the BRT thermal conductivity for s-wave superconductors or the universal κ in superconductors with lines of nodes, the field dependence of κ depends greatly on the nature of the superconductivity, the level of disorder (even for a simple d-wave gap) or more generally on the regime of magnetic field in which one is [91]. This is part of the richness of this technique as it may unveil many new phenomena. Indeed, it is fair to say that our work on borocarbides [92] has fuelled many other studies of $\kappa(H)$ in unconventional superconductors such as ruthenates (Sr_2RuO_3 [54, 93, 94]), organic superconductors (λ-$(BETS)_2GaCl_4$ [95], κ-$(BEDT\text{-}TTF)_2Cu(NCS)_2$ [96]), heavy Fermions systems ($CeCoIn_5$ [97], $PrOs_4Sb_{12}$ [98]), and multi-band superconductors (MgB_2 [99], $NbSe_2$ [55]). Before this, only few thorough studies had been performed on other heavy Fermions (most notably UPt_3 [100]). Of course, high T_c cuprates have been investigated but mostly in field ranges much below H_{c2} (see for example [88]). In all, much is left to discover and measurements of $\kappa(H)$ will surely continue to provide invaluable insight on the superconducting state of nonconventional superconductors.

Doppler shift energy

It was first pointed out by Volovik [90] that the quasiparticles outside the vortex cores of d-wave superconductors will be shifted in energy by a Doppler shift. This is due to the circulating flow of electrons around a vortex core which leads to an energy spectrum modified from that obtained in Eq. 2.26:

$$E_k(\mathbf{H}) = E_k - v_s.\mathbf{k} \tag{2.32}$$

where v_s is the superfluid velocity. Since the spectrum is shifted down, the energy gap seems smaller to exceed in an s-wave superconductor and more states are populated at the nodes of a d-wave superconductor. The superfluid velocity decreases as $v_s \propto 1/r$ away from the vortex core. To obtain the average energy shift, we must integrate over the unit cell of the vortex core such that $E_H \propto (\int_0^d d\mathbf{r}^2 r^{-1})/(\int_0^d d\mathbf{r}^2) \propto 1/d \propto \sqrt{H}$ where $d \propto 1/\sqrt{H}$ is the intervortex distance. A more detailed derivation leads to $E_H = a(H/H_{c2})^{1/2}\Delta_0$ where a is a vortex lattice geometrical constant close to 1 and Δ_0 is the gap maximum.

This new energy scale will lead directly to an increase in the density of states and subsequently in the heat capacity with a $\sqrt{H}$ dependence. Such a behavior was indeed observed in YBCO [101, 89] and in LSCO [102] (see [74] for a more complete review). The

thermal conductivity is naively expected to follow the same behavior but is in fact found to have a somewhat more complicated form. In a d-wave superconductor for example, Kübert and Hirschfeld have found that for a magnetic field applied parallel to the c-axis, the thermal conductivity will have the following form: $\frac{\kappa(T=0,H)}{\kappa_{00}/T} = \frac{\rho^2}{\rho(\rho^2+1)^{1/2}-\sinh^{-1}\rho}$ where $\rho = \sqrt{\pi/6}\ \gamma/E_H = \sqrt{\frac{6\gamma^2 H_{c2}}{\pi\Delta_0^2 a^2 H}}$ [91] in the dirty limit (for $E_H < \gamma$). This was verified experimentally in optimally doped YBCO [88].

Zeeman Energy

The Zeeman energy is linear in field and has the form $E_Z = \mu_B H$ where μ_B is the Bohr magneton ($E_Z \sim 1$ K at $H = 1$ T). It has effect of breaking Cooper pairs as the magnetic field will polarize the spin up and spin down electrons in opposite directions. This energy is usually associated to the destruction of superconductivity in a magnetic field. However, it was shown that it has little effect on the quasiparticle spectrum in an s-wave superconductor [103]. What's more, it was also shown not to have a significant effect on the density of states (or the transport properties) of d-wave superconductor [104].

It is unfortunate that this energy scale seems to have been left behind at the expense of its Doppler shift counter part. It may reveal to play a major role in thermodynamic and transport properties but has not been explored much theoretically.

2.5 Conclusion

We have reviewed the behavior of the thermal conductivity in metals and insulators with a specific interest on the Wiedemann-Franz law which will be central to Chapter 7. The thermal conductivity of superconductors, both conventional and unconventional was reviewed for $H = 0$ and in a magnetic field. This will lead us to an easier understanding of the research that is presented in this thesis.

Chapter 3

Experimental techniques

^{4}He was first liquefied in 1904 by Kammerligh-Onnes at a temperature of 4.2 K. This was the beginning of a long journey towards low temperatures. Soon after, he discovered the phenomenon of superconductivity in mercury thanks to these low temperatures and started another one of the great stories of physics. What better example of the new phenomenon that can be discovered and the exciting physics that can be studied thanks to low temperature techniques. The list is long (*e.g.* superfluidity in ^{3}He, the fractional quantum Hall effect) but what is clear is that these techniques have enabled great research throughout the years.

For the sake of continuity, we will leave the discussion of cryogenic techniques to Appendix A. This chapter will concentrate instead on describing the technical aspects of a thermal conductivity measurement at cryogenic temperatures, and especially in a dilution refrigerator. It will explain how we are able to obtain a high precision measurement of the thermal conductivity of a material down to temperatures of 50 mK and in magnetic fields as high as 15 T.

3.1 Thermal conductivity

A thermal conductivity measurement is a DC technique which uses a four-probe geometry and is almost completely analogous to a DC resistivity measurement. A heat current $\dot{Q}$ (charge current I) is applied and the resulting temperature drop ΔT (voltage drop ΔV) is measured across the sample. The thermal and electrical conductivities are defined as $\kappa = \alpha\dot{Q}/\Delta T$ and $\sigma = \alpha I/\Delta V$ where α is the geometric factor of the sample.

3.1.1 Generic thermal conductivity setup

A generic setup for the measurement of thermal conductivity is showed in Fig. 3.1. The main components include a heating device, two thermometers to measure the heat gradient and a reference thermometer. Indeed, a measurement of κ consists mainly of a high precision temperature measurement (to obtain a temperature difference).

The heating device can take many forms, the goal being to obtain a known amount of heat flowing through the sample. The simplest heater is a resistive element which is in thermal contact with the sample. Joule heating will produce an amount of heat equal to RI^2 when a DC electrical current is applied through this resistance. However, the heat could also be applied by radiation (for example with a optical fibre) or by induction. Both these methods are harder to implement and to control.

There are two main ways to measure the temperature gradient across the sample. The first is to use two calibrated thermometers and to measure the temperature of each one. The other is using a thermocouple which measures directly a temperature gradient. The latter is an attractive and simple method but has the disadvantage of loosing sensitivity below approximately 10 K. At these temperatures, it also has a nontrivial and irreproducible magnetic field dependence. We will limit further discussion to the first method as it is the one we have used for the work presented in this thesis.

Finally, the temperature is measured by a reference thermometer. It can also be used to calibrate in-situ the two other thermometers (if this is the method used) while there is no heat applied to the sample.

3.1.2 Considerations

Although the measurement of thermal conductivity is a simple one, many considerations must be kept in mind while designing the experimental setup. These are enumerated below in the following order: heat losses; thermometer temperature; choice of thermometers and heater; vibration issues; heat capacity of the components. This will lead to a natural explanation of the particular setups that will be described in other sections.

Heat losses

Heat losses is a crucial consideration one needs to keep in mind while measuring thermal conductivity. This comes back to the question of knowing how much heat $\dot{Q}$ is flowing through the sample. There are three potential sources of heat losses: via conduction,

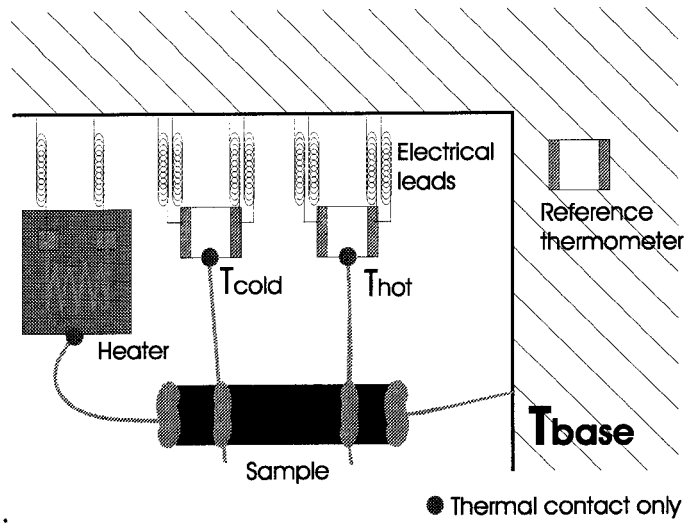

Figure 3.1: Schematic of a generic thermal conductivity setup. The main components are a heating device to apply a heat current, two thermometers to measure the temperature difference ΔT across the sample and a reference thermometer.

radiation or convection. The first will be through the measurement wires, the second, through photons and the third, through the gas in the experimental chamber.

Conduction The applied heat stems from the heating device and will flow to the temperature of the base. It can follow two parallel thermal paths as described on Fig. 3.2a. The first is through the sample (Path 1), while the other is down the measuring wires of the heater itself (Path 2). Two other paths also open to the heat current as it passes through the sample: the measuring leads of the thermometers (Paths 3 and 4). These three last paths need to have a much larger impedance (thermal resistance) than the first one such that

$$W_{path1} \ll W_{path2}, W_{path3}, W_{path4} \tag{3.1}$$

where W is the thermal resistance (a more careful analysis can be found in Appendix B). Note that one needs to be careful about knowing what these paths are to properly rule out the possibility of heat losses.

Radiation The Planck law of radiation states that the power dissipated by a black box is proportional to T^4. It is then clear that radiation problems get more pronounced at higher temperatures. Two parallel plates at different temperatures T_1 and T_2 and with

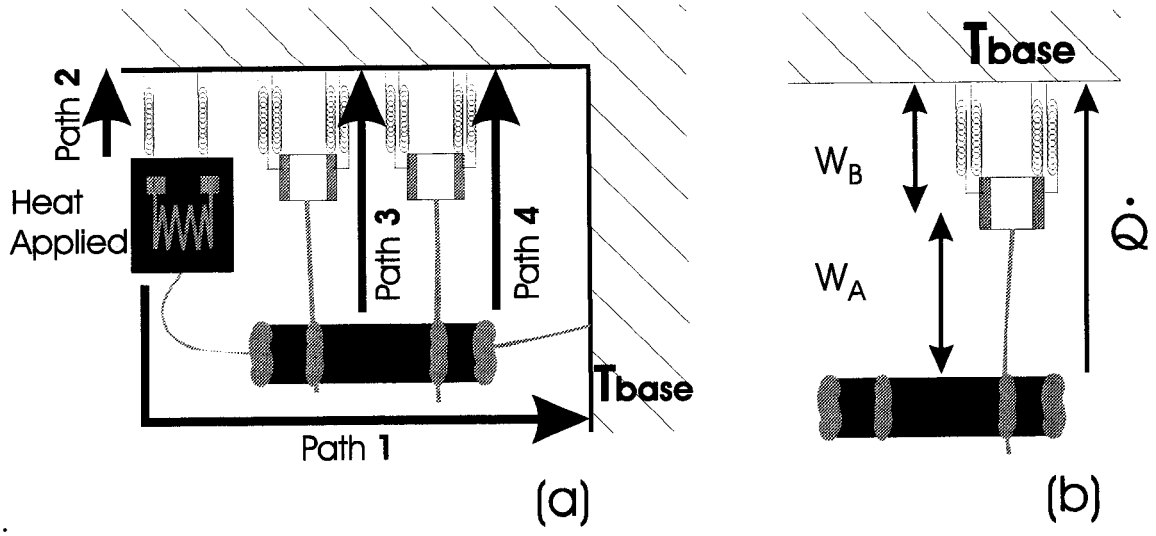

Figure 3.2: (a) The heat stems from the heater and will follow paths 1 to 4. Avoiding heat losses is obtained by having most of the heat go through Path 1. (b) To ensure a good measurement of the sample temperature, one needs $W_A \ll W_B$.

emissivities ϵ_1 and ϵ_2 and area A transfer heat from one another at the following rate:

$$\dot{Q}_{radiation} = \sigma A(T_2^4 - T_1^4)\frac{\epsilon_1\epsilon_2}{\epsilon_1 + \epsilon_2 - \epsilon_1\epsilon_2} \tag{3.2}$$

where $\sigma = 5.67 \times 10^{-8}\text{W m}^{-2}\text{ K}^{-4}$ is the Stephan-Boltzmann constant [105]. The emissivity has a maximum value equal to 1 for a perfect blackbody. However, the case of radiative heat losses in a thermal conductivity setup is more subtle. To illustrate this, consider a reference thermometer which is in a situation where it radiates a large amount of heat to its surroundings (which is, say, at $T = 4$ K). The temperature measured from it *is* the temperature at which it is. Then, any part of the measurement setup which is in good thermal contact with this thermometer, although they are also radiating a lot of heat, is at this same temperature (as long as the amount of heat they are radiating is similar to that of the reference thermometer). For a thermal conductivity setup, each component will radiate a certain amount of heat while no heat current is applied. It will then radiate an *additional* amount of heat when a heat current is applied and that some parts are at a higher temperature (for example, the heater will be the part which will be at the highest temperature). It is this *additional* amount of heat which may contribute to heat losses if it is of the same order as the heat current applied to the sample. It is

given by:

$$\dot{Q}_{rad\ loss} = \dot{Q}_{rad\ \dot{Q}\ \text{on}} - \dot{Q}_{rad\ \dot{Q}\ \text{off}} = \sigma A(T^4_{\text{heater on}} - T^4_{\text{heater off}})\frac{\epsilon_1\epsilon_2}{\epsilon_1 + \epsilon_2 - \epsilon_1\epsilon_2} \tag{3.3}$$

and is independent (to first order) of the temperature of the surroundings (this is why a radiation shield does not help in reducing the heat loss problem). However, there exists some elaborate schemes designed to reduce these types of heat losses [106].

As the discussion above describes, the losses due to radiation will come from all parts of the setup (including the sample) which has a higher temperature when a heat current is applied. The main component will be the heater which is at the highest temperature but the sample and the thermometers will also contribute.

Convection Some heat may be lost through the surrounding gas in the IVC. For this reason, the experimental setup must be in a good vacuum which is done both by evacuating the IVC before an experiment but also by the effect of cryopumping.

The heat carried by helium gas (the one most susceptible to live in our cryostats: below the freezing point of most gases) is given by:

$$\dot{Q}_{convection} \simeq 0.02\ a\ A\ [\text{cm}^2]\ P\ [\text{mbar}]\ \Delta T\ [\text{K}] \tag{3.4}$$

for parallel plates of area A [105]. a is the accommodation coefficient of the gas on the walls of the IVC (how likely they are to transfer heat to it) which is at most 1 and can be as low as 0.025 for clean surfaces. This equation holds true if the mean free path of the gas molecules is larger than the distance between the plates which is the case at low pressures and the small volume of an IVC.

Note that the same discussion as that of the heat loss through radiation can be held and the heat loss will consist of the difference of convective heat transfer for "heat on" and "heat off".

Thermometer temperature

This is an equally important but often forgotten consideration: one needs to make sure that the thermometer is at the same temperature as the sample. Consider either path 3 or path 4 of Fig. 3.2a. A small but finite heat current will flow through this path (since there is a temperature gradient across it). Starting at the sample itself, it then passes through the thermometer and through the measuring wires of the thermometer

creating two thermal resistances in series W_A and W_B (see Fig. 3.2b). In order for the thermometer to be at the same temperature as the sample, one needs to have $W_A \ll W_B$. This way, the temperature gradient is mostly set up across W_B, with a negligible gradient from the sample to the thermometer.

Choice of Thermometers

Depending on the use of the setup (temperature range, measurements in a magnetic field), different kinds of thermometers will be most appropriate. The thermometers used are resistive chips which have a highly temperature-dependent resistance. Typically, it increases dramatically at low temperature. Measuring temperature reduces to a simple resistance measurement. Here is a list of considerations for choosing them.

Sensitivity As for any measurement, one wants to obtain the largest signal to noise ratio to maximize the sensitivity. For a temperature measurement based on resistivity, it is tempting to think that one should choose a thermometer on the basis of a large dR/dT, the temperature sensitivity of the thermometer. A proper analysis shows that the correct criteria is to maximize $\frac{T}{R}\frac{dR}{dT}$ or $\frac{1}{R}\frac{dR}{dT}$ depending on the type of noise. Let us see why.

Considering that one measures the resistance of the thermometer with a standard low frequency lock-in technique, the limiting noise will most likely come either from the resolution of the measuring apparatus or from Johnson noise. In both cases, we can consider the noise as some fixed voltage value V_n, except that the Johnson noise has a linear T dependence. This naturally leads to a noise in the temperature of $T_n = V_n \; dV/dT = V_n/(I \; \frac{dR}{dT})$. Since the "signal" is T, the signal to noise ratio (SNR) is then SRN $\propto T \; I \; \frac{dR}{dT}$, where I is the applied current (and forgetting about V_n which is fixed). Note that for Johnson noise $V_J \propto T$, the signal to noise ratio will not depend on temperature and SNR $\propto I \; \frac{dR}{dT}$. But would this mean that simply increasing the current I would give an arbitrarily high SNR? This is not the case in a thermal conductivity experiment as increasing the applied current will increase the self-heating RI^2 of the thermometer which is, by nature, poorly thermally anchored to the base. This additional constraint tells us that, to obtain the same SNR (*i.e.* having the same I and the same $\frac{dR}{dT}$), a thermometer with a smaller resistance R will lead to less self-heating. For this,

one needs to maximize $\frac{T}{R}\frac{dR}{dT}$ for resolution limited noise and $\frac{1}{R}\frac{dR}{dT}$ for Johnson noise [1]. Note that the noise in the experiments presented in this thesis was resolution limited.

Temperature range Different thermometers will be chosen depending on the temperature that wants to be covered. For low temperatures, the choice arises from the resistance of the thermometer. Since it is very difficult to measure reliably a resistance higher than 50 - 100 kΩ or so, the thermometer will be chosen to have a resistance which does not surpass this value. At high temperatures, the question is simply one of sensitivity.

Low magnetic field dependence For measurements in a magnetic field, the thermometers must display a low -or better yet nil- magneto-resistance. Indeed, if it is large and positive, one may end up with a resistance which is too high to measure reliably (higher than 50 - 100 kΩ) at the lowest temperatures. This is the case, for example, with Germanium thermometers.

What's more, depending on the type of thermometer, its magneto-resistance may be simple (*e.g.* Ruthenium oxides) or complicated (*e.g.* Cernox chips) to model, an important point for the parameterization procedure (obtaining $R(T, H)$).

In special cases, the thermal conductivity is measured with respect to a rotating magnetic field direction. There, the thermometers must have an isotropic magnetoresistance (such is the case for Ruthenium oxides). However, such measurements were not performed in our group.

Size The size of the thermometers must be taken into account: as is discussed below, one wants all the components of the experimental setup to have a low heat capacity. This helps reduce the measurement time. As such, the smallest size thermometers are usually used.

Another aspect which arises at high temperatures is that of heat losses via radiation. These are limited with a small surface area of the thermometers (see Eq. 3.3).

Reproducibility The reproducibility of the thermometers upon thermal cycling is also a point to consider. In our case though, we use the safe approach and recalibrate the

[1] This may no longer be true when the resistance of the thermometer becomes smaller than that of its measuring wires. Then, the heat produced by the wires may outweigh the self-heating of the thermometer itself.

thermometers against a stable reference thermometer for each measurement. For temperatures above 1 K, we use a Cernox CX-1050 from Lakeshore which has a maximum drift of 25 mK per year for $T < 100$ K. Below 1 K a Germanium thermometer GR-200-A-30 from Lakeshore is used also for its high reproducibility and is routinely (every year) recalibrated against a RuO_2 thermometer calibrated by Oxford (this one is not thermally cycled often and we assume that its calibration does not drift).

Choice of heater

We will limit our discussion to the type of heaters that are most commonly used: a resistive element in thermal contact with the sample. A current I is applied on the heater which produces an amount of heat equal to $\dot{Q} = R_{heater}I^2 = VI = V^2/R_{heater}$ via Joule heating.

Temperature and field dependence Very often, one uses a third thermometer to act as a heater. This implies that both the DC current and voltage across the heater must be measured to know $\dot{Q}$. However, the ideal heater has no temperature nor magnetic field dependence. In this case, one must only measure either the current or the voltage across it, and this, both in temperature and in field.

Resistance value In either cases, the choice of the value of R_{heater} is based mostly on the resistance of its current carrying wires. Since these need to be highly thermally resistive to minimize heat losses (as discussed above), they are also electrically resistive (except in the case of superconducting wires). As such, they will also produce an amount of heat equal to $\dot{Q} = R_{wires}I^2$. But this heat will not have a well defined thermal path to travel: for the bottom half of the wires, it will be easier for the heat to go directly down the wires whereas for the top half, the heat may want to go through the sample. In any case, this will provide a situation where the amount of heat which crosses the sample is ill-defined. To remedy this, we must use $R_{heater} \gg R_{wires}$. This way the heat produced by the wires, wherever it chooses to go, is negligible with respect to the heat applied on the sample [1].

[1] Note that one can use superconducting wires in some cases. There the thermal conductivity is small as long as we are much below T_c and H_{c2}. However, this may pose some unwanted limits on the range of the setup.

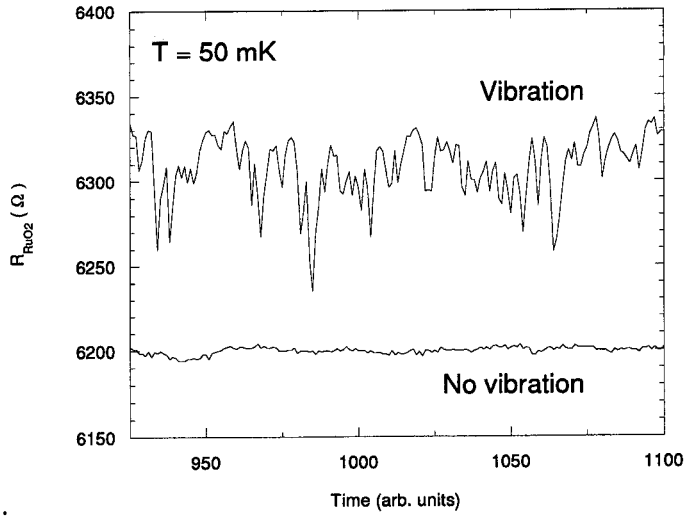

Figure 3.3: The noise level of the resistance of a vibrating and a non-vibrating RuO_2 thermometer at T=50 mK as a function of time. For the former, notice the vibration-induced heat peaks (a decreases in R corresponds to an increase in T).

Small size The same considerations discussed for the thermometers apply to the heater.

Vibration

It is observed that thermometers are much noisier when they are vibrating. This is displayed on Fig. 3.3 where, at 50 mK, the measured resistance of a vibrating thermometer is seen to have a much larger noise level than the non-vibrating one, in addition to having typical "heat peaks" once in a while where the thermometer is heated for a short instant. Indeed, vibrations have the effect of heating different parts of the setup [1]. The thermometers are especially susceptible to these effects as they are purposefully poorly thermalized to the base temperature. As such, care must be taken to ensure a proper mechanical stability for them. Note that vibration-induced heating has been well known to low temperature physicists for a long time. Nevertheless, the physical mechanism at play is still unclear [105]. Proposing possible mechanisms would be unfounded at this point.

[1] This can be verified easily by gently knocking the cryostat. It results in a severe heating of the thermometers. If they are mechanically stable, they will return quickly to the equilibrium temperature. If not, they will continue vibrating (and having a large noise level) until the system is fully damped.

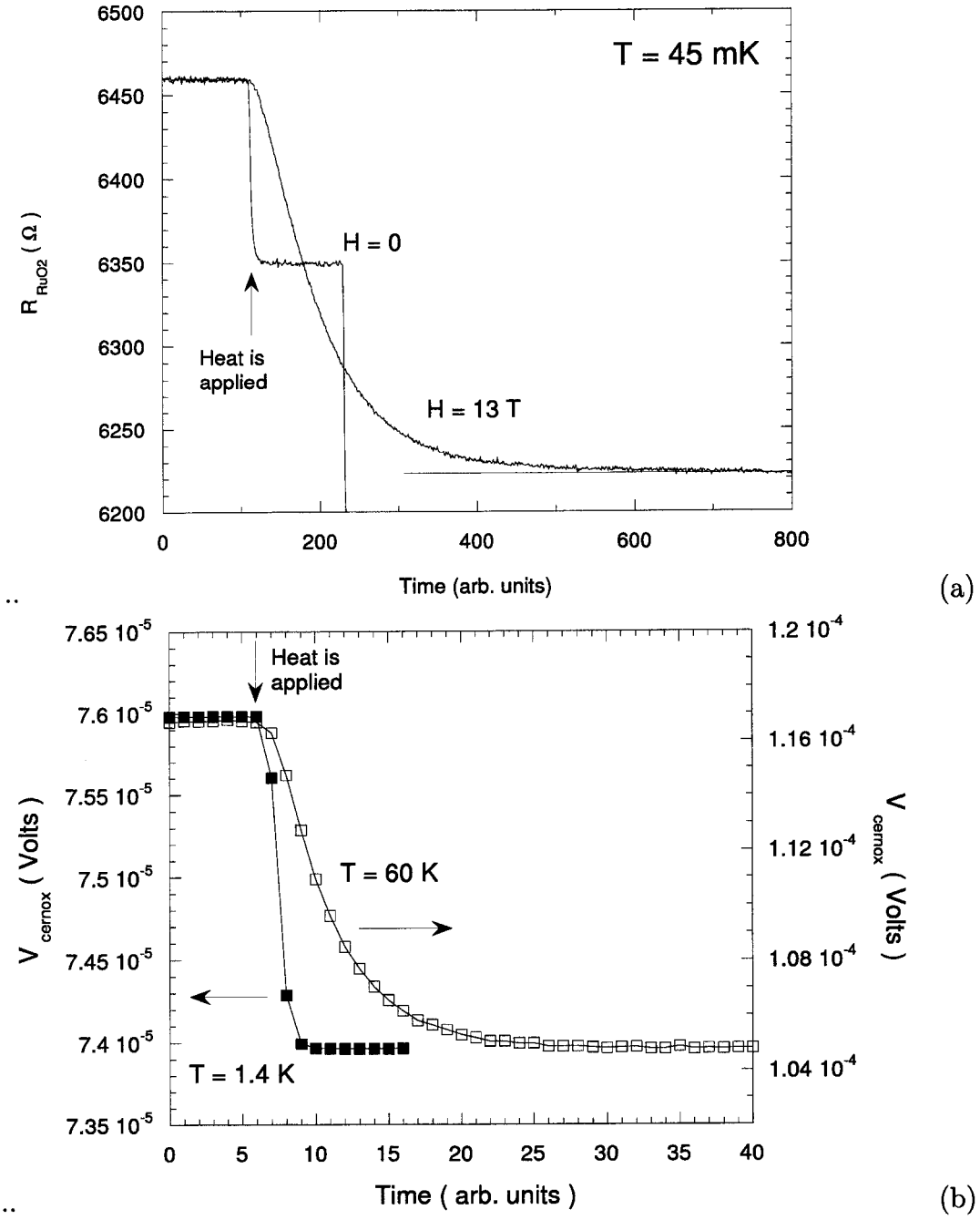

Figure 3.4: Long thermalization time in high magnetic fields (a) or at high temperature (b). This is due to thermal RC circuits within the setup. The increased heat capacity of the components increases the characteristic relaxation time $\sim \sqrt{WC}$.

Heat capacity of the components

The components of the thermal conductivity setup will be heated to various temperatures: as the heat is applied, the heater and the thermometers will go to a higher temperature, the sample and all the measuring wires will have a temperature gradient across them. This will not happen instantaneously. The setup creates a set of complex thermal resistance-capacitance ("RC") circuits with associated thermal resistance W and a heat capacity C. The characteristic relaxation time is simply $\sqrt{\mathrm{RC}}$ in an electrical circuit and $\sqrt{WC}$ here. This will be the time required to reach a steady state equilibrium to then be able to perform our measurements.

Although this effect takes place in all circumstances, it is most pronounced and pervasive at low temperatures and high fields as seen in Fig. 3.4a. This is due to the fact that the heat capacity of many materials increases dramatically in this regime: the nuclear magnetic moments make for this low-temperature increase and it is enhanced in field [107]. However, the same occurs at high temperature where the heat capacity can also become large. This is shown in Fig. 3.4b.

3.1.3 Dilution refrigerator setup

The thermal conductivity experimental setup that was used in our group is shown schematically in Fig. 3.5. The heater was made of two SR-4 strain gauge from BLH Electronic Inc. (Type FSM-A6306S-500-S13C) each having a resistance $R = 5000 \pm 1\%\ \Omega$ and wired in series (giving a resistance of 10000 Ω). It has a temperature and field independent resistance. The thermometers are commercial ruthenium oxide (RuO_2) thick films from Dale with nominal resistances at room temperature of 1 kΩ. They are suspended on thin strips of Kapton® HN gauge 30 (7.5 μm thickness) polyimide film from Dupont which are themselves supported by SP1 Vespel posts (from Dupont as well). These are glued to the copper base with low temperature epoxy. The measurements are made with coiled 25 μm diameter PtW wire (with 92% Pt and 8% W) from Sigmund Cohn Corporation (the model is called 479 Pt). The thermometers are measured with a 4 probe technique whereas the current is injected into the heater with only 2 such wires. This design will be explained in the context of the general discussion above.

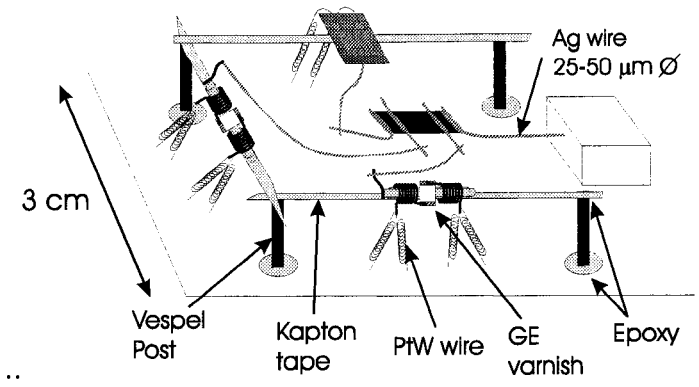

Figure 3.5: Dilution refrigerator thermal conductivity setup. The components are hanging on thin Kapton® film to insure mechanical stability.

Heat Losses

We use 7.5 μm thin Kapton® film cut in 100 μm wide strips. It extends 1 cm on each side of the thermometers and the heater. It is used due to its very low thermal conductivity. The posts are made of SP1 Vespel, also chosen for to its low κ. They have dimensions 0.5 $\times$ 0.5 mm and are 1 cm long. The Kapton® is glued purposefully poorly with epoxy to the Vespel posts in order to have a good mechanical contact but as poor a thermal contact as possible. The Vespel posts themselves are glued to the copper mount with epoxy. The thermometers and the heater are glued -again poorly- to the Kapton® film with GE 7031 varnish (from General Electric), making sure to use the smallest contact area.

We use 25 μm diameter PtW wire that is coiled up to make them very resistive and yet compact in size. Each wire has a resistance of 100 Ω and is independent of temperature.

The heater is carefully glued to a plate of 50-100 μm thick silver foil (cut to the dimension of the heater) with GE varnish in order to create a good thermal contact. A silver wire (50 or 100 μm diameter) is soldered to the silver foil with non-superconducting solder. The wire is then glued to the Ag wires attached to the sample with silver paint.

The sample itself is fixed to a copper plate which is screwed onto the experimental mount. The thermometers are thermalized in a fashion described below. The quantitative assessment of the heat losses can be found in Appendix B. As a note, at temperatures below 1 K, radiative losses are not an issue. Nor are convective losses as a very good vacuum is necessary to reach such low temperatures.

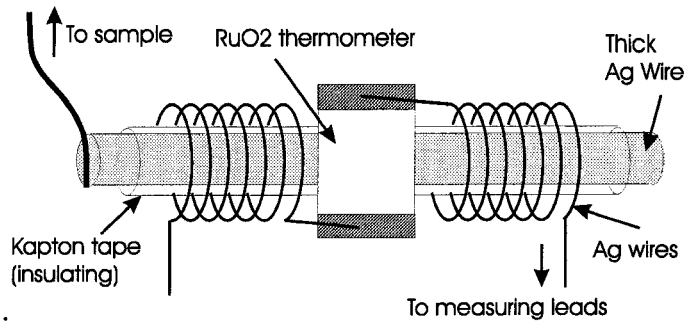

Figure 3.6: Thermalization of the RuO_2 thermometers in our dilution refrigerator setup. This ensures that the thermometer is at the same temperature as the sample.

Thermometer thermalization

The thermalization scheme used for the thermometers is showed in Fig. 3.6. It starts with a thick 0.5 mm diameter silver wire onto which the RuO_2 chip is glued with GE varnish. A thin sheet (Gauge 50 or 100, *i.e.* thickness of 12.5 or 25 μm) of Kapton® film is glued around the thick Ag wire with GE varnish. This provides an electrically insulating but thermally conductive (due to its "large" surface area) platform on which 100 μm silver wire is coiled (5 or 6 turns) to serve as additional thermalization. This wire is then soldered to the RuO_2 chip. A 50 or 100 μm Ag wire is soldered to the thick Ag wire and serves to connect the thermometer to the sample. This has the effect of insuring that $W_A \ll W_B$ (see Fig. 3.2b).

Choice of thermometers

The thermometers used are RuO_2 thick films that are commercially available at a cost of 10 CAD per 1000 pieces. They are called surface mount chips in the electronics literature and are used in most electronic devices, ironically, for the low temperature dependence of their resistance near room temperature. However these chips are available with nominal resistance values at room temperature ranging from a few Ohms to several Megohms. It turns out that the chips that have the correct temperature dependence for thermometry below 1 K have a nominal resistivity between 1 and 3 kΩ depending on the manufacturer.

The chips that were used are from Dale and had a nominal resistance of 1 kΩ at room temperature and a resistance at 40 mK (the base temperature for our measurement) around 7 kΩ. Their temperature and sensitivity ($-dR/dT$) is showed in Fig. 3.7a and b. They also have a small and well behaved magneto-resistance (Fig. 3.7c and d) [108].

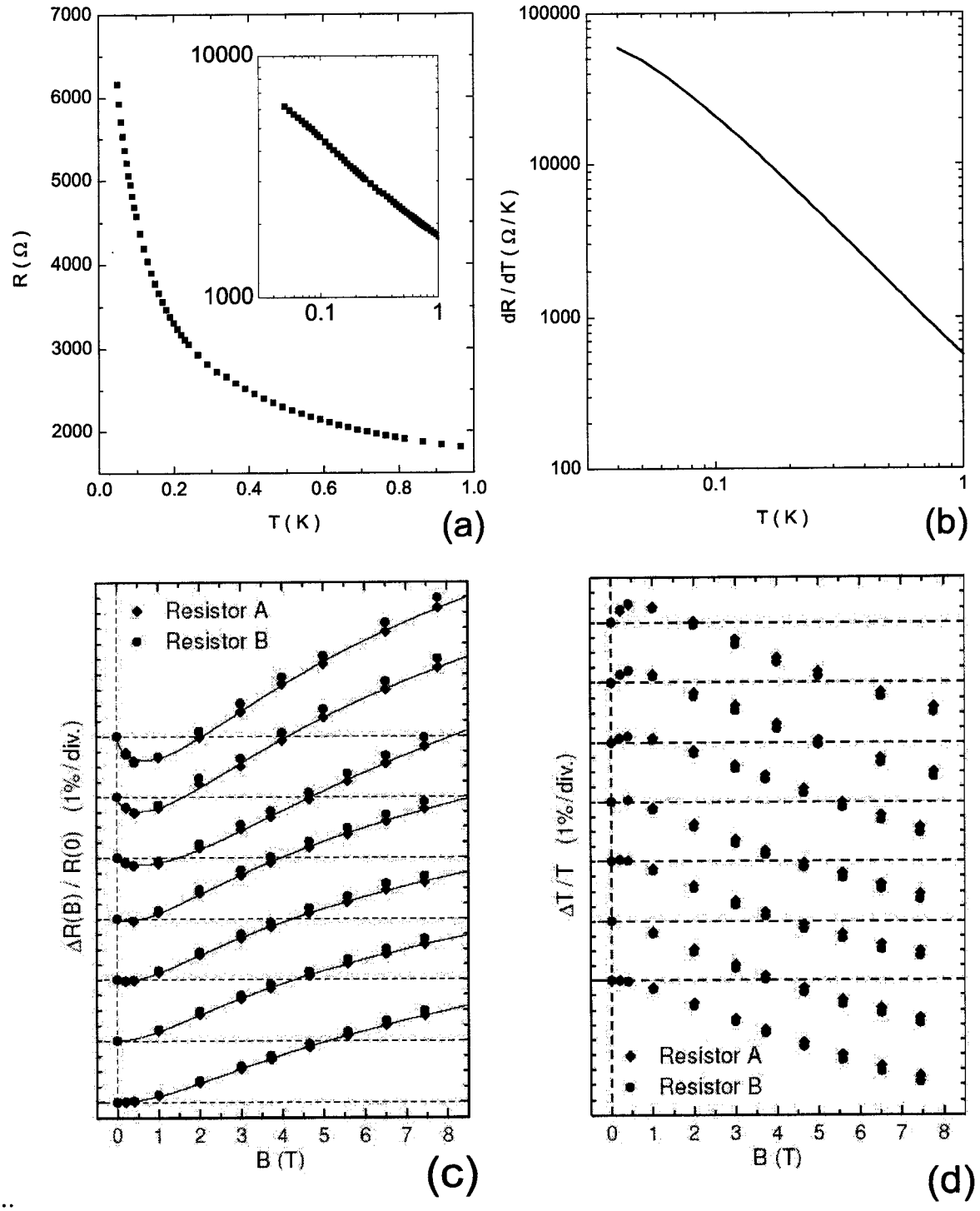

Figure 3.7: RuO_2 thermometer characteristics below 1 K. (c) and (d) are for temperatures of 0.05, 0.06, 0.09, 0.12, 0.16, 0.2 and 0.24 K from top to bottom [108].

Choice of heater

The heaters used were commercially available strain gauges from BLH Electronic Inc. (Model SR-4, Type FSM-A6306S-500-S13C) with a resistance $R = 5000 \pm 1\%\ \Omega$. Two of them were wired in series to give a resistance of 10000 Ω. They have no measurable temperature or magnetic field dependence making them the perfect heaters. Also, the value of the heater is two orders of magnitude greater than the value of the wires used to apply a current through it (100 Ω). This leads to an uncertainty in the heat that is applied which is at most 1%.

Vibration

Fig. 3.5 shows the design made specifically to avoid vibrations. The thermometers are suspended to the Kapton ® strips and held down with the measurement wires. The fact that these are coiled is very helpful: they can be stretched to ensure that the thermometers are held down firmly. Moreover, the cryostat is placed on a thick (2-3 cm) Aluminium plate which decouples vibrations from the surroundings (*e.g.* nearby footsteps). The dilution refrigerator pumps are placed on a vibration isolation platform which itself is far from the cryostat.

Heat capacity of the components

This consideration is extremely important in this temperature range, especially at very high fields. A high heat capacity of the various components can lead to an excruciatingly long stabilization time. As an example, Fig. 3.4 shows the difference in stabilization time in $H = 0$ and $H = 13$ T at 50 mK.

The main source of this long time constant associated with a thermal RC circuit is due to the heat capacity of the measurement wires (and also their high thermal resistance). A simple way to understand this is the following: when the heat current is applied, there is a thermal gradient across these wires (for example $T_{hot} - T_{base}$ for the wires on the hot thermometer). When the heat current is turned off, this thermal gradient must dissipate. It has the choice of going directly down the measuring wires or through the sample. For the bottom half of the wire, the easiest path is through itself since the thermal resistance across the sample must first go through the top half of the wire. However this path already has a large thermal resistance (necessary to avoid heat leaks). If it also has a large heat capacity, the time constant will be very large.

The wires have been chosen to be PtW, an electrically and thermally resistive alloy (as required for heat losses) because its heat capacity is small at low temperature and does not increase dramatically in a magnetic field [107]. This is in contrast with other alloys containing magnetic impurities such as manganin or constantan.

Among other considerations of this order, we have used small RuO_2 thermometers (1.5×1.5 mm^2 surface area) that were thinned down to roughly 100 μm thus reducing their heat capacity. The strain gauge used have also been chosen to be as small as possible (3.8×2.6 mm^2 surface area and roughly 100 μm thick). The other wires that are used are all silver since its heat capacity does not increase significantly with magnetic field.

Reference thermometer

The reference thermometer used for this setup is a Germanium resistor model GR-200A-30 from Lakeshore which was calibrated by Oxford instruments down to 50 mK. It is placed in a *field compensated region* in order to make sure that its calibration is unaltered while the sample is placed in a large magnetic field. This is the key element which makes it possible to obtain such a high accuracy in high magnetic fields. The thermometer is routinely recalibrated by another calibrated RuO_2 thermometer.

Measurement devices

The RuO_2 thermometers are measured using a standard low frequency (around 10 Hz) lock-in technique. The setup has been recently changed to use an LR-700 resistance bridge which is multiplexed to do the measurements. This enables to measure six thermometers (*i.e.* three thermal conductivity setups) at the same time. The current that is used ranges from 1 nA at the lowest temperature to 10 nA at 1 K. As a note, the heat produced by these thermometers is negligible with respect to the heat produced by the heater: at 50 mK, $\dot{Q}_{RuO2} = RI^2 = 7000\ \Omega \times 1\ nA = 7 \times 10^{-15}$ Watts. This is to be compared to the lowest current typically applied to a sample which is $\dot{Q} = 10000\ \Omega \times (0.5\ \mu A)^2 = 2.5 \times 10^{-8}$ Watts.

A low noise high precision current source from Keithley applies the electrical current to the heater. Two models were used: the 224 and the 220 which can apply currents with a resolution of 0.5 μA and 0.5 nA respectively.

The reference thermometer is measured using a resistance bridge coupled to a temperature controller. The latter is a PID controller which will not be described here. The

stability of the base temperature is an important issue: it will determine the maximum precision we can have on our temperature difference measurement (ΔT). Indeed, the stability will set the error on the calibration (done in-situ) of our thermometers. This may, in turn, limit our accuracy on the extracted ΔT. As an example, we achieve a stability of 0.01 mK at $T = 50$ mK routinely.

3.1.4 ^{4}He refrigerator thermal conductivity setup

The thermal conductivity setup used in the 1 K refrigerator is used from the base temperature of 1.5 K and up to 150 K. Fig. 3.8a shows one of the platforms used for the setup. Three such platforms (two for the thermometers and one for the heater) are stacked one on top of the other. They are made of fibre glass and epoxy resin (electronic circuit board) which are shaped into a "U". The thermometers are Cernox (CX-1030) chips from Lakeshore. The heater is the same strain gauge used for the dilution refrigerator setup. They are suspended by their measuring wires which are 12 μm diameter PtW (same type as used in the dilution fridge). The setup is also used to measure resistivity of the samples although it is not ideal for this task due to the high resistance of the PtW wires.

The main attraction of this design is its versatility. It is compact and can be rotated easily or even mounted on different experimental tails. All the components are suspended by their measuring wires, which are stretched to avoid vibration issues and to enable small and fragile samples to be mounted with no risk of harm. The main disadvantage is its fragility. Although the 12 μm PtW wires are amazingly robust for their size, they have a tendency to break on occasion.

Heat losses

One has to be careful in analyzing the heat losses in this setup due to the very wide range of temperature that is covered. Indeed, as seen in Chapter 2, the thermal conductivity of metals and of insulators is not monotonic in this temperature range (and neither is that of the samples that are measured). Also, heat losses due to radiation can become substantial at higher temperatures. A careful analysis is presented in Appendix B.

Measurement wires The path that may lead to heat losses is simply the PtW wire used. This alloy has a resistivity of $\rho \simeq 30$ $\mu\Omega$ cm and is roughly temperature independent.

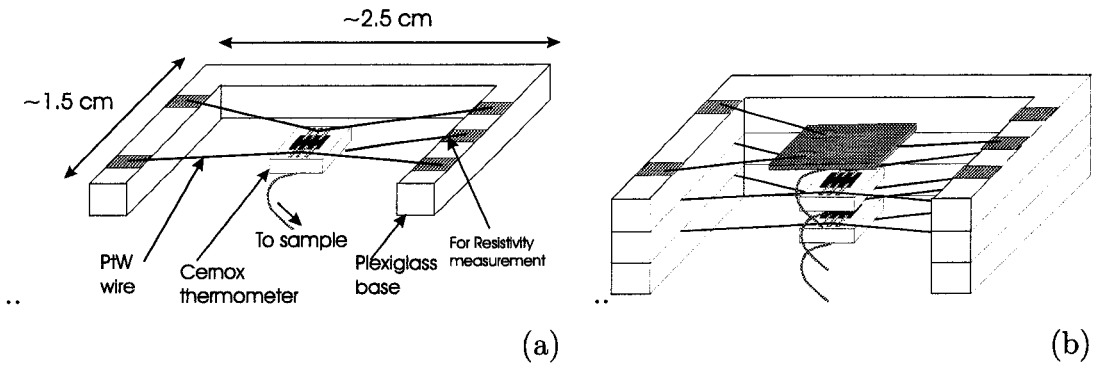

Figure 3.8: Dipper thermal conductivity setup. (a) A subset is shown here with the wires used for each thermometer. (b) The full setup includes three such parts: two thermometer platforms and one for the heater.

The wires used have a length of 1 cm and a diameter of 12 μm (it is the same type as the one used in the dilution refrigerator). There resistance is of $R \simeq 30\ \Omega$. At low temperature, the thermal conductivity is given by the Wiedemann-Franz law.

This must be compared to the path the heat will take through the sample. The heater is thermalized in the same way as in the dilution refrigerator setup. The wire used from the heater to the sample is 50 or 100 μm diameter silver. As for the thermometers, they are thermally connected to 25 μm Pt which is annealed by passing it through the flame of a lighter. They are then easily manipulated.

Radiation The loss due to radiation is probably the main problem one needs to consider at high temperatures. It will set the upper limit in temperature one can reach without suffering from these losses. However, it is difficult to make a general analysis and one must consider each sample carefully.

Convection The loss of heat through the remnant gas in the IVC may plague a measurement. A good vacuum is needed to perform thermal conductivity measurements. However, in usual circumstances, it does not pose a problem (see Appendix B).

Thermometer temperature

As displayed in Fig. 3.2, we need to ensure that the thermal path from the thermometer to the sample is much smaller than the one from the thermometer to base temperature. The Cernox thermometers are thermalized via silver epoxy to the Pt wires which then

connect to the sample.

W_A of Fig. 3.2 consists of the contact on the sample, the Pt wire that connects to the thermometer and the interface between this wire and the thermometer (Ag epoxy). W_B consists of the measurement PtW wires. This satisfies the required condition that $W_A \ll W_B$.

Choice of thermometer

The thermometers used here are Cernox chips obtained from Lakeshore (CX-1030). They have the advantage of keeping a relatively high sensitivity up to and above room temperature. However, depending on the model, the lower limit on the temperature range where they can be used differs. The CX-1030 have a resistance of roughly 5000 Ω at $T = 1.5$ K. They are actually designed for use down to $T = 0.3$ K and were used to have the possibility of using the same setup in a ^{3}He refrigerator. Their resistivity and sensitivity is be shown in Fig. 3.9a. The magneto-resistance is negligible at temperatures above $T = 7$ K [109]. At lower temperatures, it is also relatively small (less than 10 % below $H = 16$ T) but sufficiently large to require a detailed calibration [109]. This has not yet been done but the maximum error on the thermal conductivity due to this effect was measured to be 10% (see Fig. 3.14b).

They are also very small in size ($1 \times 0.75 \times 0.3$ mm^3) and have a high reproducibility upon thermal cycling. Nevertheless, we recalibrate them against a reference thermometer for each measurement.

Choice of heater

The heater is made of the same strain gauge as used in the dilution refrigerator setup (although only one is used here) and has been selected for the same reasons: a temperature and field independent resistance. It also has a high value of $R = 5000$ Ω, much larger than the measurement wires which have a value of $R = 30$ Ω which ensures that all the heat is produced by the heater itself.

Vibration

The thermometers and the heater are suspended via their measurement wires which are stretched to provide a firm mechanical anchor. There is then no risk of vibration.

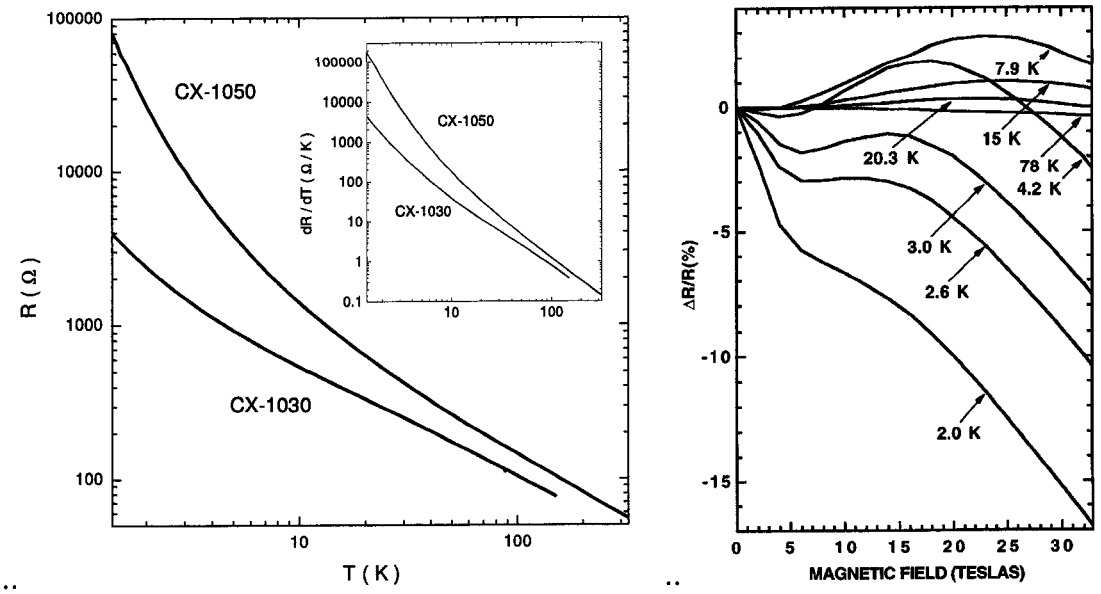

Figure 3.9: (a) Temperature dependence and sensitivity of cernox thermometers models CX-1050 and CX-1030 (from our ^{4}He thermal conductivity setup). (b) The magneto-resistance of Cernox thermometers (after [109]). They are well suited for thermometry in a magnetic field at temperatures above 7 K or so.

Heat capacity of the components

This is an issue at higher temperature also since the heat capacity increases with T. This effect can be seen in Fig. 3.4b. The small size of the components are the main effort done here to reduce the time constants associated with the thermal RC circuit that is formed.

Reference thermometer

The reference thermometer that is used is a Cernox CX-1050 calibrated by Lakeshore. Its resistance and sensitivity can be found in Fig. 3.9. It is used for the same reasons as the two measurement Cernoxes: high sensitivity up to room temperature, low magneto-resistance [109] and high reproducibility (25 mK maximum shift per year from 1 K to 100 K).

Measuring apparatus

The temperature is measured and controlled using a Lakeshore model DRC-93 temperature controller. The thermometers are measured using a standard low frequency lock-in

technique with Stanford Research SR-830 Lock-ins. The heat is applied using a home-made low noise constant-voltage source. A low noise voltmeter from Keithley (model DMM-2000) is used to measure the voltage drop across the heater thus measuring the heat current applied $\dot{Q} = V^2/R_{heater}$.

3.1.5 Data acquisition

The data is obtained in either of two ways: as a function of temperature at constant magnetic field or vice-versa. This section will describe both methods and the important steps that need to be taken in each case.

Temperature sweeps

Most of the measurements are done by measuring κ as a function of T. This is always done by starting at the base temperature and going up in temperature. For each measurement, the thermometers are re-calibrated against the reference thermometer. This is done for two main reasons:

- Avoid any shift in the calibration upon thermal cycling. This effect is negligible for Cernox thermometers but are noticeable for RuO_2. In fact the calibration of the latter shifts below 100 mK without thermally cycling to room temperature.
- Having a perfect calibration in field for the refrigerator measurements. Indeed, the reference thermometer is in a field compensated region and does not see its calibration shift. This does not apply for the setup in the 1 K refrigerator.

The measurements are done following these steps:

1. The temperature is stabilized at a certain temperature.
2. Once the thermometers have stabilized to this temperature, they are measured. The temperature of the reference thermometer is also measured to provide the calibration.
3. The heat is then applied on the sample such that the temperature gradient it produces is roughly 4% of the base temperature.
4. Once the thermometers have stabilized, they are measured along with $\dot{Q}$ (via the voltage across the heater).

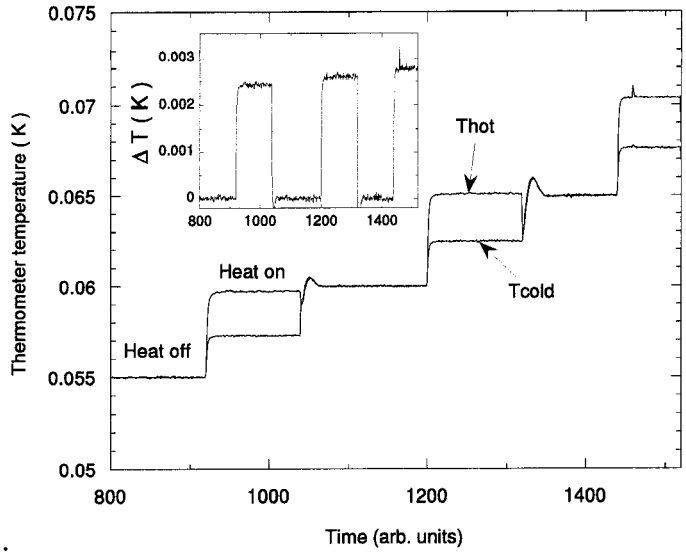

Figure 3.10: The temperature profile as a function of time for both the hot and cold thermometers. The temperature sweeps are made by (i) stabilizing the temperature, (ii) waiting for the thermometers to be stabilized at this temperature, (iii) applying heat and waiting again for stabilization, (iv) changing the base temperature before repeating the procedure. *Inset*: the time evolution of the temperature gradient.

5. The heat is then turned off and the temperature is changed and stabilized at a higher temperature.

6. This procedure is repeated through the whole temperature range.

This process is shown on Fig. 3.10 by showing the time dependence of the temperature of both hot and cold thermometers. The temperature gradient is also shown in the inset. When there is no heat applied, the temperature gradient is of course nil.

Field sweeps

Another useful way to measure κ is by keeping the temperature constant and sweeping the magnetic field. There are two main concerns for this procedure:

- Sweeping a magnetic field has the nasty effect of heating the measurement thermometers. This effect is greatest at low temperatures or while using a high sweep rate dH/dt. This can be due to several effects: magnetic induction on the measurement wires or vortices entering a superconducting sample. Care must be taken to sweep the field slowly especially at the lowest temperatures.

- The average temperature of the sample may be subject to a large change. This effect is largest when the temperature is very low and the thermal conductance of the sample and the thermal contacts are changing rapidly with field. For example, if the cold contact has a fixed conductance and the sample is changing rapidly, the amount of heat that needs to be applied to keep a constant temperature gradient will involve a huge thermal gradient across the cold contact. This would in turn increase the average temperature of the sample. There is no general way to go around this consideration and it must be dealt with case by case.

To perform a field sweep, the temperature is first fixed at some temperature. The following procedure is then repeated through the field range required.

1. Heat is applied in order to obtain a temperature gradient of roughly 4% of the base temperature.
2. We wait for the thermometers to be thermalized and measured them along with $\dot{Q}$.
3. The field is then swept to another value at a typical rate of 20 mT/min. At the same time, the heat is adjusted to keep the same temperature gradient.
4. The thermometers are allowed to thermalize and are then measured along with $\dot{Q}$.
5. This procedure is repeated.

3.1.6 Analysis

The thermal conductivity is defined as

$$\kappa = \alpha \dot{Q}/\Delta T = \frac{\alpha \dot{Q}}{(T_{hot} - T_{cold})} \tag{3.5}$$

The geometric factor α is measured with either a high precision optical microscope or a scanning electron microscope. The heat $\dot{Q}$ is measured and easily known. Clearly, the temperature gradient is the most difficult quantity to extract. With a proper calibration and a good fitting procedure, it becomes straightforward as shown in Fig. 3.11.

3.1.7 Results

The main question remains: what kinds of results do we get using all of these elaborate considerations? Thankfully, there are easy ways to assess this. To make sure that the

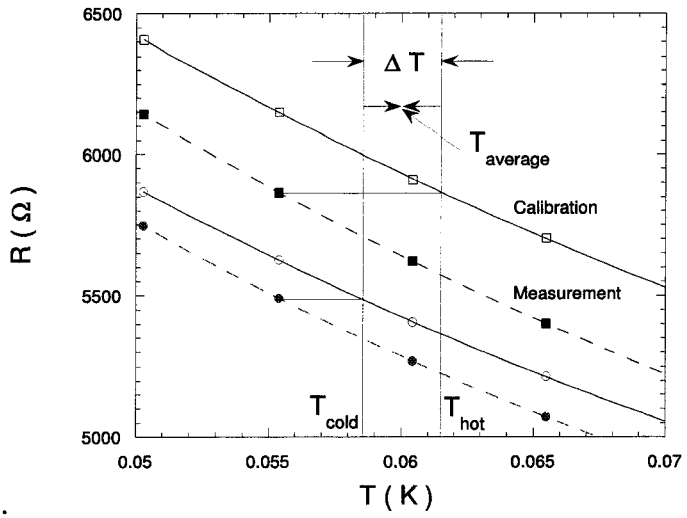

Figure 3.11: Extracting the temperature difference ΔT. The calibration is fitted with a smooth function (empty symbols). The temperature of the hot and cold thermometers (squares and circles respectively) are then extracted. The average temperature is also obtained.

setup is measuring κ accurately, we can test the Wiedemann-Franz law in any metal. This unfortunately is only true for low temperatures (typically below $T = 10$ K), where the WF law is known to hold. Also, to make sure that our measurements in high magnetic fields are dependable, we can measure a material that should have no field dependence (for example, an insulator) and see if our measurement indeed measures no change in κ.

Let us first examine the thermal conductivity tests below 1 K. To see the experimental *precision*, we have measured a silver wire. Its conduction is purely electronic and κ should be perfectly linear in temperature. This is seen in Fig. 3.12a. The inset shows that the scatter is smaller than 3%. As a note, although the resistivity of this particular piece of silver was not measured, the typical residual resistivity is $\rho_0 = 0.02$ $\mu\Omega$ cm which would translate to $\kappa/T = L_0/\rho_0 = 1225$ mW K^{-2} cm^{-1}.

Also, the *accuracy* can best be seen by plotting the Lorenz number ($L = \frac{\kappa\rho}{T}$ divided by the Sommerfeld value ($L_0 = 2.45\times10^{-8}$ W Ω K^{-2}). This is seen for a sample of $LuNi_2B_2C$ in the normal state ($H = 7$ T) in Fig. 3.12b to be equal to one within the experimental precision. Finally, κ of an insulating sample of $La_{2-x}Sr_xCuO_4$ with $x = 5$ % is shown in both $H = 0$ and $H = 8$ T (Fig. 3.13). There is no discernable difference between the two sets of data. (Measurements on LSCO were performed by D.G. Hawthorn).

As for the ^{4}He refrigerator, Fig. 3.14a shows the WF law satisfied for a Ag sample at low temperature. L/L_0 decreases below the value of one at higher temperatures

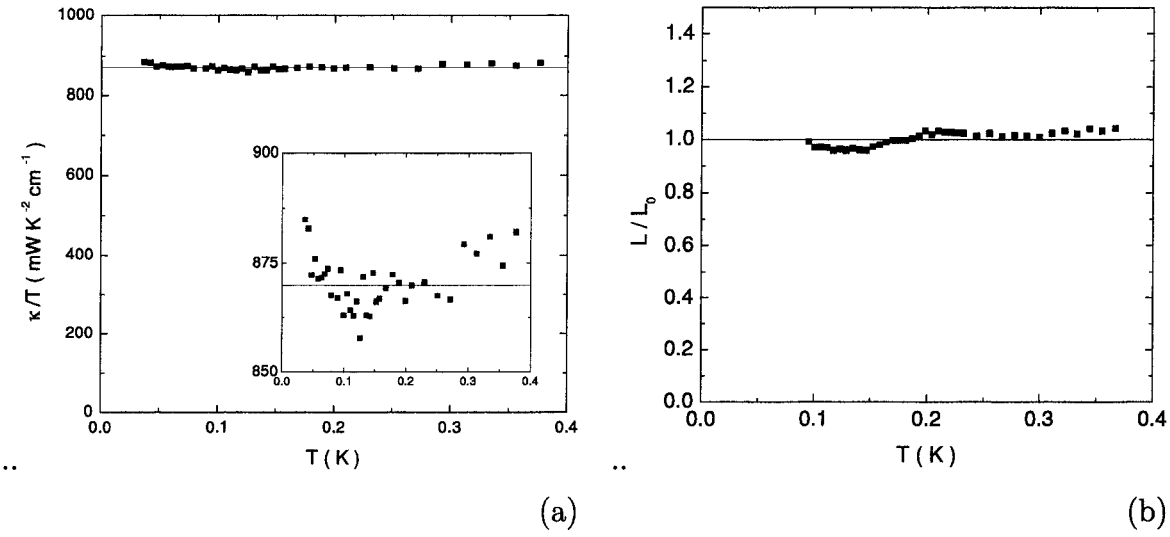

Figure 3.12: (a) κ/T as a function of T for an Ag wire. It is flat with a scatter of $\simeq$ 3 % which is representative of the *precision* of our setup. (b) L/L_0 as a function of temperature for $LuNi_2B_2C$ at $H = 7$ T. The Wiedemann-Franz law is verified within our experimental precision, a test of the *accuracy* of our setup.

as expected. Also, Kapton® film (an electrical insulator) was measured to test the sensitivity of the setup with magnetic field. We see that the effect does not surpass 10% at the lowest temperature and up to $H = 15$ T. It is below the 1 % level at $T = 7$ K (Fig. 3.14b).

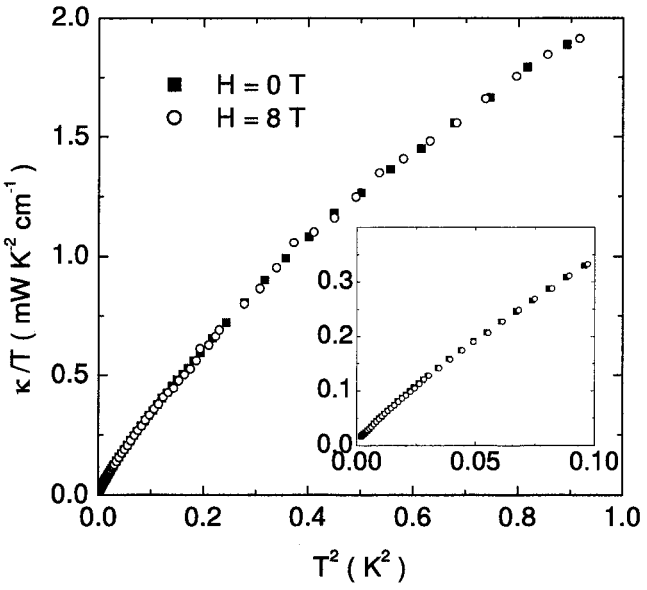

Figure 3.13: κ/T against T^2 for $La_{1.95}Sr_{0.05}CuO_4$ (an insulator) in $H = 0$ and $H = 8$ T. The data is indistinguishable which demonstrates the field independence of our setup. (Courtesy of D.G. Hawthorn).

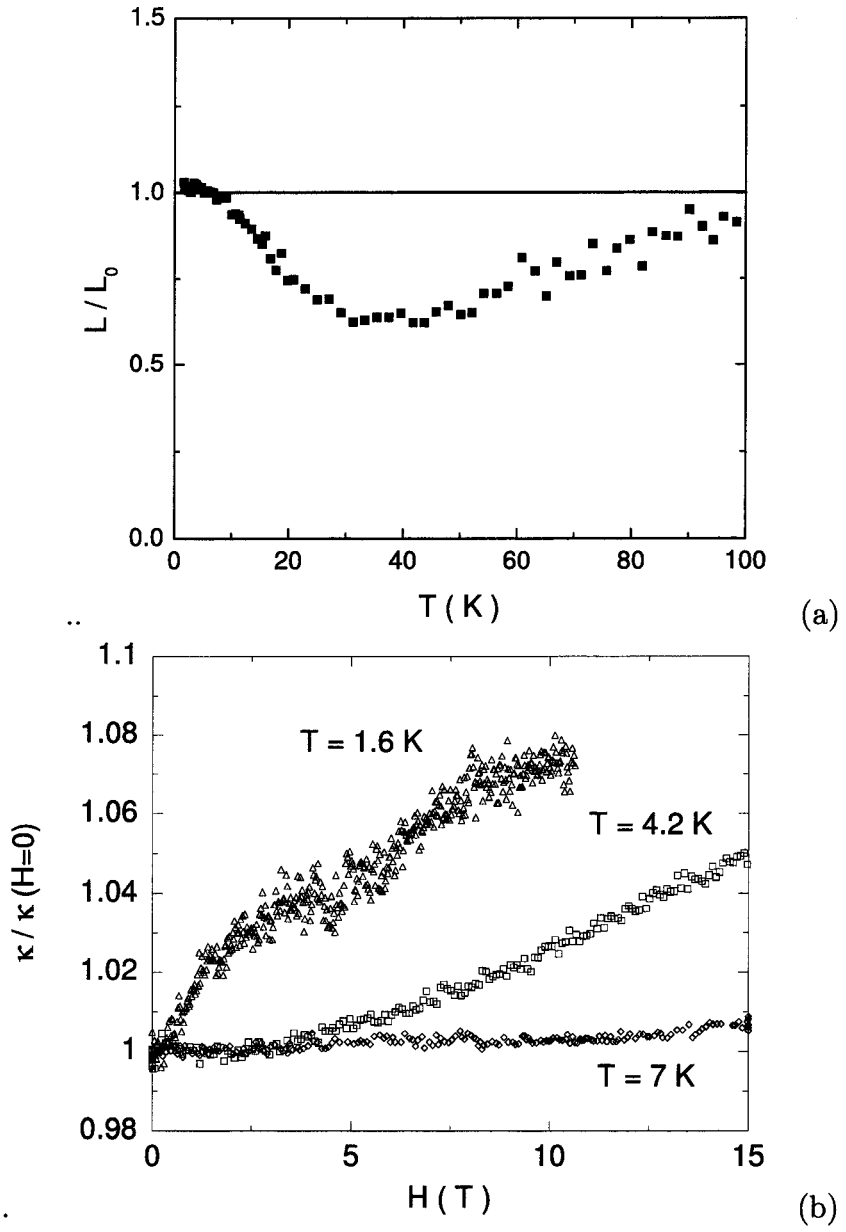

Figure 3.14: (a) L/L_0 for an Ag wire from 1.5 to 100 K. The Wiedemann-Franz law is obeyed at low temperatures and L/L_0 falls below 1 at higher temperatures. This is the expected behavior for a metal. (b) $\kappa(H)/\kappa(H=0)$ of Kapton® film (an insulator) as a function of H for several temperatures. Our setup suffers from an uncertainty of at most 10% at 1.6 K and at our highest field. This reduces to 1% at 7 K.

Chapter 4

V_3Si: test experiment

Much experimental and theoretical activity was generated by the discovery of high-T_c superconductors (HTSC). In turn, many other novel types of superconductors have been discovered and studied. In this light, the physical properties of such novel materials have been compared with those of more conventional ones. However, it is often argued that such "test-experiments" have not been performed thoroughly enough, leaving room for ambiguity in the reports of anomalous behavior. Such is the case for the transport of heat in the vortex state.

For instance, the behavior of conventional type II superconductors was studied long ago in Nb ($T_c = 9$ K, $H_{c2} \simeq 0.5$ T) down to 50 mK in zero field [66] but only to 2.0 K ($T_c/5$) in a magnetic field. It is of clear interest to study the behavior of an *extreme type II superconductor* both in zero field and in the vortex state. For this, we have chosen the A-15 compound V_3Si ($T_c = 17$ K, $H_{c2} \simeq 20$ T) to be the test case for other experiments.

In addition to providing a test case, such a system is interesting to study in its own right. Indeed, a Quantum Phase Transition (QPT) at $T \rightarrow 0$ in the vortex state of such an extreme type II superconductor was predicted [110]. Another proposal explained the possibility of a transition from a thermal insulator to a thermal metal at $T = 0$ in the vortex state through a well known effect: localization due to disorder [111]. Although we find no conclusive evidence for such a QPT, we will review critically the theoretical proposals.

In this chapter, we show the first study of the thermal conductivity of a conventional extreme type II superconductor V_3Si down to very low temperatures (50 mK) and in the vortex state (up to 11.5 T). It will serve as a good point of comparison for other studies presented in this thesis as well as for other studies of superconductors in the vortex state.

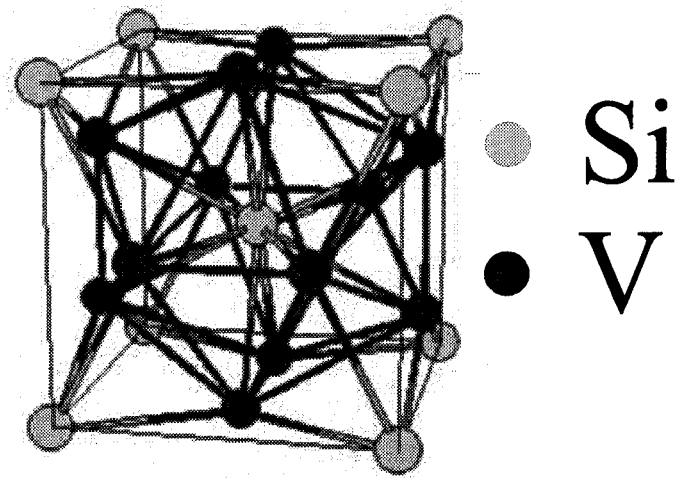

Figure 4.1: V_3Si has the A-15 crystal structure. It is cubic and has a lattice parameter $a_0 = 4.718$ Å. However, V_3Si is seen to go through a martensitic phase transition at $T_{mart} \simeq 21$ K where the lattice becomes slightly tetragonal with $a_1 = 4.715$ Å and $a_2 = 4.727$ Å.

Also, in the context of this thesis, this chapter will put emphasis on the more general behavior of the thermal conductivity of a type II superconductor in the vortex state and at finite temperature.

4.1 V_3Si: an extreme type II superconductor

Crystal structure

V_3Si has an A-15 crystal structure which is shown in Fig. 4.1 as many other superconductors with relatively high T_c such as Nb_3Sn. More generally, it is cubic and has a lattice parameter $a_0 = 4.718$ Å. This has the effect of making all properties mostly isotropic. It also has the particularity of undergoing a martensitic transition from a cubic to a slightly tetragonal unit cell near $T_{mart} \simeq 21$ K. Below this, the lattice parameters are $a_1 = 4.715$ Å and $a_2 = 4.727$ Å.

Normal state parameters

V_3Si is an isotropic metal with a complex Fermi surface (FS) [112]. The average Fermi velocity is calculated to be near $v_F = 1.5 \times 10^7$ cm/s and the density of states at the Fermi energy is 17.5 states/eV/unit cell. The heat capacity yields a normal state electronic

	T_c (K)	H_{c2} (T)	H_{c1} (mT)	$\xi(0)$ (Å)	$\lambda(0)$ (Å)
V_3Si	17	18.5	80	45	1060

Table 4.1: Superconducting parameters for V_3Si taken from the literature [114, 115]. The value for H_{c2} was measured on the crystals used in this study by magnetization.

contribution of $\gamma_N \simeq 55 - 60$ mJ mole^{-1} K^{-1} [113] and a Debye temperature $\Theta_D \simeq 350 - 500$ K.

Superconducting state parameters

One of the notable properties of V_3Si is its relatively high T_c. It also has a large upper critical field which has been reported to be between 18.5 and 25 T. Table 4.1 shows values for the superconducting parameters of V_3Si.

4.2 Characterization: $\rho(T,H)$ and $\kappa(T,H)$ of V_3Si

Transport measurements such as resistivity and thermal conductivity are well suited to characterize the superconducting state. Indeed, one can extract many parameters such as T_c, H_{c2} and give an estimate of H_{c1}. This will be presented in this section for V_3Si. Also, keeping in mind that our aim is to understand the behavior of the $T \to 0$ electronic contribution of κ in the vortex state, we will show that one needs to characterize the normal state magneto-resistance.

4.2.1 The sample

The sample used was cut into a parallelepiped rectangle using a spark-erosion method and polishing. The transport was done with the current in the [100] direction. It had dimensions 3.0 mm in this direction, 0.7 mm in the direction of the magnetic field was applied and a width of 0.25 mm. This geometry is well suited for studies in a magnetic field. The sample was from the same batch used in previous de Haas-van Alphen (dHvA) studies [114, 116]. The contacts were made with Epo-Tex H20E silver epoxy. They were first hardened at 150° C in air and then annealed in high vacuum ($P \simeq 10^{-7} - 10^{-6}$ mbar) and a temperature of 700 °C for eight hours. The contacts had values of $\simeq 100$ mΩ for current contacts and $\simeq 20$ mΩ for voltage contacts at low temperatures.

4.2.2 Resistivity

The resistivity can yield important characterization information both for the normal state (mean free path) and the superconducting state (T_c and H_{c2}). In addition, it will be important for us to be able to normalize the thermal conductivity to its normal state values via the Wiedemann-Franz law.

Resistivity in zero field

The resistivity of V_3Si as a function of temperature is shown in Fig. 4.2a. It agrees well with previous reports [117]. The superconducting transition occurs at $T_c = 16.9$ K and is very sharp with $\delta T_c = 0.1$ K, indicative of a highly homogeneous sample. At low temperature (below roughly 30 K), the resistivity has a quadratic dependence ($\rho = \rho_0 + AT^2$), as is more evident with the measurements in magnetic field (see Fig. 4.3a). This is a strange result as this temperature dependence is reminiscent of a Fermi-liquid (FL) with strong electron-electron interactions rather than the more conventional electron-phonon scattering mechanism which typically dominates the resistivity in metals (and yields $\rho \propto T^\alpha$ with $3 < \alpha < 5$). This behavior has been reported and discussed earlier [117, 118, 119] with no conclusive understanding. Let us point out that the Kadowaki-Woods empirical ratio for highly correlated electron systems gives $A/\gamma^2 = 1.0 \times 10^{-5} \mu\Omega$ cm (mole K mJ^{-1})^2 [44] whereas, in V_3Si we have $\gamma_N \simeq 60$ mJ mole^{-1} K^{-2} and $A \simeq 2.4 \times 10^{-3} \mu\Omega$ cm K^{-2} yielding $A/\gamma^2 = 0.66 \times 10^{-6} \mu\Omega$ cm (mole K mJ^{-1})^2, close to what is found in transition elements. The large residual resistivity ratio, $\rho(300\text{ K})/\rho_0 \simeq 66$, is indicative of a very pure sample. This fact is clear since dHvA measurements, a probe which requires high purity samples, were performed on these crystals [114, 116]. From these was measured the mean free path, yielding l =1500 Å at low temperature [1].

In the superconducting state, this value needs to be compared to the Pippard coherence length to estimate wether we are in the clean or the dirty limit. From the standard relation $\xi(0) = 0.74\xi_0[\chi(0.88\xi_0/l)]^{1/2}$, where χ is the Gor'kov function (equal to unity in the clean limit), we obtain for V_3Si $\xi_0/l = 0.13$, with values of $\xi(0) = 50$ Å coming from

[1] One can also get an estimate of l for this sample from transport. We can use the kinetic theory result $\kappa = \frac{1}{3} C v_F l$ and the Wiedemann-Franz law $\frac{\kappa\rho}{T} = L_0$ at $T = 0$. This leads to $\rho_0 l = \frac{3L_0}{\gamma_N v_F}$ which gives $\rho_0 l \simeq 240\ \mu\Omega$ cm Å using $\gamma = 60$ mJ mole^{-1} K^{-2} and $v_F = 1.5 \times 10^{-7}$ cm/s. For our sample, we obtain $l = 185$ Å, a value much below that obtained from dHvA. It is unclear why there is such a large discrepancy with the mean free path obtained from dHvA. A possibility is that the latter is measured only on part of the Fermi surface and is not representative of the average mean free path. However, as dHvA gives a direct measurement of l, we will use this value henceforth.

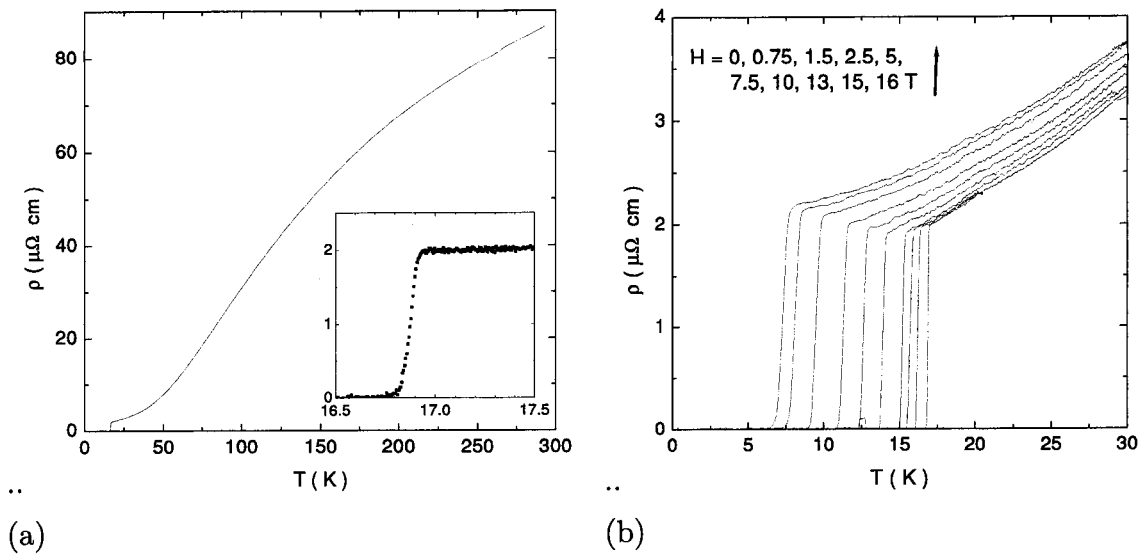

Figure 4.2: (a) Resistivity of V_3Si as a function of temperature. It agrees well with previous reports. The superconducting transition is seen at $T_c = 16.9$ K and has a width $\delta T_c = 0.1$ K indicative of a homogeneous sample. (b) The resistivity is shown for fields up to 16 T. A non-negligible magnetoresistance is observed. The superconducting transition stays sharp and gives a good measure of $H_{c2}(T)$.

H_{c2} and $l = 1500$ Å. This is a good indication that the sample is in the clean limit.

Magnetoresistance

The magnetoresistance of the sample was measured up to $H = 16$ T as shown in Figs. 4.2b and 4.3. For our purposes, we will restrict our interest to extracting a value of $H_{c2}(T)$ and to phenomenologically fitting the temperature and field dependence of $\rho(T,H)$ to be able to obtain the Lorenz number $\frac{\kappa\rho}{T}$ rather than the bare thermal conductivity.

The temperature dependence is clearly shown to have a $\rho = \rho(0) + AT^2$ behavior on Fig. 4.3a. Both ρ_0 and A have a small evolution as a function of field as can be seen in Fig. 4.3b.

The martensitic transition discussed above has a distinctive signature as seen in the resistivity at $T_{mart} = 20.5$ K (see Inset of Fig. 4.3a). This transition temperature is not seen to vary by more than 1 K under a magnetic field of up to $H = 16$ T.

The upper critical field of these crystals was measured magnetically to be $H_{c2}(0) = 18.5$ T at $T = 50$ mK (hence denoting it as the zero temperature upper critical field) along with dHvA studies [114]. Our resistive measurements (see Fig. 4.2b) lead to the

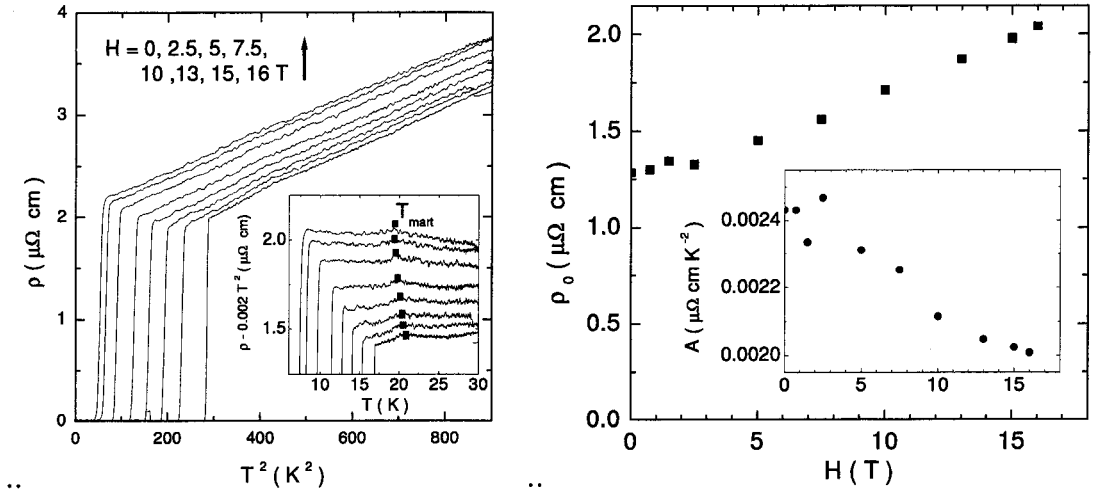

Figure 4.3: (a) Resistivity of V_3Si against T^2 for magnetic fields up to 16 T. It follows a $\rho = \rho_0 + AT^2$ temperature dependence as reported earlier [117, 118, 119]. *Inset:* the signature of the martensitic transition at $T_{mart} = 20.5$ K is emphasized by plotting $\rho - 0.002\ T^2$ versus T for the same values of H. T_{mart} is marked by black squares. (b) The field dependence of ρ_0 and A.

temperature dependence of H_{c2} seen in Fig. 4.4a (H_{c2} measured via thermal conductivity is also shown). The temperature dependence is well fitted by the standard relation:

$$H_{c2}(T) = H_{c2}(0)\ (1 - (\frac{T}{T_c})^2) \tag{4.1}$$

The three lines shown in Fig. 4.4 are for $H_{c2}(0) = 18.5$, 20 and 21.5 T. The data is consistent with that obtained from magnetization ($H_{c2} = 18.5$ T) but seem to indicate that the upper critical field is closer to 20 T. Let us note that we will use $H_{c2} = 18.5$ T nevertheless.

4.2.3 High temperature thermal conductivity

The thermal conductivity can be used to characterize both the normal and the superconducting state of our sample. In addition to the information that can be obtained in zero magnetic field, we will see how thermal conduction can be used to obtain H_{c2} and an estimate of H_{c1}.

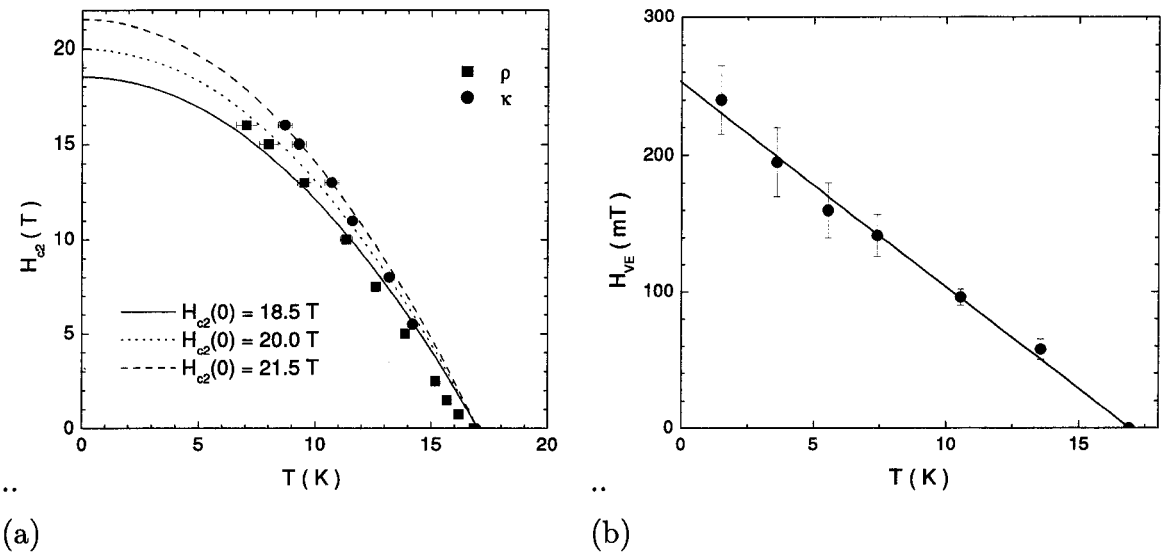

Figure 4.4: (a) The phase diagram of V_3Si. $H_{c2}(T)$ is obtained via resistivity (squares) and thermal conductivity (circles). The lines are fits to the functional form $H_{c2}(T) = H_{c2}(0)[1 - (T/T_c)^2]$ with $H_{c2}(0) = 18.5, 20$ and 21.5 T. (b) The field of vortex entry $H_{ve}(T)$ measured via thermal conductivity (see Fig. 4.6). Note that $H_{c1}(0)$ is measured to be closer to 80 mT for V_3Si.

Thermal conductivity in zero field

The thermal conductivity of V_3Si up to 100 K is shown in Fig. 4.5. The normal state is similar to that expected for a good metal (see Fig. 2.1). The Lorenz ratio normalized to its Sommerfeld value is shown in the inset of Fig. 4.5a and suggests that κ is mostly electronic at all temperatures. It is a measure of the inelastic scattering which gives $L/L_0 < 1$. An extrapolation to $T \rightarrow 0$ indicates that it will reach unity as expected in the elastic scattering regime. A signature attributed to the martensitic transition is seen near $T = 20.5$ K in accordance with the resistivity data.

The superconducting transition is seen clearly as the maximum of the thermal conductivity. That is, if superconductivity didn't occur, κ would keep rising before reducing to a linear behavior indicative of the impurity scattering limited WF law. Instead, below T_c, the electron contribution is reduced as expected by the condensation of the Cooper pairs. A small phonon peak develops around $T_c/5$ and leads to a purely phononic thermal conductivity with a temperature dependence close to cubic at the lowest temperatures (see Fig. 4.5b). This will be discussed in more detail in the next section.

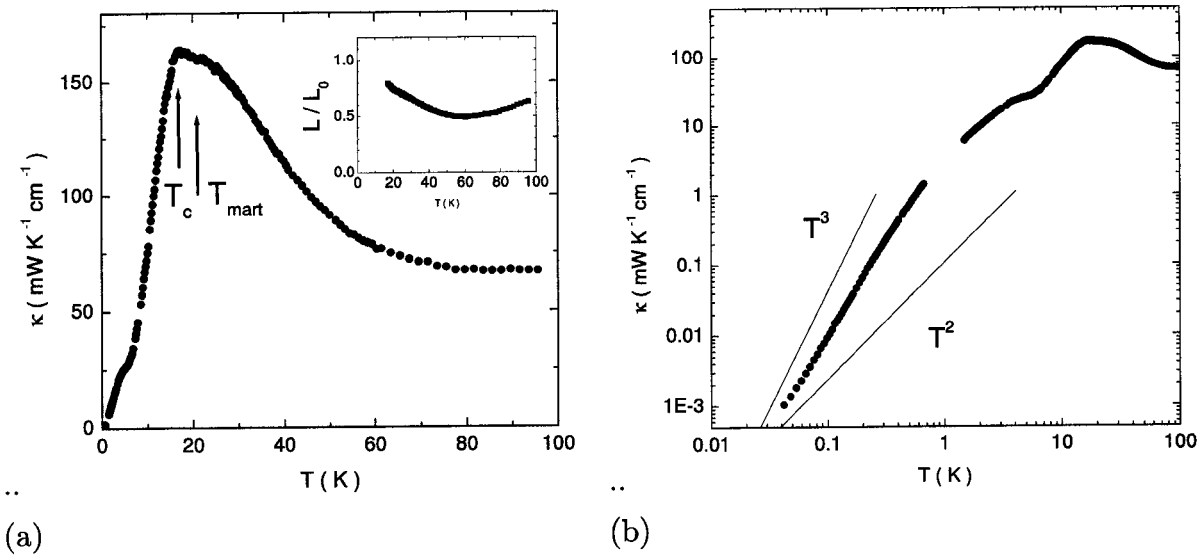

Figure 4.5: (a) The thermal conductivity of V_3Si as a function of temperature from $T = 50$ mK to $T = 100$ K. In the normal state, it has the behavior of a good metal. This is also seen in the inset where the normalized Lorenz number is plotted. The superconducting transition is seen as the maximum in κ and a dip is seen at T_{mart}. In the superconducting state, κ decreases at T_c and shows a phonon peak at $T_c/5$. (b) $\kappa(T)$ on a logarithmic scale. Below 1 K, it is purely phononic and has a temperature dependence close to T^3.

Thermal conductivity in field

Lower critical field The effect of adding vortices on the thermal conductivity is to introduce some additional electronic scattering. At temperatures much lower than T_c, this only acts on phonons since they are the sole carriers of heat. Near T_c, this effect can apply to both electrons and phonons. Regardless, one sees a distinctive signature of the entry of vortices in the sample as a sharp decrease of κ. Insofar as one can associate the "field of vortex entry" (henceforth labelled H_{ve}) with H_{c1}, one can use thermal conductivity as an indirect probe of the lower critical field. Fig. 4.6 shows such a measurement for V_3Si where κ was measured as a function of field at fixed temperatures. For each temperature, the sample was warmed above T_c and cooled back in zero field (after a careful field-zeroing procedure). The temperature dependence of H_{ve} is shown in Fig. 4.4b and is seen to be roughly linear in temperature with a $T = 0$ value near $H_{ve}(0) \simeq 250$ mT.

Upper critical field The upper critical field can also be easily measured via thermal conductivity. This was done here with measurements of κ as a function of temperature

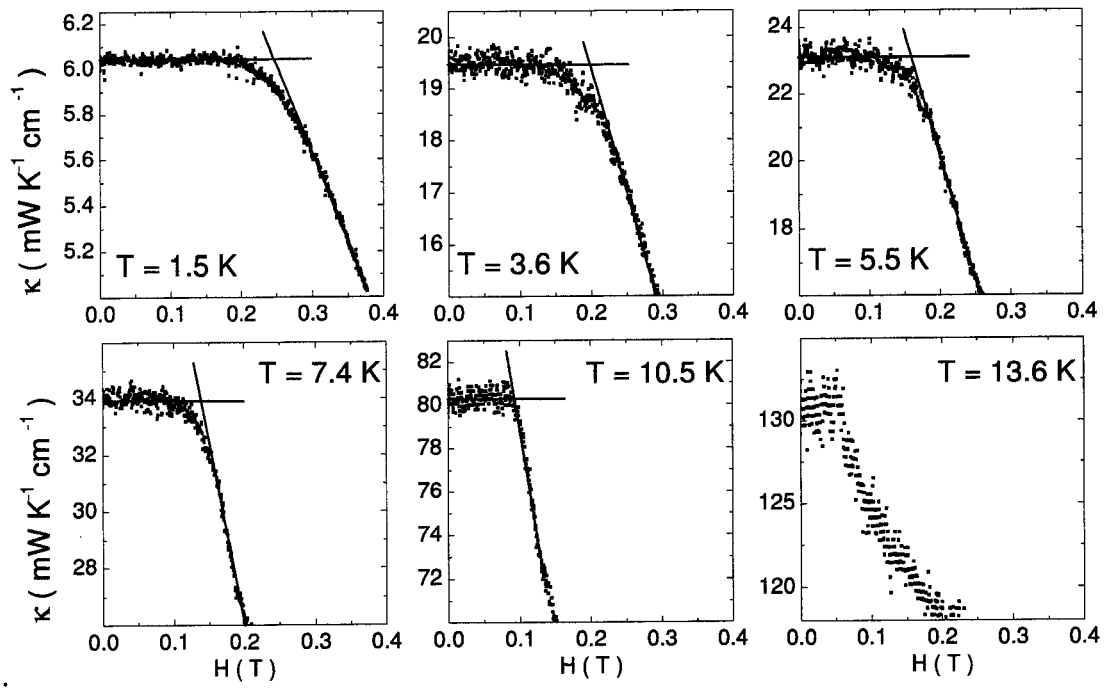

Figure 4.6: Thermal conductivity of V_3Si at low fields for several temperatures below T_c. A sharp decrease is indicative of the field H_{ve} at which vortices enter into the sample.

at a fixed magnetic field as shown in Fig. 4.7a [1]. There, we see a sharp decrease of κ at $T_c(H)$, which is equivalent to $H_{c2}(T)$. Fig. 4.4 shows that values agree well with the resistive H_{c2}. The temperature dependence and the extracted zero temperature value have already been discussed above.

However, H_{ve} is an upper limit to H_{c1}. Indeed, two main effects can lead to $H_{ve} > H_{c1}$: 1/ a geometrical demagnetization factor which can be calculated with the geometry of the sample and 2/ the effect of vortex pinning. The latter will make the magnetization as well as any other property hysteretic as observed in V_3Si [120]. It also has the effect of creating a barrier for vortex entry making them enter the sample in so-called avalanches when the barrier is overcome. The demagnetization factor can be calculated for an ellipsoidal sample [121] but is usually obtained using a superconductor with a known H_c and cut into the same shape as the studied sample. Approximating our sample to be an ellipsoid, we obtain a demagnetization factor of roughly $D/4\pi \simeq 0.25$ where $H_i = H_a - DM$ and H_i is the internal field, H_a is the applied field and $M = 4\pi\chi H_a$ is the magnetization (χ is

[1] One can also obtain the same information by performing field sweeps at constant temperature.

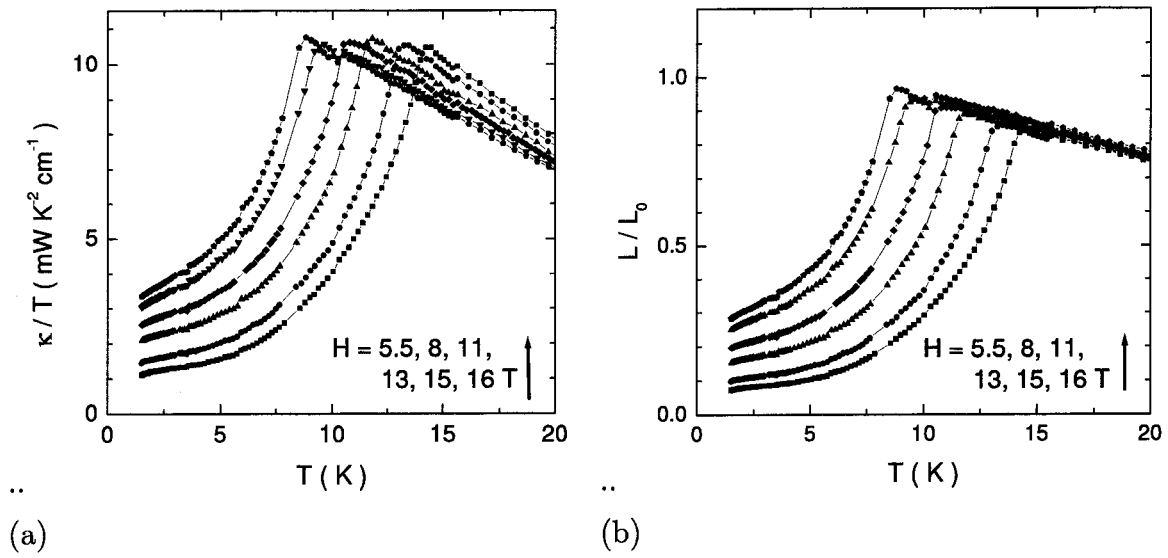

Figure 4.7: (a) κ/T of V_3Si as a function of temperature for fields up to 16 T. The superconducting transition is seen with an abrupt decrease of κ. (b) The normalized Lorenz number $\kappa\rho/TL_0$ for fields up to 16 T. In the normal state, the magnetoresistance is accounted for by this procedure. In the superconducting state, we have used the extrapolation of the resistivity below T_c. At low temperature, there is an increasing electronic residual linear term.

the magnetic susceptibility) [121] [1]. Both these effects explain that the intrinsic $H_{c1}(0)$ is measured to be closer to 80 mT [115].

The temperature dependence of κ The temperature dependence of the thermal conductivity at several fields is plotted as κ/T against temperature on Fig. 4.7a. Above T_c, there is a small decrease of κ as a function of field. This is due to the magnetoresistance and is consistent with the resistivity measurements. Indeed, if one plots the Lorenz number normalized by its Sommerfeld value $\frac{\kappa\rho}{T}/L_0$, one sees that the data collapses above T_c (see Fig. 4.7b). This also reminds us that in this case, where the magnetoresistance is not negligible for all fields below H_{c2}, the zero temperature electronic thermal conductivity κ_0/T should be normalized to the *corrected* normal state value, namely $L_0\rho_0(H)$ where $\rho_0(H)$ must be extrapolated from a fit above $T_c(H)$.

In the superconducting state, one sees an abrupt decrease at T_c which is due to the condensation of the Cooper pairs. At lower temperatures, one can easily resolve an elec-

[1] As a general note, if the demagnetization factor is the only source of discrepancy between H_{c1} and H_{ve}, then this measure of H_{ve} effectively becomes a useful parameter for the sample with the added benefit of being measured in-situ.

tronic residual linear term [1]. This will be discussed in the next section where data at low temperatures will be used. It is clear that by $H = 16$ T, the zero temperature electronic thermal conductivity is no more than a third of the normal state value. Considering that H_{c2} is around 20 T, κ_0/T will have a very sharp rise near the upper critical field as expected for a type II s-wave superconductor and as observed in pure Nb [20].

4.3 $\kappa(T,H)$ at low temperatures

The thermal conductivity of an s-wave extreme type II superconductor at low temperatures and through the vortex state has never been measured before. It is a necessary test-experiment to compare the behavior seen in unconventional superconductors. What's more, it is interesting in its own right as predictions of quantum phase transition where made for such superconductors [110, 111]. For this alone, and to obtain the true zero temperature behavior, it is necessary to go to extremely low temperatures. Technically speaking, it is also necessary since the electronic thermal conductivity can only be reliably extracted at these temperatures, especially at low magnetic fields.

In this section, we first show that the thermal conductivity of V_3Si in zero field is consistent with an s-wave superconductor. We then find a reliable way to extract the electronic thermal conductivity at $T \to 0$ to finally present its magnetic field dependence. These results are discussed and compared to present theoretical understanding and predictions. Notably, we do not find conclusive evidence for a quantum phase transition within the vortex state of V_3Si.

4.3.1 κ in zero magnetic field

In zero magnetic field, the electronic thermal conductivity of an s-wave superconductor is nil at low temperatures due to the gap in the excitation spectrum [9]. κ is then purely phononic and should follow a cubic temperature dependence when phonons are scattered solely by the sample boundaries. Fig. 4.5b shows that this behavior is indeed roughly reached below 1 K. Let us be critical and see if one can resolve a residual linear term as is predicted for a gap with nodes [81]. For this, we plot κ/T against T^2 in Fig. 4.8a for temperatures below 150 mK. There, we see that the intercept is small but

[1] Note that the measurements at lower temperature and higher fields have an increased error bar not shown on Fig. 4.7 but discussed in Chapter 3

finite: $\kappa_0/T \leq 0.01$ mW K^{-2} cm^{-1}. This may lead us to believe that there remains some electronic carriers at $T = 0$. However, many arguments stand against this conclusion:

- The linear term observed is much smaller than that expected from a gap with nodes. For example, for a d-wave gap, one expects a linear term of the order of $\kappa_0/T \simeq 1.0$ mW K^{-2} cm^{-1} [1] which is two orders of magnitude higher than the upper limit of the measured value.

- The extracted value is less than a third of the value at the lowest temperature point. This casts doubt on the extrapolation procedure.

- A much simpler explanation exists: as is observed in Nb (see Fig. 2.5b) and other materials, the phononic contribution may have a power law temperature T^α with $2 < \alpha < 3$ due to specular reflection on smooth crystal boundaries [63]. This is indeed the case here where $\kappa \propto T^{2.74}$ as shown in Fig. 4.8b.

It is worth noting that the phononic thermal conductivity is in good agreement with the theoretical estimate for boundary limited scattering. Using equation 2.22, the mean diameter $d = 0.047$ cm, and $v_{ph} = 5 \times 10^5$ cm/s, we get a phonon slope of 7.6 mW K^{-4} cm^{-1} as compared to 8.5 mW K^{-4} cm^{-1} obtained experimentally from Fig. 4.8a.

In summary, the thermal conductivity of V_3Si in zero field is purely phononic with a $T^{2.74}$ temperature dependence. This is a signature of a fully gapped Fermi surface as is expected for an s-wave superconductor.

4.3.2 Extrapolation of κ_e at $T \rightarrow 0$ in field

The thermal conductivity was measured with increasing temperature at several fields for V_3Si as shown in Fig. 4.9. The sample was cooled in field from above T_c to obtain a homogeneous vortex distribution and avoid any extrinsic effects due to vortex pinning [2].

[1] We have $\kappa_{00}/T = \frac{k_B^2}{3\hbar}\left(\frac{n}{d}\right)\left(\frac{v_F}{v_2} + \frac{v_2}{v_F}\right)$ [85]. We use the fact that $\hbar k_F v_2 = \Delta_0/2$ (for a d-wave gap) and $\hbar k_F = m^* v_F$ to obtain $\kappa_{00}/T = \frac{2k_B^2}{3\hbar}\left(\frac{n}{d}\right)\left(\frac{m^* v_F^2}{\Delta_0}\right)$. Using $d = 4.718$ Å, $n = 1$, m^* as the electron mass, $v_F = 1.5 \times 10^7$cm/s and $\Delta_0 = 2.5$ meV, we get $\kappa_{00}/T \simeq 1.0$ mW K^{-2} cm^{-1}.

[2] Strictly speaking, there may still be effects of vortex pinning, especially at low fields. However, this procedure ensures that the results are at least reproducible on this sample whereas applying the field at low temperature may have a different effect considering the history of the sample (the history of fields applied to it earlier).

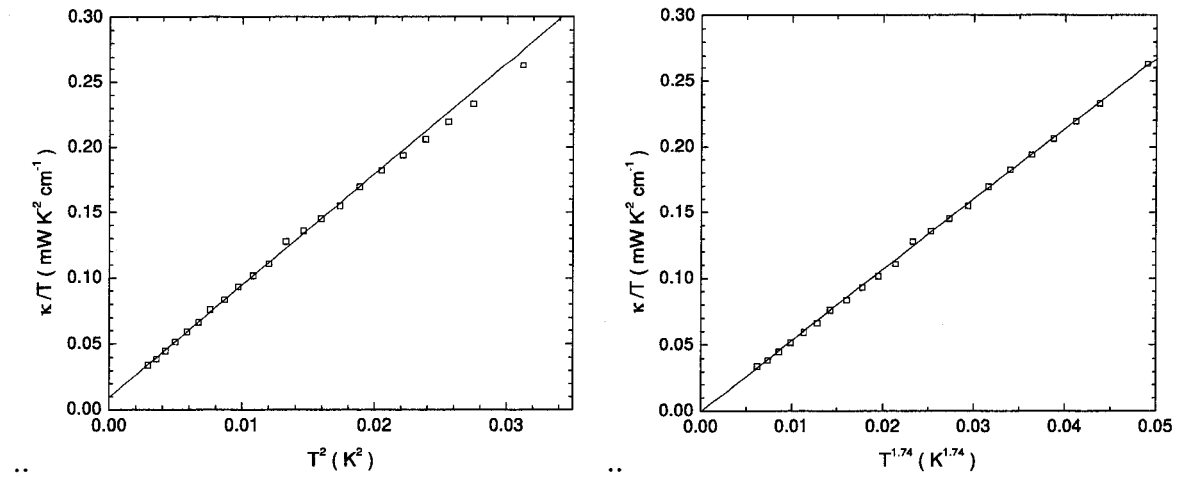

Figure 4.8: (a) and (b) κ/T of V_3Si as a function of T^2 and $T^{1.74}$ respectively in zero magnetic field. The phonon slope agrees well with what is expected (see text). One may think that there is a small electronic term as extracted from (a). More likely though, the phononic thermal conductivity obeys a power law $T^{1.74}$ due to specular reflections from the crystal boundaries as is shown in (b).

It is clear from Fig 4.9a that the magnetic field induces a linear electronic term and affects the phononic contribution as well. Since we are interested in *electron physics*, we will need to subtract the phononic contribution in a reliable way. We will then concentrate on its behavior with field.

As discussed above in the context of a measurement of the lower critical field, vortices have the effect of scattering phonons. Referring to Chapter 2, we see that we obtain a phononic thermal conductivity of the form $\kappa \propto T^3$ for boundary scattering and $\kappa = bT^2$ for electronic scattering. When both these scattering mechanisms are at play, boundary scattering will dominate at lower temperatures, consistent with a "phonon slope" which is asymptotically equal at low temperatures (see Fig. 4.9a). To fully characterize the data, we have fitted it to the following way:

$$\kappa = \kappa_{ph} + \kappa_e = \frac{1}{1/\kappa_{ph-b} + 1/\kappa_{ph-e}} + \kappa_e = \frac{1}{1/\kappa(H=0) + 1/bT^2} + aT \qquad (4.2)$$

where $\kappa(H = 0)$ is taken as the phononic contribution scattered by boundaries. This enables us to have a simple two parameter fit to the thermal conductivity and extract the electronic contribution $\kappa_e = aT$. We fit the data below $T = 400$ mK and obtain very good results as shown by the lines through the data in Fig. 4.9a. In the inset of the lower

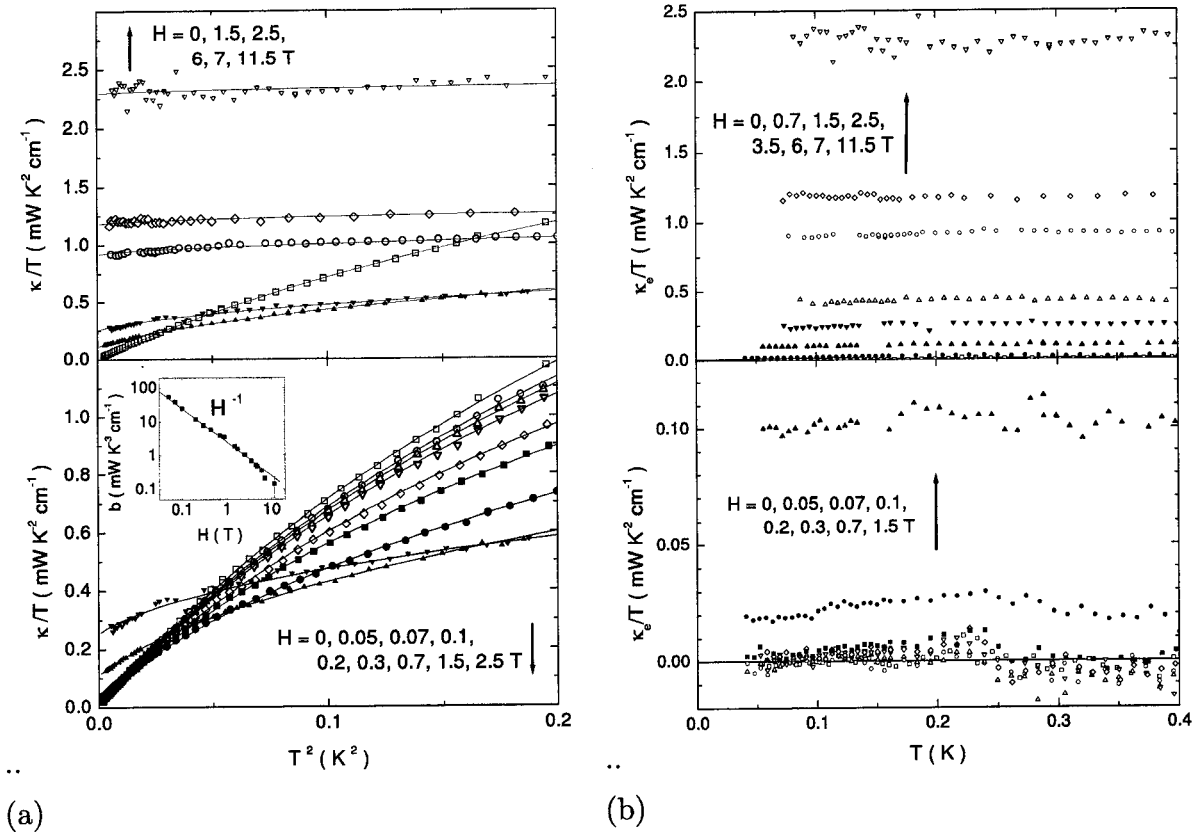

Figure 4.9: (a) Thermal conductivity of V_3Si as a function of temperature for fields up to 11.5 T. Two effects occur: 1/ a linear term develops and 2/ the phonons are increasingly scattered by the vortices. The lines are fits described in the text. *Inset:* the field dependence of b, where $\kappa_{ph-e} = bT^2$. (b) The electronic thermal conductivity as obtained from subtracting the phononic contribution. We can distinguish unambiguously an electronic contribution only for fields above 0.5 T (lowest field shown here is 0.7 T for clarity). Below this, our experimental resolution gives us an upper bound on $\kappa_e/T \leq 0.005$ mW K^{-2} cm^{-1}.

panel, we plot the field dependence of the parameter b for phonon-electron scattering. The latter is seen to vary as $1/H$ for almost two decades of field. This behavior is easily understood if one considers that the density of electronic scatterers varies linearly with magnetic field (as expected and as observed via heat capacity measurements [113, 122]). Indeed, with a larger field, the phonons will be scattered increasingly and b will decrease. The exact behavior is extracted to be $\kappa_{ph-e} = \frac{bT^2}{H}$ with $b = 2.5$ mW K^{-3} cm^{-1} T^{-1}. Note that this coefficient will surely vary for different compounds. The fact that this effect extends to fields below the measured $H_{ve}(0) = 250$ mT also tells us that our field cooling procedure has the effect of introducing vortices even at these low fields.

Finally, we show the electronic contribution κ_e/T as a function of temperature for various fields in Fig. 4.9b. The phononic contribution has been subtracted from the data. We see that our experimental resolution does not enable us to resolve an electronic term for fields below $H = 0.5$ T (although the 0.7 T data is the lowest shown in Fig. 4.9). Below this field, we can estimate the upper limit of the electronic thermal conductivity to be $\kappa_0/T \leq 0.005$ mW K^{-2} cm^{-1}. We also see that the temperature dependence is clearly linear at all fields, a good indication that our fitting procedure is reliable.

We have found a reliable way to extract the electronic contribution to the thermal conductivity at $T \rightarrow 0$. The data is well understood in terms of a phononic contribution which undergoes both boundary and electronic (vortex) scattering. The latter mechanism is seen to scale inversely with the density of vortices introduced in the sample, namely as $1/H$. Let us now turn to our main interest: the behavior of the electronic thermal conductivity as a function of magnetic field at $T \rightarrow 0$.

4.3.3 κ_e at $T \rightarrow 0$ in a magnetic field

The electronic thermal conductivity of V_3Si is shown in Fig. 4.10 against H/H_{c2} and normalized in two different ways: as $\kappa_e\rho_0(H)/L_0T$ and $\kappa_e\rho_0(H=0)/L_0T$ where $\rho_0(H)$ is the extracted residual resistivity as a function of field (see Fig. 4.3). At first sight, three main features must be emphasized:

- We observe *delocalized quasiparticle states* very deep in the vortex state (at least down to 0.027 H_{c2} or $H = 0.5$ T). This is consistent with the observation of quantum oscillations in the vortex state of V_3Si [114, 116]. Note that quantum oscillations were only observed down to $H_{c2}/2$ probably due to experimental limitations.

- At fields below 0.016 H_{c2}, our error bars put an upper limit of $\kappa_e/T \leq 3 \times 10^{-4}\ \kappa_N$.

- At 0.6 H_{c2}, we see that $\kappa_e/T \simeq 0.17\ \kappa_N$. The electronic thermal conductivity will therefore increase very quickly near H_{c2}.

The observation of delocalized quasiparticles seems unusual as the electronic states are thought to be localized within the vortex cores. However, strictly speaking, as soon as more than one vortex is in the sample, the electronic wavefunctions become extended. Another way to say this is that bands of conduction are formed, as calculated by Yasui

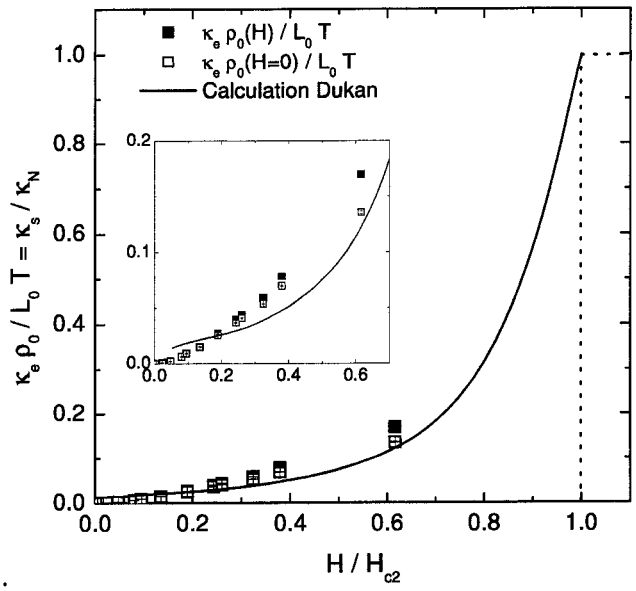

Figure 4.10: The electronic thermal conductivity at $T \rightarrow 0$ as a function of H/H_{c2} (we use $H_{c2} = 18.5$ T). The thermal conductivity is normalized to the normal state value using the extracted residual resistivity and the WF law. The solid line is a theoretical curve for V_3Si from Dukan *et al.* [72]. *Inset:* A zoom of the low field region.

and Kita [67, 68]. These are extremely flat at low fields but become increasingly dispersive at higher fields.

For low vortex densities (*i.e.* at low fields), a naive picture would have κ_e/T be proportional to the overlap of the wave functions of localized states in adjacent vortices. This would lead to an activated behavior as a function of $d/2\xi$ where d is the intervortex separation and ξ is the characteristic electronic length scale for the vortex cores, such that $\kappa \propto e^{-d/2\xi(0)}$ at $T \rightarrow 0$. Using the expressions for d (Equation 1.9) and $\xi(0)$ (Equation 1.13), we obtain:

$$\frac{\kappa_e/T(T \rightarrow 0, H)}{\kappa_N/T} \propto e^{-\alpha(H_{c2}/H)^{1/2}} \tag{4.3}$$

where $\alpha = \sqrt{2\pi}/2 \simeq 1.25$. To verify if this relation holds, we plot $(\kappa_e/T)/(\kappa_N/T)$ against $(H_{c2}/H)^{1/2}$ on a semi-logarithmic scale in Fig. 4.11a. There, we see that we obtain qualitatively the correct behavior at low fields and a quantitative agreement with a coefficient $\alpha = 1$ which is close to $\alpha = \sqrt{2\pi}/2 \simeq 1.25$. Also, this behavior holds only for fields below $\sim H_{c2}/8$. This is not particularly surprising as this simple picture is expected to break down for higher vortex densities.

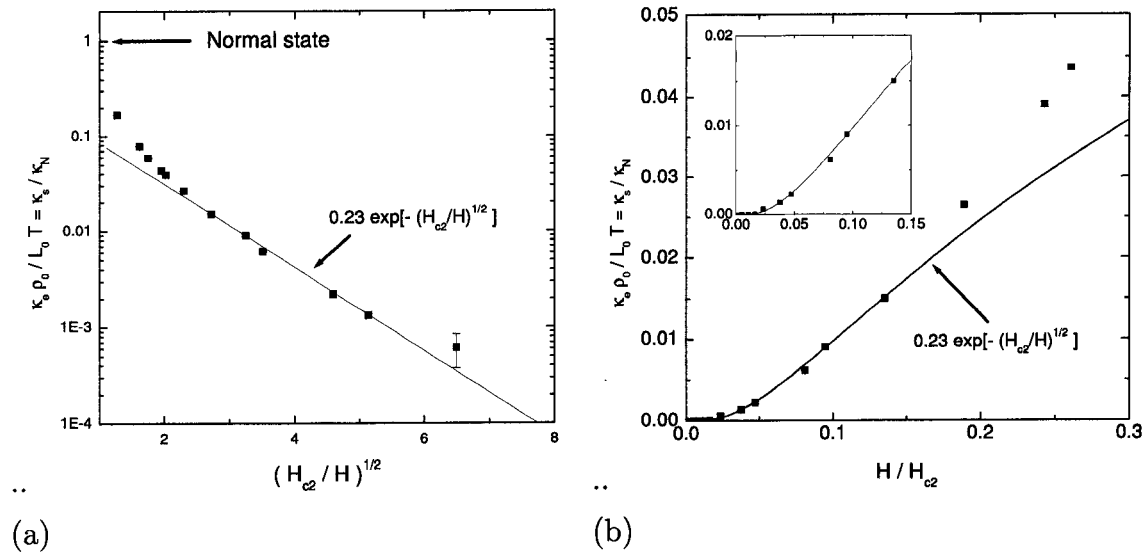

Figure 4.11: (a) The normalized electronic thermal conductivity of V_3Si against $(H_{c2}/H)^{1/2}$. The line is a fit to the low field points and yield $\kappa_s/\kappa_N = 0.23 \times e^{-(H_{c2}/H)^{1/2}}$. (b) The same data and fit shown as a function of H/H_{c2}.

Experimentally, $(\kappa_e/T)/(\kappa_N/T)$ is seen to go from zero (within error bars) to a finite value rather abruptly and for a field above H_{c1}. This may be interpreted as a transition from a thermal insulator to a thermal metal as has been proposed theoretically [111, 110]. In this light, it is interesting to plot the low field fit to Eq. 4.3 on a more natural scale, namely, against H/H_{c2} (see Fig. 4.11b). It is clear that this functional form simulates this behavior very well: a very low conductivity at extremely low fields which increases abruptly. We should point out that at fields below 0.016 H/H_{c2}, this fit is consistent with our errors bars. We are forced to conclude that, with our current experimental accuracy, we could not differentiate a thermal insulator to thermal metal transition from the naive behavior presented here.

Let us now turn our attention to the available theoretical proposals. After reviewing them briefly, we will try to compare them to experimental data.

Tešanović and co-workers

The observation of dHvA oscillations deep in the vortex state of extreme type II superconductors such as V_3Si, $NbSe_2$, Nb_3Sn, $CeRu_2$, YNi_2B_2C, URu_2Si_2 to name a few [123, 116, 114] has attracted much attention recently. The presence of such delocalized quasiparticles was contrasted with the idea of localized states in the vortex cores. The

various theoretical treatments have been reviewed critically and compared to experiment for both V_3Si and $NbSe_2$ [116]. One of these was developed by Tešanović and co-workers [110]. They predict a quantum level-crossing transition (QLCT) from the gapless regime at high fields in the vortex state to the low field regime where the spectrum is gapped. This level crossing occurs at a field $H_{c1} < H^* < H_{c2}$ which is associated with the disappearance of the dHvA oscillations. Experimentally, $H^* \simeq H_{c2}/2$ for V_3Si [114] and $H^* \simeq H_{c2}/5$ for YNi_2B_2C for example [124, 125]. A naive expectation is to find a crossing from a thermal insulator below H^* to a thermal metal above. A more detailed calculation within this framework has been carried out by Dukan *et al.* [72]. What's more, this calculation was made specifically for V_3Si and with parameters extracted from dHvA experiments on the same crystals as used in this study. It is important to note that the calculations were made with no free parameters. The results are presented in Fig. 4.10 and is seen to fit reasonably well. At low fields, the calculation becomes less and less accurate as the approximations used are no longer valid.

Although this result is stunning, it keeps the character of "consistency" rather than "proof". Indeed, we find no direct evidence from thermal conductivity for the predicted QLCT nor is it predicted to have a distinctive signature. We therefore conclude that our results are consistent with the theory of Tešanović *et al.* [110] but do not bring forth conclusive evidence for the existence of such a QLCT.

Vishveshwara and co-workers

Vishveshwara *et al.* predicted a novel transition at $T = 0$ within the vortex state of a type II superconductor [126, 127]. There, the system would evolve from a thermal insulator at low fields to a thermal metal above a critical field H_{c4}. This theory is based on the idea of Anderson localization where disorder plays a key role. In this case, the disorder would apply to the vortex lattice. In the case of a disordered vortex lattice, the thermal conduction would be suppressed whereas a metallic behavior would be recovered in the case of a ordered lattice.

Unfortunately, this theory cannot be addressed properly by our experiment on V_3Si. Indeed, we use a field cooling procedure which is known from muon spin relaxation experiments to yield a fairly well ordered vortex lattice. This is in contrast to increasing the field at low temperature. What's more, it would be difficult to characterize the level of disorder of the vortex lattice. Finally, it should be mentioned that according

to this theory, at a fixed vortex density, the conduction should be metallic in the case of an ordered lattice and insulating in the opposite case. To verify this, an interesting experiment would be to measure the thermal conductivity at some fixed vortex density (or field) and as a function of vortex lattice disorder. Such a parameter is difficult to tune and even to characterize.

In short, our experiment, although it may seem to be the natural one to test the theory developed by Vishveshwara *et al.* [126, 127], is ill-suited. A test experiment has been suggested but seems at present unfeasible.

Kusunose, Rice and Sigrist

On a final note, we mention that Kusunose *et al.* have performed a calculation of the thermal conductivity throughout the vortex state for both an *s*-wave superconductor and a multi-band superconductor [128]. They find that the effective scattering rate in the superconducting state will depend strongly on the purity of the system (in terms of Γ/Δ which is equivalent to the traditional ξ_0/l). They show the calculated thermal conductivity for the case of $\xi_0/l = 0.08$ which is close to the value for our sample. Their results are also consistent with our measurements.

4.4 Conclusion

We have studied the thermal conductivity of V_3Si in the normal and superconducting state. This has lead to a good measurement of the electronic contribution of κ at very low temperatures and through the vortex states.

The results will serve as a key reference for further studies of κ in the vortex state of novel superconductors. Although novel physics was predicted in the vortex state of conventional type II superconductors, we have found no conclusive evidence for a thermal insulator to thermal metal transition within the vortex state. However, we note that calculations of Dukan and co-workers reproduce fairly well our results within their theoretical framework and with no adjustable parameters [72].

In addition, we have shown in detail the information that can be gained via resistivity and thermal conductivity measurements of a superconductor.

Chapter 5

Borocarbides: highly anisotropic gap

The vast majority of known superconductors are characterized by an order parameter with s-wave symmetry and a gap function which is largely isotropic and without nodes (zeros). Only four families of materials are seriously thought to exhibit a superconducting state with a different symmetry: (1) heavy-fermion materials, such as UPt_3 where a line of nodes in the gap function has clearly been identified [33]; (2) high-T_c cuprates (HTSC), such as $YBa_2Cu_3O_7$ where the order parameter was clearly shown to have d-wave symmetry [26]; (3) the ruthenate Sr_2RuO_4, where there is strong evidence for a triplet order parameter [31]; and (4) organic conductors, such as κ-$(ET)_2Cu[N(CN)_2]Cl$ where there is growing evidence for unconventional superconductivity [129]. A major outstanding question is the nature of the microscopic mechanism responsible for superconductivity in any of these materials. The general belief is that unconventional symmetry of the order parameter is evidence for pairing caused by electronic interactions and not mediated by phonons. For example, the proximity to magnetic order which is found in all four families of superconductors has led to the suggestion that spin fluctuations are responsible for Cooper pairing, as is thought to be the case in superfluid ^3He.

However, the pairing mechanism may not be directly related to the nature of the gap. Indeed, even in the case of cuprates where the clearest evidence exists for a gap with nodes, there is good reason to believe that the pairing mechanism is due -at least in part- to phonons [130]. Here, we turn to the non-magnetic borocarbide superconductors $LuNi_2B_2C$ and YNi_2B_2C where we find overwhelming evidence for a strongly anisotropic s-wave gap, and where the pairing mechanism has been shown to be phonon-mediated. This scenario is interesting in its own right, as the source of such a strong anisotropy is not yet understood. In addition, these systems may serve for future studies of novel

superconductors as a reference for the case of an anisotropic gap with no topological nodes.

In this Chapter, we will present a study of heat transport through the vortex state of $LuNi_2B_2C$ [92] which provides evidence for a highly anisotropic (at least ten-fold) gap in non-magnetic borocarbides superconductors. We will then examine the body of evidence for an anisotropic gap in these compounds before briefly reviewing the evidence for a phonon-mediated pairing mechanism.

5.1 $LuNi_2B_2C$ and other borocarbides

A new family of superconductors with general formula RE-Ni_2B_2C (with RE=Lu,Y, Tm, Er, Ho, and Dy), was discovered in 1994 [131, 132] and raised much interest as it was seen as a haven to study the interplay between superconductivity and magnetism [133]. Most of them display magnetic ordering, except for two: $LuNi_2B_2C$ and YNi_2B_2C which are non-magnetic and have the highest superconducting T_c's of 16.5 K and 15.5 K, respectively [134]. Our interest will be restricted to the latter two compounds, which where long thought to be quite mundane but turn out to have a strongly anisotropic superconducting gap. Let us first review their crystallographic, electronic and superconducting properties.

5.1.1 Crystallographic properties

$LuNi_2B_2C$ and YNi_2B_2C have a tetragonal unit cell as shown in Fig. 5.1a. Its layered structure, with Ni-B planes, is reminiscent of that of HTSC. However this similarity yields no parallel as the borocarbides are 3D metals [135, 136], in contrast to the highly 2D nature of cuprates. The lattice constants are $a = 3.464$ Å and $c = 10.631$ Å for $LuNi_2B_2C$, and $a = 3.526$ Å and $c = 10.534$ Å for YNi_2B_2C.

5.1.2 Electronic properties

Both $LuNi_2B_2C$ and YNi_2B_2C are good 3D metals with nearly isotropic resistivity [138]. This agrees with band structure calculations [135, 136] which show that there are 3 bands forming the Fermi surface (FS). The FS has a complex shape which has been reconstructed successfully experimentally using the electron-positron annihilation technique [137] (see Fig. 5.1b which shows a part of the FS). The average Fermi velocity

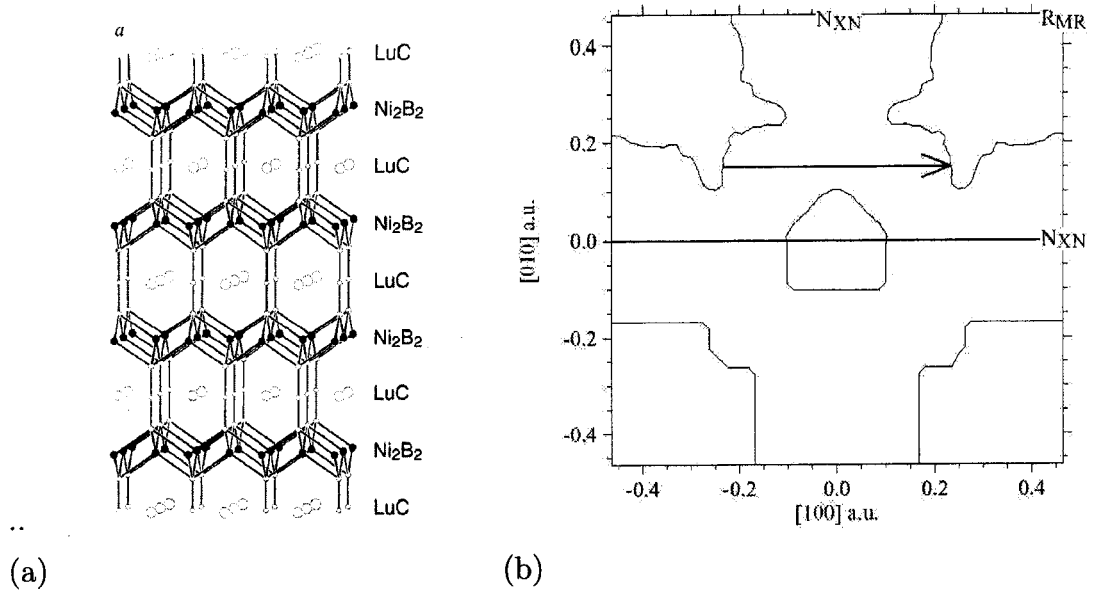

(a) (b)

Figure 5.1: (a) The crystal structure of $LuNi_2B_2C$. The unit cell is tetragonal and is reminiscent of that of HTSC due to its Ni-B planes. However, the electronic properties are 3 dimensional and isotropic. The lattice constants are $a = 3.464$ Å, $c = 10.631$ Å. (b) The calculated (bottom) and measured (top) Fermi surface of $LuNi_2B_2C$ (after [137]). This is a cross-section of the third band in the [001] plane and through the Γ point. The arrow indicates the nesting wavevector.

(in any direction) is calculated to be $v_F = 3.6 \times 10^7$ cm/s for $LuNi_2B_2C$ and is expected to be the same for YNi_2B_2C, and the density of states at the Fermi surface is $N(0) = 4.8$ states/(eV unit cell) for $LuNi_2B_2C$ and $N(0) = 4.03$ states/(eV unit cell) for YNi_2B_2C.

The temperature dependence of the resistivity of both compounds is linear for a large range of temperature (100 K < T < 300 K) but reaches a behavior close to T^2 for lower temperatures [139]. More precisely, $LuNi_2B_2C$ has a $\rho \simeq \rho_0 + AT^2$ with $A \simeq 1.8 \times 10^{-3} \mu\Omega$ cm/K^2 in the range $T_c < T < 40$ K and YNi_2B_2C displays $\rho \simeq \rho_0 + BT^{2.2}$ (with $B \simeq 8.1 \times 10^{-4} \mu\Omega$ cm/K$^{2.2}$) in a similar temperature range. Using the measured value $\gamma_N \simeq 19$ mJ/mol/K^2, one obtains $A/\gamma^2 = 5.0 \times 10^{-6} \mu\Omega$ cm (mole K mJ^{-1})^2 which is much smaller than the experimental Kadowaki-Woods ratio $A/\gamma^2 = 1.0 \times 10^{-5} \mu\Omega$ cm (mole K mJ^{-1})^2 for strongly interacting electron systems [44]. This unusual temperature dependence is thus probably not due to an electronic scattering mechanism. Instead, the resistivity was fitted over the full temperature range by Bloch-Grüneisen theory (involving only electron-phonon interaction) [140].

The normal state heat capacity yields an electronic linear term $\gamma_N \simeq 19$ mJ/mol/K^2

for both compounds [141, 142, 143, 144]. The phononic contribution yields Debye temperatures of $\Theta_{D\ Lu} \simeq 350$ K and $\Theta_{D\ Y} \simeq 500$ K which agrees with results from lattice velocity measurements [145].

Most of these properties are quite characteristic of usual metals. However, two unusual features need to be pointed out. First, there exists a nesting vector near [0.5,0,0] [137]. This is the wavevector for the ordering in antiferromagnetic borocarbides [134]. Secondly, a Kohn anomaly occurs at this wavevector in both $LuNi_2B_2C$ and YNi_2B_2C in the superconducting state [146, 147, 148]: a phonon mode with this wavevector is observed to soften below T_c. We will see later that this phonon mode may be responsible for the pairing interaction in these borocarbides.

5.1.3 Superconducting properties

The non-magnetic borocarbides have a rather high critical temperature and upper critical field, making them "extreme type II" superconductors. Loosely speaking, Tešanović *et al.* define this as a ratio $T_c/H_{c2} \simeq 1$ where the temperature and field are in units of Kelvin and Tesla [110]. Along with H_{c1}, these properties define the superconducting state rather well. Indeed, they define the H-T phase diagram, but also give a good estimate of the Ginzburg-Landau coherence length $\xi(0)$ and the penetration depth $\lambda(0)$. Table. 5.1 shows these values for $LuNi_2B_2C$ and YNi_2B_2C. They are seen to be very similar. In fact, there is little doubt that most properties of these two systems are almost identical, and results from one or the other are taken to apply to both.

However, another quantity is of interest, namely ξ_0/l, where ξ_0 is the Pippard coherence length and l is the mean free path (which depends on the quality of the sample). This tells us whether the sample is in the clean or dirty limit ($\xi_0/l < 1$ or $\xi_0/l > 1$). We find $\xi_0 = 0.57(\frac{\hbar v_F}{\pi T_c}) = 290$ Å using $v_F = 3.6 \times 10^7$ cm/s. The mean free path at low temperature can be obtained from transport and thermodynamic measurements, giving $\rho_0 l = 350\ \mu\Omega$ cm Å for $LuNi_2B_2C$ and $\rho_0 l = 420\ \mu\Omega$ cm Å for YNi_2B_2C [1]. For our sample, $\rho_0 \simeq 1.3\ \mu\Omega$ cm, giving $l = 270$ Å. Such a sample has $\xi_0/l \simeq 1$ which can still be viewed as the moderately clean regime (for a more detailed discussion, see [149]). It

[1] This is obtained by using the expression for the resistivity $\rho^{-1} = 2/3e^2N(0)v_F l$ where $N(0)$ is the density of states, v_F is the Fermi velocity. Using the calculated values of $N(0) = 4.8$ states/(eV unit cell) and $v_F = 3.6 \times 10^7$ cm/s [136]. Alternatively, the same result is obtained by using the kinetic expression for the thermal conductivity $\kappa = \frac{1}{3}Cv_F l$ and the WF law, giving an expression for the mean free path $l = \frac{3L_0}{\gamma v_F}$ where γ is the measured normal state electronic heat capacity ($\gamma = 19$ mJ mole^{-1} K^{-2}).

	T_c (K)	H_{c2} (T)	H_{c1} (mT)	$\xi(0)$ (Å)	$\lambda(0)$ (Å)	ξ_0 (Å)
Lu	16.5	7-8	80	75	760	290
Y	15.5	6.5-10.5	30-80	80	1200	290

Table 5.1: Superconducting parameters for $LuNi_2B_2C$ (Lu) and YNi_2B_2C (Y) taken from the literature. They are similar for both compounds.

should be noted that de Haas-van Alphen (dHvA) measurements on these sample obtain a slightly higher value for the mean free path [124, 125, 150].

These superconductors were long thought to be conventional, with an s-wave symmetry of the order parameter and phonon mediated pairing mechanism. Most notably, a large isotope effect was observed (indeed, boron is rather light and can give way to a large isotope shift) [151]. In light of this, further studies did not critically examine the question and analyzed their results in terms of an isotropic gap. For the most part, they found them to be consistent with this picture but none truly showed convincingly that this was the case.

There is now overwhelming evidence that the superconducting gap is strongly anisotropic. It seems however that this is not due to an unconventional pairing mechanism but rather to phonons, although this question is still under scrutiny. Let us now review this evidence starting with our own: thermal conductivity through the vortex state.

5.2 The case for a strongly anisotropic gap

The most direct evidence for a highly anisotropic gap function comes from thermal conductivity [92, 152], heat capacity [141, 153, 154, 155], photo-emission spectroscopy [156] and scanning tunnelling spectroscopy [100]. We will review these results in more detail, and refer to other less direct evidence.

5.2.1 Thermal conductivity in the vortex state of $LuNi_2B_2C$

The presence of nodes in the gap function is generally associated with unconventional (non-s-wave) symmetries. These nodes are typically inferred from the observation of quasiparticle excitations at energies much lower than the gap maximum Δ_0, as reflected, for example, in the power law temperature dependence of various physical properties,

such as London penetration depth and ultrasonic attenuation at $T \ll T_c$. Another way of detecting low-energy quasiparticles is to excite them by applying a magnetic field, which introduces vortices in the material, so that the superfluid flow around each vortex Doppler shifts the quasiparticle energy. In certain limits, the quasiparticle response is the same whether induced by a thermal energy $k_B T$ or by a field energy $\simeq \Delta_0 \sqrt{B/B_{c2}}$, where $B_{c2} \simeq H_{c2}$, the upper critical field [157].

The following thermal conductivity results present compelling evidence that the gap function of $LuNi_2B_2C$ is highly anisotropic, with a gap minimum Δ_{min} at least 10 times smaller than the gap maximum, $\Delta_{min} \leq \Delta_0/10$. This statement is based on the observation of delocalized quasiparticles at very low energies, as measured directly by heat transport. Indeed, quasiparticle conduction is induced by a magnetic field as low as $H_{c1} \simeq H_{c2}/100$ and it grows linearly with field, in dramatic contrast with the exponentially activated transport seen in Nb, for example, where it results from tunnelling between the localized states bound to the core of adjacent vortices.

Experimental details

The sample used for this study was grown by a flux method [133]. It was then cut by spark-erosion and polished such as to obtain a rectangular parallepiped for measuring transport properties in the [100] direction (along the planes of the tetragonal unit cell). The sample had a width of 0.495 mm (along [001]) and a thickness of 0.233 mm (along [010]), with a 1.59 mm separation between contacts (along [100]). This geometry was used in order to minimize the demagnetization factor for a field applied in the [001] direction. All contacts were made with non-superconducting solder and using a stainless steel flux. This gave extremely good contacts with resistances below 5 mΩ at room temperature as compared to a sample resistance of roughly 3 mΩ at room temperature.

The sample has a $T_c = 16$ K with a transition width $\Delta T_c = 1.0$ K. It is of very high quality with a residual resistivity ratio (RRR) $\rho(300\text{ K})/\rho_0 = 35\ \mu\Omega$ cm$/1.3\ \mu\Omega$ cm $= 27$ where the resistance at low temperature is extrapolated to $T = 0$ from a fit to $\rho = \rho_0 + aT^2$ between T_c and 50 K. The resistivity is shown in Fig. 5.2a [1].

The upper critical field at zero temperature is measured to be $H_{c2}(0) \simeq 7$ T. Also, we find that $H_{c1} \simeq 60$ mT at 2 K from the sharp drop of the thermal conductivity which is

[1] Note that there is a small positive magnetoresistance which gives a value of the residual resistivity $\rho_0 = 1.67\ \mu\Omega$ cm at $H = 8$ T.

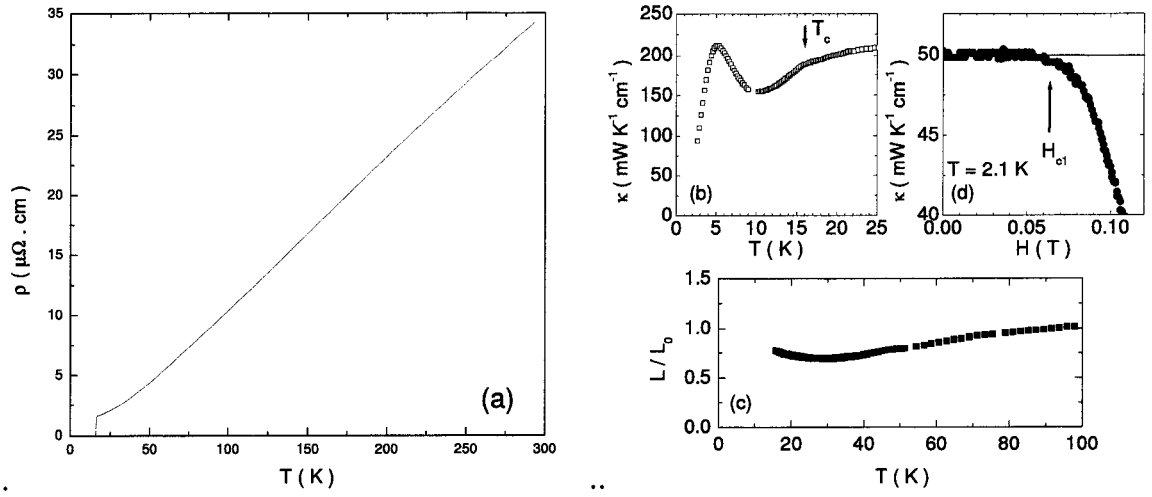

Figure 5.2: (a) The resistivity of $LuNi_2B_2C$ as a function of temperature. The superconducting transition occurs at $T_c = 16$ K. (b) The thermal conductivity at temperatures above 1 K for the sample. There is a change of slope at T_c and a phonon peak near $T_c/5$ typical for superconductors. (c) The Lorenz number $L = \frac{\kappa}{\sigma T}$ normalized to the Sommerfeld value $L_0 = 2.45 \times 10^{-8}$W Ω K^{-2} as a function of temperature. (d) κ as a function of field at $T = 2$ K. The sharp decrease indicates that vortices penetrate the sample at $H_{c1} \simeq 60$ mT.

due to the entry of vortices which scatter phonons strongly (see Fig. 5.2d).

Thermal conductivity in zero field

The thermal conductivity was measured at temperatures above 1 K as shown in Fig. 5.2b. It displays the usual features seen in a superconductor, namely, a change of slope at T_c and a phonon peak near $T_c/5$ [158]. These measurements agree well with other reports of $LuNi_2B_2C$ and are very similar to the results for YNi_2B_2C [159, 160, 161] except for the larger phonon peak, which may be due to better crystal quality. In the normal state, κ is dominated by electronic carriers near T_c as can be seen from the fact that the normalized Lorenz number, $L/L_0 = \frac{\kappa}{\sigma T L_0}$, is smaller than unity. Now, let us turn to very low temperatures where more can be learned about the superconducting state.

Fig. 5.3 shows the temperature dependence of the thermal conductivity as a function of temperature down to 70 mK. The data is plotted as κ/T against T^2 to distinguish the electronic and the phononic contributions. In a superconductor with a fully gapped Fermi surface, the electronic contribution at $T = 0$ would be nil and κ would be entirely phononic. This does seem to be the case here although a small residual linear term

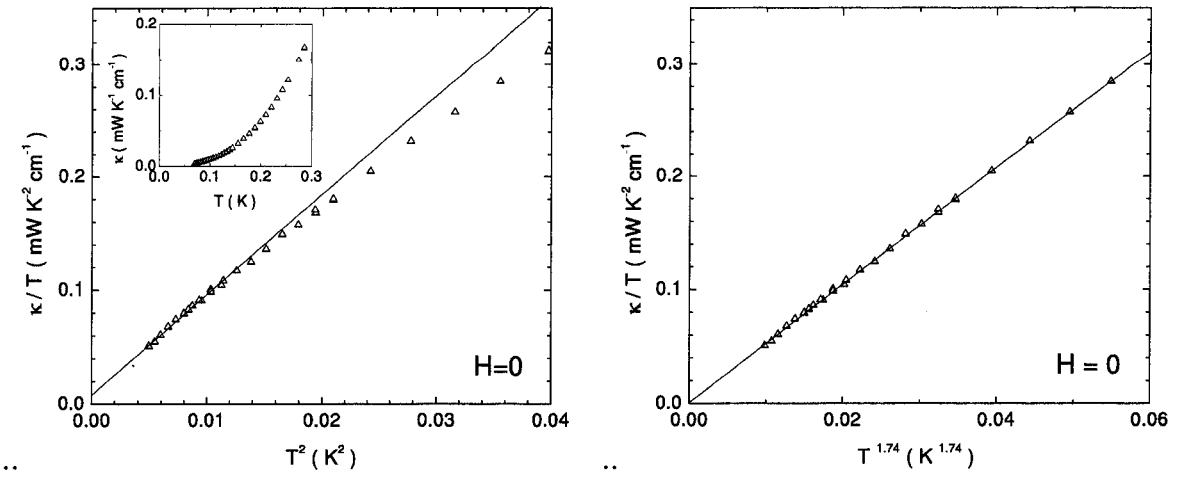

Figure 5.3: (a) Thermal conductivity of $LuNi_2B_2C$ in zero magnetic field for a heat current in the [100] direction [158]. The data is plotted as κ/T against T^2. κ reaches a cubic temperature dependence at low temperature with the expected magnitude for phonon thermal conductivity (see text). *Inset:* The same data presented as κ against T. This is to give an idea of a raw set of thermal conductivity data. (b) The same data plotted against $T^{1.74}$. This power law fits the data over a larger range of temperature and describes the phonons well, with no electronic linear term.

$\kappa_{00}/T \leq 0.01$ mW K^{-2} cm^{-1} cannot be ruled out. Let us explore the possibility of this small residual term stemming from a gap with topological nodes. One first notices that the normal state value given by the WF law is $\kappa_N/T = 18.8$ mW K^{-2} cm^{-1} (with $\rho_0 = 1.3$ $\mu\Omega$ cm) which is three orders of magnitude larger.

Let us now estimate what the electronic thermal conductivity would be for a gap with topological nodes. For simplicity, we will use the formula for a d-wave superconductor (the result will not be significantly different for other types of nodes [81]). We have $\kappa_{00}/T = \frac{k_B^2}{3\hbar}\ (\frac{n}{d})\ (\frac{v_F}{v_2} + \frac{v_2}{v_F})$ [85]. We use the fact that $\hbar k_F v_2 = \Delta_0/2$ and $\hbar k_F = m^* v_F$ to obtain $\kappa_{00}/T = \frac{2k_B^2}{3\hbar}\ (\frac{n}{d})\ (\frac{m^* v_F^2}{\Delta_0})$. Using $d = 10.631$Å, $n = 1$, m^* as the electron mass, $v_F = 3.6 \times 10^7$cm/s and $\Delta_0 = 2$ meV, we get $\kappa_{00}/T \simeq 3.3$ mW K^{-2} cm^{-1} which is two orders of magnitude larger than the experimental upper limit. In fact, for the overdoped cuprate superconductor Tl-2201, which has a similar $T_c \simeq 15$ K and $n/d = 2/23.6$Å, the electronic thermal conductivity in zero field is $\kappa_0/T = 1.41$ mW K^{-2} cm^{-1} [162].

Instead, let us look at the magnitude of the T^3 term of the thermal conductivity: $\kappa \simeq bT^3$ with $b = 8.6$ mW K^{-4} cm^{-1}. Using equation 2.22 with a mean diameter of

the sample of $2 \times \sqrt{w \times t/\pi} = 0.038$ cm and a phonon velocity of $v_{ph} \simeq 5 \times 10^5$ cm/s [163, 145], we obtain $b = 7.4$ mW K^{-4} cm^{-1} in very good agreement with experiment. It should be noted also that the phononic contribution can be better fitted using $\kappa_{ph} \propto T^{\alpha}$ (where $2 < \alpha < 3$ [63]). This is shown for $\alpha = 2.74$ on Fig. 5.3b. Such a behavior is probably due to specular (rather than diffuse) scattering on the crystal boundaries (as seen in Nb: see Fig. 2.5b), which agrees with the observed thermal conductivity being slightly larger than the calculated one (since the mean free path is effectively larger than the sample mean diameter). Using this fitting procedure, the electronic thermal conductivity is $\kappa/T = 0.000 \pm 0.002$ mW K^{-2} cm^{-1}, again in accordance with an *s*-wave gap.

In summary, the thermal conductivity of $LuNi_2B_2C$ in zero field is purely phononic with no electronic contribution. This constitutes evidence for a Fermi surface which is fully gapped, at least along the *ab* plane [1].

Thermal conductivity in a magnetic field

Let us now turn to the vortex state, where vortices introduce electronic excitations. The question that we ask is *how do these quasiparticles go from being localized at zero field to being fully delocalized in the normal state?* [92].

The thermal conductivity $\kappa(T)$ of $LuNi_2B_2C$ is plotted in Fig. 5.4, as κ/T vs T^2 for different values of the magnetic field, applied perpendicular to the heat current ($H \parallel [001]$ and $\dot{Q} \parallel [100]$). As we saw above, κ is purely phononic in zero field. However, plotting the data is this way allows us to extract an additional linear term which develops in the vortex state. This is seen as a rigid shift from the $H = 0$ T data for low values of magnetic field. Indeed, the phonons do not get scattered significantly by the electronic excitations since the strength of the scattering is too weak with respect to the dominant boundary scattering. This is made possible thanks to the low temperatures and the small cross-section of the sample. At fields above ~ 2 T, the thermal conductivity is linear

[1] In UPt_3, a superconductor with nodes in the gap, the linear term expected from theory is $\kappa_b/T = 1.4$ mW K^{-2} cm^{-1} and $\kappa_c/T = 1.9$ mW K^{-2} cm^{-1} for the heat current in the *b* and *c* directions respectively. The observed linear terms are much smaller, being $\kappa_b/T = 0.15$ mW K^{-2} cm^{-1} and $\kappa_c/T = 0.0$ mW K^{-2} cm^{-1} [51]. However, the cubic term observed at low temperatures are $b_b = 800$ mW K^{-4} cm^{-1} and $b_c = 1400$ mW K^{-4} cm^{-1}, which are one or two orders of magnitude too large for being phononic in nature. The thermal conductivity is thus clearly electronic at low temperatures although a clear linear term is not observed. This result is still ill-understood [33]. Note that the theories used for the estimates are based on the assumption of a single Fermi surface sheet, which is not the case for UPt_3.

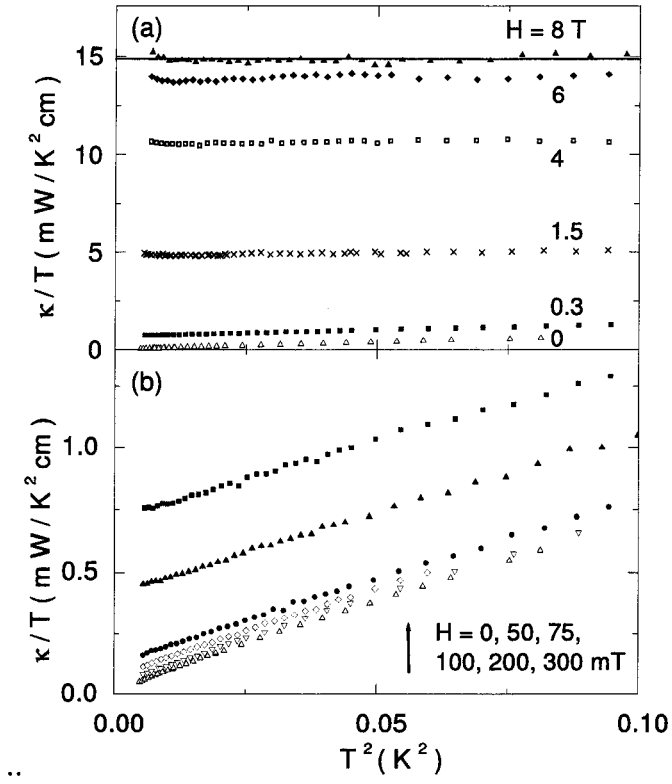

Figure 5.4: Temperature dependence of thermal conductivity at several applied fields, plotted as κ/T vs T^2, for (a) $H = 0$, 0.3, 1.5, 4, 6 and 8 T, and (b) $H = 0$, 50, 75, 100, 200 and 300 mT, in increasing order. The solid line is given by $L_0/\rho_0(H = 8\ \mathrm{T})$.

in temperature, and we cannot resolve the phononic contribution (phonons are strongly scattered by an increased density of electrons). Above $H_{c2} \simeq 7$ T, in the normal state, the WF law is perfectly satisfied as can be seen in Fig. 5.4: the solid line is the value expected by the WF law with $\rho_0(H = 8\ \mathrm{T}) = 1.67\ \mu\Omega$ cm.

Given this well-understood behavior of $\kappa_e(T)$ and $\kappa_{ph}(T)$, it is straightforward to extract the electronic contribution $\kappa_e(T)$, by simply extrapolating κ/T to $T = 0$. The result of this extrapolation is plotted as κ_e/T vs H in Fig. 5.5, where the field is normalized to unity at $H_{c2}(0)$ and κ_e/T to its normal state value κ_N/T. One immediately notices the sudden onset of κ at low fields leading to a large amount of *delocalized* quasiparticles throughout the vortex state of $LuNi_2B_2C$. This would seem to provide a natural explanation for the observation of de Haas-van Alphen oscillations down to unusually low fields ($H_{c2}/5$) in YNi_2B_2C [124, 125, 150], a close cousin of $LuNi_2B_2C$, with $T_c = 15.5$ K and $H_{c2} = 6.5$ T.

In fact, the growth of quasiparticle conduction starts immediately at $H_{c1} \simeq 60$ mT (see Fig. 5.2d) and is seen to be roughly linear in field (see Fig. 5.5b). This is in dramatic contrast to the behavior of quasiparticles in s-wave superconductors with a large finite gap for all directions of electron motion. For comparison, we show in Fig. 5.5a the electronic conductivity of Nb measured at 2 K (*i.e.* 0.22 T_c) [20]. In an isotropic s-wave superconductor, the only quasiparticle states present at $T \ll T_c$ are those associated with vortices. When vortices are far apart, these states are bound to the vortex core and are therefore localized and unable to transport heat, thus contributing to the specific heat but not to the thermal conductivity. As the field is increased and the vortices are brought closer together, tunnelling between states on adjacent vortices will cause some delocalization. This conduction is expected to grow exponentially with the ratio of intervortex separation to vortex core size ($\simeq 2\xi$), namely as $\exp(-\alpha\sqrt{H_{c2}/H})$, where α is a constant of order 1, as is found for Nb at fields below $H_{c2}/3$ [164] and in V_3Si (see Chapter 4).

In the presence of nodes in the gap, the dominant mechanism for quasiparticle transport in the vortex state is completely different: conduction results from the population of extended quasiparticle states in the bulk of the sample, *outside* of the vortex cores. The excitation of these quasiparticles proceeds via the Doppler shift of their energies as they move in the presence of the superfluid flow circulating around each vortex as seen in Chapter 2. Because, near the nodes, such states exist down to zero energy, the growth in the zero-energy quasiparticle density of states starts at H_{c1}, with a characteristic $\sqrt{H}$ dependence [90]. This leads to a $\sqrt{H}$ dependence of the specific heat at low temperature, as observed, for example, in the cuprate superconductor $YBa_2Cu_3O_7$ [101, 89].

Note that the same mechanism will operate for an anisotropic s-wave gap if the field is such that the Doppler shift exceeds the minimum gap in the quasiparticle spectrum. In addition, these excitations will be delocalized. Heat transport has the advantage over heat capacity of probing exclusively such quasiparticles.

The effect of vortices on quasiparticle transport in an unconventional superconductor with a line of nodes in the gap function was studied in beautiful detail by Suderow and co-workers [51]. Their measurements of $\kappa(T, H)$ in UPt_3 yield a roughly linear increase of κ_e/T at $T \rightarrow 0$ with H, shown in Fig. 5.5. The data is for a heat current in the basal plane of the hexagonal crystal structure, which probes the equatorial line node in the gap function of UPt_3, established by transverse ultrasound attenuation [165]. *Fig. 5.5 reveals that quasiparticle conduction in the basal plane of $LuNi_2B_2C$ is as good as in UPt_3 (or*

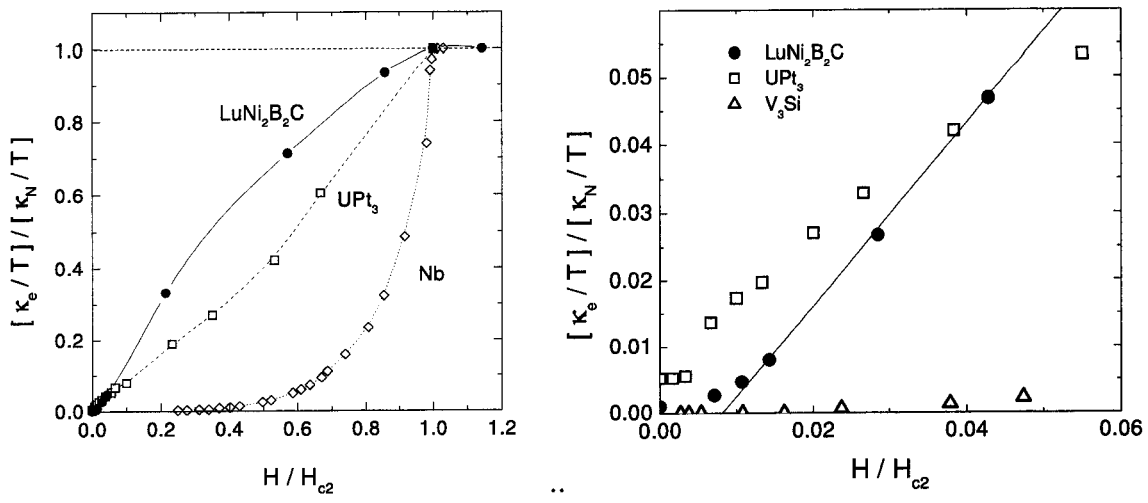

Figure 5.5: (a) Magnetic field dependence of the electronic thermal conductivity κ/T at $T \to 0$, normalized to its value at H_{c2}. Circles are for $LuNi_2B_2C$, squares for UPt_3 [51] and diamonds for Nb [20]. Note the qualitative difference between the activated conductivity of s-wave superconductor Nb and the roughly linear growth seen in UPt_3, a superconductor with a line of nodes. The lines are a guide to the eye. (b) Field dependence of the electronic thermal conductivity κ/T at $T \to 0$ at low fields, normalized to its value at H_{c2}. For $LuNi_2B_2C$, the growth is linear and starts at H_{c1}, as emphasized by the solid line. The growth is equally rapid for UPt_3 [51]. The equivalent data for the s-wave superconductor V_3Si shows a much slower growth.

even better). At low fields, the growth in the residual linear term $\kappa_0/T \equiv (\kappa/T)_{T\to 0}$ is also linear in H, starting at H_{c1}:

$$\frac{\kappa_0}{T} \simeq \frac{L_0}{\rho_0}\frac{H - H_{c1}}{H_{c2}} \quad , \tag{5.1}$$

where ρ_0 is the zero-field normal-state resistivity. This is vastly more conductive than a typical s-wave superconductor. For example, electronic conduction in V_3Si, an extreme type-II s-wave superconductor with comparable T_c (16.5 K) and ξ_0 (45 Å), is 20 times weaker at $H = 0.05\ H_{c2}$, as seen from data shown in Fig. 5.5b.

In both $LuNi_2B_2C$ and UPt_3, the thermal conductivity is roughly linear in H and the heat capacity follows approximately a $\sqrt{H}$ dependence. The latter is naturally understood in terms of a density of states which is linear in energy (coming from nodes or minima). It has recently been derived by Maki and coworkers that the thermal conduc-

tivity for a gap with point nodes and in the ultra-clean limit would indeed be linear with respect to magnetic field [166]. Although an interesting result, it is doubtful that this regime of purity applies to our sample [1].

Nohara *et al.* [153] and Izawa *et al.* [155] have attributed the $\sqrt{H}$ dependence of the specific heat they observe in YNi_2B_2C to a Doppler shift of the quasiparticle spectrum as in a *d*-wave superconductor [91] but applied in this case to a highly anisotropic *s*-wave gap, with a small minimum gap $\Delta_{\rm min}$. Interpreting the thermal conductivity data in the same way yields an estimate of $\Delta_{\rm min}$. Indeed, because quasiparticle conduction starts right at H_{c1}, the minimum gap must be smaller than the Doppler shift energy E_H at H_{c1}. In a superconductor with a line of nodes in the gap, the average E_H is given by $\simeq \Delta_0\sqrt{B/B_{c2}}$ [91] where B is the magnetic field inside the superconductor and $B_{c2} \simeq H_{c2}$. At H_{c1}, $B \simeq 0$ in a type II superconductor thus possibly implying a true zero in the gap. A conservative upper bound on the minimum field required to excite quasiparticles above $\Delta_{\rm min}$ uses $B = H_{c1}$. This gives:

$$\Delta_{\rm min} \leq E_H(H_{c1}) \simeq \Delta_0\sqrt{H_{c1}/H_{c2}} \simeq \Delta_0/10 \quad . \tag{5.2}$$

In other words, there is a huge gap anisotropy, with a minimum in the basal plane (the direction of heat current) [2]. A factor 10 in gap anisotropy is unprecedented for an *s*-wave superconductor, with a factor of 2 being the most ever inferred in elemental superconductors [29]. Note that a gap variation of a factor of three is inferred for $NbSe_2$ as will be discussed in Chapter 6.

In summary, the thermal conductivity is seen to grow linearly with field and to start at the very lowest fields, namely, H_{c1}. This behavior is strikingly different from that of an *s*-wave superconductor such as Nb or V_3Si but rather, is very similar to that of UPt_3, a superconductor with lines of nodes in the gap. These results were the first to unambiguously prove the presence of highly delocalized quasiparticles throughout the

[1] Indeed, an estimate of the purity is given above with the standard relation between the Pippard coherence length and the mean free path ξ_0/l. It can be reformulated in the language used by Maki *et al.* and gives $\hbar\Gamma/\Delta \simeq 1$ where $\Gamma = 1/2\tau_N$ (with $\tau_N = l/v_F$ being the mean scattering time). Here we used the same values as earlier, namely, $v_F = 3.5$ cm/s, $l = 270$ Å and $\Delta = 2.2$ meV. This is far from the ultra-clean regime of $\hbar\Gamma/\Delta \ll 1$.

[2] It is interesting to note that a transformation from a hexagonal to a square vortex lattice occurs in $LuNi_2B_2C$ near $H = 0.1$ T [167]. In the context of a gap with a large anisotropy, non-local corrections will play a major role for quasiparticles in the direction of the gap minima and the local density of states will be different for both geometries of the vortex lattice. However, the spatial average of the density of states should not be affected as found for a p-wave order parameter [168]. For this, the thermal conductivity will not be affected either by such a transition.

vortex state of $LuNi_2B_2C$ [92]. Previous results showed that this was the case only on parts of the Fermi surface as dHvA oscillations were seen to persist deep into the vortex state [124, 125, 150]. Also, indirect indications were given by heat capacity and electromagnetic vortex response [155]. However, the absence of a residual linear term in thermal conductivity in zero field indicates the absence of electronic excitations, which leads us to conclude that the gap function has no topological zeros, but rather has a very strong anisotropy of at least a factor of ten. This agrees with the conclusions of previous heat capacity [141, 153, 155], microwave impedance [169, 155], photo-emission spectroscopy [156] and Raman scattering [170] studies. Further work also supported these results and helped to understand the nature of the gap [152] and of the superconducting mechanism in borocarbides [100]. These will be discussed below.

5.2.2 Other evidence of an anisotropic gap

Indirect evidence of an anisotropic gap in borocarbides was reported prior to our work on $LuNi_2B_2C$, and more direct (and very convincing) evidence was unveiled afterwards. We review these studies critically and conclude that the body of evidence that now exists for a strongly anisotropic gap in the non-magnetic borocarbides is substantial.

Early reports

Several probes which can offer key signatures for an unconventional gap did show early evidence. However, more often than not, these results were obtained for temperatures that did not reach $T_c/10$ and stayed inconclusive. This problem had plagued the field of high-T_c superconductors in their early days with many reports of s-wave behavior from measurements at insufficiently low temperatures.

It is worth noting that Raman measurements did show scattering below the gap as is seen for HTSC [170]. Nuclear Magnetic Resonance measurements of the relaxation rate $1/T_1$ were first thought to display BCS behavior. The results were different though when the measurements were extended to lower temperatures ($T_c/50$) and showed power law dependencies, suggestive of an unconventional gap [171].

Studies of de Haas-van Alphen oscillations observed extended quasiparticle states deep into the superconducting state ($H_{c2}/5$) [124, 125]. The quantum oscillations were seen not to be attenuated as strongly below H_{c2}, as they are in V_3Si [114, 116]. Although there has not been a thorough study of the different models proposed to explain dHvA

oscillations in the vortex state (for a review, see [116] and [68]), the one proposed by Tešanović and co-workers [110] was used to fit one set of data, and was successful at doing so [1]. However, the presence of oscillations in the vortex state was only revealed on small parts of the Fermi surface.

Effect of disorder

A powerful tool for exploring unconventional superconductivity is to introduce disorder in a system. This is usually done by substitution. In the case of borocarbides, Pt and Co have been used to replace Ni: $R(Ni_{1-x}S_x)_2B_2C$ with R=Lu,Y and S=Pt,Co [144, 149, 154, 153]. The response to disorder is substantially different for gaps with and without topological nodes. For example, superconductivity is destroyed by the presence of non-magnetic impurities for a superconductor with topological nodes (see for example [86]) whereas it has no effect on s-wave superconductors. Another key feature lies in the fact that *an anisotropic gap with no topological nodes will see its anisotropy decrease with increasing disorder*, whereas topological nodes cannot be removed [79].

In the case of borocarbides, the substitution of Ni by Pt or Co has the effect of decreasing the transition temperature significantly [144, 149] as one may expect for a superconductor with topological nodes. However, this suppression of T_c is due to the effect of a decreasing density of states in the case of $Y(Ni_{1-x}Co_x)_2B_2C$ [144] (and probably for $Lu(Ni_{1-x}Co_x)_2B_2C$ as well). However, heat capacity [153, 154] and photo-emission spectroscopy [156] studies have compared the behavior of pure and impure borocarbides to conclude that the gap anisotropy was suppressed with disorder and that the gap did not have topological nodes.

Heat capacity Nohara and co-workers compared the effect of disorder on the specific heat for $Y(Ni_{1-x}Pt_x)_2B_2C$ with several levels of disorder [153, 154]. In zero field, the temperature dependence was shown to go from a T^3 behavior for the clean sample to an exponential one in the impure sample as shown in Fig. 5.6 [153]. In field, the behavior went from a $\sqrt{H}$ dependence in the pure sample to a linear one in the impure sample.

[1] The parameters that were obtained from this analysis were later used by Dukan *et al.* [72] to calculate the thermal conductivity in the vortex state of borocarbides with no free parameters. This reproduced surprisingly well our own results on $LuNi_2B_2C$ presented above [92] although it could not explain the presence of delocalized quasiparticles at fields down to H_{c1}. Indeed, measurements in a magnetic field are most conclusive (in obtaining an energy scale) at fields much below H_{c2} where the Doppler shift energy is sufficiently small.

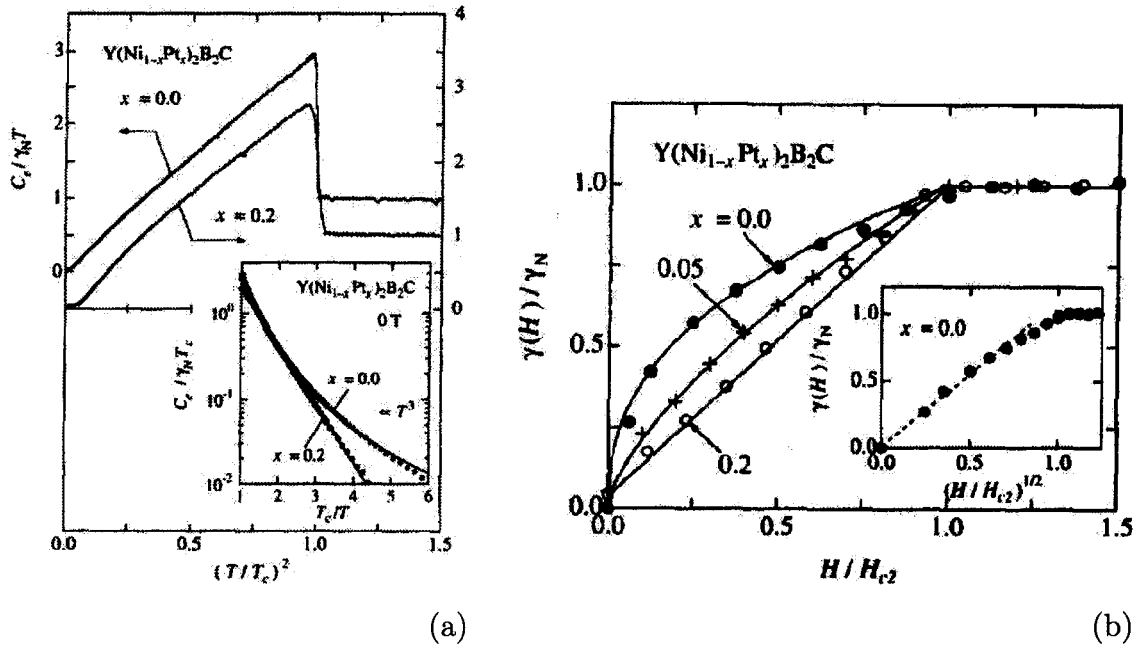

(a) (b)

Figure 5.6: (a) The temperature dependence of the electronic contribution to the specific heat for $Y(Ni_{1-x}Pt_x)_2B_2C$ with $x = 0.0$ and $x = 0.2$ in zero magnetic field [153]. The temperature dependence of the clean sample is cubic in temperature while it is exponential for the dirty one. (b) The field dependence of the electronic specific heat. The clean sample shows a $\sqrt{H}$ dependence while a linear dependence is recovered with increasing disorder.

This crossing from the typical behavior of unconventional superconductors to more BCS behavior is interpreted as evidence for an anisotropic s-wave gap.

Photo-emission spectroscopy A high resolution photo-emission spectroscopy study was performed on samples with 0% and 20% Pt [156]. Both samples show a typical superconducting coherence peak below T_c and the opening of a gap (see Fig. 5.7a). However, the lineshape in the superconducting state ($T = 6$ K) is best fit with a anisotropic gap function which is parameterized by a maximum and minimum gap (Δ_{max} and Δ_{min}). The best fit gives values of $\Delta_{max} = 2.2 \pm 0.2$ meV and $\Delta_{min} = 0.0 \pm 0.2$ meV for the pure sample and $\Delta_{max} = 1.5 \pm 0.2$ meV and $\Delta_{min} = 1.3 \pm 0.2$ meV for the dirty sample (see Fig. 5.7b). The anisotropy is concluded to be reduced by disorder, another indication that there are no topological nodes in the gap function [1].

[1] Although this unprecedented energy resolution does unambiguously show the opening of a gap in the energy spectrum below T_c, one may be skeptical about these measurements -if only in principle- being able to resolve the kind of anisotropy that are claimed. However, the evidence for a difference in the level of anisotropy is convincing [156] although the numerical values quoted may be questioned.

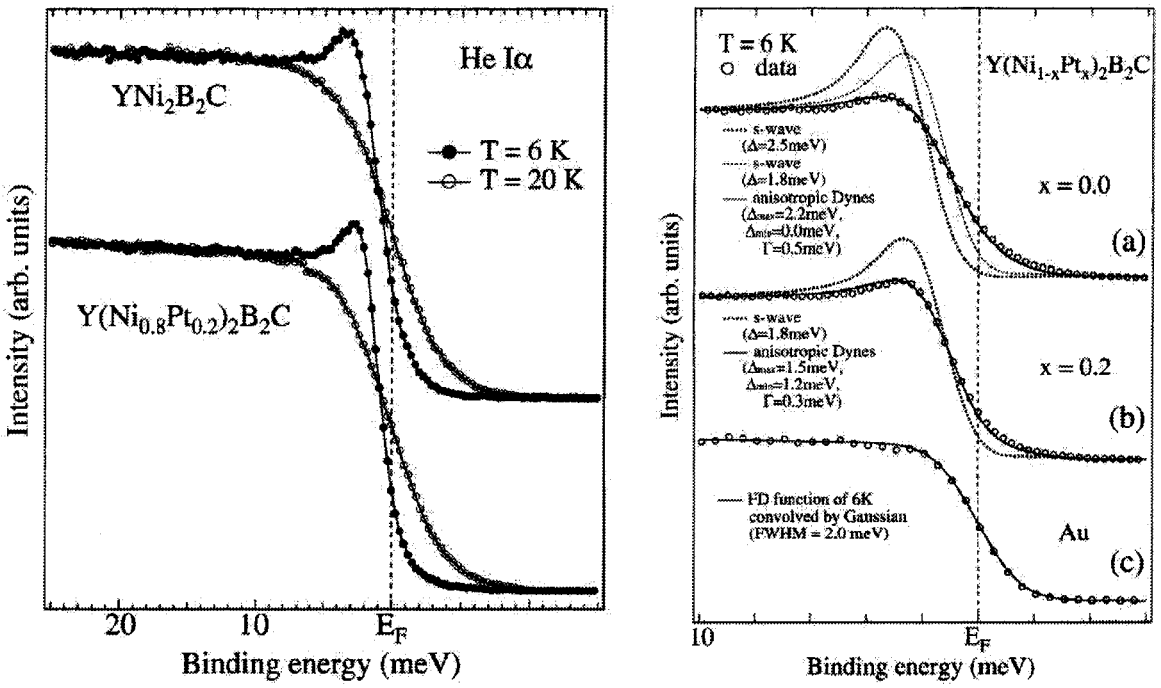

Figure 5.7: (a) Photo-emission spectroscopy lineshapes of $Y(Ni_{1-x}Pt_x)_2B_2C$ with $x = 0.0$ and $x = 0.2$ [156]. Below T_c, the typical superconducting coherence peaks appear and a gap opens for both samples. (b) The lineshapes are best fitted with an anisotropic gap parameterized by a maximum and a minimum value of the gap. The fit gives a much smaller gap minimum for the pure sample.

The effect of disorder has proved to be very useful in the case of borocarbides and seem to indicate that the gap, although anisotropic, does not have topological nodes.

Tunnelling Spectroscopy

Tunnelling spectroscopy gives direct access to the energy gap. However, early tunnelling spectroscopy measurements were performed only at temperatures above 4.2 K [172, 23, 24]. This factor among others had the effect of broadening the spectra and even showing a non-zero density of states at zero energy. Although fits to a BCS gap were successful, no anisotropy of the gap could be resolved. However, recent Scanning Tunnelling Spectroscopy (STS) measurements at lower temperatures ($T_c/30$) and with a high energy resolution were performed on both $LuNi_2B_2C$ and YNi_2B_2C [100].

Martinez-Samper *et al.* saw a large anisotropy in the superconducting gap as shown

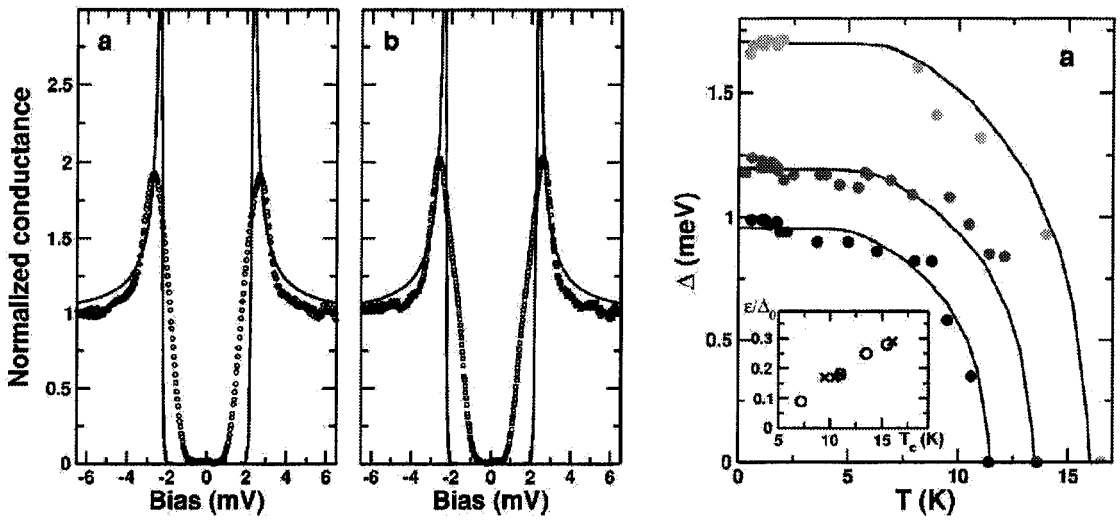

Figure 5.8: (a) The tunnelling spectra for $LuNi_2B_2C$ (left) and YNi_2B_2C (right) at $T = 0.5$ K = $T_c/30$ [100]. The gap is seen to deviate strongly from a simple BCS shape (black lines) and is consistent with a highly anisotropic gap. (b) The temperature dependence of the mean value of the superconducting gap at different locations on the sample. *Inset:* The anisotropy parameter ϵ -using a gap of the form $\Delta = \Delta_0(1 + \epsilon\ cos(4\theta))$- as a function of T_c and normalized to the average gap Δ_0.

in Fig. 5.8a. One can see that the conductance departs from zero around 0.8 meV and peaks around 2.6 meV for $LuNi_2B_2C$ and 2.3 meV for YNi_2B_2C on these figures. The tunnelling spectra was also found to be different at different positions on the sample. The average gaps were found to be different. These were fit to a BCS temperature dependence with different T_c (see Fig. 5.8b). This indicated that different sites were locally more or less disordered. The spectra were seen to change accordingly: a reduced anisotropy was found at the sites with lower T_c, a direct indication that the gap anisotropy is reduced with disorder. This is seen in the inset of Fig. 5.8b. There, an anisotropy factor was used to fit the tunnelling spectra (using a gap of the form $\Delta = \Delta_0(1 + \epsilon\ cos(4\theta))$ as described in reference [21]) and is plotted against the observed local T_c. However, as pointed out by the authors, STM spectra only probe a part of the Fermi surface and may not give the full distribution of gap values of these systems. However, it does undeniably present direct evidence for an anisotropic gap.

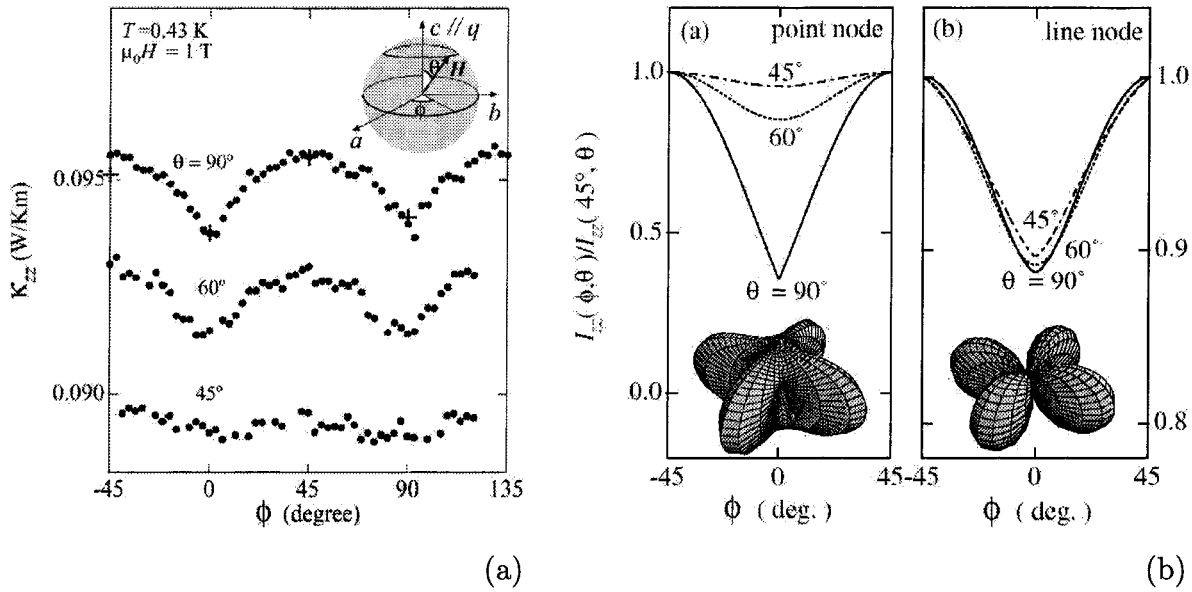

Figure 5.9: (a) The thermal conductivity of YNi_2B_2C with a heat current along the [001] direction and at $H = 1$ T as a function of field orientation. At $\theta = 90°$, a fourfold oscillation is observed whereas it is not for $\theta = 45°$ [152]. (b) Theoretical predictions for point nodes and line nodes [152, 166]. The experimental behavior shows conclusive evidence for point-like minima.

The shape of the gap

A directional probe is needed to obtain further information about the shape of the gap. Indeed, it is interesting to know where the minima in Δ are whether they resemble point nodes or line nodes. For HTSC, Angle Resolved Photo-Emission Spectroscopy (ARPES) has proved to be ideal for this task [87], but it is unfortunately not suited for compounds that have 3D electronic properties. Ultrasound attenuation studies were key in the case of UPt_3 (for example, see [33]) and Sr_2RuO_4 [173]. An alternate approach is to measure thermal properties such as heat capacity or thermal conduction in a magnetic field as a function of the angle at which the field is applied with respect to the sample. Such studies were performed on the borocarbides and give insight on the nature of the minima in the gap.

The thermal conductivity of YNi_2B_2C was measured with a heat current along the [001] direction and as a function of field angle [152]. The authors found that, in addition to having a similar behavior of κ as a function of field, as found in $LuNi_2B_2C$ [92], the dependence on the direction of the applied field was consistent with point nodes along the [100] and [010] directions. They found a fourfold oscillation for a field rotated with

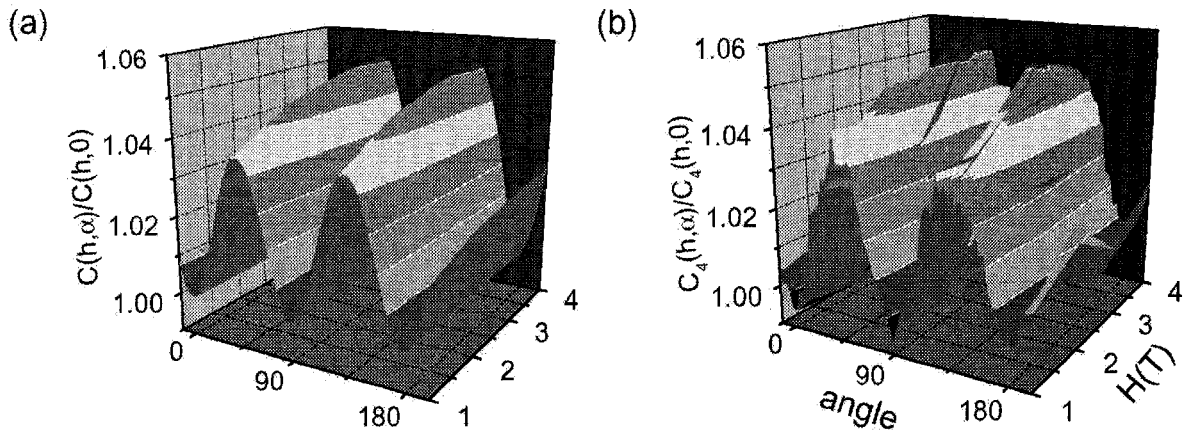

Figure 5.10: The heat capacity as a function of both field and angle of the applied field $C(H, \text{angle})/\text{C}(\text{H}, \text{angle} = 0)$ after [174]. A numerical calculation shows the behavior expected for quasiparticles in a 3D system with nodes as shown in (a). The experimental data is in good agreement as shown in (b).

respect to ϕ for $\theta = 90°$, but saw no change in κ for $\theta = 45°$ (see Fig. 5.9), consistent with theory for a point node rather than a line node [152, 166]. Note that the authors emphasize that these would be "point-like minima" and not topological point nodes, in agreement with the idea of a highly anisotropic gap, rather than an unconventional gap.

One should note that Izawa *et al.* [152] gave a misleading estimate of the gap minimum. Their estimate comes from the fact that they resolve an oscillation down to $T = 0.3$ K whereas the average gap is of the order of $1.57\ k_B T_c \simeq 30$ K, yielding a factor of 100 anisotropy. However, the measurements are performed in a magnetic field of 1 T, which gives rise to a severe Doppler shift of the quasiparticles of the order of $E_H = \sqrt{H/H_{c2}}\ \Delta \simeq \frac{1}{3}\Delta$. So they are not able to access energies lower than E_H.

A similar study of the magnetic field orientation dependence of the heat capacity has recently reported a fourfold anisotropy indicative of nodes in the same directions ([100] and [010]) as shown in Fig. 5.10 [174]. From this measurement, Park and co-workers conclude that the gap has true topological lines of nodes, rather than pointlike ones. However, the body of evidence that exists against the presence of actual nodes (found by disorder studies, thermal conductivity and STS measurements) is in their disfavor. Nevertheless, these results do raise questions about the exact shape of the anisotropic s-wave gap (point-like minima or line-like minima).

The source of the anisotropy

It is natural to wonder what could be the cause of such a pronounced gap anisotropy. Recall that borocarbides exhibit Fermi surface nesting with a wavector near [0.5,0,0], and that a softening of phonon modes below T_c is associated with it. This nesting applies to the [110] direction of the third FS sheet (see Fig. 5.1b) [137]. Maki *et al.* have suggested that this may be the source of a suppressed pairing potential (and consequently a smaller gap) along the [110] direction [166]. However, the minima in the gap seem to be along the [100] direction as found from thermal conductivity and heat capacity measurements [152, 174]. This is puzzling and will certainly be the source of further theoretical work.

Summary A considerable body of evidence exists which shows unambiguously that the gap function is strongly anisotropic [92, 153, 154, 156, 155, 152, 100]. Our thermal conductivity data shows that the gap has no topological nodes. In addition, the shape of the gap is known to have its minima along the [100] and [010] directions, although it is not yet entirely clear whether these minima are point-like [152] or line-like [174]. This is not understood by the natural idea that the pairing potential is suppressed along the nested parts of the FS (namely along [110] [137, 166]). One is naturally brought to the question of the mechanism for superconductivity in these non-magnetic borocarbides.

5.3 The mechanism for superconductivity

A gap function with topological nodes is invariably associated with an unconventional pairing mechanism. In the case of the borocarbide superconductors, the possibility of an electronic pairing mechanism has been brought up by several authors [175, 141, 92, 152, 174]. However, with strong evidence against the existence of topological nodes, one is tempted to conclude that the pairing mechanism is phononic. We will show here the argument made by Martinez-Samper and co-workers on the basis of STS experiments which argues that the pairing is phonon-mediated [100].

Very early on, Carter *et al.* concluded that the pairing mechanism was phononic simply on the basis of the plot of T_c vs γ_N, the normal state electronic specific heat [142]. Also, a large isotope effect was observed (see for example [151]). More detailed studies require an analysis with the strong-coupling Eliashberg theory, as described by Carbotte [176]. Several authors [140, 177] have argued that such a standard Eliashberg analysis

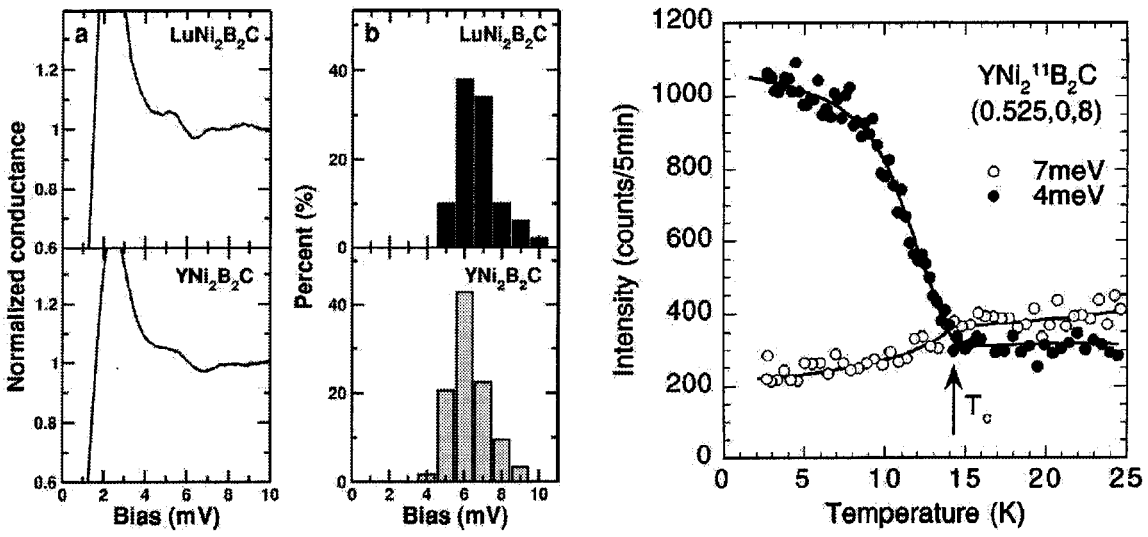

(a) (b)

Figure 5.11: (a) The tunnelling spectra for RNi_2B_2C (R=Lu,Y) at high energy in the superconducting state. A distinctive dip is seen around $E = 6$ meV (as seen by the percentage of times the dip was seen as a function of its energy) [100]. This corresponds to the energy $\Delta + \hbar\omega$ where $\hbar\omega$ is the energy of a phonon mode which softens below T_c at an energy of 4 meV as seen in (b) [147].

of $H_{c2}(T)$ and resistivity leads to a quantitatively satisfactory and consistent description of $LuNi_2B_2C$ in terms of the measured phonon spectrum and a largely isotropic gap function. However, it remains to be seen whether such an analysis survives the inclusion of a very anisotropic gap.

More recently, direct evidence for phonon-mediated superconductivity was provided by tunnelling spectroscopy [100]. One expects to find the signature of the bosonic mode (phononic or electronic) responsible for the pairing mechanism at an energy $\Delta + \hbar\omega$ where Δ is the energy gap and $\hbar\omega$ is the energy of the phonon mode. Indeed, a feature is revealed at an energy of 6 meV for both $LuNi_2B_2C$ and YNi_2B_2C as can be seen in Fig. 5.11a. Knowing that the gap has an approximate value of 2 meV, this leads to a phonon mode at 4 meV which is precisely the energy of the mode that softens in the superconducting state [146, 147, 148]. This is shown in Fig. 5.11b where the intensity of this mode (at 4 meV and momentum wavevector [0.5,0,0]) starts to increase at T_c. It is concluded that this phonon mode in particular is responsible for the superconductivity in borocarbides, although other higher energy phonon modes may also play a role in the pairing.

This conclusion represents a clear warning for the study of novel superconductors where unusual temperature and field dependences are often prematurely associated with an unconventional pairing mechanism.

5.4 Conclusion

In conclusion, we have presented a study of the thermal conductivity through the vortex state of the borocarbide superconductor $LuNi_2B_2C$ which has provided unambiguous evidence for the existence of highly delocalized quasiparticles down to the very lowest fields [92]. This shows the presence of a gap which is strongly anisotropic with a gap minimum at least 10 times smaller than the gap maximum. A more complete review has shown other evidence that this is the case for both the non-magnetic members of the borocarbide family: $LuNi_2B_2C$ and YNi_2B_2C. However, even with this strong anisotropy, it is found that the nodes (or minima) are not topological and the anisotropy is strongly reduced with disorder. The position of the minima are in the [100] and [010] directions, although there is still controversy about whether they are point-like or line-like. It is tempting to associate this unprecedented anisotropy to a pairing mechanism which is electronic in nature. However, a low energy phonon mode which softens in the superconducting state is most likely responsible for the pairing mechanism.

The source of the strong gap anisotropy is yet to be understood. One natural explanation involved a reduced electron-phonon coupling from a partly nested FS, which incorrectly predicted the gap maxima rather than minima to be in the [100] and [010] directions. A more rigorous theoretical treatment may be necessary to understand the strong gap anisotropy.

In the general study of novel forms of superconductivity, the borocarbides offer a useful point of comparison, as the most dramatic example of conventional superconductors with a highly anisotropic gap, relative to unconventional superconductors with true topological nodes in the gap.

Chapter 6

$NbSe_2$: a multi-band superconductor

Multi-band superconductivity (MBSC) is the existence of a superconducting gap of significantly different magnitude on distinct parts (sheets) of the Fermi surface. This unusual phenomenon has recently emerged as a possible explanation for the anomalous properties of some s-wave superconductors. Although the first experimental observation of MBSC was reported twenty years ago [178], the possibility of MBSC has not often been raised since then. The current interest has been fuelled by the peculiar properties of the 40-K superconductor MgB_2, where the case for MBSC is now rather compelling [179]. In particular, a gap much smaller than the expected BCS gap (of order $k_B T_c$) has been resolved in tunneling experiments [180, 181, 182, 25]. A consequence of this small gap is the much more rapid excitation of quasiparticles (with temperature or field) than usual. This can make the properties of this s-wave superconductor similar to those of d-wave superconductors, for example.

Based on angle-resolved photoemission (ARPES) measurements, it has recently been proposed that the 7-K layered superconductor $NbSe_2$ is also host to MBSC [183]. They reveal a sizable difference in the magnitude of the superconducting gap on the two sets of Fermi surface (FS) sheets, with no observed gap on the smallest sheet. These conclusions are supported by our recent studies of heat transport [55] which provide bulk evidence at temperatures much below T_c, and are consistent with several previous anomalous reports.

In this chapter, we will give a brief review of multi-band superconductivity before reviewing the case of $NbSe_2$.

6.1 A brief introduction to MBSC

Multi band superconductivity (MBSC) was first reported in 1980 in $SrTiO_3$ [178]. Since then, little work was done on the topic until its recent re-emergence with the discovery of MgB_2 for which the case for MBSC is very strong [179]. We will review briefly some important properties of a superconductor which displays MBSC, namely, the gap function, the behavior in a magnetic field and the source of this effect. A good review of the properties of MgB_2 and of the physics of MBSC can be found in [30].

The mechanism

Although most materials have a complicated Fermi surface, often with several sheets, it is common to disregard this complexity and treat the material as having a single isotropic Fermi surface and a single superconducting gap. There is a good reason to do this as Fermi sheets are usually strongly coupled by interband scattering, *i.e.* the quasiparticles and the Cooper pairs can easily scatter from one band to another. This leads to a gap of the same magnitude on all Fermi sheets. MBSC is the presence of superconducting gaps of significantly different magnitudes on two (or more) sets of Fermi surfaces. For this to occur, it is required that these be decoupled. In the extreme case that the two bands are not coupled at all, one of the FS will not display superconductivity. More likely though, superconductivity will be induced onto the other FS but will have a smaller gap associated with it. It should be noted that within this picture, disorder will have the effect of coupling the FS increasingly as impurities (which are scattering centers) will facilitate the scattering between bands. In turn, this should wipe out the MBSC. We can view MBSC as occurring only if the two following conditions are satisfied:

- The coupling between two sets of Fermi surface sheets is weak.
- Superconductivity occurs naturally on one of these sets but not the other.

The physical mechanism leading to the first condition being satisfied is not yet clearly known. Speculations include the different dimensionality of the different sheets but further work will be required to answer this question. The second condition has been verified in MgB_2 where the electron-phonon coupling strength has been found to be three times larger for the 2D σ orbits than for the 3D π ones [184, 185]. In this chapter, we will concentrate instead on a simpler task, namely that of knowing whether a superconductor

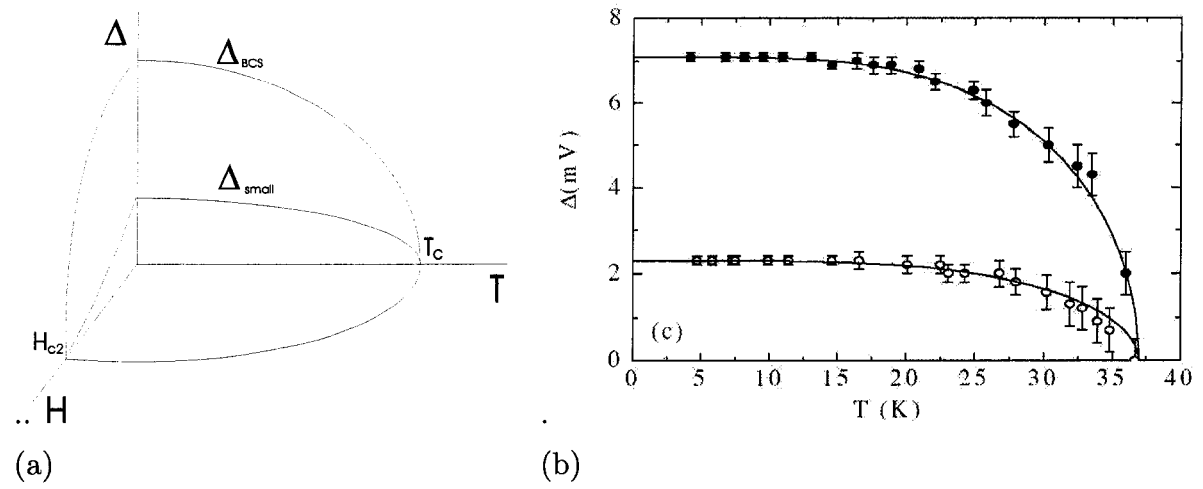

Figure 6.1: (a) Both superconducting gaps as a function of temperature and magnetic field for a two-band superconductor. (b) The temperature dependence of both gaps in MgB_2 as determined by tunneling (from [180]).

displays MBSC or not. Indeed, it has only been reported in doped $SrTiO_3$, MgB_2 and $NbSe_2$ while *unconventional* MBSC has been proposed for Sr_2RuO_4 [186, 187, 188].

The Properties

The case for MBSC is well established in the 40 K superconductor MgB_2. For this, one can view the extensive literature relevant to MgB_2 as a reference point of the properties of a MBSC. We will first emphasize the behavior of the two gaps as a function of temperature and magnetic field as illustrated on Fig. 6.1. The small gap does opens at T_c but has a smaller zero temperature value. In a magnetic field, superconductivity will be destroyed more easily for the Fermi surface with a small gap. In other words, a second field scale (remembering that $H_{c2} \propto \Delta^2/v_F^2$) and, in turn, another length scale (since $\xi \propto 1/\sqrt{H_{c2}} \propto v_F/\Delta$) is associated with the small gap. Note that the small gap does not go to zero at some different upper critical field as this would indicate the presence of two superconducting phases. This phase diagram was confirmed as a function of temperature directly by scanning tunneling spectroscopy (STS) measurements, for example (see Fig. 6.1) [180]. In a magnetic field, indirect evidence exists from heat capacity [189] and thermal conductivity [99] which show a distinct shoulder near this characteristic field. Also, the associated length scale was observed by imaging vortex cores [25] and was subsequently explained by Koshelev and Golubov with such a phase diagram [190].

From this basic idea, one can obtain the behavior both in temperature and magnetic field of most properties of MgB_2 such as heat capacity, tunneling, thermal conductivity, angle resolved photoemission spectroscopy (ARPES) and many more. We will not review these in detail as the literature is already rich and is much beyond the scope of this section.

We will now turn our attention to $NbSe_2$ where there is an increasing body of evidence in favor of MBSC. We will also briefly address the two conditions to obtain MBSC to see that they may be satisfied.

6.2 $NbSe_2$

$NbSe_2$ is a well characterized s-wave superconductor with a relatively high transition temperature $T_c \simeq 7$ K. It is an extreme type II superconductor with $H_{c2} \simeq 4$ T for $H \parallel c$ (and $\kappa = \lambda(0)/\xi(0)$ is between 5 and 30 as measured by μSR [191] such that $\kappa \gg 1$). After reviewing its properties, we will present the case for MBSC in $NbSe_2$.

6.2.1 Crystal structure

$NbSe_2$ is a layered material with a hexagonal crystal lattice (see Fig. 6.2a) and parameters $a = 3.45$ Å and $c = 12.54$ Å. The layers are weakly coupled via van der Waals interactions which leads to crystals that are easily cleaved in the c direction. This structural property has been a key feature in the study of $NbSe_2$ as it gives the possibility of obtaining clean and atomically flat surfaces. Because of this, several powerful surface probes such as STS and ARPES have been applied successfully.

6.2.2 Normal state properties

$NbSe_2$ is a quasi-2D metal which is seen to display a transition to a charge density wave (CDW) state around $T \simeq 35$ K. The resistivity is strongly anisotropic with a ratio of the in-plane to out-of-plane resistivity ρ_{ab}/ρ_c around 30 from room temperature to 80 K [193]. At low temperatures, the anisotropy of the ideal resistivity decreases to a factor of 10 although the residual resistivity for the same crystals give $\rho_{0c}/\rho_{0ab} \simeq 500/10 = 50$ [193]. The effective mass is nine times smaller in the plane than in the c direction [194]. Its Fermi surface has been measured at low temperatures by both the de Haas-van Alphen effect (dHvA) [192] and ARPES measurements [183]. These agree with band structure calculations which derive a Fermi surface made of a number of sheets (4 or 5), shown

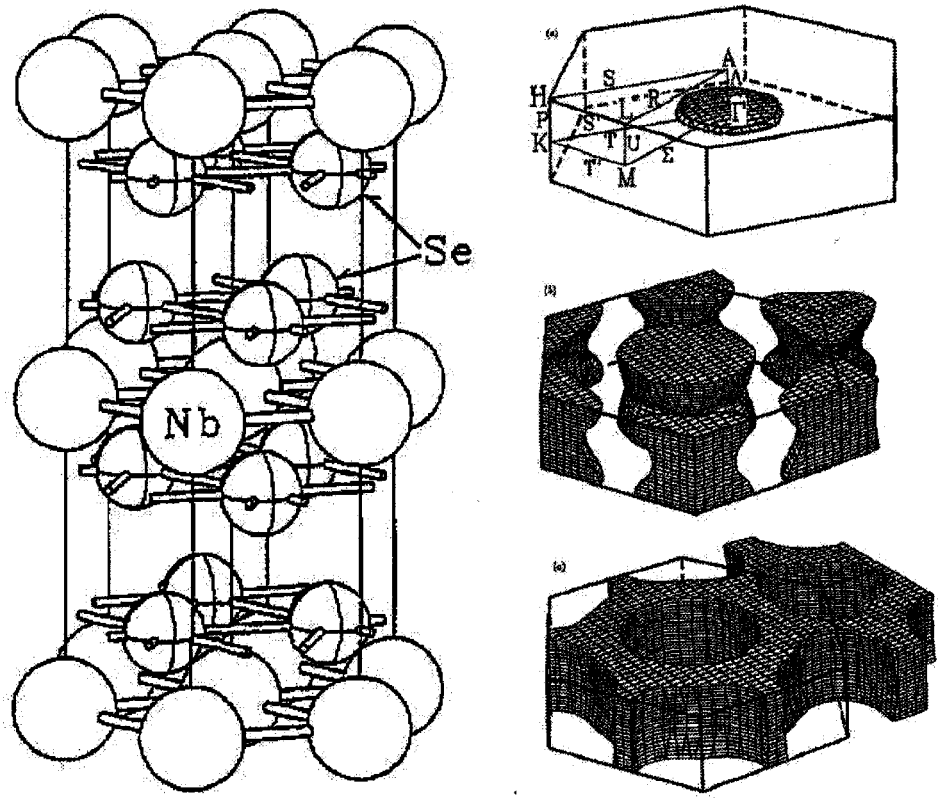

(a) (b)

Figure 6.2: (a) The crystal structure of $NbSe_2$ is layered and hexagonal with lattice parameters $a = 3.45$ Å and $c = 12.54$ Å. (b) The three Fermi surface sheets of $NbSe_2$ as derived from band structure calculation [192]. At the top is a Se $4p$ derived Γ centered pocket which has a more 3D nature than two other highly 2D Nb $4p$ derived sheets.

in Fig. 6.2b. These sheets divide into two groups: a small Γ-centered pocket derived from the Se $4p$ band (denoted as Γ band from now on) and larger more two-dimensional sheets derived from Nb $3d$ bands. The average density of states at the Fermi level is calculated to be $N(E_F) = 2.85$ states/eV/Nb $= 2.71 \times 10^{22}$ states/eV/cm^3 [192] and the average Fermi velocity is $v_F \simeq 1.5 \times 10^7$ cm/s [114]. This leads to a calculated electronic specific heat of $\gamma = 6.7$ mJ mole^{-1} K^{-2} which should be compared to measured values of $\gamma \simeq 18$ mJ mole^{-1} K^{-2} [195, 191, 154]. The Debye temperature derived from heat capacity is $\Theta_D = 230$ K [195].

The resistivity is roughly linear at high temperature and reaches a behavior close to $\rho(T) = \rho_0 + bT^3$ for temperatures below 20 K (see [196] for example). This temperature dependence can be understood in terms of electron-phonon scattering [197]. $\rho(T)$ displays

	T_c	$H_{c2\parallel}$	$H_{c2\perp}$	H_{c1}	$\xi_\parallel(0)$	$\xi_\perp(0)$	$\lambda(0)$
$NbSe_2$	7.2 K	4 T	11-12 T	20-25 mT	85 Å	55-60 Å	1400 Å

Table 6.1: Superconducting parameters for $NbSe_2$ taken from the literature. The upper critical fields are obtained from H_{c2} and $\lambda(0)$ from muon spin resonance [199].

the signature of a CDW at $T \simeq 35$ K: in the case where the FS is fully gapped in the CDW state, one should observe localization of the carriers. Here, the gap is incomplete and the resistivity only has a small bump (see Fig. 6.3a). The residual resistivity can give a good estimate of the mean free path. We obtain $\rho_0 l = 2300$ $\mu\Omega$ cm Å using the relation $\rho_0 l = \frac{3}{2e^2 N(E_F) v_F}$ and the values above [1].

6.2.3 Superconducting state properties

The superconducting properties are also anisotropic. For example, the upper critical field has a three-fold anisotropy [198, 194] for a field applied perpendicular or parallel to the plane. Values from the literature are presented in Table 6.1.

The BCS coherence length is another significant parameter for the vortex state. It is usually compared to the mean free path of a sample to know whether it is in the clean or dirty limit. This has been done by Prober *et al.* [194] and by Takita and Masuda [200] with samples of similar quality. They both obtain $\xi_0/l = 0.15$ which places the sample in the clean limit.

$NbSe_2$ is an *s*-wave superconductor in the sense that the FS is fully gapped, and the pairing mechanism is most likely mediated by phonons. This has lead many authors to believe that its superconducting gap was uniform and isotropic. Instead, we will show that there is now much evidence for the occurrence of MBSC and that $NbSe_2$ has a small gap on the Γ-pocket and a BCS-type one on the rest of the FS.

6.3 The case for MBSC in $NbSe_2$

In the past ten years or so, there have been several unusual reports in $NbSe_2$. STS studies at 50 mK resolves a density of states which departs from zero near 0.7 meV but has superconducting peaks near 1.4 meV (see Fig. 6.10) which indicates some level of

[1] Note that using the relation $\rho_0 l = \frac{3L_0}{\gamma v_F}$ gives a similar value of $\rho_0 l = 1700$ $\mu\Omega$ cm Å.

gap variation (1991). The vortex core radius was measured to change as a function of magnetic field [199] and temperature [201] (1997). The magnetic field dependence of the heat capacity was found to have a low field anomaly [191, 154, 195] reminiscent of the $\sqrt{H}$ behavior found in d-wave superconductors (1995). dHvA oscillations were found to persist deep in the superconducting state with an unusually small additional damping [114, 116] (1994). In 2002, ARPES measurements showed direct evidence for MBSC in $NbSe_2$ [183]. We were able to confirm this claim by thermal transport measurements in the vortex state at low temperature [55] (2003). This new evidence and interpretation gives a natural way of understanding the prior unusual behavior reported.

We will review these reports and explain them in the context of MBSC, starting with the heat transport through the vortex state. This will also lead us to speculate on the origin of this peculiar form of superconductivity in $NbSe_2$.

6.3.1 Thermal conductivity and specific heat in the vortex state

We have studied the thermal conductivity of $NbSe_2$ at very low temperatures throughout the vortex state. By measuring the degree of delocalization of quasiparticle states in the vortex state, heat transport probes the overlap between core states on adjacent vortices, *i.e.* the size of the vortex core ($\sim \xi$), and hence the magnitude of the gap ($\sim 1/\xi$). We resolve two regimes of behavior: one limited to very low fields (up to $\sim 5H_{c1}$), where delocalization is slow and activated as in conventional (single-gap) superconductors like V_3Si, and one for all other fields up to H_{c2} where quasiparticles transport heat extremely well, as in unconventional superconductors with nodes in the gap. Note that in the case of $NbSe_2$ the absence of any residual linear term in the thermal conductivity confirms that there are no nodes in the gap.

Experimental details

The sample is from the same batch as the one used by Sonier *et al.* [191, 199, 201] and had a superconducting transition temperature $T_c = 7.0$ K with a width $\delta T_c = 0.1$ K (see Fig. 6.3a). The residual resistivity ratio is 40, with $\rho_0 \simeq 3\ \mu\Omega$ cm from an extrapolation to $T \to 0$ of the form $\rho = \rho_0 + bT^3$ (with $b = 3.1 \times 10^{-4} \mu\Omega$ cm K^{-3}). This dependence describes the sample well for $T < 20$ K (see Fig. 6.3a). The upper and lower critical fields are respectively $H_{c2} = 4.5$ T and $H_{c1} = 20$ mT for $H \parallel c$. H_{c1} was determined from the scattering of phonons by vortices at $T = 900$ mK (see Fig. 6.6c). As discussed

above, the sample is in the clean limit with a ratio of the BCS coherence length ξ_0 to the mean free path l in the plane being $\xi_0/l \simeq 0.15$ [194, 200].

The crystals were grown by a standard vapor transport technique [202] and the sample was a rectangular parallelepiped with dimensions 1.2 × 0.5 mm in the plane, and 0.1 mm along the c-axis. It was cut with a razor blade and the top layers were cleaved by applying and removing tape on these surfaces to provide six fresh surfaces for contacts. These where made shortly after with Dupont 4929N silver paint to give contact resistances of roughly 20 mΩ at low temperatures. For the thermal conductivity measurements, the sample was cooled in field to obtain a homogeneous vortex density. Measurements as a function of field at fixed temperature resulted in nearly no difference as compared to the field-cooled data (see Fig. 6.6a).

Thermal conductivity in zero field

The thermal conductivity was measured above 1 K (Fig. 6.3b). It agrees well with the WF law above T_c but decreases smoothly below. This is best seen by plotting κ/T and $L_0/\rho(T)$ (extended to below T_c) where the formation of Cooper pairs reduces the thermal conductivity below T_c. At low temperatures, κ becomes purely phononic. The absence of a phonon peak is easily understood as explained by the following scenario. The phonons have two relevant channels of scattering: electrons and crystal boundaries. Above T_c, electronic scattering dominates. Below T_c, this channel is reduced steadily to zero as Cooper pairs are formed which usually leads to an enhanced κ. However, it will only increase until the mean free path reaches the crystal dimensions, leading to an ultimate decrease of κ. From this, a phonon peak is sometimes observed. In this case, the same mechanism is at play, only the phonon peak is much smaller than the remaining electronic contribution (unpaired electrons) due to the lower T_c of $NbSe_2$. It is therefore not observed.

At low temperatures, κ is purely phononic and has a temperature dependence close to T^3 (see Fig. 6.4). We can place an upper value on the electronic contribution of $\kappa/T = 0.000 \pm 0.003$ mWK^{-2} cm^{-1} by fitting the data with $\kappa/T = a + bT^2$. This should be contrasted to the value in the normal state ($\kappa_N/T \simeq 8.2$ mW K^{-2} cm^{-1}) and to the expected value for a gap with nodes (for example, a d-wave gap) which is 0.55 mW K^{-2} cm^{-1} [1], both orders of magnitude larger than our upper limit.

[1] For a d-wave superconductor in 2D, we have $\kappa_{00}/T = \frac{k_B^2}{3\hbar}\left(\frac{n}{d}\right)\left(\frac{v_F}{v_2} + \frac{v_2}{v_F}\right)$ [85]. We use the fact that

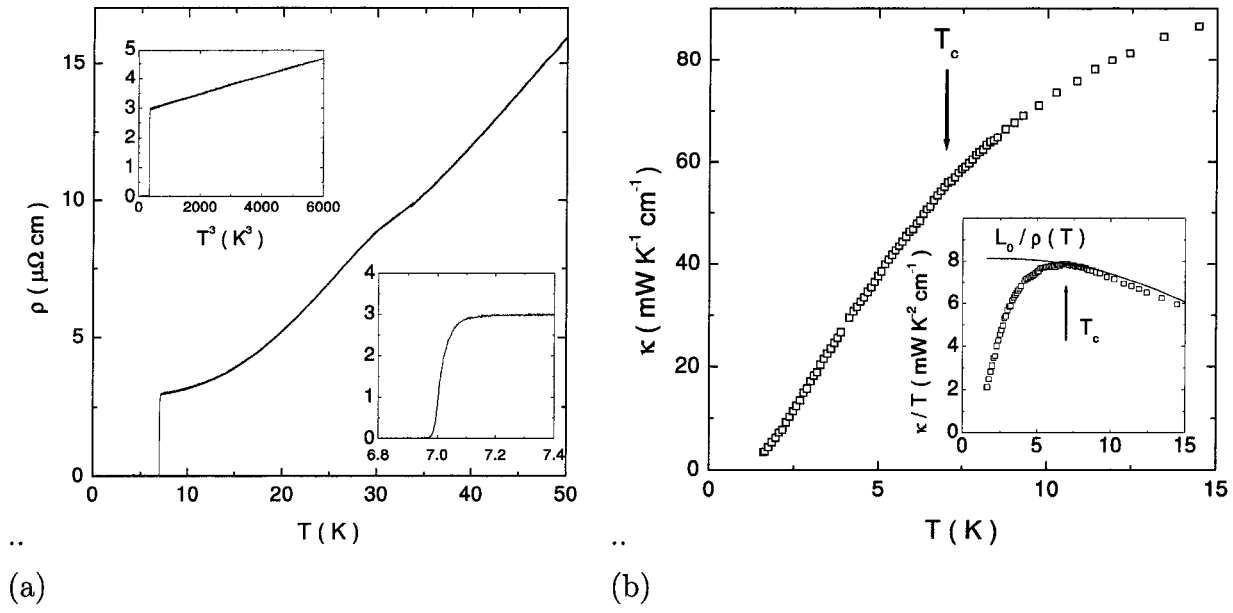

Figure 6.3: (a) The resistivity of $NbSe_2$ as a function of temperature. Charge density wave order is seen to onset near $T = 35$ K. Below $T = 20$ K, the resistivity has the form $\rho = \rho_0 + bT^3$ (inset). This sample has a sharp superconducting transition with $T_c = 7.0$ K and $\delta T_c = 0.1$ K. (b) The thermal conductivity of $NbSe_2$ above 1 K plotted as κ and as κ/T (inset). The latter shows the resistivity (dark line) plotted as $L_0/\rho(T)$ extended to below T_c using $\rho = \rho_0 + bT^3$. κ/T agrees well with the WF above T_c and is reduced in the superconducting state by the formation of Cooper pairs. (Note that the measured thermal conductivity was multiplied by a small factor (0.93) to agree perfectly with the WF law at T_c. This small discrepancy may be due to our experimental accuracy which can overestimate the thermal conductivity by this amount as seen in Fig. 3.14a).

Instead, let us estimate what the expected phononic contribution should be in the limit of boundary scattering. We use equation 2.22 with a mean diameter of $d \simeq 2\sqrt{w \times t/\pi} = 0.024$ cm and a phonon velocity of $v_{ph} = 3.7 \times 10^5$ cm/s as reported in the plane for $NbSe_2$ [203]. This predicts $\kappa_{ph}/T^3 = 7.2$ mW K^{-4} cm^{-1} and is in good agreement with our results which finds 4.0 mW K^{-4} cm^{-1}.

In conclusion, the thermal conductivity at low temperature and in zero field is purely phononic for $NbSe_2$. This is a clear indication that the FS is fully gapped and has no nodes.

$\hbar k_F v_2 = \Delta_0/2$ and $\hbar k_F = m^* v_F$ to obtain $\kappa_{00}/T = \frac{2k_B^2}{3\hbar}\left(\frac{n}{d}\right)\left(\frac{m^* v_F^2}{\Delta_0}\right)$. Using $d = 12.54$ Å, $n = 1$, m^* as the electron mass, $v_F = 1.5 \times 10^7$cm/s and $\Delta_0 = 1.1$ meV, we get $\kappa_{00}/T \simeq 0.55$ mW K^{-2} cm^{-1}

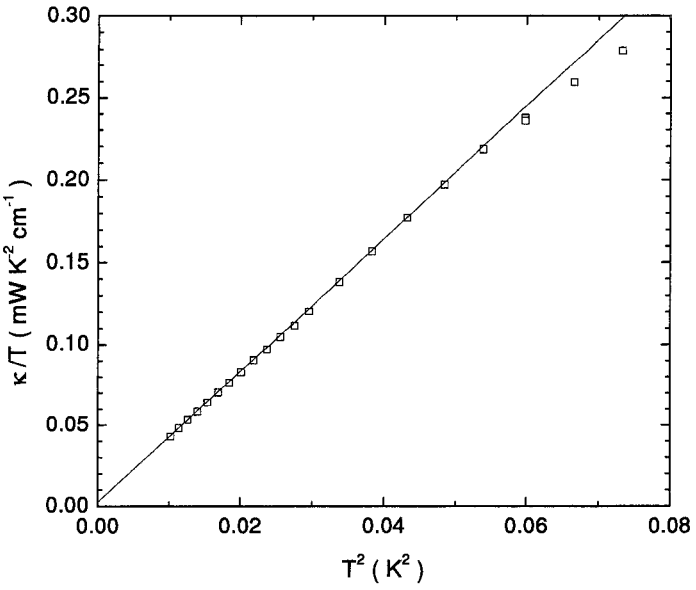

Figure 6.4: Thermal conductivity of $NbSe_2$ in zero field and at low temperature. The data is plotted as κ/T against T^2. The linear term is extracted to be $\kappa_e/T = 0.000 \pm 0.003$ mW K^{-2} cm^{-1} and the phononic term is $b = 4.0$ mW K^{-4} cm^{-1}. κ_e/T zero within our error bars, a clear indication of a fully gapped FS. The phononic contribution agrees quantitatively with the theoretical prediction for boundary limited scattering.

Thermal conductivity through the vortex state

In zero field, we saw that the thermal conductivity is purely phononic. We now turn to the behavior in a magnetic field to see the growth of the electronic thermal conductivity through the vortex state.

The thermal conductivity of $NbSe_2$ is plotted in Fig. 6.5, as κ/T against T^2. This enables a separation of the electronic and the phononic thermal conductivities, since the asymptotic T dependence of the former as $T \rightarrow 0$ is linear while that of the latter is cubic. The electronic thermal conductivity κ_0/T is thus obtained as the extrapolated $T \rightarrow 0$ value. We saw above that in zero field, $\kappa_0/T = 0.000 \pm 0.003$ mW K^{-2} cm^{-1}, and the thermal conductivity is purely phononic. However, by applying a small magnetic field ($H \geq H_{c1}$), an electronic contribution develops as a rigid shift from the $H = 0$ curve in Fig. 6.5. At higher fields ($H \geq 1.5$ T), the electronic contribution dominates the conduction over the entire temperature range and κ/T is constant in temperature within our experimental resolution. Above H_{c2}, the Wiedemann-Franz (WF) law is satisfied and the thermal conductivity saturates. Note that for $H = 4.5$ T, the residual resistivity is

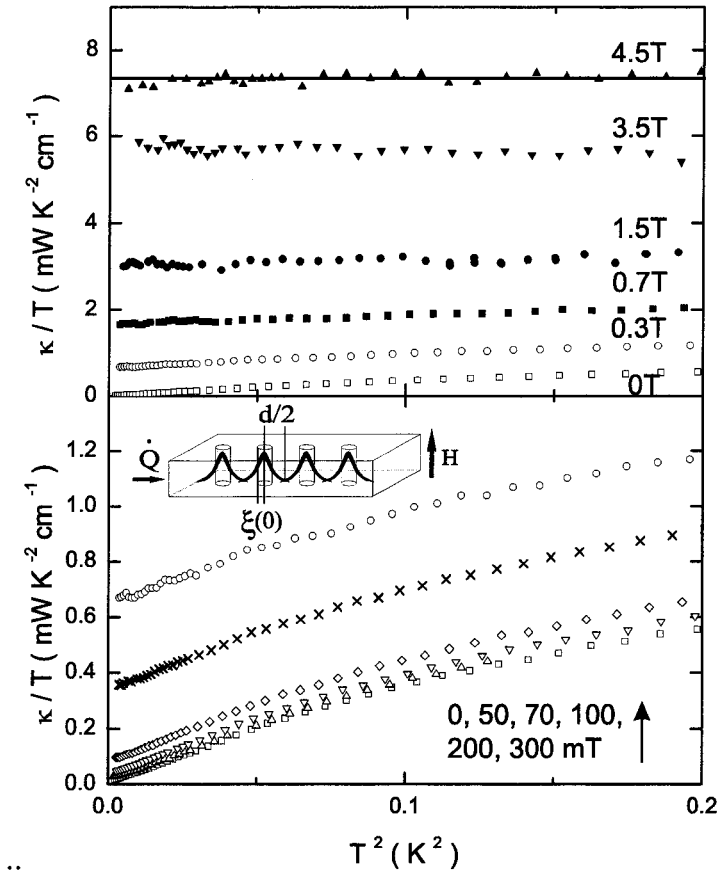

Figure 6.5: Thermal conductivity of $NbSe_2$ at several applied fields, plotted as κ/T vs T^2. The solid line indicates the value expected from the Wiedemann-Franz law as obtained from resistivity measurements at $H = 4.5$ T. The field is applied parallel to the c-axis and perpendicular to the heat current $\dot{Q}$.

measured to be $\rho_0(H = 4.5\ \text{T}) = 3.34\ \mu\Omega$ cm.

The κ_0/T values are plotted as a function of H on a reduced scale in Fig. 6.6. Also plotted is a field sweep at $T = 130$ mK from which the zero-field value (the phononic contribution) has been subtracted. As seen in Fig. 6.6c, heat conduction starts to increase right at H_{c1} in what could be qualified as an activated behavior, although in a very limited range of fields: $H_{c1} \leq H \leq 0.03 H_{c2}$. (The value of H_{c1} is determined in situ as the drop in the phonon κ due to vortex scattering as shown in Fig. 6.6c.) At higher fields, κ_0/T increases rapidly, *i.e.* faster than $(H/H_{c2})\ \kappa_N/T$, where κ_N/T is the normal state value. This shows the presence of *highly delocalized quasiparticle states almost throughout the vortex state of $NbSe_2$*.

This is in stark contrast to the behavior expected of a type-II s-wave superconductor.

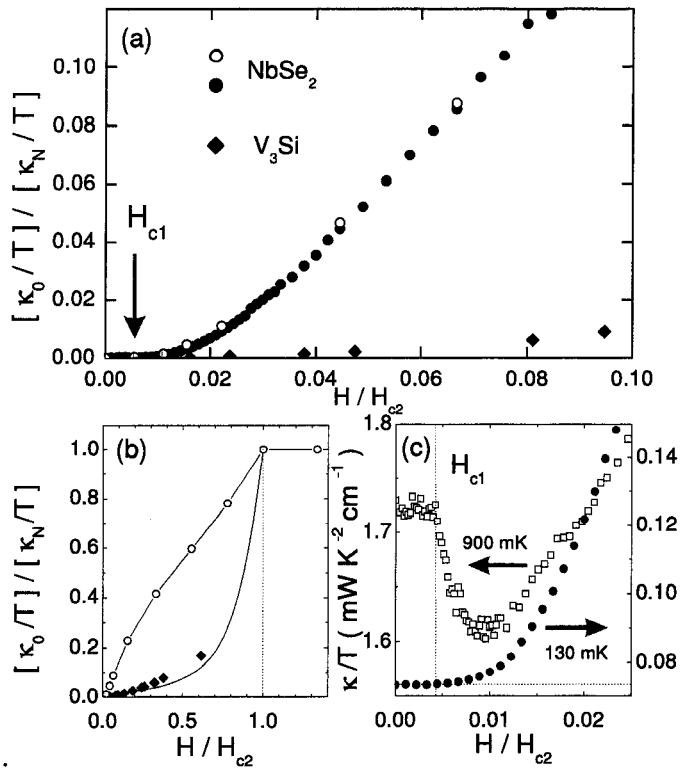

Figure 6.6: (a,b) Thermal conductivity of $NbSe_2$ (empty circles) and V_3Si (diamonds) at $T \to 0$ vs H, normalized to values at H_{c2}. Filled circles come from a sweep in field at $T = 130$ mK from which the $H = 0$ thermal conductivity (phononic contribution) has been subtracted. The thick solid line in (b) is a theoretical curve for the thermal conductivity of V_3Si [72]. The thin line is a guide to the eye. (c) κ/T vs H for $NbSe_2$ at $T = 130$ mK (circles) and $T = 900$ mK (squares). The latter shows a typical drop in the phononic thermal conductivity at $H_{c1} = 20$ mT. The former shows that the electronic thermal conductivity starts to increase right at H_{c1} but has a slow activated-like behavior for fields below $0.03\ H_{c2}$.

Indeed, when a field in excess of H_{c1} is applied, and vortices enter the sample, the conventional picture is that the induced electronic states are *localized* within the vortex cores. As one increases the field, the intervortex spacing $d \simeq \sqrt{\Phi_0/B}$ decreases. The localized states in adjacent vortices will have an increasing overlap leading to enhanced tunneling between vortices, and the formation of conduction bands. Strictly speaking, the electronic states are actually always delocalized but with extremely flat bands at low fields [67, 68]. As these gradually become more dispersive, the thermal conductivity should increase accordingly and grow exponentially with the ratio $d/2\xi$, as is indeed observed in Nb [164] and V_3Si (see Chapter 4) at low fields.

In fact, V_3Si is a good point of comparison for $NbSe_2$. It is an extreme type-II superconductor with comparable superconducting parameters (T_c = 17 K, ξ = 50 Å). This is done in Fig. 6.6, where the thermal conductivity of V_3Si is seen to grow much more slowly with H than that of $NbSe_2$, as described by theory [72]. Quantitatively, at $H = H_{c2}/20$, $\kappa_0/T = \frac{1}{20} \times \kappa_N/T$ for $NbSe_2$ and $\frac{1}{400} \times \kappa_N/T$ for V_3Si (see Chapter 4). Note that the samples compared in Fig. 6.6 are in the same regime of purity. From the standard relation $\xi(0) = 0.74\xi_0[\chi(0.88\xi_0/l)]^{1/2}$, we obtain for V_3Si $\xi_0/l = 0.13$, with $\xi(0)$ = 50 Å from H_{c2} and l = 1500 Å from dHvA [116]. This is similar to the value of 0.15 for $NbSe_2$ [200, 194]. Our results are consistent with dHvA measurements [116, 114]: while extended quasiparticles are seen deep into the vortex state in both $NbSe_2$ and V_3Si, the additional damping attributed to the superconducting gap below H_{c2} increases more slowly in $NbSe_2$.

The high level of delocalization in $NbSe_2$ is a clear indication of either a gap with nodes (*e.g. d*-wave) or a nodeless gap which is either highly anisotropic or small on one FS and large on another. A gap with nodes is ruled out by the absence of a residual term in the thermal conductivity in zero field [81].

It is revealing to compare $NbSe_2$ to MgB_2, for which the thermal conductivity has a similar field dependence. Strikingly, κ follows roughly the same field dependence as the specific heat C for both $NbSe_2$ and MgB_2. This is shown in Fig. 6.7 where $\kappa(H)$ and $C(H)$, are plotted on a reduced field scale for single crystals of $NbSe_2$ [191, 154], MgB_2 [99, 189], and V_3Si [122, 113], with $H||c$ for hexagonal $NbSe_2$ and MgB_2, and $H||a$ for cubic V_3Si. In conventional superconductors like V_3Si, $\kappa(H)$ and $C(H)$ are very different (see Fig. 6.7c) because the excited electronic states are largely localized.

MgB_2 is a well established case of MBSC with a small gap on one FS (Δ_π = 1.8 meV) and a large gap on the other (Δ_σ = 6.8 meV). The field dependence of its heat capacity is well understood in this context [189], with a distinctive shoulder at a field of $H_{c2}/10$ (see Fig. 6.7b) [1]. A similar shoulder is also manifest in $NbSe_2$ around $H_{c2}/9$ (see Fig. 6.7a). Empirically, the striking fact that heat transport and heat capacity have the same field dependence in both materials points to a common explanation, and hence suggests that *$NbSe_2$ is host to multi-band superconductivity* [2]. This is consistent with recent ARPES

[1] A similar shoulder was observed in Sr_2RuO_4 [186], possibly host to *unconventional* MBSC [187].

[2] It should be noted that having such a similar behavior of the thermal conductivity and the specific heat is not what is expected theoretically for either a MBSC or a superconductor with an anisotropic gap in the case of superconductors in the clean regime (relevant for our crystals) as suggested by calculations of Kusunose *et al.* [71].

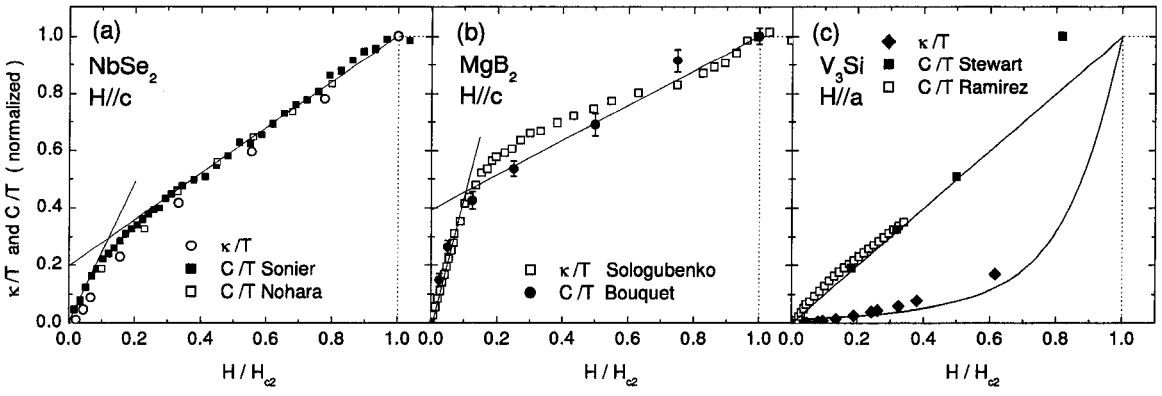

Figure 6.7: (a) Thermal conductivity and heat capacity of $NbSe_2$ normalized to the normal state value vs H/H_{c2}. The heat capacity was measured in two different ways: i) at $T = 2.4$ K on the same crystals as used in this study [191], and ii) extrapolated to $T \to 0$ from various temperature sweeps on different crystals [153]. (b) Equivalent data for MgB_2 single crystals [99, 189]. (c) Equivalent data for V_3Si, with a theoretical curve for κ/T [72]. The specific heat is measured at $T = 3.5$ K [122] and extrapolated to $T = 0$ [113]. The straight line is a linear fit. The thermal conductivity is seen to follow the specific heat very closely for both $NbSe_2$ and the multiband superconductor MgB_2. It does not, however, for the conventional s-wave superconductor V_3Si.

measurements at $T = 0.8\ T_c$ [183].

In conventional superconductors, the delocalization of vortex core bound states occurs gradually on the scale of H_{c2}, and the characteristic length scale is $\xi(0) \simeq \sqrt{\Phi_0/2\pi H_{c2}}$. It appears that in $NbSe_2$ (and MgB_2), there are two characteristic length scales for delocalization: ξ^* and $\xi(0)$. To see this, we focus on the low field region. For $NbSe_2$, both κ/T and C/T have been measured with high precision on the same crystals, thereby making a detailed comparison possible. Fig. 6.8a shows the comparison for fields below $H_{c2}/10$, where the two do not coincide: C/T increases abruptly above H_{c1} while κ/T grows slowly, in an activated way. This is consistent with the presence of localized states at very low fields as imaged by STS (see Fig. 1.6) [18, 204, 205]. Then this behavior gives way to a rapid increase of the thermal conductivity at fields above $0.03\ H_{c2}$. This is a clear indication that the field scale associated with delocalization in $NbSe_2$ is much smaller than H_{c2}.

In fact, we can scale the behavior of the low-field thermal conductivity of $NbSe_2$ to that of V_3Si using $H^* \simeq H_{c2}/7$ (Fig. 6.8b). This is also seen clearly if we plot the

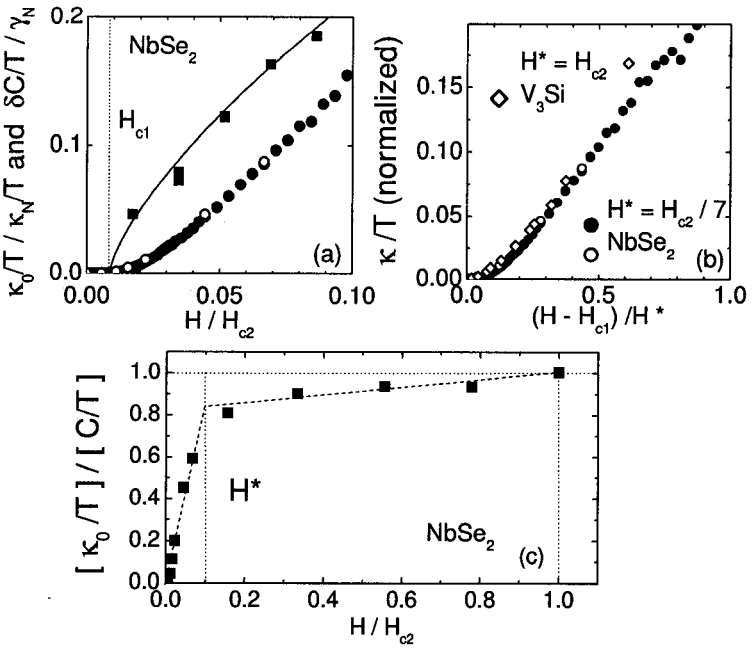

Figure 6.8: (a) Thermal conductivity (circles) and the field evolution of the heat capacity $\delta C/T = [C(T,H) - C(T,H=0)]/T$ (squares) [191] of $NbSe_2$ normalized to the normal state values vs H/H_{c2} at very low fields. The line is a guide to the eye. (b) Normalized thermal conductivity vs $(H - H_{c1})/H^*$ for $NbSe_2$ and V_3Si with $H^* = H_{c2}/7$ and H_{c2} respectively. (c) Ratio of heat transport to heat capacity in $NbSe_2$. This is a measure of the degree of delocalization.

ratio of the thermal conductivity to the specific heat (Fig. 6.8c) which measures the degree of delocalization. The ratio is seen to have two regimes: a rapid increase below $H^* \simeq H_{c2}/9$ and a slow one above. In summary, the second length scale associated with delocalization in $NbSe_2$ is $\xi^* \simeq \xi(0)/\sqrt{9} = \xi(0)/3$. This may explain naturally the shrinking of the vortex cores observed with muon spin rotation [199, 191].

Considering the fact that the upper critical field is related to the superconducting gap by $H_{c2} \propto \Delta^2/v_F^2$ where v_F is the Fermi velocity, we estimate the gap to vary over the FS by a factor of 3 ($\Delta^* \simeq \Delta_0/3$). (Note that we assume v_F to be constant, within the direction of the *ab*-plane, as found by band structure calculations [192]). This value is consistent with other observations as will be discussed in the next section.

In summary,me asurements of heat transport in the vortex state of $NbSe_2$ at low temperatures reveal the existence of highly delocalized quasiparticles down to fields close to H_{c1}. This is in striking contrast with what is expected in a *s*-wave superconductor where

well-separated vortices should support only localized states, as is observed in V_3Si. We identify two characteristic length scales that govern the destruction of superconductivity in $NbSe_2$: the usual one associated with H_{c2} and another associated with a much smaller field $H^* \simeq H_{c2}/9$. We attribute this to multi-band superconductivity, whereby the gap on the pocket-like Γ band is approximately 3 times smaller than the gap on the other two Fermi surfaces.

6.3.2 Other evidence

$NbSe_2$ has been characterized in a number of ways. Recent direct evidence for MBSC has emerged from high precision ARPES measurements [183]. This new viewpoint, which constitutes a true change of paradigm, has turned a number of anomalous reports into an impressive body of evidence in favor of the case for MBSC in $NbSe_2$. We will review these reports from this perspective.

ARPES

$NbSe_2$ has been a very good candidate for ARPES studies since one can obtain very clean surfaces by cleaving (see for example [206]). However, the superconducting state has not been studied for two main reasons: 1/ the low T_c which is close to the typical base temperature of an ARPES setup ($\sim 6-7$ K) and 2/ the low value of the superconducting gap ($\sim$ 1 meV) which is also near the resolution of current ARPES measurements. Nevertheless, Yokoya and co-workers have been able to perform high resolution ARPES measurements in the superconducting state of $NbSe_2$, albeit at T= 5.3 K $\simeq$ 0.75 T_c [183].

After having successfully mapped the FS of $NbSe_2$ which is consistent with calculations [192], the spectral function was measured on different Fermi surfaces near the Fermi energy both in the normal and superconducting state. These are shown on Fig. 6.9. Below T_c, a superconducting gap opens on the two large FS and the typical coherence peaks are seen. The gap is measured to be 1.0±0.1 meV and 0.9±0.1 meV at $T = 5.3$ K for both bands giving gap of 1.22 and 1.13 meV at $T = 0$ using the BCS temperature dependence. This is in reasonable agreement with the weak-coupling BCS prediction which predicts $\Delta(0) = 1.76\ k_B T_c = 1.09$ meV. The Γ-band shows no such behavior and although no gap is actually resolved, the experimental precision imposes a limit of $\Delta \leq 0.2 \pm 0.1$ meV.

Such momentum and energy resolved results represent conclusive evidence for MBSC

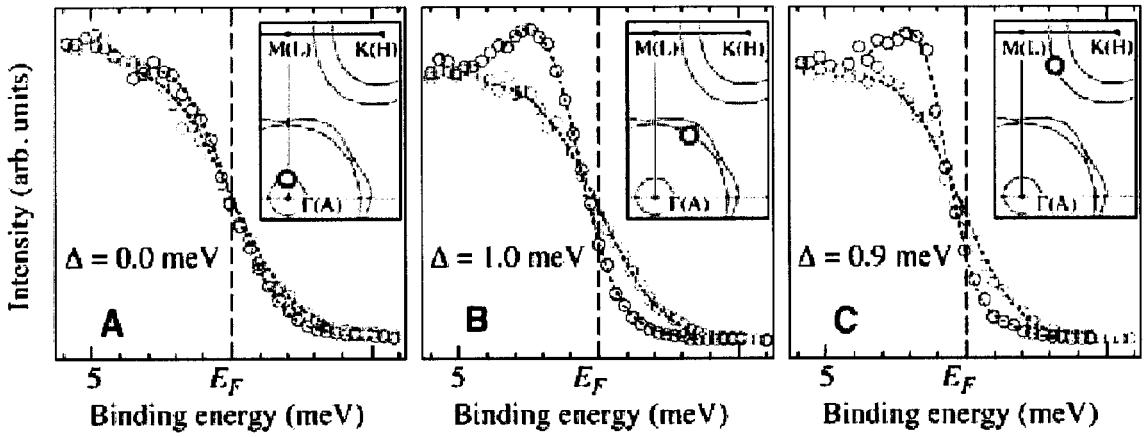

Figure 6.9: ARPES spectra for $NbSe_2$ on different Fermi surfaces (see the red circles in each inset) taken above (red) and below (blue) T_c (at 10 and 5.3 K respectively). For the large FS, the typical superconducting coherence peak is seen and an energy gap is clearly resolved. On the Γ-band, there is no evidence for either a superconducting peak nor an energy gap. The resolution of the experiment allows to give an upper value of $\Delta \leq 0.2 \pm 0.1$ meV for this band.

in NbSe2. However, this study was only made at temperatures close to T_c. ARPES is also a surface probe and may be scrutinized as not necessarily being representative of the bulk behavior. In this sense, our thermal conductivity measurements complemented this study well by providing bulk measurements at very low temperatures [162]. What's more, it may be of importance to remember that the Γ-band is calculated to be substantially dispersive in the c-direction [192]. This leads to complications for ARPES measurements which assume perfectly 2D electronic properties of the conduction bands.

ARPES measurements present clear and direct evidence for MBSC in $NbSe_2$. Bulk studies at low temperatures such as κ measurements support and complement these findings.

Scanning Tunneling Spectroscopy

Scanning tunneling spectroscopy (STS) has also been used extensively to study $NbSe_2$ thanks to its easily available clean surfaces [18, 204, 205]. In fact, STS was first successfully used to probe superconductivity in $NbSe_2$. Hess and co-workers have been able to measure the superconducting gap and to image bound states in vortices at low vortex densities. Both studies lead to the conclusion of an average gap which is not uniform.

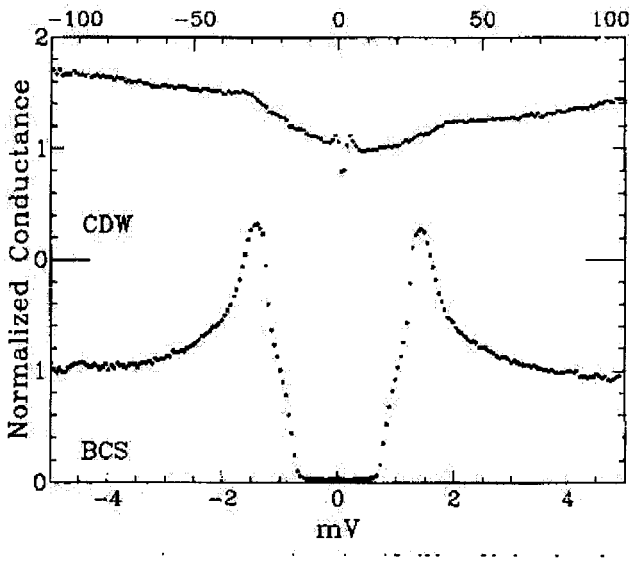

Figure 6.10: The tunneling spectra of $NbSe_2$ at $T = 50$ mK [205]. It is consistent with a distribution of gaps ranging from 0.7 meV to 1.4 meV.

The density of states was imaged with high precision and at very low temperatures (50 mK) as shown in Fig. 6.10 [205]. It is zero below energies of 0.7 meV consistent with a superconducting gap without nodes. However, the coherence peaks are located at a much higher energy of 1.4 meV. This is consistent with a distribution of gaps which differs by a factor of at least two (in reasonable agreement with our assessment of a factor of three difference between the small and large gap). Notably also, there is no evidence of a second set of coherence peaks below the gap maximum as observed in MgB_2. However, STS probes parts of the FS differently as evident in MgB_2 for example. There, STS along the planes or along the c-axis coupled very differently to the π and the σ bands [184, 185]. This may account for these small discrepancies.

What's more, the imaging of the vortex cores have revealed very rich behavior both in energy and space (distance away from the core) [204, 205] as reviewed in [21]. After much theoretical work, Hayashi and co-workers have been able to identify the single source which was able to reproduce this behavior, namely, an anisotropy of the gap [21]. In fact, they used a gap anisotropy of a factor of three to reproduce the experimental results.

STS studies are seen to be consistent with MBSC in $NbSe_2$ both by measuring the gap function directly and indirectly since theoretical modelling of the spectra in a magnetic

field require a gap anisotropy of order 3. Further studies may be performed to distinguish between an anisotropic gap and MBSC by tunneling from a different directions than the c-axis (as was done in MgB_2) and looking for a second set of superconducting coherence peaks.

Heat capacity

ARPES and STS are both surface probes and lead one to ask if bulk properties also provide supporting evidence for MBSC in $NbSe_2$. This is indeed the case as both the temperature and field dependence and, to a lesser extent, the effect of disorder lead to the same conclusion.

The temperature dependence of the electronic specific heat was carefully studied by Sanchez *et al.* [195]. It was seen to deviate from the simple BCS behavior and be better fit by a model which assumes a gap anisotropy of a factor of 2.5 (see Fig. 6.11a,b).

In the vortex state, the specific heat is seen to have a low field anomaly in the sense that it deviated from a linear behavior expected for s-wave superconductors. It has been related to the shrinking of the vortex cores [191]. It was already shown above to be easily understandable in terms of MBSC in the same way as in MgB_2(see Fig. 6.7).

It is also interesting to note that MBSC requires a very small coupling or interband scattering between the different FS. This coupling is predicted to be increased with disorder due to increased inter-band scattering, and thus induce the usual BCS gap onto the intrinsically decoupled band (or bands). This seems to be the case for $NbSe_2$ where the field dependence of the specific heat is seen to recover a linear behavior with increased disorder as seen in Fig. 6.11c [154].

Finally, one of the sources of MBSC may come from significantly different electron-phonon coupling λ on different bands. This was recently beautifully resolved with dHvA measurements on the different sheets of MgB_2 where λ was found to be much smaller on the π-band ($\lambda_\pi = 0.47$) than on the σ-bands ($\lambda_\sigma = 1.25$ for both) [184, 185]. In $NbSe_2$, dHvA measurements have only been able to resolve the Γ-band where $\lambda = 0.3$ and cannot give a direct comparison of the different electron-phonon coupling parameter [192]. However, by comparing the measured and calculated specific heat, one obtains an average $\lambda = 1.8$, much larger than that of the Γ-band. This large difference may be the source of MBSC in $NbSe_2$ and is consistent with the idea that the superconductivity originates from the larger bands and is only induced weakly onto the Γ-band.

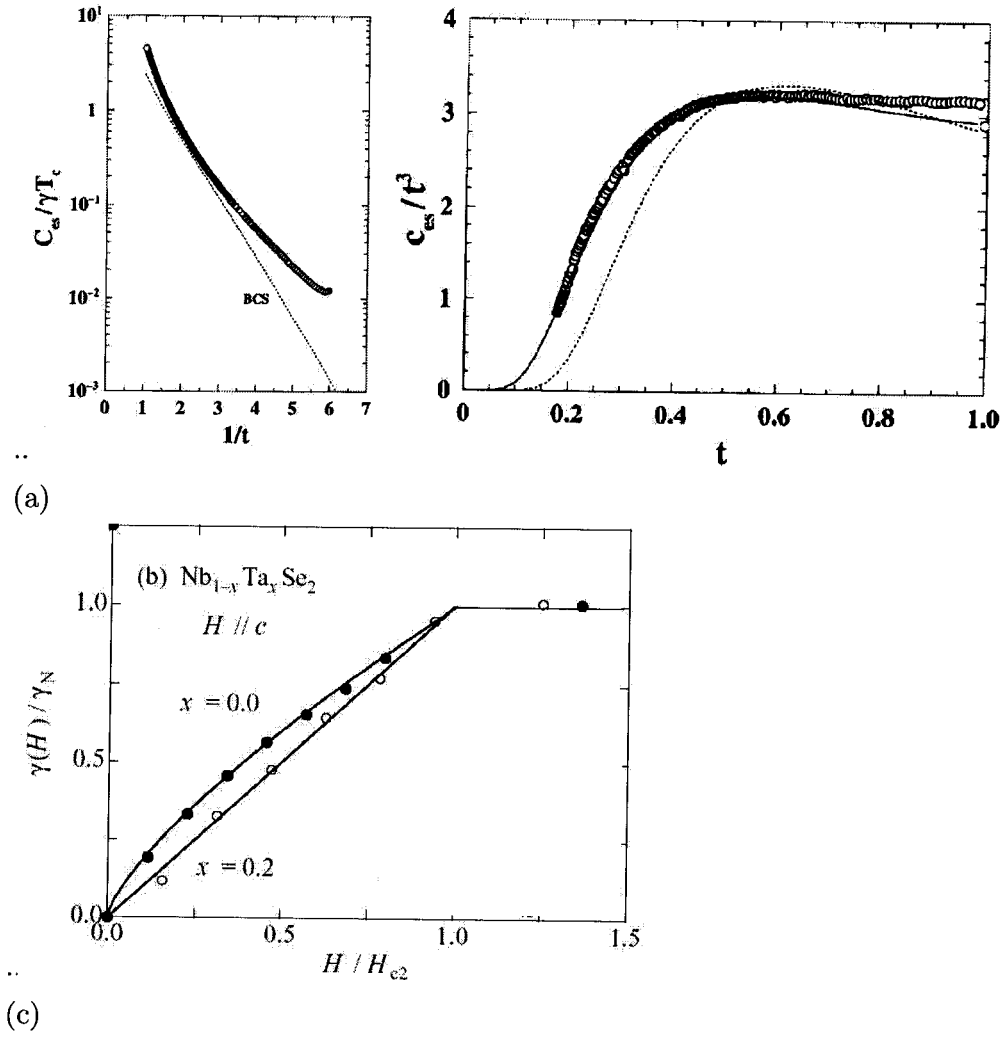

Figure 6.11: (a) The electronic specific heat of $NbSe_2$ in the superconducting state against $1/t = T_c/T$ (after [195]). It is seen to deviate from the simple BCS prediction. (b) The best fit is obtained using a model with a gap anisotropy of a factor of 2.5 (solid line). (c) The field dependence of the specific heat for $Nb_{1-x}Ta_xSe_2$wi th $x = 0.0$ and $x = 0.2$ (after [154]). The linear behavior is recovered in the dirty sample.

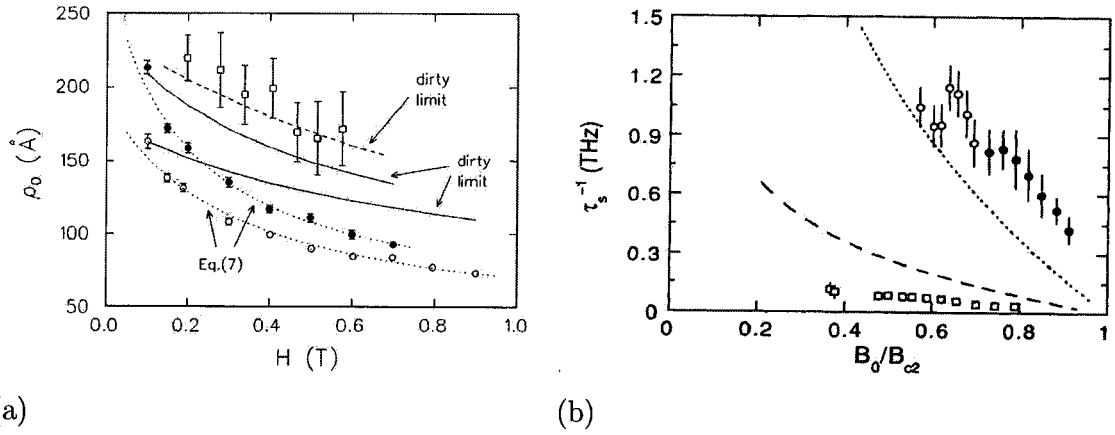

(a) (b)

Figure 6.12: (a) The vortex radius as a function of magnetic field measured by μSR at 2.3 K (empty circles) and 4.2 K (filled circles) along with that extracted from STS (squares) [199]. The shrinking of the vortex cores can be understood in the context of MBSC. (b) The additional damping extracted by dHvA measurement for both $NbSe_2$ (squares) and V_3Si (circles) plotted at the scattering rate in the superconducting state τ_s^{-1} [192]. It is seen to increase much more rapidly for V_3Si than for $NbSe_2$ which is consistentwi th thermal conductivity measurements [162] and with $NbSe_2$ displaying MBSC.

In summary, the temperature and field behavior as well as the effect of disorder of the specific heat in $NbSe_2$ are consistent with that expected for a MBSC. What's more, the average electron-phonon coupling obtained from it is much larger than that measured with dHvA on the Γ-band, a strong indication that the superconductivity originates from the larger bands.

Muon Spin Resonance

The radius of the vortex cores has always been assumed to have no magnetic field dependence. Muon spin Resonance (μSR) has provided evidence that this is not the case in $NbSe_2$ (see Fig. 6.12a) [199]. This result was highly unexpected. We now propose that this result may not be general for all superconductors but rather is a natural consequence of MBSC.

Indeed, as explained above, MBSC will lead to two "upper critical fields" associated with the two different superconducting gaps and also two different coherence lengths. An easy way to picture this is to realize that the supercurrent flow around each vortex (which decays with ξ as the characteristic length scale) will have two *decoupled* components

associated with the different sheets of the FS. This will lead to strange objects: vortices with two distinct radii. In turn, the larger radius will produce a featureless background at much smaller fields and the smaller radius will be detected as a clearer feature in the magnetic profile. This may be interpreted as shrinking vortex core radii as the field is increased, consistent with what is observed in $NbSe_2$ [199]. It remains to be seen if the μSR spectra are better fit with two vortex radii instead of one.

In this picture, the ratio of the radii will be the same as the ratio of the superconducting gaps. For $NbSe_2$, it is roughly a factor of three [162] and is also consistent with the measurements of Sonier *et al.* [199]. There, the coherence length reaches a value consistent with H_{c2} at higher fields and is a factor of 2-2.5 larger at the lowest fields reached in the experiment.

In summary, one can easily understand previous μSR studies which reported a shrinking of the vortex cores in the context of MBSC. We also obtain quantitative agreement between these results and those of thermal conductivity.

de Haas-van Alphen effect

$NbSe_2$ was the first system where dHvA oscillations were observed within the vortex state [123]. Since then, detailed studies have been performed but only to resolve one of the Fermi sheets, namely, the Γ-band [114, 192, 116] which was measured by ARPES to have a superconducting gap smaller than $\Delta \leq 0.2 \pm 0.1$ meV.

In the vortex state, dHvA oscillations have an additional damping factor attributed to the superconducting gap. This damping has the same form as an additional scattering rate which is referred to as τ_s^{-1}. It has been compared for the Γ-band of $NbSe_2$ and for V_3Si to show that the quasiparticles seem to be scattered more strongly in the latter as shown in Fig. 6.12b [114, 116]. It should be noted that the normal state scattering rates are $\tau_N^{-1} = 2.1 \times 10^{12}$ s^{-1}and $\tau_N^{-1} = 1.1 \times 10^{12}$ s^{-1}for $NbSe_2$and V_3Si respectively.

This result agrees very well with thermal conductivity results [162]. They also suggest that there may be a much smaller gap on the Γ-band of $NbSe_2$ than in V_3Si. Theoretical modelling does not lead to a straightforward understanding as reported by Janssen *et al.* [116]. There, the data for both compounds is compared to four different theoretical treatments and yield different quality fits and very different values for the superconducting gap. For each though, the reduced gap $\Delta/1.76k_BT_c$ is estimated to be smaller for $NbSe_2$tha n for V_3Si.

In conclusion, a detailed comparison of the Γ-band of $NbSe_2$ and V_3Si seem to indicate that there is a much reduced gap for $NbSe_2$i n accordance with the picture of MBSC.

6.3.3 Summary

In summary, there has been direct evidence for MBSC in $NbSe_2$ from ARPES measurements [183]. Our thermal conductivity studies confirm this to be true in the bulk and provide an estimate of a factor of three ratio between the gaps on different Fermi surfaces. Many other experimental reports such as STS, specific heat and dHvA are now seen to be consistent with this picture by reporting an anisotropy of the average gap of a factor close to three. The shrinking of the vortex cores as measured from μSR is also easily understood in this context. Finally, there is evidence that MBSC stems from a much different electron-phonon coupling for the Se $4p$ Γ band and the Nb $4d$ bands.

6.4 Conclusion

The properties of $NbSe_2$ havel ong been thought to be representative of conventional s-wave superconductors. The case for MBSC in this compound is now compelling from ARPES [183] and heat transport [162] measurements. Previous STS [18, 204, 205, 21], heat capacity [195, 199, 154], μSR [191, 199] and dHvA [114, 192, 116] studies can now all be explained quite naturally in terms of MBSC. We estimate the gap to be roughly a factor of three larger on the Nb $4d$ bands than on the Se $4p$ Γ pocket. This may be due to a significantly different electron-phonon coupling on both sets of bands [192]. This is an indication that superconductivity originates from the Nb $4d$ bands and is induced onto the Se $4p$ Γ pocket. However, the reason for the weak coupling between these bands is still unclear. It may stem from the different dimensionalities (2D vs 3D) or from the nesting of part of the Fermi surface which is argued to be the source of the charge density wave state (see for example [206]).

Chapter 7

$Tl_2Ba_2CuO_{6+\delta}$: WF law in overdoped cuprates

7.1 Introduction to High T_c Cuprates

High T_c cuprates where discovered in 1986 by Bednorz and Müller [207] and have been the subject of much study. The crystal structure of these materials is generic and is composed of Copper-Oxygen conducting planes separated by planes of other atoms whose role is to transfer charge to the CuO_2 planes. This charge transfer can be tuned by doping and will add either holes or electrons to the planes. The resulting phase diagram as a function of carrier concentration (or doping) in seen in Fig. 7.1 with hole doping (the most common) being on the rightside and electron doping on the left [208]. Atzer o doping, there is one electron per copper site and one obtains a Mott insulator. The Coulomb interactions localize the electrons on the copper sites and their spins order antiferromagnetically. However, a superconducting phase is soon reached near $p \simeq 0.05$ holes/Cu atom and disappears around $p \simeq 0.3$ holes/Cu atom showing a superconducting dome. It is usual to distinguish three regions of the phase diagram as follows: *optimally doped* where T_c is maximum, *overdoped* at higher doping and *underdoped* at lower dopings.

A good understanding of the phase diagram has unanimously been thought to be central for understanding high T_c cuprates. In this light, more work has unveiled a much richer (or more complex depending on the point of view) phase diagram. Such richness also brings forth different interpretations of its idealized form. This is true both experimentally where several important details are still under scrutiny, and theoretically where such experimental uncertainties leave room for different idealized phase diagrams. The

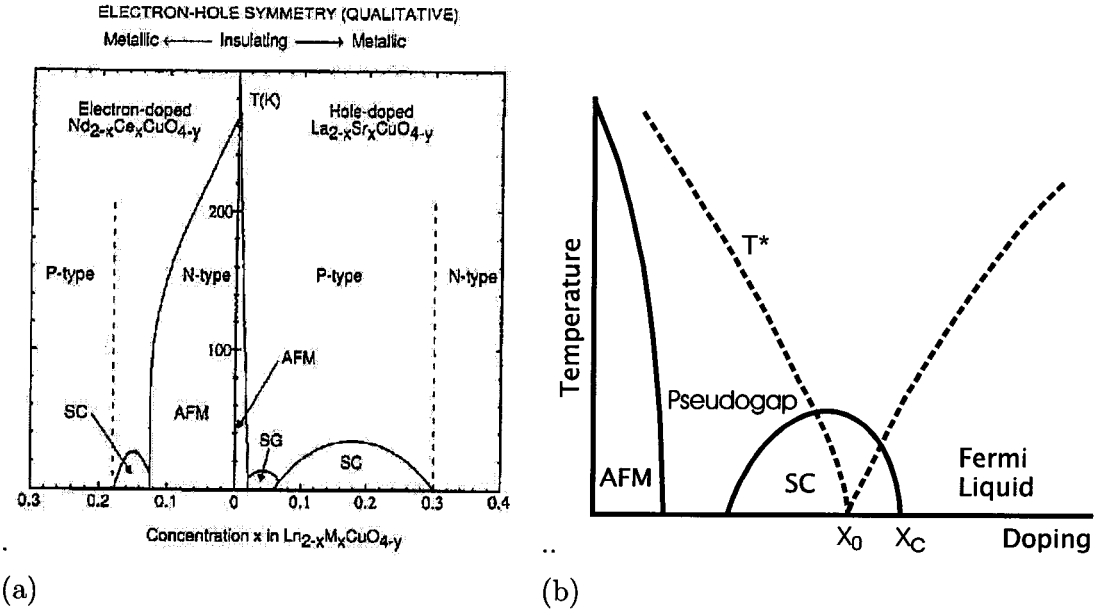

Figure 7.1: (a) The phase diagram of hole doped $La_{2-x}Sr_xCuO_4$ and electron doped $Nd_{2-x}Ce_xCuO_4$ (after Maple [208]). The striking features are the passing from an antiferromagnetic insulator to a superconducting dome with increased doping. Also note the approximate electron-hole symmetry. (b) An idealized phase diagram of high T_c cuprates. A notable feature is the opening of the pseudogap at a temperature T^*. There was little solid evidence that the overdoped side of the phase diagram forms a Fermi liquid before our verification of the Wiedemann-Franz law in overdoped Tl-2201. Two possible quantum critical points are showed, the first being at the edge of the superconducting dome and a second which is thought to be near $p = 0.2$ holes/Cu atom.

main components of the phase diagram are sketched in Fig. 7.1: an antiferromagnetically (AFM) ordered phase at very low doping (Mott insulator) and a superconducting dome. The overdoped region is metallic and a Fermi liquid ground state is thought to be recovered. On the underdoped side, there is much evidence for a pseudogap [209]w hich opens much above the superconducting T_c. It is however not yet clear whether it constitutes a new phase which competes with the superconducting order or if has the same origin and is a precursor to superconductivity.

What's more, we easily identify three possible quantum critical points (QCP): the disappearance of the AFM order, the appearance of superconductivity near $p = 0.05$ holes/Cu atom and its disappearance near $p = 0.3$ holes/Cu atom. But a fourth QCP has often been proposed within the superconducting dome, for example, near $p = 0.2$ holes/Cu

atom [210]. The nature of this critical point is still being investigated. These quantum critical points are interpreted in various ways in different theoretical frameworks. This has the beneficial effect of making experimental verifications of these theories easier. More realistically, experiments will be able to either lend credibility, put strong constraints, or sometimes rule out these theories.

Finally, the most notable success within this field has been to unambiguously prove that the order parameter (or the superconducting gap) has $d_{x^2-y^2}$ symmetry with nodes in the $[\pi, \pi]$ direction [26]. The presence of a gap with such topological nodes has been confirmed by many thermodynamic, transport and spectroscopic probes [26]. The smoking gun was obtained by phase-sensitive experiments which are well described in [26]. It was verified in many compounds in both the hole-doped and electron-doped side of the phase diagram but was mainly done at optimal doping. Although this result does not lead directly to a detailed knowledge of the pairing mechanism for high T_c cuprates, it imposes strong constraints on potential theories. It suggests that the pairing mechanism is electron-mediated rather than phonon-mediated as in BCS superconductors [1].

From this, it has been concluded that a change in paradigm may be necessary to understand the underlying physics of the cuprates and that a simple extension of BCS superconductivity may not be sufficient. Many of these novel treatments involve some type of spin charge separation (SCS) [35, 34, 36] in various forms while others, such as the SO(5) theory [211], the d-density wave picture [212] and the QED3 theory [213], do not.

In this chapter, we will present the results of a study of the thermal conductivity in highly overdoped Tl-2201 ($T_c \simeq 15$ K) which was set out to put strong constraints on theories invoking SCS. By testing the Wiedemann-Franz law in the normal state of Tl-2201, we show unambiguously that *there is no SCS in overdoped cuprates.* It is also the first solid evidence that a Fermi liquid ground state is recovered on the overdoped side of the phase diagram. In the superconducting state, we find quantitative agreement with BCS theory for a d-wave gap. This is the first report of evidence for d-wave pairing in such a highly overdoped cuprate. Finally, we are able to put constraints on the nature of a possible QCP within the superconducting dome.

[1] This point is still under debate with recent reports that phonons may have a significant role in the pairing mechanism [130]

7.2 $Tl_2Ba_2CuO_{6+\delta}$

This Chapter will focus on the high temperature cuprate $Tl_2Ba_2CuO_{6+\delta}$ or Tl-2201 for short. It was chosen because it can easily be overdoped. Indeed, by changing the oxygen content, one can tune the carrier concentration and move from optimal doping all the way past the superconducting dome in the far overdoped region. This can also be achieved with LSCO by doping with 30 % Sr or more but this often leads to disordered crystals. Indeed, even when the samples are grown homogeneously (an arduous task in itself), they remain much more disordered than what is obtained in Tl-2201, with the best quality crystals having $\rho_0 \simeq 20$ $\mu\Omega$ cm [83] as compared to $\rho_0 \simeq 6$ $\mu\Omega$ cm for Tl-2201.

In many ways, Tl-2201 is the ideal cuprate material. Its crystal structure is tetragonal, without the CuO chains that complicate the properties of the orthorhombic compounds $YBa_2Cu_3O_{6+x}$ (Y-123) and $YBa_2Cu_4O_8$ (Y-124), or the buckling that alters the unit cell of $Bi_2Sr_2CaCu_2O_8$ (Bi-2212). It is made of a stack of single CuO_2 planes, and is therefore not subject to possible bi-layer effects such as encountered in Bi-2212. It has a high maximum critical temperature T_c^{max} of 90 K, at optimal doping, much as in Y-123 and Bi-2212. In this sense, it is free of the possible concerns about the low T_c found in single-plane $La_{2-x}Sr_xCuO_4$ (LSCO). Finally, the $d_{x^2-y^2}$ symmetry of its superconducting state has been confirmed by a phase-sensitive experiment [26], tunneling [214] and microwave conductivity [215] measurements, at least at optimal doping [26]. What's more, very clean samples are readily available with mean free paths of the order of 1000 Å [216].

7.2.1 Crystal structure

$Tl_2Ba_2CuO_{6+\delta}$ is a single plane cuprate superconductor and its crystal structure is found in Fig. 7.2. Both tetragonal and orthorhombic phases have been reported for this system [217]. The lattice parameters are $a = 3.86$ Å and $c = 23.2$ Å. The crystals used here are tetragonal [216]. Studies on Tl-2201 have been rather limited for two main reasons: 1/ the available samples are small in size and 2/ the synthesis of the crystals is not only difficult but requires care as thallium oxides are poisonous.

7.2.2 Important properties

Tl-2201 is the ideal cuprate for the study of the overdoped side of the phase diagram for the reasons stated above. It has also been well characterized providing a good base for

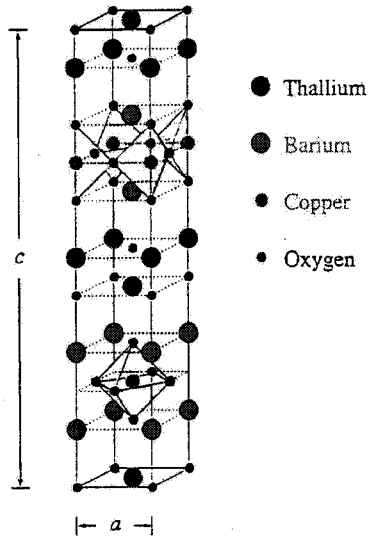

Figure 7.2: Crystal structure of Tl-2201. It is made of a single layer of CuO_2 planes. Both a tetragonal and an orthorhombic phase are found with approximate lattice parameters $a = 3.86$ Å and $c = 23.2$ Å.

comparison.

Doping

Tl-2201 is stoichiometric for $\delta = 0$ where it is optimally doped with a $T_c \simeq 90$ K. Overdoping is achieved by adding oxygen. Tl-2201 is fully overdoped and no longer superconducting for $\delta \simeq 0.1$. This should be compared to $YBa_2Cu_3O_{6+x}$ where $x = 0$ is the undoped insulator and $x = 1$ gives a slightly overdoped sample with $T_c \simeq 89$ K while $T_c^{max} = 93$ K. The disadvantage of having such a small window of oxygenation is the increased difficulty in obtaining a homogeneous oxygen content in a sample. In fact, attempts at reliably mapping the critical temperature as a function of oxygen content were not successful (although see [219]). What's more, in YBCO, the oxygen dopant is known to be in a specific location (the chains) whereas it is not clear how the oxygen arranges itself in Tl-2201. It should be noted that doping with oxygen, in general, has an elegant advantage: the same crystal can be studied as several doping levels thus reducing the possible errors due to different samples and different growths.

This was used to study the evolution of the resistivity with doping on the same crystal as shown in Fig. 7.3 [218]. There, one recognizes the linear resistivity with $d\rho/dT \simeq$

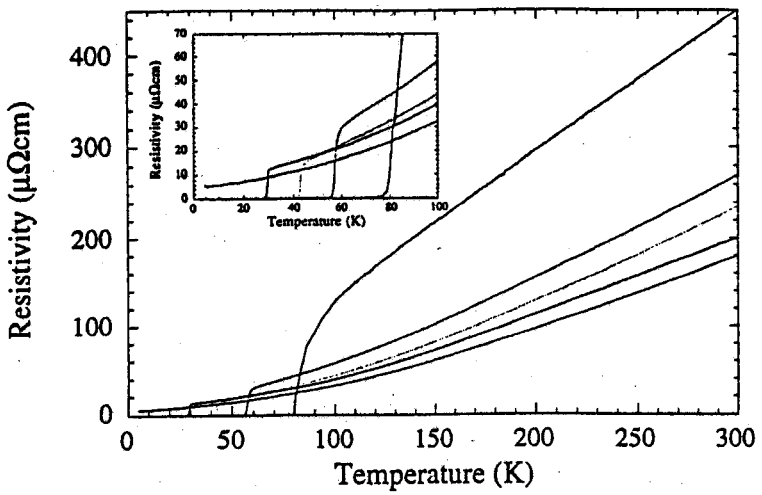

Figure 7.3: The resistivity of Tl-2201 as a function of oxygen doping. At optimal doping, the resistivity is linear with a slope near 1 $\mu\Omega$ cm K^{-1} (after [218]). As the sample becomes overdoped, the resistivity acquires an upward curvature which is taken to be evidence for the recovery of a Fermi liquid.

$1\mu\Omega$ cm K^{-1} at optimal doping. An upward curvature develops as one overdopes. More quantitatively, the resistivity was analyzed in terms of a single power law $\rho = \rho_0 + bT^{\alpha}$. Fig. 7.4 shows the resulting α against transition temperature for the same crystals used in our study (Fig. 7.4a) [218] and for other crystals of Tl-2201 and LSCO (Fig. 7.4b) [220]. The power law is seen to tend towards $\alpha = 2$, the value expected for a Fermi liquid. This was interpreted as evidence that the overdoped state of cuprates does recover a Fermi liquid ground state. However, it was also found that the resistivity was better fit by a form $\rho = \rho_0 + bT + cT^2$ where the ratio c/b is shown as a function of T_c in Fig. 7.4a. We will discuss this behavior further below.

We will now focus on the properties of highly overdoped crystals with $T_c \simeq 15$ K which are relevant to our study.

Upper Critical Field

In conventional superconductors, one can readily suppress the superconductivity and access the normal state by simply applying a magnetic field which surpasses the upper

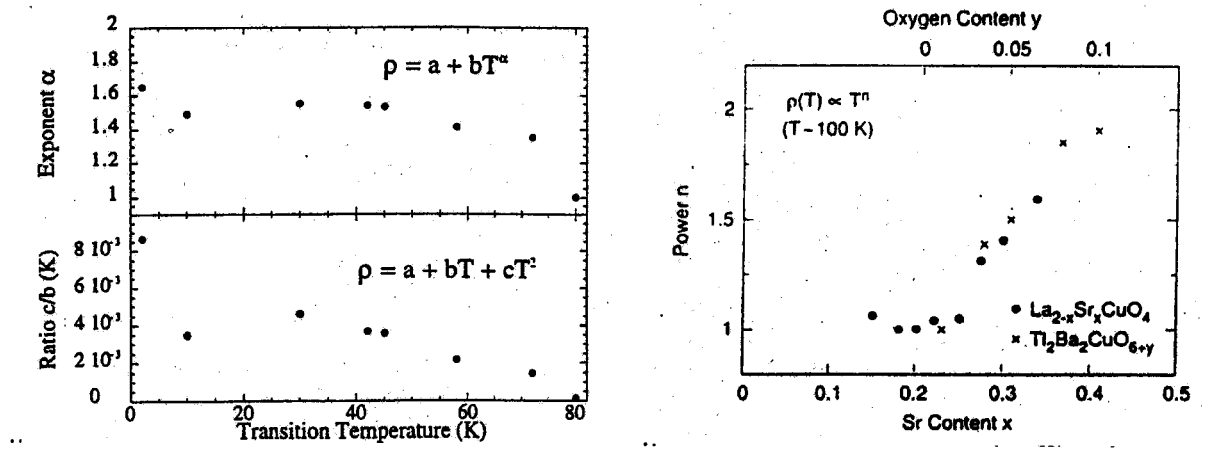

Figure 7.4: (a *upper*) The resistivity of Tl-2201 was fitted with a single exponent power law $\rho = \rho_0 + bT^\alpha$ which is plotted against T_c (after [218]). α goes from 1 at optimal doping to around 1.8 when non-superconducting. (a *lower*) The resistivity was better fit with a form $\rho = \rho_0 + bT + cT^2$, especially at low temperatures for samples with low T_c. The ratio b/c is plotted as a function of T_c. It is clear that the T^2 term becomes more significant as the T_c is reduced. (b) The resistivity of Tl-2201 and LSCO was fitted by a single exponent (labelled n on this figure) which was found to go from 1 at optimal doping to close to 2 on the overdoped side [220].

critical field H_{c2}. Instead, it has proven difficult to study the normal state properties of cuprate superconductors at low temperatures due to the extremely high upper critical fields associated with the high transition temperatures. To counter this difficulty, three approaches were used: 1/ studying systems with a reduced optimal T_c (and subsequently H_{c2}) such as electron doped PCCO and NCCO, 2/ the use of pulsed magnetic fields of up to 60 T through the phase diagram of systems with an optimal T_c around 40 K such as LSCO and Bi-2201 [221, 222] and 3/ studying systems with reduced T_c by either sufficiently overdoping or underdoping. We use the latter approach and study highly overdoped Tl-2201 with $T_c \simeq 15$ K and $H_{c2} \simeq 15$ T.

The upper critical field of cuprates has been the object of much debate over the years. This was first raised by Mackenzie and co-workers [216] which reported a resistive upper critical field with a positive curvature down to $T_c/1000$ of overdoped Tl-2201 as shown in Fig. 7.5a. This cast doubt on the ability of resistivity to adequately measure H_{c2}. The resulting critical field is instead associated with the irreversibility line as reported from

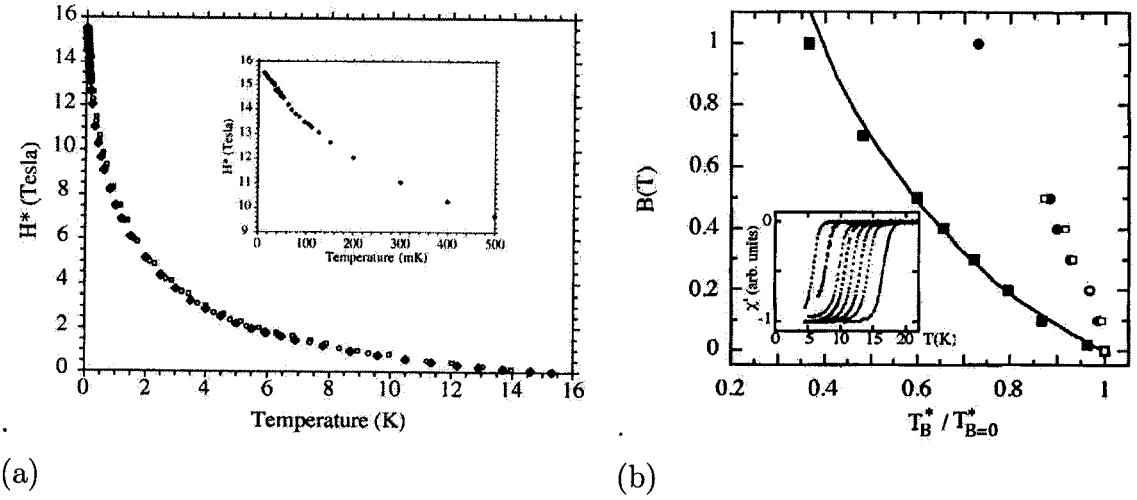

(a) (b)

Figure 7.5: (a) The resistive upper critical field for Tl-2201 with $T_c \simeq 15$ K [216]. It is seen to have a positive curvature all the way to $T_c/1000$ and reaches a value of $H_{c2}(0) \simeq 16$ T at zero temperature. (b) The upper critical field near T_c as obtained from resistivity (black line), magnetization (black squares) and heat capacity (black circles and white squares) [223]. The thermodynamic upper critical field is seen to be larger than the one obtained from resistivity and magnetization. At $T = 0$, it is believed that the thermodynamic H_{c2} is the same as the one obtained from resistivity [175].

magnetization studies [223]. Also, further specific heat measurements at temperatures near T_c on the same samples reported a thermodynamic H_{c2} above the resistive upper critical field as shown in Fig. 7.5b [223]. A more conventional negative curvature was also seen. It is believed that at zero temperature, both the thermodynamic H_{c2} and the irreversibility line meet, as argued by Wang *et. al.* [175].

For Tl-2201 with $T_c \simeq 15$ T, the zero-temperature $H_{c2}(0)$ is between 12 and 16 T depending on the criterion used for a field applied parallel to the c-axis [216]. Note that this upper critical field is much reduced for a crystal with a smaller lower transition temperature (e.g. Tl-2201 with $T_c \simeq 11$ K shows $H_{c2}(0)$ between 3 and 6 T [224]). Also, with the field parallel to the planes, H_{c2} is much larger (see [225]). We will use the fact that superconductivity can be suppressed by a magnetic field available in our laboratory to probe the normal state of the overdoped cuprate Tl-2201 with a $T_c \simeq 15$ K.

7.2.3 The samples

The overdoped samples of Tl-2201 used in this study were graciously supplied by A.P. Mackenzie (University of St. Andrews, Scotland). They were rectangular single crystals with typical dimensions of 0.4 mm and 0.2 mm in the tetragonal basal plane and 10 μm along the c-axis. The voltage pads had a width of 25 μm and the spacing between the electrodes was 0.3 mm. They were grown by the same technique as used by Mackenzie and co-workers in previous studies [216, 223, 225]. They have $T_c \simeq 15$ K, in zero magnetic field. Using the empirical formula $T_c/T_c^{max} = 1 - 82.6(p - 0.16)^2$ [226], this translates into a carrier concentration of $p = 0.26$ hole/Cu atom.

The resistivity of our samples is essentially identical to that obtained previously [216], with $\rho_0 = 5.6$ $\mu\Omega$ cm. Both heat and charge transport were measured using the same contacts, made by diffusing silver epoxy. A typical value for the contact resistance was 0.1 Ω at 4 K. A description of the procedure to obtain these contacts and the homogeneous oxygen distribution in our crystals can be found in Appendix C. The geometric factor used to convert from resistance (electrical or thermal) to electrical resistivity ρ or thermal conductivity κ was set by requiring that $\rho(300\text{ K}) = 180$ $\mu\Omega$ cm, the value obtained by Mackenzie and co-workers in previous studies of numerous crystals with the same doping level [216, 223, 225, 227]. The uncertainty on this value is estimated at ± 10 $\mu\Omega$ cm.

7.3 Charge transport

The charge transport of Tl-2201 has been studied in great detail in the past ten years for the full range of available doping [216, 228, 225, 227, 229, 230]. Our results on highly overdoped Tl-2201 are completely consistent with those reported before and do not bring forth any new information. We are mainly interested in the resistivity to be able to compare it to the thermal conductivity in the context of the Wiedemann-Franz law. It is nonetheless interesting to review the results from charge transport in overdoped cuprates.

As mentioned earlier, the power law dependence of the resistivity tends towards a T^2 behavior on the overdoped side of the phase diagram (see Figs. 7.3 and 7.4). This early report was seen as evidence that a Fermi-liquid state is recovered at high doping. However, resistivity yields true information about the ground state only at very low temperatures. Fortunately, this can be studied with fully overdoped non-superconducting samples (see [83] for example) or samples where the superconductivity can be suppressed

by a magnetic field [227, 221, 231, 222]. A more careful analysis leads to the conclusion that overdoped cuprates may be near a QCP. We will also briefly review the magnetoresistance of Tl-2201 and estimate the purity regime of our samples.

7.3.1 $\rho(T)$

The resistivity is shown as a function of temperature in Fig. 7.6, for fields ranging from zero to above $H_{c2}(0)$. A slight positive magnetoresistance is observed, in agreement with previous work [225]. The resistivity below 30 K (and above T_c) is best fit by the function $\rho = \rho_0 + bT + cT^2$, with a substantial linear term (*i.e.* $bT > cT^2$ for $T < 15$ K). The fitting parameters are $\rho_0(H) = 5.84$, 5.99 and 6.15 $\mu\Omega$ cm at $H = 7$, 10 and 13 T, respectively, and $b = 0.064$ $\mu\Omega$ cm K^{-1}, $c = 0.0054$ $\mu\Omega$ cm K^{-2} at 13 T. This unusual dependence was reported previously by Mackenzie *et. al.* [227] who found the coefficient of the linear term to be between 10 to 15 times smaller than the one at optimal doping (which is roughly 1 $\mu\Omega$ cm K^{-1} for all cuprates) in agreement with our fitting parameters. It was interpreted as "non-Fermi-liquid" behavior, in the sense that no linear term is expected in conventional FL theory.

Let us see what physical sense can be made of the magnitude of these parameters. The quadratic term can be compared to the experimental Kadowaki-Woods ratio [44]. The latter relates the normal state specific heat and the magnitude of the T^2 resistivity which gives $c/\gamma^2 \simeq 1 \times 10^{-5} \mu\Omega$ cm (mJ^{-1} mole K)$^2 \equiv$ a$_0$ (where $\rho = \rho_0 + cT^2$) for strongly interacting electron systems. In Tl-2201, using $\gamma \simeq 3 - 6.5$mJ mole^{-1} K^{-2} [223, 232] giving $c/\gamma^2 \simeq 13 - 60\ a_0$. This large discrepancy was pointed out by Nakamae and coworkers and was also found in overdoped LSCO ($c/\gamma^2 \simeq 5\ a_0$) and PCCO ($c/\gamma^2 \simeq 10\ a_0$) [83]. Although this behavior is not yet understood, it suggests that electron-electron scattering is very strong (and surely dominant) even in highly overdoped cuprates.

As for the linear term, it is interesting to point out that Greco and Dobry have obtained a linear term similar in magnitude to ours ($c \simeq 0.0074$ $\mu\Omega$ cm K^{-2}) by fitting the lineshape of the imaginary part of the self-energy (as measured by ARPES in overdoped Bi-2212) [233]. They obtain this result in the context of a marginal Fermi liquid theory which has an additional electron-phonon scattering mechanism (which would be responsible for the additional term in the resistivity). However, the authors point out that their result implies that the electron-phonon term is nil at optimal doping while there is no physical reason to expect this. What's more, we saw above that the additional

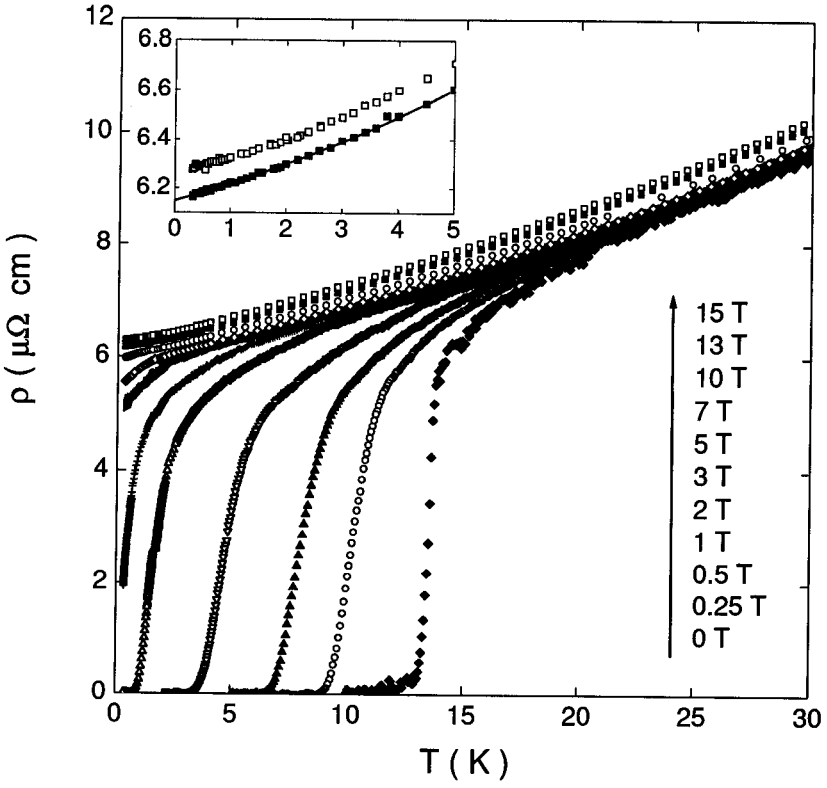

Figure 7.6: Electrical resistivity of Tl-2201 vs temperature for a current in the basal plane at different values of the magnetic field applied normal to the plane. All trace of superconductivity has vanished by 13 T. *Inset*: $\rho(T)$ at $H = 13$ T (filled symbols) and 15 T (open symbols). The line is a fit of the 13 T data to the functional form $\rho(T) = \rho_0 + bT + cT^2$.

quadratic term is most likely due to electron-electron scattering and not electron-phonon scattering.

In a more qualitative way, deviations from the standard T^2 dependence have been observed in a number of heavy-fermion materials, for example, $T^{1.2}$ in $CePd_2Si_2$ below 20 K [234]. In this material, this is associated with the proximity to a quantum critical point (QCP), where antiferromagnetic order sets in as a function of pressure. Other systems also reveal a linear (or near linear) temperature dependence of the resistivity in the proximity of a QCP, as found recently in $Sr_3Ru_2O_7$ [235], $YbRh_2Si_2$ [236] and $CeCoIn_5$ [237] where the tuning parameter is the magnetic field. In the case of cuprates, the obvious QCP would be the onset of superconductivity at a critical concentration p_c close to 0.3 hole/Cu atom, but a QCP has also been postulated to exist inside the superconducting region [210].

7.3.2 $\rho(H)$

The effect of a magnetic field on the resistivity has two effects. The most apparent is to lower the transition temperature as is shown in Fig. 7.6 in accordance with previous studies [216, 225]. We see that for our samples, the superconductivity is fully suppressed by 13 T. The second is a weak magnetoresistance. For our purposes, it is of interest to provide a good measurement of $\rho_0(H)$ only to enable a reliable test of the WF law. However, it was studied in great detail by others both for ρ_{ab} [227, 230] and ρ_c [229]. Our results are consistent with those reported, namely a magnetoresistance of $d[ln(\Delta\rho/\rho)]/dB^2 = 4.0 \pm 0.1 \times 10^{-4}$ T^{-2} [225].

7.3.3 Purity regime

Our Tl-2201 samples have a residual resistivity $\rho_0 = 6$ $\mu\Omega$ cm which is the lowest reported for any cuprate superconductor. It is a value characteristic of a dirty metal. In fact, the mean free path for these samples is calculated to be of the order of 1000 Å [216, 227].

It should be recognized that even with such high quality samples, the scattering rate Γ is not small compared to T_c. It may be estimated using the standard transport expression for the normal state conductivity: $\kappa_N/T = L_0/\rho_0 = \frac{1}{3}\gamma_N v_F^2 \tau = \frac{1}{3}\gamma_N v_F l$, where γ_N is the specific heat coefficient, $\tau = 1/(2\Gamma)$ is the scattering lifetime and l is the mean free path. With $\gamma_N \simeq 3$ mJ K^{-2} mole^{-1} [223] and $v_F = 2.5 \times 10^7$ cm/s, one gets $l = 1700$ Å and $\hbar\Gamma \simeq 0.4\ k_B T_c$. This is to be compared to the critical $\Gamma = 0.88\ k_B T_c$ at which d-wave superconductivity is predicted to be destroyed [78]. Our sample is therefore in a moderately dirty regime.

7.3.4 Summary

In summary, we have performed resistivity measurements in a magnetic field of Tl-2201 with a $T_c \simeq 15$ K. The superconductivity is completely suppressed by a magnetic field of 13 T. The temperature dependence of the resistivity at low temperature is best fit by a functional form $\rho = \rho_0 + bT + cT^2$ form with a substantial linear term. The T^2 term is indicative of a strong electron-electron scattering mechanism. The linear term points to the proximity of a quantum critical point. The resistivity also displays a small magnetoresistance consistent with earlier reports. The residual resistivity enabled us to obtain an estimate of the mean free path ($\simeq 1000$ Å) and of the purity regime in the su-

perconducting state ($\hbar\Gamma/k_BT_c \simeq 0.4$). Most importantly, our thorough characterization allows us to obtain a reliable value of the residual resistivity as a function of magnetic field. This is a mundane task but it is crucial for a reliable test of the WF law.

7.4 Heat Transport

The thermal conductivity κ is shown in Fig. 7.7. The sample was cooled in field to insure a homogeneous vortex distribution. The data is plotted as κ/T vs T^2 to separate the contribution of electrons from that of phonons, given that the asymptotic dependence of the former as $T \rightarrow 0$ is linear in T while that of the latter is cubic. In other words, in Fig. 7.7, the electronic contribution is the residual linear term κ_0/T given by the intercept of a linear fit with the $T = 0$ axis. The value of κ_0/T obtained in this way is: 1.41, 2.76, 3.47, 3.75, 3.87, 3.90, 3.95, and 3.95 mW K^{-2} cm^{-1}, at $H = 0, 1, 2.5, 4, 5.5, 7, 10$, and 13 T, respectively. As explained above, the uncertainty on the overall absolute value is approximately $\pm 5\%$. However, the relative uncertainty, *e.g.* between different fields, is much lower, around 1 %. This high degree of reliability in extracting κ_0/T is due to the fact that in these samples electrons conduct much better than phonons, and hence the slope of $\kappa(T)/T$ in Fig. 7.7 is weak relative to the intercept. Note that at high fields, electrons scatter phonons very effectively and $\kappa(T)$ is entirely electronic below 1 K.

In zero field, one sees a positive slope associated with phonon conductivity. Its magnitude is of the correct order as expected from the size of the crystal and a typical sound velocity in solids. From equation 2.22 we obtain $\kappa_{ph}/T^3 \simeq 0.8$ mW K^{-4} cm^{-1} using a mean diameter $d \simeq 2\sqrt{0.001 \text{ cm} \times 0.02 \text{ cm}/\pi} = 5 \times 10^{-3}$ cm and a phonon velocity of $v_{ph} = 5 \times 10^5$ cm/s (as observed in $Tl_2Ba_2CaCu_2O_8$ [238]). This is in very good agreement with the experimental value of $\kappa_{ph}/T^3 = 0.87$ mW K^{-4} cm^{-1}. However, as one increases the magnetic field, the phonons are scattered more strongly by a growing density of delocalized electrons and the slope disappears for $H > 4$ T. Above this field, the thermal conductivity is purely electronic.

We now turn to a discussion of these results, first in the normal state by comparing the thermal conductivity to the resistivity in the context of the Wiedemann-Franz law, and in the superconducting state in the context of BCS theory for a d-wave superconductor.

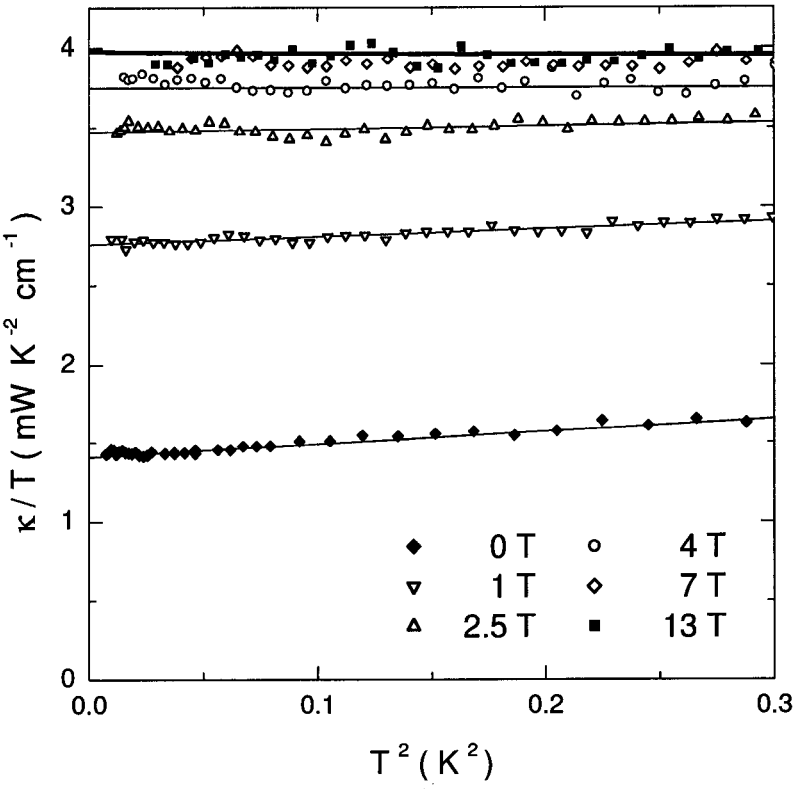

Figure 7.7: Thermal conductivity of Tl-2201 for a heat current in the basal plane, plotted as κ/T vs T^2, at different values of the magnetic field applied normal to the plane. The thin lines are linear fits to the data. The thick line is $L_0/\rho(T)$ where $\rho(T)$ is a fit to the resistivity at 13 T (see inset of Fig. 7.6).

7.5 Normal State

The origin of superconductivity in cuprates is not yet understood. Much of this confusion stems from the fact that the normal state of these systems has also eluded comprehension. Let us indeed remember that one of the foundations of BCS theory is that superconductivity forms from a Fermi liquid state and the instability of the Fermi sea to Cooper pairing (see Chapter 1). It is well known that the ground state is a Mott insulator at half filling ($p = 0$), but a simple question remains: how does one move away from this ground state with doping? It has been suggested that at optimal doping, one reaches a Marginal Fermi liquid [239]. At higher dopings, a Fermi liquid ground state has long been assumed to be recovered although there is no solid evidence to support this lore.

In this section, we turn our attention to the WF law in the normal state of cuprates which turns out to be a powerful and elegant way to address this issue. It has recently

been reported to be violated at optimal doping for an electron-doped cuprate PCCO, a clear sign of non Fermi liquid behavior [46]. Here we show that the WF law is perfectly satisfied for the overdoped cuprate Tl-2201. We will also review further work that has emerged on another overdoped systems [83] and on the underdoped side of the phase diagram [240]. What's more, we will examine very recent reports of a verification of the WF law at optimal doping in a hole doped cuprate [241].

7.5.1 The Wiedemann-Franz law in cuprate superconductors

Fundamentally, the linear term in κ at $T = 0$ reveals the presence of fermionic excitations in the electron system. We can then ask whether these excitations carry charge. This question can only be addressed in the absence of any superfluid that can also carry charge, which amounts to testing the Wiedemann-Franz law in the normal state. This law is one of the most fundamental properties of a Fermi liquid, reflecting the fact that the ability of a quasiparticle to transport energy is the same as its ability to transport charge, provided it cannot lose energy through collisions. It states that the heat conductivity κ and the electrical conductivity σ of a metal are related by a universal constant:

$$\frac{\kappa}{\sigma T} = \frac{\pi^2}{3}\left(\frac{k_B}{e}\right)^2 \equiv L_0 \tag{7.1}$$

where T is the absolute temperature, k_B is Boltzmann's constant and $L_0 = 2.45 \times 10^{-8}$ W Ω K^{-2} is Sommerfeld's value for the Lorenz ratio $L \equiv \kappa/\sigma T$. Theoretically, electrons are predicted to obey the WF law at $T \to 0$ in a wide range of environments: in both three or two dimensions (but not strictly in one dimension), for any strength of disorder and interaction [242], scattering and magnetic field [50]. Experimentally, the WF law does appear to be universal at $T \to 0$: until recently, no material had been reported to violate it. For a detailed discussion of this law, see Chapter 2. The first exception was found in optimally-doped $Pr_{2-x}Ce_xCuO_4$ (PCCO), an electron-doped cuprate where heat conduction exceeds the electrical conduction by a factor of two or so as shown in Fig. 7.8b [46] [1] It was concluded that Fermi liquid theory breaks down in a fundamental way for cuprates, at least near optimal doping. An obvious question is raised: is the WF

[1] It should be pointed out that we will assume that the violation of the WF law in optimally doped PCCO shows that $L/L_0 \simeq 2$ [46] and will not discuss the strange behavior of $L/L_0 \to 0$ at $T \to 0$ which is still being scrutinized experimentally. The same type of low temperature downturn has been observed in overdoped LSCO [83] and is currently thought to be an experimental artifact which is not yet understood.

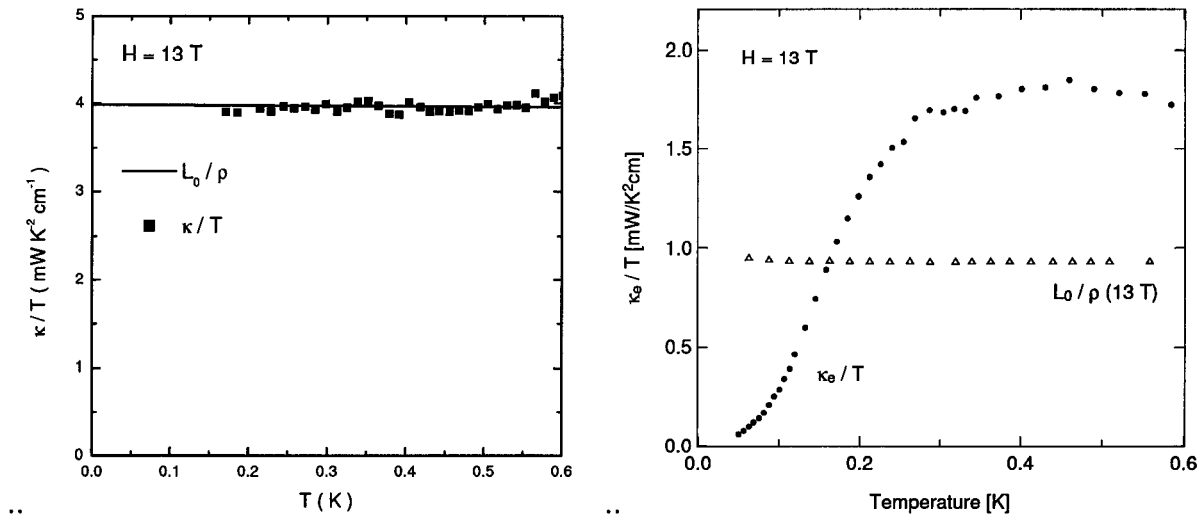

(a) (b)

Figure 7.8: (a) The thermal conductivity and the resistivity in the normal state of overdoped Tl-2201 plotted as κ/T and L_0/ρ at $H = 13$ T. The WF law is seen to be perfectly satisfied. (b) Equivalent data for optimally-doped PCCO [46]. There, the WF is strongly violated, which constitutes clear non Fermi liquid behavior.

law obeyed in any part of the phase diagram? We have found that it is in an overdoped cuprate with $T_c \simeq 15$ K [162].

Wiedemann-Franz law in Tl-2201

It is in general difficult to test the WF law in cuprate superconductors because of their high upper critical fields. Fortunately, in strongly-overdoped Tl-2201, the normal state can be reached in moderate fields. In our crystals, the superconductivity has completely vanished by 13 T, at which field we find $\kappa_0/T = 3.95 \pm 0.04$ mW K^{-2} cm^{-1} and $\rho_0 = 6.15 \pm 0.03$ $\mu\Omega$ cm, so that $L = \rho_0\kappa_0/T = 0.99 \pm 0.01$ L_0, in perfect agreement with the WF law. Note that the Lorenz ratio does not suffer from the 5% uncertainty associated with the geometric factor, as both transport measurements are performed using the same sample with the same contacts. The error bars are therefore on the order of 1 %. In Fig. 7.7 and 7.8a, the transport of heat and charge of Tl-2201 are compared directly by reproducing the charge conductivity at 13 T from the inset of Fig. 7.6. This is done by plotting $L_0/\rho(T)$ vs T using the fit to the 13 T data for $\rho(T)$ (inset of Fig. 7.6). The charge conductivity $L_0\sigma(T)$ is seen to be equal to the heat conductivity $\kappa(T)/T$ at 13 T.

The basic implication of this result is that *the fermions which carry heat also carry*

charge e and are therefore indistinguishable from standard Landau quasiparticles. In particular, there is no evidence of any spin-charge separation. Indeed, if electrons were to fractionalize into neutral spin-carrying fermions (spinons) and charged bosons (chargons) [36], there would be no reason to expect the WF law to hold, as the heat-carrying fermions would not take part in the transport of charge. This result therefore imposes a constraint on theories of spin-charge separation (SCS): the critical hole concentration p_{SCS} at which electron fractionalization starts to occur is not the zero temperature point of the phase diagram where superconductivity starts to occur (on the overdoped side), but can only be at lower p. In other words, any hypothetical onset of SCS must obey $p_{SCS} < 0.26 < p_c$. *It therefore appears that the mechanism for superconductivity in this overdoped region of the phase diagram is not the condensation of charge-e bosons*, but most likely Cooper pairing. Note that (barring any profound electron-hole asymmetry) this conventional picture is expected to break down with underdoping, as suggested by the violation of the WF law in PCCO near optimal doping [46].

Although the standard FL description fails, as revealed by the non-quadratic T dependence of $\rho(T)$, the basic nature of the electronic excitations in the limit of zero energy is that of Landau FL quasiparticles. (A similar situation is seen in heavy-fermion materials [57].)

Wiedemann-Franz law in optimally doped cuprates

The astonishing result of a violation of the WF law in optimally doped PCCO has brought much activity both experimentally and theoretically. However, it is the only report of such a violation and remains to be reproduced in another system or at another doping level. In this light, a very recent study by Bel and co-workers claims to have verified the WF law in hole doped Bi-2201 at optimal doping [241]. There, the samples had a reduced T_c near 10 K (possibly due to disorder). This enabled a complete suppression of superconductivity with currently available static magnetic fields of 25 T. These contradictory results may be due to one of two things: 1/ a drastic electron-hole asymmetry which leads to a breakdown of Fermi liquid theory only with electron doping, or 2/ one of the reports is flawed due to some unknown reason. Before jumping to either of these disturbing conclusions, it is wise to inspect the available experimental data critically.

The recent report of Bel and co-workers is very commendable as great experimental difficulties were dealt with beautifully. The data they present can regrettably not rule

out a violation of the WF law. They indeed find L/L_0 to be 1.2 and 1.3 for two optimally doped samples (as compared to 1.7 in PCCO). They attribute this small departure from the WF law to thermal and electrical contacts not being the same due to their large widths with respect to the distance between them. However, the possibility that the WF law is truly violated cannot be ruled out. What's more, their data does not extend to temperatures lower than 200 mK which may lead to an incorrect extrapolation to $T \rightarrow 0$ of the electronic thermal conductivity. This fact may of course lead one to observe a perfectly verified WF law or, instead, to a definite violation. As the authors point out, a more careful experiment will be necessary to obtain a more definite conclusion.

In all fairness, one must be equally critical about the experimental data on PCCO [46]. In this light, let us remember that the data is seen to have two regimes: below 250 mK where the electronic thermal conductivity is seen to go to zero at $T \rightarrow 0$, and above 250 mK where it surpasses the expected WF law by a factor of two or so. The low temperature part is thought to possibly be due to an extrinsic experimental problem such that we will not discuss it here and wait until it is better understood. At higher temperature, a coherent analysis was used to obtain $L/L_0 \simeq 2$ [46]. However, it should be noted that alternate analyses can lead to a different temperature dependence of the thermal conductivity and consequently a different L/L_0. Nevertheless, a violation of the WF law is inevitably obtained.

With the lack of a more convincing verification of the WF law, we will simply keep in mind the above discussion and assume, for now, that the WF law is violated at optimal doping in cuprate superconductors.

Wiedemann-Franz law in other cuprate superconductors

The WF law was verified in another system, namely fully overdoped non-superconducting LSCO as shown in Fig. 7.9a [83]. They found L/L_0 to be 0.83 and 0.86 for samples with $\rho_0 = 23$ and 49 $\mu\Omega$ cm respectively. It should be pointed out that their data suffers from a large phononic background which is non-existent in Tl-2201. In order to deal with this problem, the authors have measured the c-axis thermal conductivity κ_c/T (which is purely phononic) and assumed that the lattice thermal conductivity in the $a-b$ plane was proportional to it such that $\kappa_{ph\ ab} = 1.6 \times \kappa_c$. From this analysis, they obtained the electronic contribution in the plane as $\kappa_e/T = \kappa_{ab}/T - 1.6 \times \kappa_c$ which is constant in temperature, in accordance with the fermionic nature of the excitations. It is important

to be critical about this necessity to model the phononic contribution. Indeed, although it is possible that the reported values of L/L_0 may be flawed, one doesn't know to which extent. In all likelihood, it may explain the small departure from the WF law, but it leaves some ambiguity with respect to a possible violation of the same type as observed in PCCO where $L/L_0 > 1$.

The resistivity was found to obey a perfectly T^2 law at low temperature which was seen as an additional indication of a Fermi-liquid ground state. The magnitude of the quadratic term revealed to be larger than expected from the experimentally universal Kadowaki-Woods ratio [44] for strongly correlated systems. This interesting result, which has yet to be understood, may serve as a strong reminder that a T^2 resistivity should not be automatically associated to a Fermi liquid ground state.

The overdoped side of the phase diagram has been convincingly showed to form a FL but the violation of the WF law in optimally-doped PCCO indicates that this picture may break down at lower doping. In fact, it may be expected to break down most significantly on the strongly underdoped side of the phase diagram. The task of testing the WF law for underdoped cuprates may seem possible as the superconductivity may also be destroyed by a small magnetic field due to the reduced T_c. This was attempted in LSCO at the very edge of the phase diagram (with x=0.06) [240]. However, a new problem is imposed at such low dopings, namely, the normal state is seen to cross over to an insulating ground state, at least in LSCO and Bi-2201 [221, 222]. In the normal state, the charge transport at zero temperature is therefore nil (infinite resistivity). The resistivity of LSCO (x=0.06) is shown in Fig 7.9b. According to the WF law, this would lead to no electrical transport in the normal state. Within experimental errors, this is seen to be the case (see Fig. 7.9b). However, although consistent with the WF law, this experiment neither proves nor disproves its validity for underdoped cuprates.

Speculating further, one can obtain the expected value for the WF law from resistivity measurements in high fields [221, 222]. Although the same cannot be done with thermal conductivity in the absence of such high static magnetic fields, some information can be gathered nonetheless. Indeed, in zero field, there is a residual electronic linear term κ_{00}/T over the whole phase diagram which is associated with nodal quasiparticles [243, 63, 240]. In LSCO, Takeya and co-workers found that $\kappa_{00}/T > L_0/\rho_0$ for underdoped samples and $\kappa_{00}/T < L_0/\rho_0$ for overdoped samples [243, 221]. Qualitatively, we expect the following behavior for the thermal conductivity in a magnetic field if the WF law is obeyed in the normal state: $1/\ \kappa(T = 0, H)/T$ decreases for underdoped LSCO and

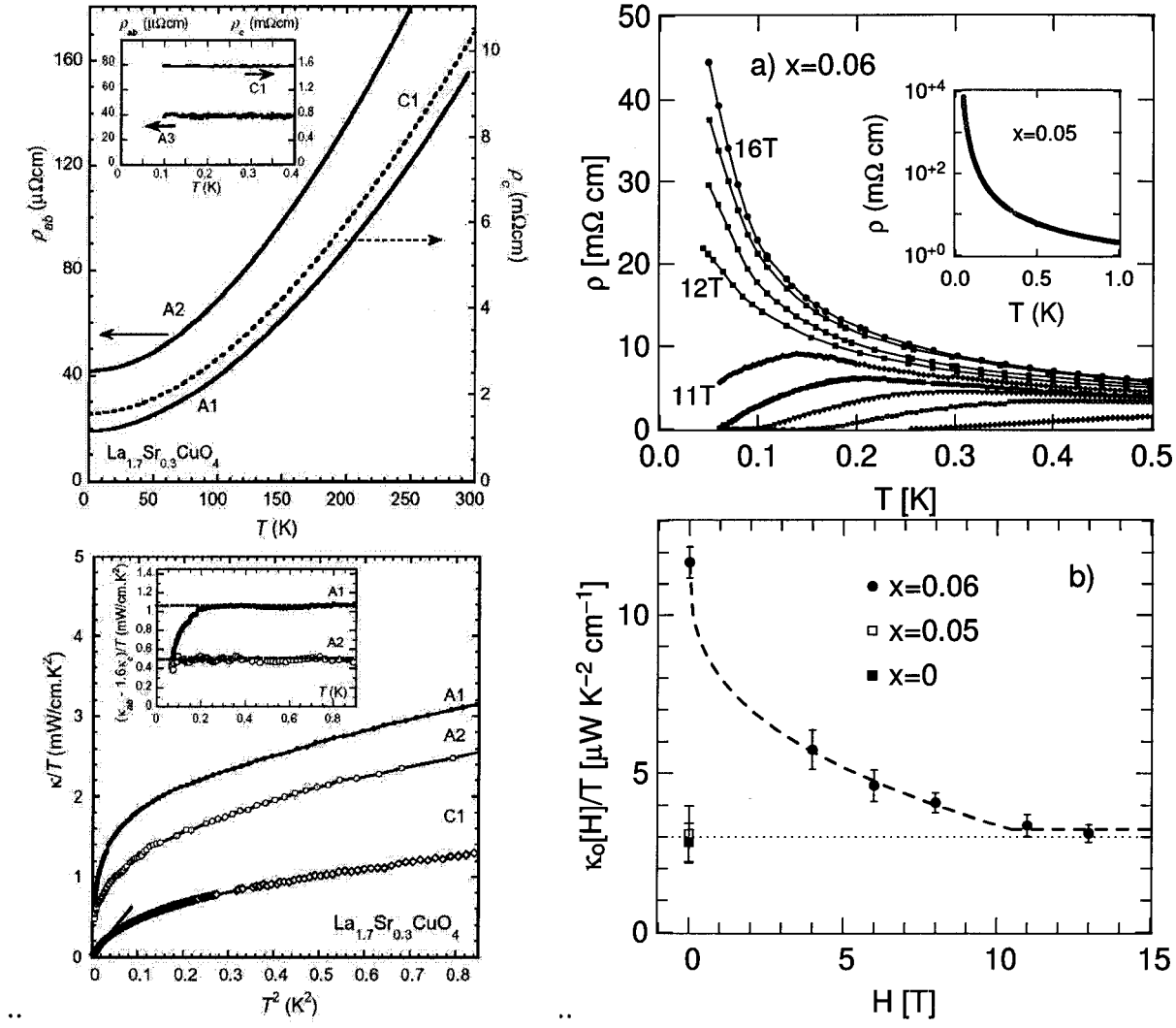

Figure 7.9: (a) The electrical and thermal conductivity of fully overdoped LSCO (with x = 0.3) [83]. The electrical κ is seen to agree well with the WF law with L/L_0 being 0.83 and 0.86 for samples with $\rho_0 = 23$ and 49 $\mu\Omega$ cm respectively. (b) The electrical and thermal conductivity of highly-underdoped LSCO with x=0.06 all the way into the normal state [240]. The resistivity is seen to be insulating at low temperatures and the electronic thermal conductivity in the normal state is below experimental resolution (indicated by the spurious linear term measured in insulating LSCO with x = 0 and x=0.05).

2/ $\kappa(T = 0, H)/T$ increases for overdoped LSCO. This has indeed been reported very recently by Hawthorn *et al.* and Sun *et al.* [240, 244]. This *qualitatively* consistent picture needs to be contrasted with a *quantitative* test of the WF law. In PCCO, the violation is only of a factor 2. The qualitative evidence presented above can draw no conclusion with regards to such a quantitative violation. This leaves room for much future work, for example at higher fields and in cleaner samples.

Inhomogeneity issues

The issue of inhomogeneity is important to address for high T_c superconductors. In particular, inhomogeneity is always found in both LSCO and PCCO compounds. Note that whether it is intrisic to these superconductors or not is still an open issue. Regardless, one may ask what effect this could have on an experimental verification of the WF law?

It turns out that inhomogeneity cannot be the cause of a violation of the WF law at $T = 0$ although it may lead to some violation at finite temperature. To better illustrate this, imagine two extreme cases of inhomogeneity: 1/ two different metals in series linked with a metallic interface, and 2/ two different metals in parallel linked with either a metallic or an insulating interface. In these cases, it is easy to convince oneself that the WF law will still be satisfied at $T = 0$. At finite temperature, an additional phononic contribution may come from the interface but will constitute no more (or no less) of a violation of the WF law as any additional phononic term from the sample itself.

In short, it is clear that inhomogeneity is not the cause of the observed violation of the WF in cuprate superconductors.

Antiferromagnetic correlations

It is interesting to note that recent reports show that their exists antiferromagnetic correlations in cuprate superconductors when a magnetic field is applied [245, 246, 247]. As these may cause some localization of charge, it may lead one to wonder whether or not it may be the cause of the reported violation of the WF law in cuprates. This turns out not to be the case. Indeed, it is not expected theoretically as the effect of localization does not affect the WF law. More convincingly though, the WF law was recently studied near a field tuned quantum critical point in $CeCoIn_5$, a Heavy Fermion system [59]. There, antiferromagnetic fluctuations are found above the QCP, and the WF law is satisfied at $T = 0$ even very near the QCP where the AFM fluctuations are most

prominent. Subsequently, the presence of AFM fluctuations in cuprates are probably not responsible for the violation of the WF law.

7.5.2 Theoretical proposals

The intriguing results of a violation of the WF law in PCCO has generated much theoretical work both to understand what is expected from different theoretical frameworks which pertain to high T_c superconductors [248, 249, 250, 251, 252, 253] but also in a more general context of the validity of the WF law in extreme situations [254]. We will review the main contributions and discuss them in terms of the non-violation of the WF in overdoped cuprates.

$t-J$ model: doped Mott insulator

Cuprate superconductors have long been thought to be well described by the simple $t-J$ model in two dimensions [34]. The main idea of this treatment is that of starting from a well-known state, the Mott insulator, and doping it with holes (or electrons). High T_c cuprates at zero doping are indeed thought to form a Mott insulating state where J is the antiferromagnetic exchange constant. Once holes (or electrons) are added, they still feel a strong Coulomb repulsion, now with some degree of delocalization is parameterized by a hopping term t. In this picture, the electron spins are ordered at low doping (Mott insulator) but then electrons undergo spin-charge separation: the elementary excitations are no longer electrons but rather spinons which have spin 1/2 and carry no charge and another (or other) excitation(s) carrying the charge. The simplest such manifestation would be a particle which has spin 0 and carries charge e. This spin charge separation would take place through the phase diagram although, at sufficient doping, one may expect the Coulomb interaction to be weak enough to recover a Fermi liquid state.

A direct implication of such a spin charge separated ground state would be a violation of the WF law. Indeed, the fermionic heat transport (linear in T) would only arise from the spin 1/2 spinons which do not carry charge, leading to no direct relation between the heat and charge transport. This was derived to be the case by Houghton, Lee and Marston [248] for the large-N solution of the $t-J$ model. Using parameters relevant for cuprates, they obtain a doping dependence of the Lorenz ratio shown in Fig. 7.10. It is pointed out that at optimal doping, one expects $L/L_0 \simeq 2$ as was reported in PCCO [46]. However, the violation remains large at higher dopings and one expects $L/L_0 \simeq 1.5$

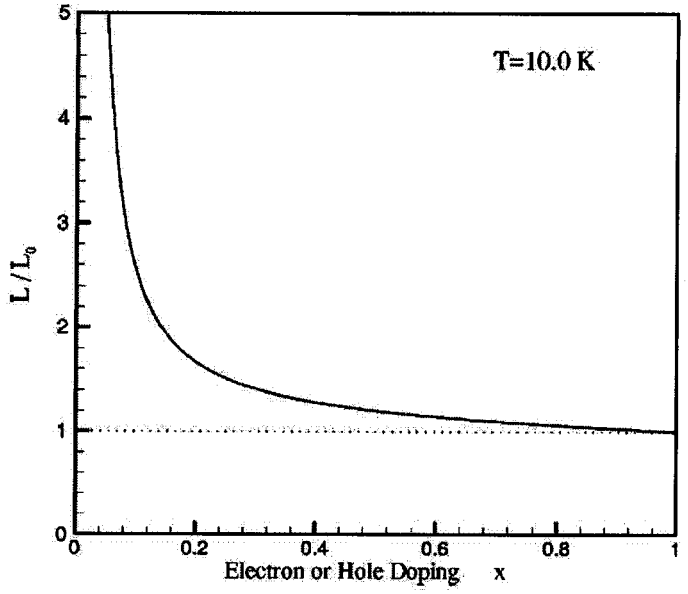

Figure 7.10: The violation of the WF law as a function of doping obtained in the large-N limit of the $t-J$ model [248].

for $p = 0.26$, the doping relevant to our Tl-2201 crystals. The authors propose that this discrepancy may be due to the large-N approximation. A proper derivation may result in the restoration of a Fermi liquid at a doping lower than $x = 0.26$.

This result strongly emphasizes the power of our verification of the WF law on the overdoped side of the phase diagram. It provides a clear constraint over this theory in the fact that such spin-charge separation does not occur at all dopings and that a Fermi liquid is restored at a doping no higher than $x = 0.26$ which, importantly, still hosts superconductivity.

It is interesting to note that Loram *et al.* have reported long ago (1994) that the elementary excitations of cuprates in the normal state were indeed charge e fermions for a large range of doping (in $YBCO_{6+\delta}$ for $0.5 < \delta < 1$) [232]. They investigated quantitatively the Wilson ratio $(S/T)/[\frac{(k_B/\mu_B)^2}{3} \times \chi]$ which relates the electronic specific heat γ (or more generally the entropy S/T) and the magnetic susceptibility χ. The Wilson ratio is expected to be 1 for weakly-interacting electrons as is found for YBCO. This ratio was also studied and yielded a ratio near 2 (expected for strongly correlated electrons) in fully overdoped LSCO where the WF law is also seen to be satisfied [83].

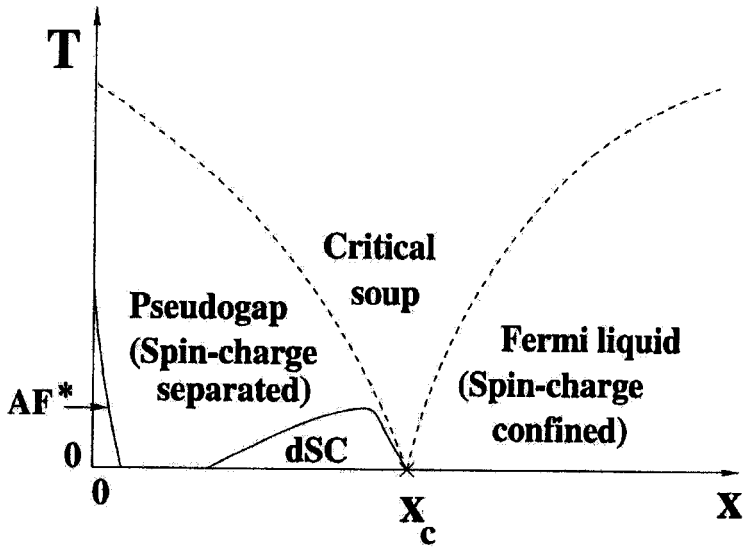

Figure 7.11: The phase diagram for the Z2 gauge model of Senthil and Fisher [36]. Below x_c, the WF law would be violated in this picture.

Z2 gauge model

Senthil and Fisher have proposed a theory for the superconductivity in cuprates which is also based on spin-charge separation with electrons fractionalizing into [spin 1/2, charge 0] "spinons" and [spin 0, charge e] "holons" [36, 255, 256, 257, 258]. The theoretical treatment is based on a so-called Z2 gauge theory for which topological vortex excitations ("visons") are supported. The phase diagram obtained is shown in Fig. 7.11. At low dopings, the visons are gapped below T^* and lead to electron fractionalization. The superconductivity is directly related to this fractionalization as it stems from the condensation of holons. At higher dopings, the visons condense and effectively glue the holons and spinons to form "conventional" electrons [spin 1/2, charge e] and recover a Fermi liquid. Of course, at $T = 0$, this occurs at the critical doping where superconductivity disappears (see Fig. 7.11).

In this picture, the WF law is naturally expected to break down as long as the visons are gapped. For this reason, the verification of the WF law at a doping lower than x_c of Fig 7.11 (in other words, still under the superconducting dome) presents a direct proof of the failure of this model. The same conclusion was reached at the same time by very elegant studies of highly underdoped YBCO [259, 260] and B-2212 [261]. One of these was a direct search for visons which were not found experimentally [259]. Another elegant

experiment showed that the superconductivity, even in highly underdoped cuprates, has a condensate made of charge $2e$ excitations: Copper pairs [260]. This was seen by showing that each vortex carries one flux quantum $h/2e$ rather than h/e expected if the superconductivity stems from the condensation of charge e holons.

In summary, the verification of the WF law at a doping lower than x_c (see Fig. 7.11) provided a strong proof that the theory proposed by Senthil and Fisher [36] is not adequate for cuprate superconductors. The same conclusion was reached at the same time from beautiful experiments on the underdoped side of the phase diagram [259, 260, 261].

d-density wave

Theoretical investigation of the expected behavior for the WF law has been studied in the context of the *d*-density wave theory for cuprate superconductors [249, 176, 251]. The main motivation behind the *d*-density wave picture is that of a order parameter competing with superconductivity and which is responsible for the pseudogap. The T^* line is thought to reach zero temperature near optimal doping ($p \simeq 0.15 - 0.2$). Beyond this point, a pure *d*-wave state is recovered. Although this theory has yet to be proved or disproved to apply successfully to cuprates, it is interesting to see if it is at least consistent with our observations of the WF law.

Yang and Nayak have studied the charge and heat transport in this context and show that a violation reminiscent of that observed in PCCO is possible but only in unrealistic limits, namely, in the ultra-clean regime and for $\mu = 0$ where μ is the chemical potential [249]. However, they also point out that in the absence of *d*-density wave order (*i.e.* on the overdoped side of the phase diagram), the WF law would be recovered. The authors conclude that further experiments at lower dopings and in cleaner samples would be required to verify their theory.

Other treatments by Kim and Carbotte [250] and Shaparov *et. al.* [251] have seen that the WF law is not violated at $T = 0$. However, they argue that L/L_0 has a strong temperature dependence, either due to a frequency dependent scattering rate [250] or to the presence of a magnetic field [251] which may be relevant for PCCO.

The treatments within the *d*-density wave formalism have the attractive behavior of leading to no violation of the WF law in the overdoped region. It is however not clear that they provide a good explanation of the violation of the WF law as observed in PCCO. More work on clean underdoped cuprates will be necessary to verify this picture.

Polarons

Work was also reported for the bi-polaron picture [252]. There, the expected behavior of L/L_0 at $T \rightarrow 0$ is not calculated although it is thought to be in violation of the WF law. The verification of the WF law in overdoped Tl-2201 suggests that their proposed mechanism for superconductivity breaks down before the superconductivity disappears (at $p = 0.3$). The authors suggest that a cross-over may occur between Bose condensation at low dopings to Copper pairing (on the overdoped side) as the only way to reconcile their picture with our experimental findings.

Summary

Our results on overdoped Tl-2201 have set some strong constraints on many theoretical frameworks for high T_c cuprates, even ruling out one of them [36]. It also sets a difficult challenge to reconcile the observed violation of the WF law in optimally doped PCCO and its verification in strongly overdoped Tl-2201. This will surely stimulate more theoretical work.

7.5.3 Summary

In summary, we have studied the normal state of overdoped Tl-2201 by applying a magnetic field large enough to destroy superconductivity [162]. The WF was verified to hold perfectly within experimental errors which are estimated at 1%. This provides unambiguous evidence that spin-charge separation does not occur in overdoped cuprates but that instead, a Fermi liquid ground state is recovered. This is in contrast to a reported violation of the WF law in optimally doped PCCO [46]. This one is currently under scrutiny with a recent claim of the verification of the WF law in a hole doped cuprate at optimal doping [241]. Our results were verified in another system: fully overdoped non-superconducting LSCO which gives confidence in its universality in cuprate superconductors [83]. Note that their results are less precise ($L/L_0 = 0.83$ and 0.86 for samples with $\rho_0 = 23$ and 49 $\mu\Omega$ cm respectively) due in part to the large phononic contribution to the thermal conductivity in their samples. Our findings have set some strong constraints on several theories of high T_c cuprates invoking spin-charge separation and went as far a to rule out one of them.

7.6 Superconducting state

Thermal conductivity has proved to be a powerful probe of unconventional superconductors. For an order parameter with d-wave symmetry, the electronic thermal conductivity was predicted to be universal with respect to impurity content [80, 81]. This was confirmed experimentally at optimal doping in both YBCO and Bi-2212 [82, 84, 262].

In essence, thermal conductivity probes the low-energy excitations very near the gap nodes, at energies as low as the temperatures reached: typically 100 mK ($\simeq 10^{-2}$ meV) or so. This should be compared to a typical gap maximum of an optimally-doped cuprate which is near $\Delta_0 \simeq 35$ meV. This leads to a powerful tool to probe the nature of the gap near the nodes which can then be compared to reports at higher energies (for example ARPES) and can also put strong constraints on theories invoking small finite gaps rather than a pure d-wave order parameter.

In this section, we will see that the results in the superconducting state of highly overdoped Tl-2201 are in quantitative agreement with the BCS treatment of d-wave quasiparticles. We will also put a stringent upper limit on the magnitude of a subdominant imaginary order parameter ix in an order parameter of the form $d_{x^2-y^2} + ix$, with $x = s, d_{xy}$.

7.6.1 BCS theory for a d-wave superconductor

In the absence of a magnetic field, there is a large residual linear term in the thermal conductivity of Tl-2201, namely $\kappa_0/T = 1.41$ mW K^{-2} cm^{-1}. A similar term has also been observed in other hole-doped cuprates, albeit at optimal doping, where it is much smaller: $\kappa_0/T = 0.14$, 0.15 and 0.11 mW K^{-2} cm^{-1}, in YBCO [82, 63], Bi-2212 [263, 84, 83] and LSCO [264, 243, 240, 63], respectively. The results are showed in Fig. 7.12 along with those of s-wave superconductor V_3Si. Within BCS theory applied to a d-wave superconductor, this residual heat conduction is expected, arising from zero-energy quasiparticles induced by impurity scattering near the nodes in the $d_{x^2-y^2}$ gap function. In the clean limit, where the scattering rate $\Gamma \ll k_B T_c/\hbar$, it is universal (in the sense that it is independent of Γ) and it depends only on the ratio of the two quasiparticle velocities (v_F and v_2) which govern the Dirac-like spectrum of nodal quasiparticles, $E = \hbar\sqrt{v_F^2 k_1^2 + v_2^2 k_2^2}$ [85]:

$$\frac{\kappa_0}{T} = \frac{k_B^2}{3\hbar}\frac{n}{c}\left(\frac{v_F}{v_2} + \frac{v_2}{v_F}\right) \tag{7.2}$$

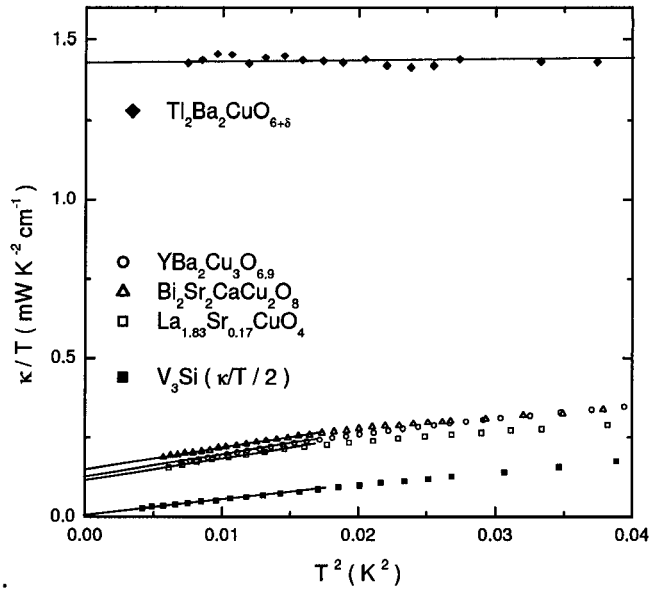

Figure 7.12: The thermal conductivity as a function of temperature for overdoped Tl-2201, optimally doped YBCO, LSCO and Bi-2212, and for s-wave superconductor V_3Si (the data is divided by two for clarity). The presence of a finite linear term κ_0/T is a clear indication of nodes in the gap. In Tl-2201, a very large linear term is observed which constitutes the first report of a d-wave order parameter in such a highly overdoped cuprate.

where n is the number of CuO_2 planes per unit cell of height c (along the c-axis), and $\vec{k_1}$ and $\vec{k_2}$ are unit vectors pointing in directions normal and tangential to the Fermi surface at the node, respectively. In other words, v_F is the Fermi velocity in the nodal direction and v_2 is proportional to the slope of the gap at the node, $d\Delta/d\phi = \hbar k_F v_2$, with k_F the Fermi wavevector.

Applying Eq. 7.2 to Tl-2201, for which $n = 2$ and $c = 23.2$ Å, we get $v_F/v_2 = 270$. A rough estimate using Fermi surface parameters typical of cuprates, namely $v_F = 2.5 \times 10^7$ cm/s and $k_F = 0.7$ Å^{-1} [1], and the simplest d-wave gap function, $\Delta = \Delta_0 \cos 2\phi$ (where $d\Delta/d\phi = 2\Delta_0$), with the weak-coupling relation for a d-wave superconductor, $\Delta_0 = 2.14\ k_B T_c$, gives $v_F/v_2 = 210$. This shows that the magnitude of κ_0/T is in good agreement with the simplest BCS analysis. In itself, this is the first evidence that *such a highly overdoped cuprate still displays d-wave superconductivity.*

However, we have estimated earlier the purity regime of our sample via the resid-

[1] Both v_F and k_F were measured to be independent of doping and roughly equal in magnitude for LSCO and Bi-2212 [87, 130, 265]

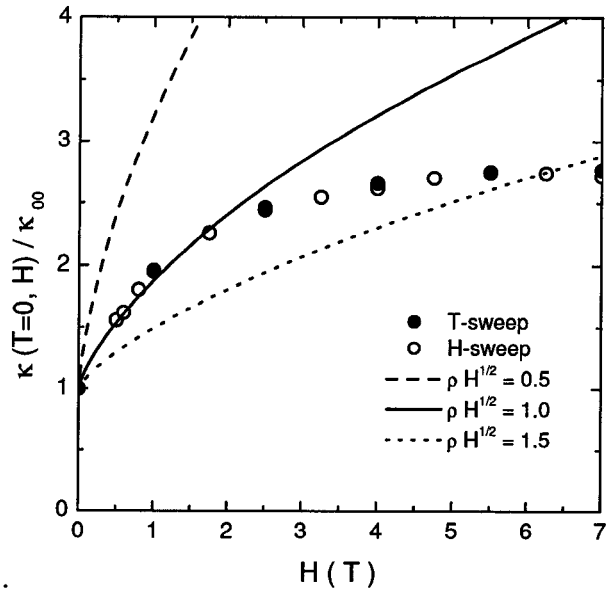

Figure 7.13: The thermal conductivity of Tl-2201 as a function of magnetic field and normalized to its value at $H = 0$. The full circles are obtained by extrapolating to $T = 0$ while the empty circles come from a field sweep at $T = 150$ mK. The expected behavior is given by Eq. 7.3 and the best fit is obtained with $\rho\sqrt{H} = 1$.

ual resistivity. This showed that our samples are in a moderately dirty regime with $\hbar\Gamma/k_BT_c \simeq 0.4$. At finite Γ, corrections to Eq. 7.2 give an increase in κ_0/T [86]. Assuming $\Delta_0 = 2.14\ k_BT_c$, the correction for $\hbar\Gamma/k_BT_c = 0.4$ is by a factor of approximately 1.5 [86]. Thus the correct value of v_F/v_2 is probably closer to $270/1.5 = 180$ [1]. It will be interesting to pursue studies of the effect of inducing additional disorder on these samples.

It is interesting to note that this value of Γ is consistent with the magnitude of the measured field dependence of κ at low H [91]. Let us first note that a good quantitative agreement was found in Zn-doped YBCO [88]. Although one expects roughly a field dependence which is roughly proportional to $\sqrt{H}$, the proper relation has the following form:

$$\frac{\kappa_{00}/T}{\kappa(0,H)/T} = \frac{\rho^2}{\rho\sqrt{1+\rho^2} - sinh^{-1}\rho} \tag{7.3}$$

where ρ is given by $\rho = \sqrt{\frac{6\gamma^2 H_{c2}}{\pi\Delta_0^2 a^2 H}}$ in the dirty limit and where a is a geometrical constant

[1] Although it seems clear that Γ must be a sizable fraction of the gap maximum, the numerical estimate for Δ_0 used here (based on T_c) is open to question. In particular, a naive estimate of Δ_0 based instead on $H_{c2}(0)$ gives a significantly larger gap maximum.

close to 1. A fit of the low field data of Tl-2201 to this functional form gives $\rho\sqrt{H} = 1.0 \pm 0.1$ as seen in Fig. 7.13. This fit is reasonable only for $H < 2$ T as is expected with an upper critical field near 13 T. Note that this is a good indication that we are in the dirty limit ($\rho > 1$) through this whole field range. We can compare this fit to an estimate using $\hbar\Gamma/k_BT_c \simeq 0.4$. We get $\rho\sqrt{H} = 1.3$ using $\Delta_0 = 2.14\ k_BT_c$, $\gamma = 0.61\ \sqrt{\hbar\Gamma\Delta_0}$, $H_{c2} = 13$ T and $a = 1$. This quantitative agreement to theoretical predictions lends credibility to both our data and to the theory which describes it.

The doping dependence of the zero temperature thermal conductivity has been investigated recently in LSCO and YBCO [243, 63]. It has provided a way to probe the nodes of the gap and, indirectly, the gap maximum (assuming it has the simplest d-wave shape). From optimal doping and in the overdoped side of the phase diagram, it seems that the standard BCS relation between gap magnitude and transition temperature, $\Delta_0 \propto T_c$, holds well (although see Appendix D). Indeed, in optimally-doped YBCO ($T_c = 93$ K) and Bi-2212 ($T_c \simeq 90$ K), it is found that $v_F/v_2 = 14$ and 19, respectively [263]. (The value of 19 for Bi-2212 agrees very well with the value of 20 obtained from ARPES measurements of v_F and v_2 separately [263, 87].) Note that preliminary measurements on optimally-doped Tl-2201 give a value of $v_F/v_2 \simeq 17$ [266]. With the assumption that $\Delta = \Delta_0 cos2\phi$ (giving $\Delta_0 \propto \hbar k_F v_2/2$), and that both v_F and k_F do not change as a function of doping [87, 130, 265], we can see that Δ_0 scales with T_c on the overdoped side of the phase diagram.

This picture breaks down on the underdoped side of the phase diagram as described by Sutherland *et. al.* [63]. There, the extracted gap maximum is seen to grow with underdoping while T_c is reduced. The latter agrees instead with reported values of the pseudogap [267, 268, 269, 270]. It is therefore identified to it and constitutes the first evidence of the pseudogap at very low energies. This has been taken as evidence that the pseudogap must have a d-wave symmetry with a linear density of state which leads to the conclusion that the pseudogap is most likely of superconducting origin.

In summary, we have found a large residual linear term in the thermal conductivity of overdoped Tl-2201. It is in quantitative agreement with BCS theory for a d-wave superconductor and provides the first experimental evidence that d-wave superconductivity is maintained at such a high level of overdoping. There, the gap maximum scales with T_c, as observed on the overdoped side of the phase diagram. This picture breaks down on the underdoped side where the low energy excitations are governed by the pseudogap which is concluded to be of superconducting origin.

7.6.2 Limit on a subdominant order parameter

Several authors have proposed the existence of a quantum critical point (QCP) within the superconducting dome in the phase diagram of cuprates, either as a theoretical prediction [271] to explain the diagram itself or as suggested in various experiments [210]. Its location is usually taken to be near optimal doping, in the neighbourhood of $p = 0.2$. Although there is much evidence for its location, the nature of the QCP is still under debate. If it is associated with a change in the symmetry of the superconducting order parameter, Vojta *et al.* have argued that the most likely scenario is a transition from a pure $d_{x^2-y^2}$ state to a complex order parameter of the form $d_{x^2-y^2} + ix$, where x can have either s or d_{xy} symmetry [28, 272]. Dagan and Deutscher have recently reported a split zero-bias anomaly in their tunneling on Y-123 thin films as soon as the material is doped away from optimal doping, a feature which they attribute to the appearance of a complex component to the order parameter in the bulk [273, 274]. The presence of a subdominant component ix in the order parameter causes the nodes to be removed, as the gap can no longer go to zero in any direction. The observation of a residual linear term in the thermal conductivity, a direct consequence of nodes in the gap, therefore excludes the possibility of any such subdominant order parameter. (More precisely, since our measurement goes down to 100 mK, it puts an upper bound on the magnitude of $|x|$ relative to $|d_{x^2-y^2}|$ at about 0.5 %.) Moreover, there is no subdominant order parameter in Tl-2201 at optimal doping [26]. In fact, a residual linear term is observed throughout the phase diagram in LSCO and YBCO [63, 243]. In other words, *if there truly is a QCP between optimal doping at* $p \simeq 0.16$ *and the critical point* $p_c \simeq 0.3$, *it does not appear to be associated with the onset of a complex component in the order parameter.*

7.7 Conclusion

In conclusion, the low-temperature transport properties of Tl-2201 with $T_c = 15$ K show that spin-charge separation does not occur in strongly overdoped cuprates. The normal state at $T \to 0$ satisfies the Wiedemann-Franz law perfectly, demonstrating that the only electronic excitations carrying heat and charge are Landau quasiparticles. The superconducting state obeys BCS theory in that the residual heat conduction is of the expected magnitude for a pure d-wave gap and the dependence of the low-energy spectrum on doping strongly suggests that the gap scales with T_c in the conventional way

for overdoped cuprates. This is the first clear experimental confirmation that a d-wave order parameter is retained in such highly overdoped cuprates. Also, the possibility of a sub-dominant order parameter (ix) is ruled out. Finally, Tl-2201 seems to be a textbook d-wave superconductor and it may serve as a reference for studies of the field dependence and the effect of disorder of the thermal conductivity.

Chapter 8

Conclusion

The field of superconductivity has lived a strong revival of interest in the past twenty years or so. One of the main reasons for this is the discovery of new materials where the superconductivity eludes comprehension. In this thesis, we have first studied the archetypal s-wave superconductor V_3Si to obtain a solid basis for comparison. We then moved to several other materials displaying a spread of new phenomena such as highly anisotropic gap functions, multi-band superconductivity and the rich physics of the high T_c cuprates. To do so, we have performed systematic studies of the electronic thermal conductivity at temperatures as low as 50 mK through their vortex states and into their normal states with the help of magnetic fields of up to 13 T.

In V_3Si, we were able to study the behavior of the thermal conductivity of an extreme type II supercondutor at very low vortex densities for the first time. It was found that it obeys the expected behavior for localized states tunneling between the vortex cores. This also provided a basis for comparison for the unconventional superconductors that were studied.

Indeed, the behavior in borocarbide $LuNi_2B_2C$ was found to deviate very strongly from this conventional picture and the thermal conductivity was found to increase linearly with field starting as soon as vortices entered the sample (at H_{c1}). This was assigned to an unprecedented anisotropy in the gap of a factor of at least 10. Our conclusion was later verified by other measurements which also lead to a better understanding of the shape of the gap. What's more, borocarbides are probably mediated by a conventional phonon mechanism. They serve as a great exemple of superconductors where the gap is highly anisotropic but has no topological nodes and reminds us not to assign prematurely a non-phononic mechanism to some anomalous behavior.

In the layered $NbSe_2$, we found two regimes for the level of delocalization of the quasiparticles. At low fields, the states are localized within the vortex cores whereas they get highly delocalized at a field much below H_{c2}. These two regimes were identified with the presence of two length scales for the superconductivity and, in turn, two gaps of different magnitudes (a factor of roughly 3) on two different sets of Fermi sheets. This makes $NbSe_2$ a multi-band superconductor much like the newly discovered MgB_2. Our results offered bulk evidence at low temperatures and complemented an angle resolved photoemission spectroscopy study which came to the same conclusion but was only performed at temperatures near T_c. Moreover, a number of previous anomalous reports are now understood naturally within this picture, such as the shrinking of vortex cores.

The overdoped cuprate superconductor $Tl_2Ba_2CuO_{6+\delta}$ with $T_c \simeq 15$ K was also studied in the superconducting state and all the way into its normal state, above H_{c2}. The Wiedemann-Franz law was verified with an experimental accuracy of 1%. This was the first solid evidence that the ground state of cuprates is a Fermi-liquid in the overdoped side of the phase diagram and displays no sign of spin-charge seperation. This result puts strong constraints on the possible mechanisms of superconductivity in high T_c cuprates and will surely help lead to a comprehensive understanding of the phase diagram. In the superconducting state, the BCS theory for a d-wave gap is satisfied quantitatively. This lends additional credibility to this formalism.

In summary, we have studied a wide variety of superconductors ranging from conventional V_3Si to the elusive high T_c cuprates and found very different behaviors of the thermal conductivity throughout the vortex state. This work has already stimulated much theoretical interest as well as other experiments which have confirmed our conclusions. It is my hope that this thesis will be used as a reference for the behavior of the thermal conductivity in the vortex state of unconventional superconductors.

Appendix A

Cryogenics techniques

A.1 Cryogenic techniques

In this Appendix, we will discuss the technical aspects of the most common cryogenic refrigerators: ^{4}He, ^{3}He and dilution refrigerators. They typically reach temperatures of 1 K, 0.3 K and 0.01 K respectively. All of these were used for this thesis.

A.1.1 ^{4}He refrigerator

A ^{4}He refrigerator is the simplest form of cryogenic refrigerators that go below liquid nitrogen temperature (77 K). It typically reaches a temperature of 1.2 K . It is also used as the first cooling stage in more elaborate refrigerators as described below. In our lab, our use of such a refrigerator is mostly for characterization purposes: it is easy to use, has a low helium consumption and a short turnaround time.

Principle of operation The first step for cooling to or below 4 K is to immerse the refrigerator in liquid helium which has a temperature of 4.2 K at atmospheric pressure. The temperature is then lowered by decreasing the pressure of the helium bath, or, in other words, pumping on it. This has the effect of taking away the most energetic particles of the liquid, the ones that form the vapor pressure (which have the most kinetic energy). This process is very important to understand as it is also used with slight (but important) variations for the refrigerators we will discuss below.

Design The design that we use is seen in Fig. A.1 and is well described in [275]. The sample stage is concealed in a vacuum can called the IVC (inner vacuum can). This is

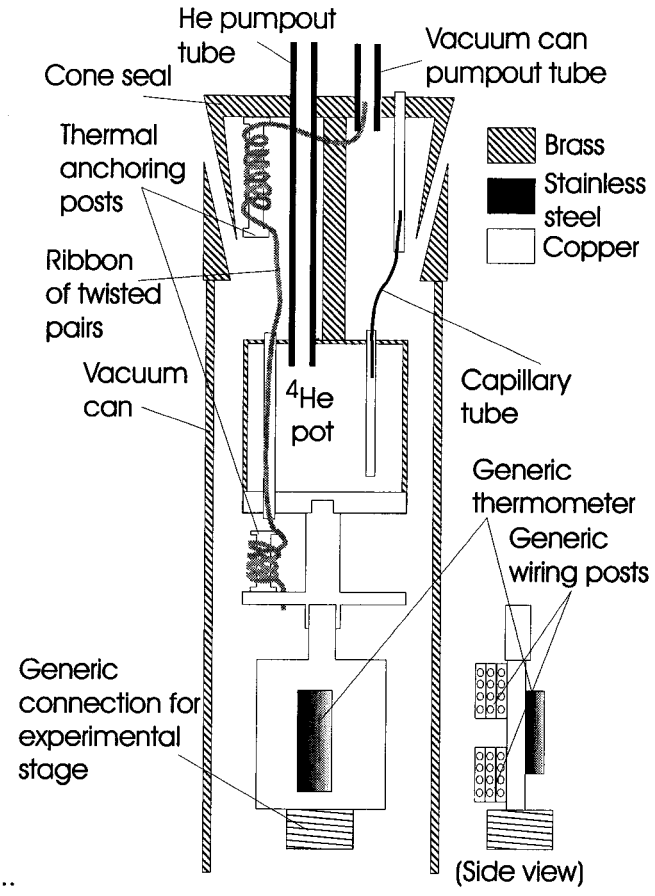

Figure A.1: The IVC of our ^{4}He refrigerator. This design is well explained in [275] and in the text.

in contrast to other designs where the experiment sits directly in the liquid.

Also, instead of pumping on the helium bath (which would be costly and inefficient), the cryostat is designed with a pot opened at one end to the helium bath and to a pumping line on the other. This will allow the pot to fill with liquid helium after which, pumping on this small volume of liquid will be enough to cool the experimental stage.

However, the task is not that simple. If one wishes to reach 1 K, the main concern is to reduce the heat leak to the 1 K pot and the experimental stage. These heat leaks come from (i) the helium bath which stays at 4.2 K, and (ii) the wires which go from room temperature to the 1 K stage. For (i), several steps are taken: one needs a good vacuum in the IVC to short out the heat channel from the bath to the experimental stage that comes from surrounding gas. Next, the 1 K pot is connected to the cone seal

via a brass link which is a poor conductor of heat. Finally, we use a very thin and long stainless steel capillary tube to fill the pot with helium. Stainless steel is also a very poor heat conductor. The size of the tube is determined to provide a perfect impedance: a small enough flow so as not to create a strong thermal link to the helium bath, but large enough to fill the pot at the same rate as it is depleted by pumping on it. As a note, one can use a needle valve instead of a capillary. It has the advantage of being a variable impedance but makes the design more complex. For (ii), we use thermalizing anchors at both the 4 K stage and the 1 K stage. We are also careful in our choice of wires: we use highly resistive alloys (manganin and constantan) whenever possible and copper ones (very good conductors of heat) only when necessary, for example, to measure the resistivity of low resistance samples.

The 1 K refrigerator used here is also equipped with generic thermometry that allows the use of several experimental stages which can also be used in a ^{3}He system.

A.1.2 ^{3}He refrigerator

A ^{3}He refrigerator has a typical base temperature of 0.3 K. The principle is identical: lowering the pressure of a cold liquid. In practice, one uses both a ^{4}He pot as a first cooling stage to condense ^{3}He (1.2 K), and an additional ^{3}He pot to reach 0.3 K. A lower temperature is reached by pumping on ^{3}He simply because the vapor pressure is higher for this isotope of helium. The design is more complex in that it requires a closed pumping system for ^{3}He due to its high cost. It is also more elaborate in the sense of properly isolating each stages of the cryostat (4 K, 1.2 K and 0.3 K.).

A.1.3 Dilution refrigerator

A dilution refrigerator has a typical base temperature of 10 mK. It is more complex, harder to use and has a longer turnaround time than the two refrigerators described above.

Principle Again, a dilution refrigerator is equipped with a ^{4}He pot as a first cooling stage. However, one can reach 10 mK by pumping on a mixture of ^{3}He and ^{4}He. Fig. A.2 shows the phase diagram for such a mixture. Below the triple point, the mixture will separate into two distinct phases: one has a high concentration of ^{3}He (the concentrated phase) and the other, a low concentration (the dilute phase). They correspond to points

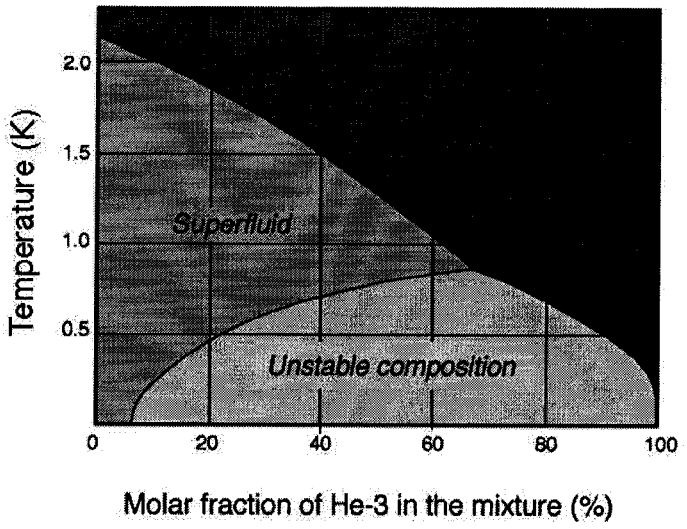

Figure A.2: ^{3}He-^{4}He phase diagram. Below the triple point, the mixture phase separates into a ^{3}He rich phase (right equilibrium line) and a ^{3}He dilute phase (left equilibrium line). The operation of a dilution refrigerator involves "diluting" the ^{3}He dilute phase.

on the equilibrium line which are respectively to the right and to the left of the triple point. However, in the dilute phase, the concentration of ^{3}He can never go below 6.6% at any temperature. These two phases are separated by a boundary much as oil and water are at room temperature. The cooling process involves *"diluting"* the ^{3}He dilute phase, that is, reduce its concentration of ^{3}He. The system will then be out of equilibrium. To recover it, ^{3}He will have to migrate from the rich to the dilute phase and across the phase boundary. This will cost energy to these ^{3}He particles. It will be taken from the walls of the container of the helium mixture, cooling it down in the process. This can be continued ad-infinitum and to as low a temperature as is desired since there will always be at least 6.6 % ^{3}He in the dilute phase.

Design In practice, many considerations have to be taken into account. The main ones will be discussed here.

A schematic design is shown in Fig. A.3. Let us start by the dilution process and follow the flow of ^{3}He through its closed circulation path. Once the mixture has been cooled below the triple point of the phase diagram (Fig. A.2), the phase separation will occur in the mixing chamber (MC). The ^{3}He rich phase floats above the ^{3}He dilute phase. The latter will also have a phase boundary in the still. This is achieved by a proper design and by using the correct amount of helium mixture. Diluting the ^{3}He dilute phase will

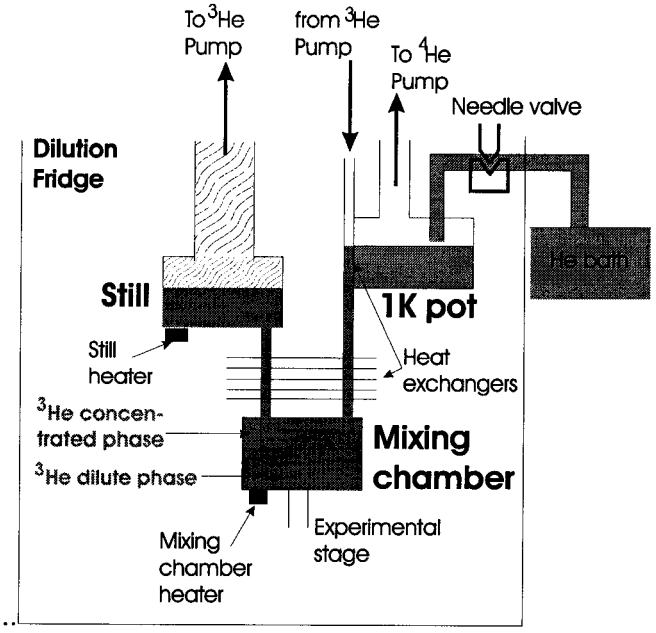

Figure A.3: Schematic of a dilution refrigerator. The principle of operation is described in the text.

be done by pumping on its boundary which is in the still (note that it is mostly ^{3}He that will evaporate due to its higher vapor pressure). This process is sometimes accelerated and intensified by applying heat onto the still to help evaporate ^{3}He.

Once this is done, the process described above will take place and the walls of the MC will be cooled. It is crucial to have an efficient process for the heat to be transferred from the walls of the MC to the ^{3}He which is in the rich phase. This is achieved by using a sintered silver powder on these walls which will increase the contact area of the ^{3}He rich phase and the walls. The efficiency of this process can limit the base temperature of a dilution refrigerator.

Also, since one reduces the concentration of ^{3}He in the rich phase, it must be replenished, otherwise the process cannot continue. To do so, the ^{3}He that is pumped away from the dilute phase is then injected back directly into the ^{3}He rich phase. However, it must first be pre-cooled otherwise, it will warm the MC. The first stage of precooling involves the 1 K pot. It will cool the ^{3}He from room temperature to 1.2 K and condense it back to a liquid phase. Heat exchangers are then used to cool the incoming ^{3}He further to the same temperature as the mixture. It then leaks back into the ^{3}He rich phase and the process can continue.

Finally, the temperature of the MC can be varied and controlled by directly heating it. This provides a variable temperature cryostat with a base temperature of typically 10 mK.

A.1.4 Summary

In summary, experiments can be performed at temperatures ranging from 0.01 K to room temperature. In may instances, a dilution refrigerator is used to freeze out various mechanisms which cloud the physics that we wish to study. This "freezing out" may be in the form of reducing thermal fluctuations such that one reaches a regime where quantum mechanical effects are most visible, or, in our case, to reduce (or "freeze") the contribution of phononic thermal conductivity. However, a ^{4}He refrigerator is often sufficient to perform characterization experiments.

Appendix B

Heat losses

The problem of heat losses is central in a thermal conductivity experiment. This appendix will serve to give a quantitative analysis of the losses due to heat in both the dilution refrigerator and ^{4}He refrigerator that have been used for this thesis.

B.1 Dilution refrigerator

As explained in the text, heat losses can have several sources: through the measurement wires (conduction), via radiation to the walls of the cryostat (radiation) or through gas in the inner vacuum chamber (IVC) (convection). The latter two mechanisms are negligible for experiments below 1 K (see the section for the ^{4}He refrigerator) unless there is a leak in the inner vacuum chamber. Only the conduction channel is left and will be analyzed below.

Fig. B.1a shows a detailed diagram of the thermal conduction paths. The discussion will be fully analogous to one of a electrical diagram. It is worth noting that the heat current $\dot{Q}$ stems from the heater which acts as a constant current source. The thermal paths are represented as thermal resistances and denoted by $W = 1/K$ (with K being the thermal conductance).

The thermal resistance of these paths is estimated in Table B.1. It is obvious from these numbers that we can neglect $W3$ and $W4$ on the thermal path from the heater to the sample and $W4$, $W5$ and Wc from the path from the sample to the thermometer (note: This is important for the thermalisation of the thermometer as discussed in Chapter 3.). The diagram reduces then to that on Fig B.1b. There, we have $1/W7 \simeq 1/W1 + 1/W2$ and $1/W8 \simeq 1/W6 + 1/W2$ thus giving $W7 \simeq \frac{1.7\times10^{+6}}{T}$ mW K^{-1} and $W8 \simeq$

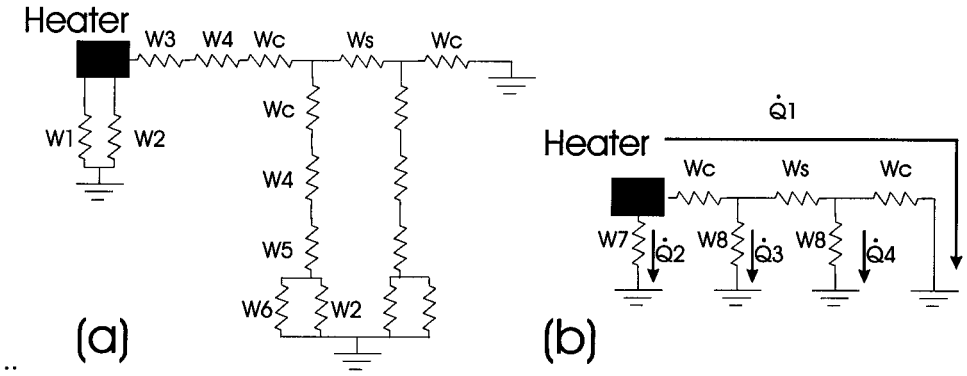

Figure B.1: The resistive diagram for the dilution refrigerator thermal conductivity setup. (a) Extensive diagram showing the full paths for heat conduction: W1 = 2 PtW wires in parallel; W2 = 2 Kapton® film strips in parallel; W3 = Interface between heater and Ag foil (Ge varnish); W4 = Ag wire; Wc = contact to the sample; Ws = sample; W5 = interface from the wire to the thermometer (see Fig. 3.6); W6 = 4 PtW wires in parallel. (b) A simplified version of the diagram taking into account which thermal resistances are negligible. The heat loss will be given by $\frac{\dot{Q}_2+\dot{Q}_3+\dot{Q}_4}{\dot{Q}_1}$.

$\frac{0.9\times10^{+6}}{T}$mW K^{-1}.

The heat loss analysis is now substantially simplified. As shown on Fig. B.1b, there are three heat currents that will flow in our diagram. The relative amount of heat loss is given by $\frac{\dot{Q}_2+\dot{Q}_3+\dot{Q}_4}{\dot{Q}_1}$. If one assumes that $\dot{Q}_1 \gg \dot{Q}_2+\dot{Q}_3+\dot{Q}_4$,the n a further simplification can be made and yields $\frac{\dot{Q}_2+\dot{Q}_3+\dot{Q}_4}{\dot{Q}_1} = \frac{Wc+Ws+Wc}{W1} + \frac{Ws+Wc}{W2} + \frac{Wc}{W2}$. (As a note, both the thermal resistance of the sample and of the contact nearest the cold base are actually measured. For the latter, instead of using the thermal gradient across the sample, we use the gradient across the cold thermometer and the base temperature. We need then to assume that the hot contact has roughly the same value as the cold contact.)

This analysis is done for several samples in Fig. B.2. The level of heat loss stays below the 1 % level except for $NbSe_2$ in $H = 0$ where it reaches 3 %. This analysis shows that the heat loss in our dilution refrigerator setup can be neglected in most cases and reaches tolerably small values for the most resistive samples.

	w	t	l	κ (mW K^{-1} cm^{-1})	W (mW^{-1} K)
PtW wire	25 μm ø		16 cm	0.8 T	0.4 $10^{+7}/T$
Kapton® film	100 μm	7 μm	1 cm	6.5 $10^{-2}T$	2.2 $10^{+7}/T$
Vespel posts (SP1 type)	0.5 mm	0.5 mm	1 cm	18 $10^{-3}T^{1.2}$	0.22 $10^{+5}/T^{1.2}$
Ag Wire	50 μm ø		2 cm	1.25 $10^{+3}T$	0.8 $10^{+3}/T$
Interface 1	0.5 mm ø		5 mm		0.7/ Area [mm^2]T^3 $= 0.1/T^3$
Interface 2	2 mm		3 mm		0.7/ Area [mm^2] T^3 $= 0.1/T^3$

Table B.1: The thermal resistance of the various components of the dilution refrigerator thermal conductivity setup. These values are correct for $T < 1$ K [107] . Interface 1 and 2 designate respectively the interface from the heater to the Ag foil $W3$ and from each thermometer to the thermal Ag wire $W5$ (see Fig. 3.6). For these, we have taken the value for a glue-copper interface [107], the closest data available to a Ge varnish-Kapton® interface.

B.2 ^{4}He refrigerator

Here the heat loss analysis is more complex for several reasons: (i) there may be different contributions (conduction, radiation and convection), (ii) the temperature range is much larger and the thermal conductance of the different samples varies significantly. For these reasons, it is wise to have the relevant numbers for our setup at hand and check if we suffer from heat losses case by case. This section will survey these relevant numbers and will show examples of measured samples.

B.2.1 Conduction

The analysis as done for the dilution refrigerator can be done here. Fig. B.3 shows the effective resistive diagram. For this, we have neglected a number of thermal interface resistances because they are thought to be negligible due to the temperature range and their relatively large cross section.

The measurement wires are 12 μm diameter PtW with a length of 1 cm. They have an electrical resistance of roughly 30 Ω. The wire that is used between the heater and the sample is usually 50 μm diameter Ag wire with a length of typically 1 cm. In Fig. B.4,

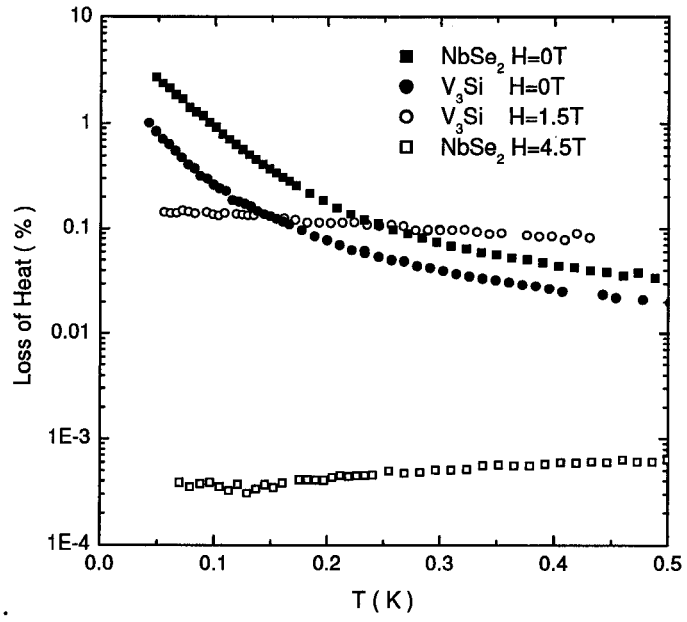

Figure B.2: The relative heat loss is shown as a function of temperature from 40 mK < T < 500 mK for V_3Si and $NbSe_2$ in zero field (the most resistive samples measured) and in $H = 1.5$ T for V_3Si (the most resistive sample at higher temperatures) and $H = 4.5$ T, in the normal state of $NbSe_2$ (as an example of a sample with a high conductivity). The level of heat loss is below the 1 % level in all cases except for $NbSe_2$ where is reaches 3 % at the lowest temperature.

we have plotted the heat loss as a function of temperature for V_3Si as an example. It remains below 0.1 % throughout the range of temperature. To do this, we have assumed that the thermal conductivity of the PtW wire has the same temperature dependence as that of silver.

B.2.2 Radiation

It is difficult to obtain a general analysis of the heat loss for a setup. It requires to knowing the characteristics of the samples that is measured, or more precisely, the thermal resistance of its contacts and of $W1$ from Fig. B.3 with respects to that of the sample itself. Indeed, we typically always use a temperature gradient across the sample of $\Delta T/T = 4$ % but the gradient it creates across the contacts and across W1 can vary widely. As a result, the temperature difference between "heat on" and "heat off" for the sample, the thermometers and most importantly, the heater will vary. The heat current to which the loss must be compared also varies depending on the thermal resistance of

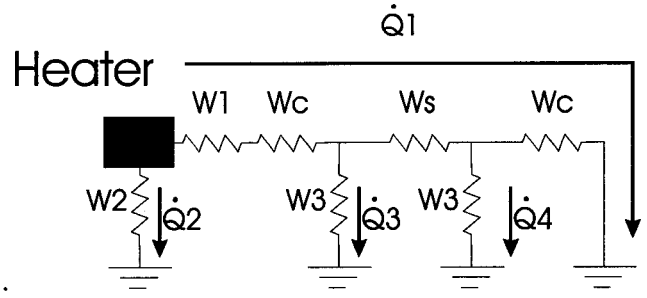

Figure B.3: The effective resistive diagram for the ^{4}He refrigerator thermal conductivity setup with the following thermal paths: W1 = Ag wire from the heater to the sample; $W2 = 3$ PtW wire in parallel; $W3 = 5$ PtW wires in parallel; Wc = contact; Ws = sample. The heat loss will be given by $\frac{\dot{Q}_2+\dot{Q}_3+\dot{Q}_4}{\dot{Q}_1}$.

the sample such as to obtain $\Delta T/T = 4$ %.

The best way to present this analysis is to show the heat current that would be lost for a number of different temperature profiles. This can then be compared to the heat applied to any sample as long as the temperature profile is known.

To simplify the analysis, we will make a series of assumptions:

- We neglect the heat lost via the sample itself and only consider the one lost via the heater and the thermometers. They have respectively surface areas of roughly 12 mm^2(2 sides of 2 mm by 3 mm) and 5 mm^2(2 sides of 1.5 mm by 1.5 mm).

- The thermal resistance of each contact is the same and is proportional to the thermal resistance of the sample. This is usually a good approximation [1]. The constant of proportionality is usually between 0.5 and 2.

- The thermal resistance $W1$ (see Fig. B.3) is proportional to that of the sample.

- The temperature gradient across the sample is $\Delta T/T = 4$ %.

- The emissivities of the heater and the vacuum can are equal to 1 (the worse possible scenario).

[1]This approximation is valid not necessarily when good electrical contacts are obtained as phonons will often dominate the transfer of heat across the contacts at high temperature. More important is the geometry of the sample: its thermal *conductance* must be comparable to that of the contacts. Long samples with a thin cross-section are therefore favorable.

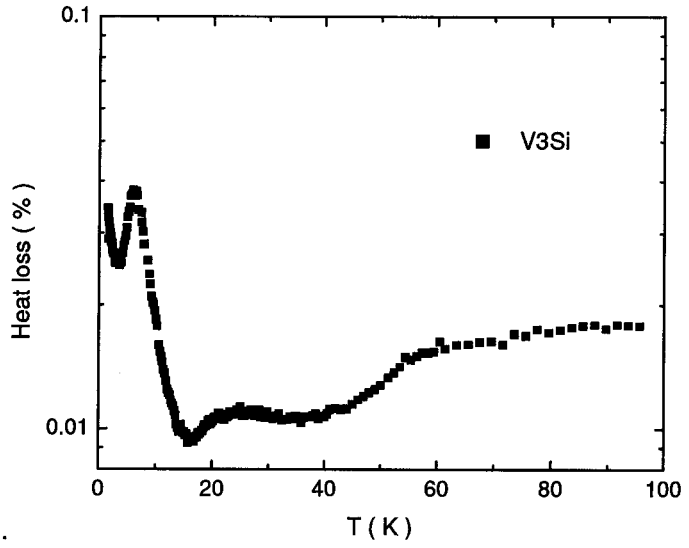

Figure B.4: Heat loss in the dipper due to the measurement wires for V_3Si.

The amount of heat lost via radiation $\dot{Q}_{\text{radiation loss}}$ is plotted in Fig. B.5 for different values of $W1/W_{sample}$ and of $W_{contact}/W_{sample}$ as a function of temperature. The heat that was applied to a V_3Si sample is also shown. It must be first noted that the heat lost is negligible at low temperature. However, it increases very fast at higher temperature. To minimize the heat loss, it is important to have "good contacts", or more accurately, a small $W_{contact}/W_{sample}$. Also, a smaller heat gradient will decrease any radiative heat loss. It is also interesting to note that one must be very careful in the choice of $W1$: it may seem counter-intuitive but for the same $W1$, a sample with lower resistance may suffer a greater heat loss. We are usually in the case where $W1/W_{sample} < 0.1$.

For V_3Si, we are in the situation where $W_{contact}/W_{sample} = 0.5$ and $W_1/W_{sample} = 0.01$. This leads to a heat loss of 3×10^{-3} Watt, roughly 3 % of the heat applied ($\dot{Q} = 8 \times 10^{-4}$). It is safe to say that there is minimal heat loss up to 100 K.

Note that heat loss via radiation has the distinct signature of giving a measured κ that is dependent of the heat that is applied. This is simply because the higher the applied heat, the higher the temperature of the components are and the higher the heat loss. Seeing the present analysis has taken a number of assumptions, a direct way to know whether we suffer from heat losses is to verify that κ is independent of applied $\dot{Q}$.

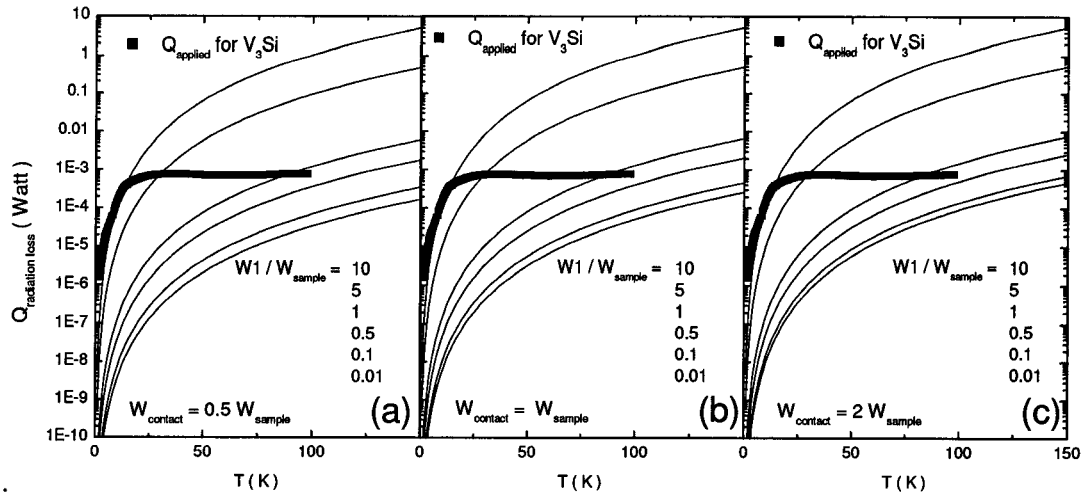

Figure B.5: Relative heat loss in the dipper due to radiation for different parameters, namely, $W1/W_{sample}$. Panel a, b and c use respectively $W_{contact}/W_{sample}$ equal to 0.5, 1 and 2. The heat current applied to a V_3Si sample is shown for comparison. For heat loss by radiation to be negligible, one must have $\dot{Q}_{rad} \ll \dot{Q}_{applied}$.

B.2.3 Convection

The heat loss through convection is very low as long as one keeps a good vacuum in the IVC. A typical value for this vacuum is $P = 10^{-6}$ mbar. The same analysis is done as for the case of radiation but with the following formalism:

$$\dot{Q}_{convection}\ [\text{Watt}] \simeq 0.02\ \text{a}\ \text{A}\ [\text{cm}^2]\ \text{P}\ [\text{mbar}]\ \Delta\text{T}\ [\text{K}] \tag{B.1}$$

where ΔT is the difference of temperature of the components (heater and thermometers) when the heat is applied and when it is off. We use $a = 1$, the worse possible case. This is shown as a function of the same parameters as for the radiation analysis in Fig. B.6. As is immediately obvious, even in the worse cases, this contribution is completely negligible.

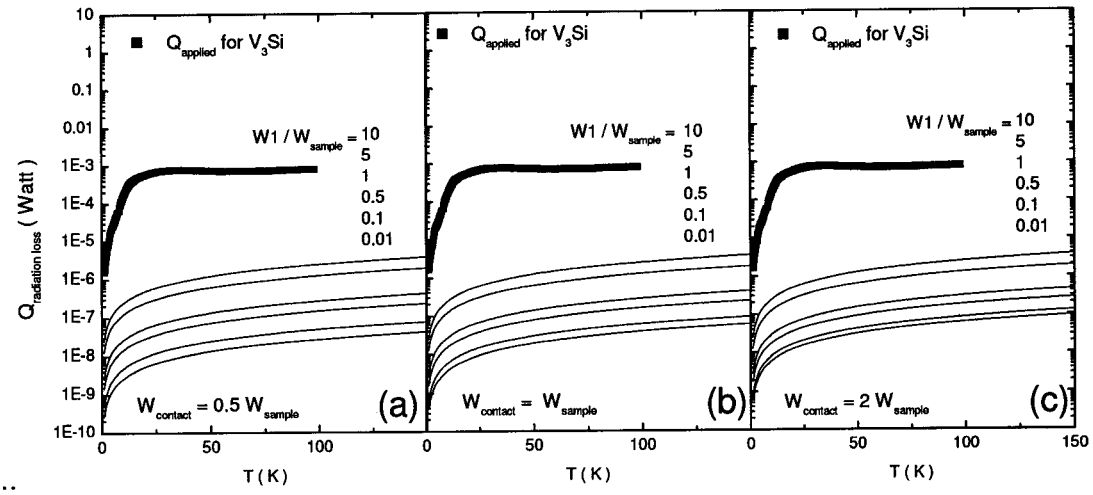

Figure B.6: Heat loss in the dipper due to convection for different parameters, namely, $W1/W_{sample}$. Panel a, b and c use respectively $W_{contact}/W_{sample}$ equal to 0.5, 1 and 2. The heat current applied to a V_3Si sample is shown for comparison.

Appendix C

Contacts and oxygenation of Tl-2201

Obtaining good quality contacts on cuprate superconductors have proven to be difficult as an insulating oxyde layer is often found on the surface of crystals. It is usually necessary to anneal the contacts (such that the silver diffuses into the crystal) for them to be metallic. What's more, the samples of Tl-2201 that were used were extremely small, making it difficult to make such contacts. In addition, the samples had to be annealed in oxygen to fix the doping level. The procedure used is described in this appendix.

The contacts were made with Epo-Tex H20E silver epoxy by first applying it to the sample using a thin 12 micron gold wire. Care was taken to apply the epoxy on the side (thickness) of the sample for both current and voltage pads. The epoxy was then hardened in air at 150 °C for a few minutes. To obtain good metallic contacts, the sample then had to be annealed in 1 bar of flowing O_2 at a temperature of 450 °C for one hour, to ensure diffusion of the silver into the sample. The oxygenation procedure (to set the oxygen content or doping level) was done immediately after in the same conditions (same oven and same flow of oxygen) but a reduced temperature of 350 °C for 48 hours. A complete phase diagram of Tl-2201 can be found in [276] but the one relevant for our crystals is found in [218]. The oxygenation setup is shown in Fig. C.1: the sample was placed in a clean quartz crucible (designed by Harry Zhang and myself) which was put in a quartz tube (both of them were made by the glass blowing shop at the university of Toronto). The oxygen atmosphere was obtained by continuously flowing clean oxygen from the top of the quartz tube and having it escape from the other side to air (although through regular oil both to avoid a backflow of air and to avoid a vapor pressure of the liquid which may contaminate the oxygen atmosphere). The quartz tube was introduced through a hole at the top of a muffle furnace (Thermolyne model F48000). We used high-

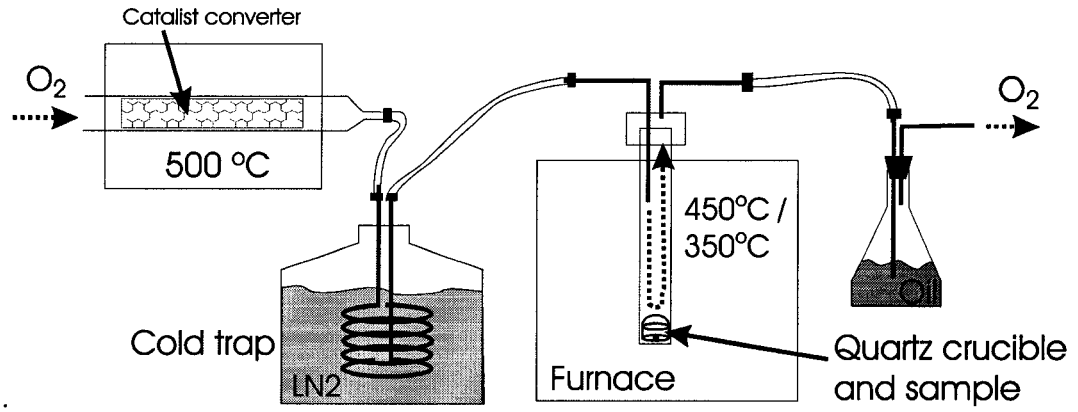

Figure C.1: The oxygenation setup used to anneal the silver epoxy contacts (450 °C for 1 hour) and set the oxygen content (350 °C for 48 hours) of Tl-2201 crystals as described in the text.

purity 5N oxygen but cleaned it further by first putting it through a catalyst converter (usually used to filter the exhaust from cars) which was heated to 500 °C for maximum efficiency and then cryogenically filtering it through a liquid nitrogen cold trap.

After the annealing procedure, we attached measurement leads onto the sample. 25 μm silver wires were used. They were "glued" to the current and voltage pads using Dupont 4929N silver paint. For this delicate work to be possible, we used 1-acetoxy-2-butoxyethane with chemical formula $C_8H_16O_3$ (from Sigma Aldrich) as a solvent for the silver paint. It has the advantage of not drying very quickly, thus giving enough time to apply very small beads of paint onto the contacts. These were applied under a microscope with a tool made of a 15-25 μm wire. Note that great care was taken to have a good mechanical contact between the silver wire and the contact pads. This ensures a better electrical contacts.

This procedure resulted in typical contact resistance of the order of 0.1 Ω at low temperature and homogeneous oxygen content with transition temperature as narrow as 1 K.

Appendix D

Penetration depth for overdoped Tl-2201

In the BCS formalism for a d-wave superconductor, the thermal conductivity and the penetration depth are related directly as they both depend on the ratio of v_F/v_2. This has been worked out in detail by Durst and Lee [85] who show that while κ_{00}/T will be independent of Fermi-liquid and vertex corrections, the penetration depth will not, and may contain an additional "fudge" factor named α^2 stemming from Fermi liquid corrections. The resulting relations for these quantities are:

$$\kappa_{00}/T = \frac{k_B^2}{3\hbar}\frac{n}{d}(\frac{v_F}{v_2} + \frac{v_2}{v_F}) \simeq \frac{k_B^2}{3\hbar}\frac{n}{d}(\frac{v_F}{v_2}) \tag{D.1}$$

$$\frac{\rho_n(T)}{m^*} = \frac{c^2\lambda^{-2}(T)}{4\pi e^2} = \frac{2ln2}{\pi}\frac{k_B}{\hbar^2}\frac{n}{d}\alpha^2(\frac{v_F}{v_2})T \tag{D.2}$$

where n/d is the average distance between CuO_2 planes, v_F and v_2 are the velocities associated with a d-wave gap, ρ_n is the normal fluid density, m^* is the effective mass and λ is the penetration depth. From these, we obtain the following relation between the slope of the temperature dependence of the penetration depth at low temperature and the thermal conductivity:

$$\frac{d\lambda^{-2}(T)}{dT} = -2.93 \times 10^{13}\ \kappa_{00}/T\ \alpha^2 \tag{D.3}$$

with λ in meters and κ_{00}/T in W K^{-2} m^{-1}. This relation has been applied at optimal doping in both YBCO and BSCCO [263] giving values of α^2 being 0.46 for YBCO and 0.43 for BSCCO, while $\alpha^2 = 1$ when there are no Fermi liquid corrections.

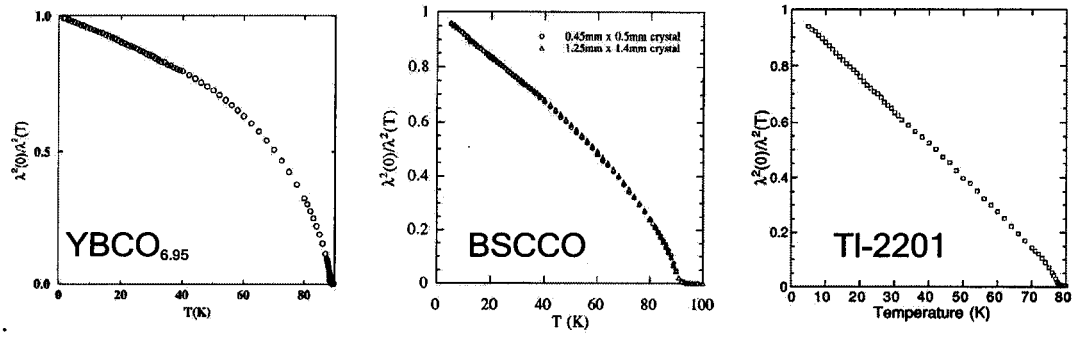

Figure D.1: The penetration depth plotted as $\lambda^2(0)/\lambda^2(T)$ versus temperature for optimally doped YBCO [277, 278], BSCCO [279] and Tl-2201 [215].

In the light of the quantitative agreement of our thermal conductivity data in strongly overdoped Tl-2201 assuming a pure d-wave gap and the weak coupling relation for d-wave superconductors ($\Delta_0 = 2.14\ k_B T_c$), it is worthwhile investigating whether or not the penetration depth is also in accordance with this analysis. Although there is no good quality data on the temperature dependence of λ in overdoped Tl-2201 (see [175] for the only report to date), we can still conclude that a strong discrepancy occurs on the basis of the celebrated Uemura plot [280, 281].

It was found very early on that the zero temperature superfluid density ($\rho_s(0)/m^* \propto \lambda^{-2}(0)$) scales with T_c both on the underdoped and the overdoped side of the phase diagram of cuprates. This was a great surprise as the superfluid density would be expected to scale with the normal state carrier density (proportional to the doping) but instead, this picture breaks down for overdoped cuprates. For our purposes, it suffices to realize that the zero temperature penetration depth of overdoped cuprates and Tl-2201 in particular is known and scales with T_c. It is then also natural to argue that it would be unphysical to have a negative curvature for $\lambda^{-2}(T)$ [1].

Let us start with optimally doped samples. For these, $\lambda^{-2}(T)$ has been measured reliably [215] and is shown in Fig. D.1. Along with it are the same figures for optimally doped YBCO and BSCCO. In all cases, we see the typical linear temperature dependence at low T. However, this slope extrapolates to a temperature near T_c for Tl-2201 and higher for both BSCCO and YBCO (to varying degrees). Using $\lambda(0) = 1650$ Å, we have $d\lambda^{-2}(T)/dT = -4.59 \times 10^{11}$ m^{-2}K^{-1} which leads to $\alpha^2\kappa_{00}/T = 0.16$ mW K^{-2}cm^{-1}.

[1] This is actually verified by these early experiments although the temperature dependence of $\lambda^{-2}(T)$ is surely not reliable [280, 281]

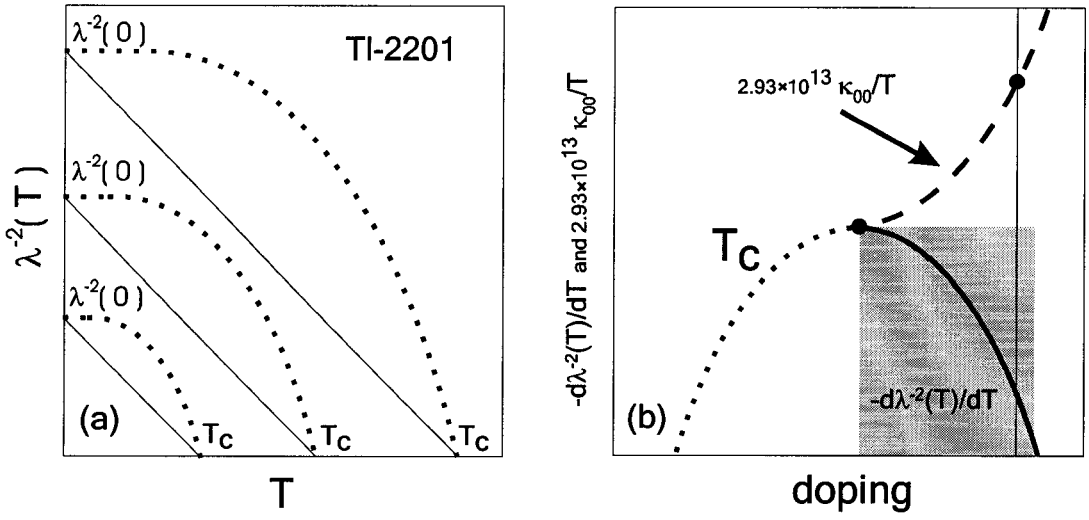

Figure D.2: (a) A schematic of the limiting behavior of the penetration depth as a function of temperature for various T_c using the fact that the zero temperature λ scales with T_c (the Uemura plot). (b) For overdoped Tl-2201, $-d\lambda^{-2}(T)/dT$ will lie inside the grey box according to our analysis. In contrast, the corresponding value of the thermal conductivity $2.93 \times 10^{13}\kappa_{00}/T$ (in the appropriate units) drawn schematically with points being measured data and the broken line is obtained using the BCS analysis with a simple d-wave gap which leads to $\kappa_{00}/T \propto 1/\Delta_0 \propto 1/T_c$. The discrepancy may be accounted for by the Fermi-liquid correction factor α^2 but this one will have to be smaller than 0.1 for a $T_c \simeq 15$ K which may be unphysical.

Preliminary results on optimally doped Tl-2201 give $\kappa_{00}/T \simeq 0.09$ mW K^{-2}cm $^{-1}$ and leads to $\alpha^2 \simeq 1.8$ [?].

On the overdoped side, we use the following:

- $\lambda^{-2}(0)$ scales with T_c (Uemura plot). This can be written as $\lambda^{-2}(0) = \lambda^{-2}_{opt}(0)\ T_c\ /\ T_c^{opt}$ where *opt* stands for optimal doping.

- The slope at low temperature of $\lambda^{-2}(T)$i s between zero and $-1/T_c$, *i.e.* $\lambda^{-2}(T)$ has no positive curvature (the contrary would not be physical).

This is shown schematically on Fig. D.2a where the penetration depth is plotted against temperature for samples with different T_c. The solid lines shows the limiting slope at low temperature which yield no negative curvature and the dotted line shows the limiting case of a slope equal to zero. Note immediately that the limiting slope will have a constant

magnitude thus leading to the relation:

$$0 < \alpha^2 \kappa_{00}/T < \frac{1}{2.93 \times 10^{13}} \frac{1}{T_c^{opt}} \tag{D.4}$$

Since the slope of $\lambda^{-2}(T)$ for the optimally doped sample is $-1/T_c$, then $0 < \alpha^2 \kappa_{00}/T <$ 0.16 mW $K^{-2}cm^{-1}$ for overdoped Tl-2201. This is displayed in Fig. D.2b along with the expected dependence of κ_{00}/T using a pure d-wave gap and $\Delta_0 = 2.14\ k_B T_c$ which leads to $\kappa_{00} \propto 1/T_c$ (as seems to be the case according to our measurements). Indeed, we find $\kappa_{00}/T = 1.41$ mW $K^{-2}cm^{-1}$ for a sample with $T_c \simeq 15$ K, nearly a factor of ten larger than the maximum expected from our analysis of the penetration depth.

This picture mayb e reconciled if one assumes that the Fermi-liquid corrections (parametrized by α^2) becomes more pronounced ($\alpha^2 < 0.1$ for $T_c \simeq 15$ K) as one overdopes. It would imply that the quasiparticles are increasingly interacting which may be counter-intuitive if one believes that a more conventional Fermi-liquid is approached by overdoping.

It will therefore be interesting to obtain more reliable data for the penetration depth in overdoped Tl-2201 and the equivalent data for thermal conductivity. Once this is done, one may make more specific statements about the breakdown of the BCS picture of d-wave quasiparticles on the overdoped side of the phase diagram.

Bibliography

[1] L.N. Cooper. *Physical Review*, 104:1189, 1956.

[2] J. Bardeen, L.N. Cooper, and J.R. Schrieffer. Theory of superconductivity. *Physical Review*, 106:162, 1957.

[3] J. Bardeen, L.N. Cooper, and J.R. Schrieffer. Microscopic theory of superconductivity. *Physical Review*, 108:1175–1204, 1957.

[4] L.D. Landau. *Sov. Phys. JETP*, 3:925, 1957.

[5] P.G. de Gennes. *Superconductivity of Metals and Alloys.* Addison-Wesley, Reading, MA, 1989.

[6] L.P. Gor'kov. *Sov. Phys. JETP*, 9:1364, 1959.

[7] Neil W. Ashcroft and N. David Mermin. *Solid State Physics.* W. B. Saunders Company, 1976.

[8] N.E. Phillips. *Physical Review*, 114:676, 1959.

[9] Bardeen, G. J. Rickayzen, and L. Tewordt. *Physical Review*, 113:982, 1959.

[10] C.B. Satterthwaite. *Physical Review*, 125:873, 1962.

[11] L.C. Hebel and C.P. Schlichter. *Physical Review*, 107:901, 1957.

[12] A.A. Abrikosov. *Sov. Phys. JETP*, 5:1174, 1957.

[13] W.H. Kleiner, L.M. Roth, and S.H. Autler. *Physical Review A*, 133:1226, 1964.

[14] V.L. Ginzburg and L.D. Landau. *Zh. Eksp. Theor. Fiz.*, 20:1024, 1950.

[15] B.S. Deaver and W.M. Fairbank. *Physical Review Letters*, 7:43, 1961.

[16] R. Doll and M. Näbauer. *Physical Review Letters*, 7:51, 1961.

[17] C. Caroli, P.G. de Gennes, and J. Matricon. *Physical Letters*, 9:307, 1964.

[18] H.F. Hess *et al. Physical Review Letters*, 62:214, 1989.

[19] Harold F. Hess. *Scanning Tunneling Microscopy (edited by J.A. Stroscio and W.J. Kaiser).* Academic Press, San Diego, 1993.

[20] J. Lowell and J.B. Sousa. *Journal of Low Temperature Physics*, 3:65, 1970.

[21] N. Hayashi *et al. Physical Review Letters*, 77:4074, 1996.

[22] S.H. Pan, E.W. Hudson, A.K. Gupta, K.-W. Ng, H. Eisaki, S. Uchida, and J.C. Davis. *Physical Review Letters*, 85:1536, 2000.

[23] Y. De Wilde, M. Iavarone, U. Welp, V. Metlushko, A.E. Koshelev, I. Aranson, G.W. Crabtree, and P.C. Canfield. *Physical Review Letters*, 28:4273, 1997.

[24] H. Sakata, M. Oosawa, K. Matsuba, N. Nishida, H. Takeya, and K. Hirata. *Physical Review Letters*, 84:1583, 2000.

[25] M.R. Eskildsen, M. Kugler, G. Levy, S. Tanaka, J. Jun, S.M. Kazakov, J. Karpinski, and Ø. Fischer. *Physica C*, 385:169, 2003.

[26] C.C. Tsuei and J.R. Kirtley. *Review of Modern Physics*, 72:969, 2000.

[27] V.P. Mineev and K.V. Samokhin. *Introduction to Unconventional Superconductivity.* Gordon and Breach Science Publishers, 1999.

[28] M. Vojta, Ying Zhang, and Subir Sachdev. *Physical Review Letters*, 85:4940, 2000.

[29] H.W. Weber. *Anisotropy effects in superconductors.* Plenum Press, NY, 1977.

[30] Paul C. Canfield and George W. Crabtree. *Physics Today*, March:34, 2003.

[31] Yoshiteru Maeno, T. Maurice Rice, and Manfred Sigrist. *Physics Today*, 54:42, 2001.

[32] A.J. Leggett. *Review of Modern Physics*, 47:331, 1975.

[33] Robert Joynt and Louis Taillefer. *Review of Modern Physics*, 74:235, 2002.

[34] P.W. Anderson. *Science*, 235:1196, 1987.

[35] S.A. Kivelson, D.S. Rokhsar, and J.P. Sethna. *Physical Review B*, 35:8865, 1987.

[36] T. Senthil and Matthew P.A. Fisher. *Physical Review B*, 62:7850, 2000.

[37] A.V. Sologubenko, K. Giann, H.R. Ott, A. Vietkine, and A. Revcolevschi. *Physical Review B*, 62:R6108, 2000.

[38] A.V. Sologubenko, E. Felder, K. Giann, H.R. Ott, A. Vietkine, and A. Revcolevschi. *Physical Review B*, 2001:054412, 64.

[39] T. Lorenz, M. Hofmann, M. Gruninger, L. Freimuth, G.S. Uhrig, M. Dumm, and M. Dressel. *Nature*, 418:614, 2002.

[40] Jack Bass, William Pratt Pratt Jr., and Peter A. Schroeder. *Review of Modern Physics*, 62:645, 1990.

[41] R. Berman. *Thermal Conduction in Solids.* Clarendon Press, Oxford, 1976.

[42] Philip B. Allen. *Physical Review B*, 36:R2920, 1987.

[43] M. Gurvitch. *Physical Review Letters*, 56:647, 1986.

[44] K. Kadowaki and S.B. Woods. *Solid State Communications*, 58:507, 1986.

[45] M.J. Rice. *Physical Review Letters*, 20:1439, 1968.

[46] R.W. Hill, Cyril Proust, Louis Taillefer, P. Fournier, and R.L. Greene. *Nature*, 414:711, 2001.

[47] G. Wiedemann and R. Franz. *Annals of Physics*, 89:497, 1853.

[48] G.V. Chester and A. Tellung. *Proceedings of the Physical Society*, 77:1005, 1961.

[49] L. Smrcka and P. Streda. *Journal of Physics C*, 10:2153, 1977.

[50] M.J. Kearney and P.N. Butcher. *Journal of Physics C*, 21:L265, 1988.

[51] H. Suderow *et al.* *Journal of Low Temperature Physics*, 108:11, 1997.

[52] H.R. Ott, O. Marti, and F. Hulliger. *Solid State Communications*, 49:1129, 1984.

[53] A. Amato *et al. Journal of Magnetism and Magnetic Materials*, 63-64:300, 1987.

[54] M.A. Tanatar, S. Nagai, Z.Q. Mao, Maeno Y., and T. Ishiguro. *Physical Review B*, 63:064505, 2001.

[55] Etienne Boaknin, M.A. Tanatar, Johnpierre Paglione, F. Hawthorn, D. Ronning, R. W. Hill, M. Sutherland, Louis Taillefer, Jeff Sonier, S.M. Hayden, and J.W. Brill. *Physical Review Letters*, 90:117003, 2003.

[56] S. Belin and K. Behnia. *Physical Review Letters*, 79:2125, 1999.

[57] S. Kambe *et al. Journal of Low Temperature Physics*, 117:101, 1999.

[58] R. Ronning *et al.* To be published.

[59] J. Paglione *et al.* To be published.

[60] V. Bayot, L. Piraux, J.P. Michenaud, and J.P. Issi. *Physical Review Letters*, 65:2579, 1990.

[61] Philip D. Thatcher. *Physical Review*, 156:975, 1967.

[62] Joseph Callaway. *Physical Review*, 113:1046, 1959.

[63] Mike Sutherland, D.G. Hawthorn, R.W. Hill, F. Ronning, S. Wakimoto, H. Zhang, C. Proust, Etienne Boaknin, C. Lupien, Louis Taillefer, Ruixing Liang, D.A. Bonn, W.N. Hardy, Robert Gagnon, N.E. Hussey, T. Kimura, M. Nohara, and H. Takagi. *Physical Review B*, 67:174520, 2003.

[64] P. Lindenfeld and W.B. Pennebaker. *Physical Review*, 127:1881, 1962.

[65] P.H. Kes *et al. Journal of Low Temperature Physics*, 17:341, 1974.

[66] A.C. Anderson and S.C. Smith. *Journal of Physics: Chemistry of Solids*, 34:111, 1973.

[67] K. Yasui and T. Kita. *Physical Review Letters*, 83:4168, 1999.

[68] K. Yasui and T. Kita. *Physical Review B*, 66:184516, 2002.

[69] Kazumi Maki. *Physical Review*, 158:397, 1967.

[70] A. Houghton and K. Maki. *Physical Review B*, 4:843, 1971.

[71] Hiroaki Kusunose, T.M. Rice, and Manfred Sigrist. *Physical Review B*, 66:214503, 2002.

[72] Saša Dukan, T. Paul Powell, and Zlatko Tešanović. *Physical Review B*, 66:014517, 2002.

[73] C. Caroli and M. Cyrot. *Phys. Kondensierten Materie*, 4:9285, 1965.

[74] N.E. Hussey. *Advances in Physics*, 51:1685, 2002.

[75] Gianfraco Preosti, Heesang Kim, and Paul Muzikar. *Physical Review B*, 50:1259, 1994.

[76] T. Shiba. *Progress in Theoretical Physics*, 40:435, 1968.

[77] C. Kübert and P.J. Hirschfeld. *Solid State Communications*, 105:459, 1998.

[78] Ye Sun and Kazumi Maki. *Physical Review B*, 51:6059, 1995.

[79] L.S. Borkowski and P.J. Hirschfeld. *Physical Review B*, 49:15404, 1994.

[80] P.A. Lee. *Physical Review Letters*, 71:1887, 1993.

[81] M. Graf *et al.* *Physical Review B*, 53:15147, 1996.

[82] Louis Taillefer, Benoit Lussier, Robert Gagnon, Kamran Behnia, and Hervé Aubin. *Physical Review Letters*, 79:483, 1997.

[83] S. Nakamae, K. Behnia, N. Mangkorntong, M. Nohara, H. Takagi, S.J.C. Yates, and N.E. Hussey. *cond-mat/0212283*, 2002.

[84] K. Behnia, S. Belin, H. Aubin, F. Rullier-Albenque, S. Ooi, T. Tamegai, A. Deluzet, and P. Batail. *Journal of Low Temperature Physics*, 117:1089, 1999.

[85] A.C. Durst and P.A. Lee. *Physical Review B*, 62:1270, 2000.

[86] Y. Sun and K. Maki. *Europhysics Letters*, 32:355, 1995.

[87] J. Mesot *et al.* *Physical Review Letters*, 83:840, 1999.

[88] May Chiao, R.W. Hill, Christian Lupien, Louis Taillefer, Patrick Lambert, R. Gagnon, and P. Fournier. *Physical Review B*, 62:3554, 2000.

[89] Yuxing Wang, Bernard Revaz, Andreas Erb, and Alain Junod. *Physical Review B*, 63:094508, 2001.

[90] G.E. Volovik. *Sov. Phys. JETP Letters*, 58:469, 1993.

[91] C. Kübert and P.J. Hirschfeld. *Physical Review Letters*, 80:4963, 1998.

[92] Etienne Boaknin, R.W Hill, Cyril Proust, Louis Taillefer, and P.C. Canfield. *Physical Review Letters*, 87:237001, 2001.

[93] M.A. Tanatar, M. Suzuki, S. Nagai, Z.Q. Mao, Y. Maeno, and T. Ishiguro. *Physical Review Letters*, 86:2649, 2001.

[94] K. Izawa, H. Takahashi, H. Yamaguchi, Y. Matsuda, M. Suzuki, T. Sasaki, T. Fukase, Y. Yoshida, R. Settai, and Y. Onuki. *Physical Review Letters*, 86:2653, 2001.

[95] M.A. Tanatar, T. Ishiguro, H. Tanaka, and H. Kobayashi. *Physical Review B*, 66:134503, 2002.

[96] K. Izawa, H. Yamaguchi, T. Sasaki, and Y. Matsuda. *Physical Review Letters*, 88:027002, 2002.

[97] K. Izawa, H. Yamaguchi, Y. Matsuda, H. Shishido, R. Settai, and Y. Onuki. *Physical Review Letters*, 87:057002, 2001.

[98] K. Izawa, Y. Nakajima, J. Goryo, Y. Matsuda, S. Osaki, H. Sugawara, H. Sato, P. Thalmeier, and K. Maki. *Physical Review Letters*, 90:117001, 2003.

[99] A.V. Sologubenko, J. Jun, S.M. Kazakov, J. Karpinski, and H.R. Ott. *Physical Review B*, 66:014504, 2002.

[100] P. Martinez-Samper, H. Suderow, S. Vieira, J.P. Brison, N. Luchier, P. Lejay, and P.C. Canfield. *Physical Review B*, 67:014526, 2003.

[101] K.A.Moler *et al.* *Physical Review Letters*, 73:2744, 1994.

[102] S.J. Chen, C.F. Chang, H.L. Tsay, H.D. Yang, and J.-Y. Lin. *Physical Review B*, 58:R14753, 1998.

[103] W.A. MacFarlane, R.F. Kiefl, S. Dunsiger, J.E. Sonier, J. Chakhalian, J.E. Fischer, T. Yildirim, and K.H. Chow. *Physical Review B*, 58:1004, 1998.

[104] Kun Yang and S.L. Sondhi. *Physical Review B*, 57:8566, 1998.

[105] G.K. White. *Experimental Techniques in Low TemperatureP hysics.* Clarendon Press, Oxford, 1968.

[106] Juan H. Talpe, Victoria I. Bekeris, Maria J. Sanchez, and Gabriela Simonelli. *Review of Scientific Instruments*, 62:1054, 1991.

[107] Frank Pobell. *Matter and Methods at Low Temperatures, 2^{nd} Ed.* Springer-Verlag, Berlin -Hei delberg - New-York, 1996.

[108] Michio Watanabe, Masashi Morishita, and Youiti Ootuka. *Cryogenics*, 41:143, 2001.

[109] B.L. Brandt, D.W. Liu, and L.G. Rubin. *Review of Scientific Instruments*, 70:104, 1999.

[110] Z. Tešanović and P.D. Sacramento. *Physical Review Letters*, 80:1521, 1998.

[111] S. Vishveshwara, T. Senthil, and M.P.A. Fisher. *Physical Review B*, 61:6966, 2000.

[112] T. Jarlborg, A.A. Manuel, and M. Peter. *Physical Review B*, 27:4210, 1983.

[113] G.R. Stewart and B.L. Brandt. *Physical Review B*, 29:3908, 1984.

[114] R. Corcoran, N. Harrison, S.M. Hayden, P. Meeson, M. Springford, and P.J. van der Wel. *Physical Review Letters*, 72:701, 1994.

[115] D. Eckert and K.H. Berthel. *Cryogenics*, 15:479, 1975.

[116] T.J.B.M. Janssen *et al.* *Physical Review B*, 57:11698, 1998.

[117] M. Milewits, S.J. Williamson, and H. Taub. *Physical Review B*, 13:5199, 1976.

[118] R. Caton and R. Viswanathan. *Physical Review B*, 25:179, 1982.

[119] G.W. Webb, Z. Fisk, J.J. Engelhardt, and S.D. Bader. *Physical Review B*, 15:2624, 1977.

[120] M. Isino, T. Kobayashi, T. Toyota, N. andFukase, and Y. Muto. *Physical Review B*, 38:4457, 1988.

[121] J.A. Osborn. *Physical Review*, 67:351, 1945.

[122] A.P. Ramirez. *Physics Letters A*, 211:59, 1996.

[123] J.E. Graebner and M. Robbins. *Physical Review Letters*, 36:422, 1976.

[124] T. Terashima *et al. Solid State Communications*, 96:459, 1995.

[125] T. Terashima *et al. Physical Review B*, 56:5120, 1997.

[126] Smitha Vishveshwara, T. Senthil, and Matthew P.A. Fisher. *Physical Review B*, 61:6966, 2000.

[127] Smitha Vishveshwara and Matthew P.A. Fisher. *Physical Review B*, 64:174511, 2001.

[128] H. Kusunose, T.M. Rice, and M. Sigrist. *Physical Review B*, 66:214503, 2002.

[129] S. Lefebvre and *et. al. Physical Review Letters*, 85:5420, 2000.

[130] A. Lanzara, P.V. Bogdanov, X.J. Zhou, S.A. Kellar, D.L. Feng, E.D. Lu, T. Yoshida, H. Eisaki, A. Fujimori, K. Kishio, J.-I. Shimoyama, T. Noda, S. Uchida, Z. Hussain, and Z.-X. Shen. *Nature*, 412:510, 2001.

[131] R.J. Cava *et al. Nature*, 367:146, 1994.

[132] T. Siegrist *et al. Nature*, 367:254, 1994.

[133] P.C. Canfield, P.L. Gammel, and D.J. Bishop. *Physics Today*, October:40, 1998.

[134] J.W. Lynn, S. Skanthakumar, Q. Huang, S.K. Sinha, Z. Hossain, L.C. Gupta, R. Nagarajan, and C. Godart. *Physical Review B*, 55:6584, 1997.

[135] L.F. Mattheiss. *Physical Review B*, 49:13279, 1994.

[136] W.E. Pickett and D.J. Singh. *Physical Review Letters*, 72:3702, 1994.

[137] S.B. Dugdale, M.A. Alam, I. Wilkinson, R.J. Hughes, P.C. Fisher, I.R. andCanfield, T. Jarlborg, and G. Santi. *Physical Review Letters*, 83:4824, 1999.

[138] I.R. Fisher, J.R. Cooper, and Canfield. P.C. *Physical Review B*, 56:10820, 1997.

[139] K.D.D. Rathnayaka *et al. Physical Review B*, 55:8506, 1997.

[140] R.S. Gonnellia, V.A. Stepanovb, A. Morelloa, G.A. Ummarinoa, G. Behrc, G. Grawc, S.V. Shulgac, and S.-L. Drechslerc. *Physica C*, 341-348:1957, 2000.

[141] M. Nohara *et al. Journal of the Physical Society of Japan*, 66:1888, 1997.

[142] S.A. Carter *et al. Physical Review B*, 50:4216, 1994.

[143] H. Michor, T. Holubar, C. Dusekand, and G. Hilscher. *Physical Review B*, 52:16165, 1995.

[144] C.C. Hoellwarth, Klavins P., and R.N. Shelton. *Physical Review B*, 53:2579, 1996.

[145] P.M.C. Rourke, Johnpierre Paglione, F. Ronning, Louis Taillefer, and K. Kadowaki. *cond-mat/0210174*, 2002.

[146] P. Dervenagas *et al. Physical Review B*, 52:9839, 1995.

[147] H. Kawano *et al. Physical Review Letters*, 77:4628, 1996.

[148] C. Stassis *et al. Physical Review B*, 55:R8678, 1997.

[149] K.O. Cheon, I.R. Fisher, V.G. Kogan, P.C. Canfield, P. Miranovic, and P.L. Gammel. *Physical Review B*, 58:6463, 1998.

[150] M. Heinecke and K. Winzer. *Zeitschrift für Physik B*, 98:147, 1995.

[151] K.O. Cheon, I.R. Fisher, and P.C. Canfield. *Physica C*, 312:35, 1999.

[152] K. Izawa, K. Kamata, Y. Nakajima, Y. Matsuda, T. Watanabe, M. Nohara, H. Takagi, P. Thalmeier, and K. Maki. *Physical Review Letters*, 89:137006, 2002.

[153] M. Nohara *et al. Physica C*, 341-348:2177, 2000.

[154] M. Nohara *et al. Journal of the Physical Society of Japan*, 68:1078, 1999.

[155] K. Izawa *et al. Physical Review Letters*, 86:1327, 2001.

[156] T. Yokoya, T. Kiss, T. Watanabe, S. Shin, M. Nohara, H. Takagi, and T. Oguchi. *Physical Review Letters*, 85:4952, 2000.

[157] S.H. Simon and P.A. Lee. *Physical Review Letters*, 78:1548, 1997.

[158] E. Boaknin, R.W. Hill, C. Lupien, L. Taillefer, and P.C. Canfield. *Physica C*, 341-348:1845, 2000.

[159] B.D. Hennings, D.G. Naugle, and P.C. Canfield. *Physical Review B*, 66:214512, 2002.

[160] B.I. Belevtsev, B.D. Hennings, K.D.D. Rathnayaka, and D.G. Naugle. *cond-mat/0301207*, 2003.

[161] M. Sera, S. Kobayash, M. Hiroi, N. Kobayashi, H. Takeya, and K. Kadowaki. *Physical Review B*, 54:3062, 1996.

[162] Cyril Proust, Etienne Boaknin, R. W. Hill, Louis Taillefer, and A. P. Mackenzie. *Physical Review Letters*, 89:147003, 2002.

[163] M. Bullock *et al. Physical Review B*, 57:7916, 1998.

[164] W.F. Vinen *et al. Physica A*, 55:94, 1971.

[165] B.S. Shivaram *et al. Physical Review Letters*, 56:1078, 1986.

[166] K. Maki, P. Thalmeier, and H. Won. *Physical Review B*, 65:R140502, 2002.

[167] M.R. Eskildsen, P.L. Gammel, B.P. Barber, A.P. Ramirez, D.J. Bishop, N.H. Andersen, K. Mortensen, C.A. Bolle, C.M. Lieber, and P.C. Canfield. *Physical Review Letters*, 79:487, 1997.

[168] Masanori Ichioka and Kazushige Machida. *Physical Review B*, 65:224517, 2002.

[169] T. Jacobs *et al. Physical Review B*, 52:R7022, 1995.

[170] In-Sang Yang *et al. Physical Review B*, 62:1291, 2000.

[171] Y. Iwamoto, K. Ueda, and T. Kohara. *Solid State Communications*, 113:615, 2000.

[172] Toshikazu Ekino, Hironobo Fujii, Makato Kosugi, Yuji Zenitani, and Jun Akimitsu. *Physical Review B*, 53:5640, 1996.

[173] C. Lupien, W.A. MacFarlane, Cyril Proust, Louis Taillefer, Z.Q. Mao, and Y. Maeno. *Physical Review Letters*, 86:5986, 2001.

[174] Tuson Park, M.B. Salomon, Eun Mi Choi, Heon Jung Kim, and Sung-Ik Lee. *Physical Review Letters*, 90:177001, 2003.

[175] Guangfeng Wang and Kazumi Maki. *Physical Review B*, 58:6493, 1998.

[176] J.P. Carbotte. *Review of Modern Physics*, 62:1027, 1990.

[177] S. Manalo and E. Schachinger. *Journal of Low Temperature Physics*, 149:149, 2001.

[178] G. Binnig *et al. Physical Review Letters*, 45:1352, 1980.

[179] H.J. Choi *et al. Nature*, 418:758, 2002.

[180] M. Iavarone, G. Karapetrov, A.E. Koshelev, W.K. Kwok, G.W. Crabtree, D.G. Hinks, W.N. Kang, Eun-Mi Choi, Hyun Jung Kim, Hyeong-jin Kim, and S.I. Lee. *Physical Review Letters*, 89:187002, 2002.

[181] G. Rubio-Bollinger, H. Suderow, and S. Vieira. *Physical Review Letters*, 86:5582, 2001.

[182] P. Martinez-Samper, J.G. Rodrigo, G. Rubio-Bollinger, H. Suderow, S. Vieira, Lee S., and S. Tajima. *Physica C*, 385:233, 2003.

[183] T. Yokoya *et al. Science*, 294:2518, 2001.

[184] E.A. Yelland, J.R. Cooper, A. Carrington, N.E. Hussey, P.J. Meeson, S. Lee, A. Yamamoto, and S. Tajima. *Physical Review Letters*, 8:217002, 2002.

[185] J.R. Cooper, A. Carrington, P.J. Meeson, E.A. Yelland, N.E. Hussey, L. Balicas, S. Tajima, S. Lee, S.M. Kazakov, and J. Karpinski. *Physica C*, 385:75, 2003.

[186] S. NishiZaki *et al. Journal of the Physical Society of Japan*, 69:572, 2000.

[187] D.F. Agterberg *et al. Physical Review Letters*, 78:3374, 1997.

[188] M.E. Zhitomirsky and T.M. Rice. *Physical Review Letters*, 87:057001, 2001.

[189] F. Bouquet *et al. Physical Review Letters*, 89:257001, 2002.

[190] A.E. Koshelev and A.A. Golubov. *Physical Review Letters*, to appear, 2003.

[191] J. Sonier *et al. Physical Review Letters*, 82:4914, 1999.

[192] R. Corcoran *et al. Journal of Physics: Condensed Matter*, 6:4479, 1994.

[193] J. Edwards and R.F. Frindt. *Journal of Physics: Chemistry of Solids*, 32:2217, 1971.

[194] D.E. Prober, Schwall R.E., and M.R. Beasley. *Physical Review B*, 21:2717, 1980.

[195] D. Sanchez *et al. Physica B*, 204:167, 1995.

[196] Michio Naito and Shoji Tanaka. *Journal of the Physical Society of Japan*, 51:219, 1982.

[197] V.I. Beletskii, O.A. Gavrenko, B.A. Merisov, M.A. Obolenskii, A.V. Sologubenko, G. Ya. Khadjai, and Kh. B. Chashka. *Low Temperature Physics*, 24:273, 1998.

[198] Y. Muto, N. Tokoya, K. Nato, and A. Hoshi. *Physics Letters A*, 45:99, 1973.

[199] J.E. Sonier *et al. Physical Review Letters*, 79:1742, 1997.

[200] K. Takita and K. Masuda. *Journal of Low Temperature Physics*, 58:127, 1985.

[201] R.I. Miller, R.F. Kiefl, J.H. Brewer, J. Chakhalian, S. Dunsinger, G.D. Morris, J.E. Sonier, and W.A. MacFarlane. *Physical Review Letters*, 85:1540, 2000.

[202] H. Drulis, Z.G. Xu, J.W. Brill, L.E. De Long, and J.C. Hou. *Physical Review B*, 44:4731, 1991.

[203] M.H. Jericho, A.M. Simpson, and R.F. Frindt. *Physical Review B*, 22:4907, 1980.

[204] H.F. Hess *et al. Physical Review Letters*, 64:2711, 1990.

[205] H.F. Hess *et al. Physica B*, 169:422, 1991.

[206] Th. Straub, Th. Finteis, R. Claessen, P.Ste iner, S. Hüfner, P.Bl aha, C.S. Oglesby, and E. Bucher. *Physical Review*, 82:4504, 1999.

[207] Bednorz J.G. and K.A. Müller. *Zeitschrift für Physik B*, 64:189, 1986.

[208] M.B. Maple. *Journal of Magnetism and Magnetic Materials*, 177-181:18, 1998.

[209] Tom Timusk and Bryan Statt. *Rep. Prog. Phys.*, 62:61, 1999.

[210] J.L. Tallon and J.W. Loram. *Physica C*, 349:53, 2001.

[211] S.C. Zhang. *Science*, 275:1089, 1997.

[212] S. Chakravarty, R.B. Laughlin, D.K. Morr, and C. Nayak. *Physical Review B*, 63:094503, 2001.

[213] M. Franz and Z. Tešanović. *Physical Review Letters*, 87:257003, 2001.

[214] L. Ozyuzer, Z. Yusof, J.F. Zasadzinski, R. Mogilevsky, D.G. Hinks, and K.E. Gray. *Physical Review B*, 57:R3245, 1998.

[215] D.M. Broun, D.C. Morgan, R.J. Ormeno, S.F. Lee, A.W. Tyler, A.P. Mackenzie, and .R. WaldramJ. *Physical Review B*, 56:R11443, 1997.

[216] A.P. Mackenzie *et al.* *Physical Review Letters*, 71:1238, 1993.

[217] M.A.G. Aranda, D.C. Sinclair, J.P. Attfield, and A.P. Mackenzie. *Physical Review B*, 51:12747, 1995.

[218] A.W. Tyler. *Ph.D. Thesis, Cambridge press*, 1998.

[219] Yuichi Shimakawa. *Physica C*, 204:247, 1993.

[220] B. Batlogg, H.Y. Hwang, H. Takagi, R.J. Cava, H.L. Kao, and J. Kwo. *Physica C*, 235-240:130, 1994.

[221] G.S. Boebinger, Y. Ando, A. Passner, T. Kimura, M. Okuya, J. Shimoyama, K. Kishio, K. Tamasaku, N. Ichikawa, and S. Uchida. *Physical Review Letters*, 77:5417, 1996.

[222] S. Ono, Yoichi Ando, T. Murayama, F.F. Balakirev, J.B. Betts, and G.S. Boebinger. *Physical Review Letters*, 85:638, 2000.

[223] A. Carrington, A.P. Mackenzie, and A. Tyler. *Physical Review B*, 54:R3788, 1996.

[224] A.P. Mackenzie *et al.* Private communication.

[225] A. Carrington *et al.* *Physical Review B*, 49:13243, 1994.

[226] J.L. Tallon, C. Bernhard, H. Shaked, R.L. Hitterman, and J.D. Jorgensen. *Physical Review B*, 51:12911, 1995.

[227] A.P. Mackenzie, S.R. Julian, D.C. Sinclair, and C.T. Lin. *Physical Review B*, 53:5848, 1996.

[228] A.P. Mackenzie, S.R. Julian, A. Carrington, G.G. Lonzarich, D.C.J. Walker, J.R. Cooper, and D.C. Sinclair. *Physica C*, 235-240:233, 1994.

[229] N.E. Hussey, J.M. Cooper, J.R. andWheatly, I.R. Fischer, A. Carrington, A.P. Mackenzie, C.T. Lin, and O. Milat. *Physical Review Letters*, 76:122, 1996.

[230] A.W. Tyler, Yoichi Ando, F.F. Balakirev, A. Passner, G.S. Boebinger, A.J. Schofield, A.P. Mackenzie, and O. Laborde. *Physical Review B*, 57:R728, 1998.

[231] P. Fournier, P. Mohanty, E. Maiser, S. Darzens, T. Venkatesan, C.J. Lobb, G. Czjzek, R.A. Webb, and R.L. Greene. *Physical Review Letters*, 81:4720, 1998.

[232] J.W. Loram, K.A. Mirza, J.M. Wade, J.R. Cooper, and W.Y. Liang. *Physica C*, 235-240:134, 1994.

[233] A. Greco and A. Dobry. *Solid State Communications*, 122:111, 2002.

[234] N.D. Mathur *et al. Nature*, 39:394, 1998.

[235] S.A. Grigera, R.S. Perry, A.J. Schofield, M. Chiao, S.R. Julian, G.G. Lonzarich, S.I. Ikeda, Y. Maeno, A.J. Millis, and A.P. Mackenzie. *Science*, 294:329, 2001.

[236] P. Gegenwart, J. Custers, C. Geibel, K. Neumaier, T. Tayama, K. Tenya, O. Trovarelli, and F. Steglich. *Physical Review Letters*, 89:056402, 2002.

[237] Johnpierre Paglione, M.A. Tanatar, D.G. Hawthorn, Etienne Boaknin, R.W. Hill, F. Ronning, M. Sutherland, Louis Taillefer, C. Petrovic, and P.C. Canfield. *cond-mat/0212502*, 2002.

[238] K.J. Sun, W.P. Winfree, M.-F. Xu, M. Levy, Bimal K. Sarma, A.K. Singh, M.S. Osofsky, and V.M. Le Tourneau. *Physical Review B*, 42:2569, 1990.

[239] C.M. Varma, P.B. Littlewoods, S. Schmitt-Rink, E. Abrahams, and A.E. Ruckenstein. *Physical Review Letters*, 63:1996, 1989.

[240] D.G. Hawthorn, R.W. Hill, C. Proust, F. Ronning, Mike Sutherland, Etienne Boaknin, C. Lupien, M.A. Tanatar, Johnpierre Paglione, S. Wakimoto, H. Zhang, Louis Taillefer, T. Kimura, M. Nohara, H. Takagi, and N.E. Hussey. *Physical Review Letters*, 90:197004, 2003.

[241] Romain Bel, Kamran Behnia, Cyril Proust, Peter van der Linden, Duncan Maude, and Sergey I. Vedeneev. *cond-mat/0304111*, 2003.

[242] C. Castellani *et al. Physical Review Letters*, 59:477, 1987.

[243] J. Takeya, Yoichi Ando, Seiki Komiya, and X.F. Sun. *Physical Review Letters*, 88:077001, 2002.

[244] X.F. Sun, Seiki Komiya, J. Takeya, and Yoichi Ando. *Physical Review Letters*, 90:117004, 2003.

[245] B Lake, G. Aeppli, K.N. Clausen, N.E. Hussey, N. Mangkorntong, M. Nohara, H. Takagi, T.E. Mason, and A. Schröder. *Science*, 291:1759, 2001.

[246] V.F. Mitrovic, E.E. Sigmund, M. Eschrig, H.N. Bachman, W.P. Halperin, A.P. Reyes, P. Kuhns, and W.G. Moulton. *Nature*, 413:501, 2001.

[247] R.I. Miller, R.F. Kiefl, J.H. Brewer, J.E. Sonier, J. Chakhalian, S. Dunsiger, G.D. Morris, A.N. Price, D.A. Bonn, W.H. Hardy, and R. Liang. *Physical Review Letters*, 88:137002, 2002.

[248] A. Houghton, S. Lee, and J.B. Marston. *Physical Review B*, 65:R220503, 2002.

[249] Xiao Yang and Chetan Nayak. *Physical Review B*, 65:064523, 2002.

[250] Wonkee Kim and J.P. Carbotte. *Physical Review B*, 66:033104, 2002.

[251] V.P. Shaparov, S.G. Gusynin and H. Beck. *Physical Review B*, 67:144509, 2003.

[252] K.K. Lee, A.S. Alexandrov, and W.Y. Liang. *cond-mat/0301559*, 2003.

[253] R.S. Liu, S.D. Hughes, R.J. Angel, T.P. Hackwell, A.P. Mackenzie, and P.P. Edwards. *Physica C*, 198:203, 1992.

[254] Douglas R. Niven and Robert A. Smith. *cond-mat/0301451*, 2003.

[255] T. Senthil and Matthew P.A. Fisher. *Physical Review Letters*, 86:292, 2001.

[256] T. Senthil and Matthew P.A. Fisher. *Physical Review B*, 63:134521, 2001.

[257] C. Lannert, Matthew P.A. Fisher, and T. Senthil. *Physical Review B*, 64:014518, 2001.

[258] T. Senthil and Matthew P.A. Fisher. *Physical Review B*, 64:214511, 2001.

[259] D.A. Bonn, Janice C. Wynn, Brian W. Gardner, Yu-Ju Lin, Ruixing Liang, W.N. Hardy, J.R. Kirtley, and K.A. Moler. *Nature*, 414:887, 2001.

[260] J.C. Wynn, D.A. Bonn, B.W. Gardner, Yu-Ju Lin, Ruixing Liang, W.N. Hardy, J.R. Kirtley, and K.A. Moler. *Physical Review Letters*, 87:197002, 2001.

[261] J.R. Kirtley, C.C. Tsuei, H. Raffy, Z.Z. Li, V.G. Kogan, J.R. Clem, and K.A. Moler. *cond-mat/0103474*, 2001.

[262] S. Nakamae, K. Behnia, L. Balicas, F. Rullier-Albenque, H. Berger, and T. Tamegai. *Physical Review B*, 63:184509, 2001.

[263] May Chiao, Christian Lupien, Bojana Popić, Robert Gagnon, and Louis Taillefer. *Physical Review Letters*, 82:2943, 1999.

[264] Louis Taillefer and R.W. Hill. *Physics in Canada*, 56:237, 2000.

[265] Z.X. Shen. *Private communication.*

[266] D.G. Hawthorn *et al. To be published.*

[267] J.C. Campuzano *et al. Physical Review Letters*, 83:3709, 1999.

[268] M.R. Norman *et al. Nature*, 392:157, 1998.

[269] P.J. White, Z.-X. Shen, C. Kim, J.M. Harris, A.G. Loeser, P. Fournier, and A. Kapitulnik. *Physical Review B*, 54:R15669, 1996.

[270] A.G. Loeser, Z.-X. Shen, M.C. Shabel, C. Kim, M. Zhang, A. Kapitulnik, and P. Fournier. *Physical Review Letters*, 54:14185, 1996.

[271] Subir Sachdev. *Science*, 288:475, 2000.

[272] Matthias Vojta, Ying Zhang, and Subir Sachdev. *Physical Review B*, 62:6721, 2000.

[273] Y. Dagan and G. Deutscher. *Physical Review Letters*, 87:177004, 2001.

[274] A. Sharoni, O. Millo, A. Kohen, Y. Dagan, R. Beck, G. Deutscher, and G. Koren. *Physical Review B*, 65:134526, 2002.

[275] E.T. Swartz. *Review of Scientific Instruments*, 57:2848, 1986.

[276] C. Opagiste, G. Triscone, M. Couach, T.K. Jondo, J.-L. Jorda, A. Junod, A.F. Khoder, and J. Muller. *Physica C*, 213:17, 1993.

[277] A. Hosseini, R. Harris, Saeid Kamal, P. Dosanjh, J. Preston, Ruixing Liang, W.N. Hardy, and D.A. Bonn. *Physical Review B*, 60:1349, 1999.

[278] D.A. Bonn, S. Kamal, Kuan Zhang, Ruixing Liang, D.J. Baar, E. Klein, and W.N. Hardy. *Physical Review B*, 50:4051, 1994.

[279] Shih-Fu Lee, D.C. Morgan, R.J. Ormeno, D.M. Broun, R.A. Doyle, J.R. Waldram, and K. Kadowaki. *Physical Review Letters*, 77:735, 1996.

[280] Y.J. Uemura, A. Keren, L.P. Le, G.M. Luke, W.D. Wu, Y. Kubo, T. Manako, Y. Shimakawa, M. Subramanian, J.L. Cobb, and J.T. Markert. *Nature*, 364:605, 1993.

[281] Ch. Niedermayer, C. Bernhard, U. Binninger, H. Glückler, J.L. Tallon, E.J. Ansaldo, and J.I. Budnick. *Physical Review Letters*, 71:1764, 1993.